



THÈSE DE DOCTORAT
DE L'UNIVERSITÉ PSL

Préparée à l'Observatoire de Paris

**Revisiting mass estimates of the Milky Way and nearby
spiral galaxies**

Soutenue par

Yongjun Jiao

Le xx mois 202x

École doctorale n°127

**Astronomie et
astrophysique d'Ile de
France**

Spécialité

Astrophysique

Préparée au

Galaxies, Etoiles, Physique et
Instrumentation

Composition du jury :

Jacques LASKAR
Observatoire de Paris

*Président du jury
Examinateur*

Xiaowei LIU
Yunnan University

Rapporteur

Stacy MCGAUGH
Case Western Reserve University

Rapporteur

Philippe AMRAM
Université Aix-Marseille

Examinateur

Carine BABUSIAUX
Université Grenoble Alpes

Examinateur

Annie ROBIN
Université de Franche-Comté

Examinateur

François HAMMER
Observatoire de Paris

Directeur de thèse

Yanbin YANG
Observatoire de Paris

Invité

Remerciements

I can no longer remember where my original interest in astronomy came from. Perhaps it was in quiet sleepiness under a sky full of stars, or the excitement by the story of the Cowherd and the Weaver Girl, or maybe it was the imagination of soaring into the heavens like Su Shi, transcending this world to explore the cosmos. However, the moment that really opened the door of astronomy for me was that unforgettable afternoon when my supervisor, Francois Hammer, spoke to me with so much passion about the Milky Way and its dwarf galaxies. Since then, Francois has been my closest guide in the field of astronomy. His guidance has been crucial in completing my Ph.D.

I am also very grateful to my co-supervisor, Yanbin Yang, whose scientific and technical mentorship has been invaluable during my Ph.D. His support has been a cornerstone in shaping my research, and I deeply appreciate his mentorship.

I would like to thank Jianling Wang, Haifeng Wang, Laurent Chemin, Philippe Amram, Gary Mamon, and other teachers, all of whom played significant roles in my Ph.D. work. Whether through sharing data, offering new perspectives, or pointing out critical corrections, their input has enriched my research and deepened my understanding of astronomy.

I would also like to thank my friends in Paris, Yuhao Liu, Yin Guo, Jiali Zhong, Yilun Li, Ting Tan, Akib Istiak, Neel Kolhe, and my friends in China, including Shizheng Wang, Yilei Chen, Yilong Shi, Yuliang Li, Xiangyu Fang, and many others not named here. You have filled this journey with friendship and happiness, making the challenges of this path feel lighter and less solitary. I truly appreciate your presence and encouragement.

A special thanks to my girlfriend, Fan Liu, whose unwavering support and constant encouragement have been a source of strength throughout this journey.

Finally, I would like to express my deepest gratitude to my parents, my grandmother, and all of my family in China. Their unconditional love and support have given me the courage to pursue my dreams in a foreign land.

Résumé

La masse est une quantité physique fondamentale dans l'étude des galaxies, influençant notre compréhension de la formation et de l'évolution des galaxies. Dans cette thèse, j'étudie les méthodes d'estimation de la masse des galaxies, en me concentrant sur la Voie Lactée et les galaxies spirales voisines.

La mission *Gaia* fournit des données en six dimensions sur les étoiles, permettant de dériver la courbe de rotation de la Voie Lactée la plus précise. En utilisant la courbe de rotation basée sur *Gaia* DR2, j'ai comparé divers profils de matière sombre et j'ai constaté que le profil Einasto fournit une meilleure estimation de la masse par rapport aux profils NFW et gNFW, qui sont trop peu profonds pour ajuster la courbe de rotation décroissante. Avec *Gaia* DR3, j'ai dérivé une nouvelle courbe de rotation de la Voie Lactée, menant une analyse complète des incertitudes systématiques. Pour la première fois, nous avons détecté un déclin Képlérien dans la courbe de rotation, commençant au bord du disque (19 kpc). Nos estimations actuelles placent la masse de la Galaxie à environ $2,5 \times 10^{11} M_{\odot}$ dans 25 kpc, avec une limite supérieure de $5,6 \times 10^{11} M_{\odot}$. En conséquence, la fraction de masse baryonique semble plus grande que l'estimation universelle du modèle Λ CDM, suggérant que la Voie Lactée ne fait pas face au problème des baryons manquants, mais plutôt à un excès de baryons. Cette découverte remet en question notre compréhension de la distribution de masse entre la matière sombre et les baryons pour notre Galaxie.

Le déclin Képlérien observé dans la courbe de rotation de la Voie Lactée contraste avec les courbes de rotation plates trouvées dans la plupart des galaxies spirales. Cependant, les observations suggèrent que la plupart des galaxies spirales ont subi une grande fusion en moyenne il y a environ 6 Gyr. Cela m'a amené à étendre mes recherches aux galaxies voisines, évaluant la fiabilité de leurs courbes de rotation à grands rayons pour déterminer si ces courbes de rotation suivent la distribution de masse après des fusions récentes. J'ai sélectionné neuf galaxies des bases de données SPARC et THINGS et, en examinant leurs caractéristiques morphologiques, leurs structures cinématiques et leurs histoires de formation stellaire, j'ai conclu que certaines d'entre elles ont probablement connu une grande fusion récente. En comparant ces observations avec des simulations hydrodynamiques, j'ai évalué l'impact de ces fusions sur les courbes de rotation et les estimations de masse. Cette étude suggère que l'utilisation des courbes de rotation pour estimer la distribution de masse des galaxies spirales à grands rayons doit être abordée avec prudence, en particulier l'état d'équilibre des galaxies.

Le scénario de formation hiérarchique prédit une corrélation entre le temps de chute des satellites dans le halo de la Galaxie et leur énergie de liaison, une relation soutenue par des simulations cosmologiques avec une faible dispersion. Nous avons dérivé cette relation pour

diverses simulations cosmologiques. En comparant ces relations avec les mesures de *Gaia* des amas globulaires et des galaxies naines autour de la Voie Lactée avec une hypothèse de potentiel de la Voie Lactée, nous avons constaté que cette relation suggère que la plupart des galaxies naines sont arrivées bien plus récemment dans le halo de la Galaxie et qu'une masse de la Galaxie de $2 \times 10^{11} M_{\odot}$ dans les 21 kpc s'aligne bien avec la relation prédictive entre le temps de chute et l'énergie de liaison.

Mots clés :

Galaxies: cinématique et dynamique, Galaxies: contenu stellaire, Galaxies: structure, Galaxies: paramètres fondamentaux

Abstract

The mass is a fundamental physical quantity in galaxy studies, influencing our understanding of galaxy formation and evolution. In this thesis, I investigate mass estimation methods for galaxies, focusing on the Milky Way (MW) and nearby spiral galaxies.

The *Gaia* mission provides six-dimensional data of stars, enabling the derivation of the most accurate MW rotation curve (RC). Using the RC based on *Gaia* DR2, I compared various dark matter (DM) profiles and found that the Einasto profile provides a better mass estimate compared to the NFW and gNFW profiles, which are too shallow to fit the declining RC. With *Gaia* DR3, I derived a new MW RC, conducting a comprehensive analysis of systematic uncertainties. For the first time, we detected a Keplerian decline in the RC, starting at the edge of the disk (19 kpc). Our current estimates place the MW mass within 25 kpc at approximately $2.5 \times 10^{11} M_{\odot}$, with an upper limit of $5.6 \times 10^{11} M_{\odot}$. Consequently, the baryonic mass fraction appears larger than the universal estimate from the Λ CDM model, suggesting that the MW may not face the missing baryon problem, but rather an excess baryon problem. This finding challenges our current understanding of the mass distribution between DM and baryons for our Galaxy.

The observed Keplerian decline in the MW RC contrasts with the flat RCs found in most spiral galaxies. However, observations suggest that most spiral galaxies underwent a major merger on average approximately 6 Gyr ago. This led me to extend my research to nearby galaxies, assessing the reliability of their RCs at large radii to determine whether these RCs follow the mass distribution after recent major mergers. I selected nine galaxies from the SPARC and THINGS databases and, by examining their morphological features, kinematical structures, and star formation histories, concluded that some of them likely experienced a recent major merger. By comparing these observations with hydrodynamical simulations, I assessed the impact of these mergers on the RCs and mass estimations. This study suggests that using RCs to estimate the mass distribution of spiral galaxies at large radii should be approached with caution, particularly regarding the equilibrium state of galaxies.

The hierarchical formation scenario predicts a correlation between the infall lookback time of satellites and their binding energy, a relationship supported by cosmological simulations with a small scatter. We derived this relation for various cosmological simulations and compared it with *Gaia* measurements of globular clusters and dwarf galaxies around the MW, assuming an MW potential. Our results suggest that most dwarf galaxies are newcomers in the MW halo, and that the MW mass of $2 \times 10^{11} M_{\odot}$ within 21 kpc aligns well with the predicted relationship between infall lookback time and binding energy.

Keywords : Galaxies: kinematics and dynamics, Galaxies: stellar content, Galaxies: structure, Galaxies: fundamental parameters

Table des matières

Remerciements	i
Résumé	ii
Abstract	iv
Table des matières	v
Liste des figures	ix
Liste des tableaux	xi
1 Introduction	0
1 Introduction	1
2 The Classification of Galaxies	1
3 Formation and Evolution of Galaxies	5
3.1 Cosmological Context	5
3.2 Monolithic Collapse Model	6
3.3 The Hierarchical Merger Model	8
4 Rotation Curve	13
5 Dark Matter	14
6 Milky Way	16
6.1 Structure of the Milky Way	17
6.2 The Milky Way Mass	21
7 Structure of This Dissertation	24
2 Milky Way	25
1 Introduction	26
1.1 Milky Way rotation curves before <i>Gaia</i>	26
1.2 Revolution of <i>Gaia</i>	27
2 Milky Way mass based on the rotation curve from <i>Gaia DR2</i>	28
2.1 Subsequent summary of Paper I	28
3 Milky Way rotation curve from <i>Gaia DR3</i>	29
3.1 Subsequent summary of Paper II	29
3.2 Discussion about Paper II	30
3.2.1 Systematic uncertainties	30
3.2.2 First tests on varying scale length of the MW disk	31
3.2.3 Is the MW disk out of equilibrium ?	33
4 A further analysis of the Milky Way rotation curve	35

4.1	Introduction	35
4.2	Methodology	37
4.2.1	Resampling the data from Ou et al. (2024)	37
4.2.2	Scale length estimation	37
4.2.3	Systematic uncertainties	42
4.3	Rotation curve and maximal mass estimation	43
4.4	Discussion	47
4.4.1	Compare with MW mass based on Gaia DR2	47
4.4.2	Keplerian decline	48
4.5	Conclusion	49
Appendix A : Which Milky Way masses are consistent with the slightly declining 5-25 kpc rotation curve ? (Paper I)	50	
Appendix B : Detection of the Keplerian decline in the Milky Way rotation curve (Paper II)	60	
3	Nearby galaxies	74
1	Introduction	75
2	Galaxy sample	76
3	Studies of NGC 3521	79
3.1	Morphology of NGC 3521	79
3.1.1	Optical images	79
3.1.2	HI images	80
3.2	Kinematics	81
3.2.1	Rotation curve of NGC 3521	81
3.2.2	Position-velocity diagram of NGC 3521	82
3.3	Ionized properties of NGC 3521	83
3.4	Stellar population of NGC 3521	85
3.4.1	Spectrum and photometry fit of NGC 3521	87
3.4.2	Estimation of last major star formation episode of NGC 3521	88
4	Hydrodynamical simulations	91
4.1	Comparison of HI observation	91
4.2	Comparison of position-velocity diagram	95
4.3	Analysis of rotation curve from mock HI observation	96
5	Discussion	98
5.1	Could we consider NGC 3521 experienced a recent major merger ?	98
5.2	Other galaxies	100
5.2.1	NGC 2841	100
5.2.2	NGC 5055	100
5.2.3	NGC 6946	100
5.2.4	NGC 7331	100
4	Dwarf galaxies	105
1	Introduction	106
1.1	Historical perspective	106
1.2	Observations	107
1.2.1	Surface brightness	107
1.2.2	Kinematics	108
1.3	Ram-pressure and tidal shock scenario	110
1.4	MW mass estimator	114
2	Comparison to cosmological simulations	116

Table des matières

2.1	Simulation samples	117
2.2	Methodology	119
2.3	Results	126
2.4	Discussion	128
3	Fornax	134
3.1	Data	134
3.2	Models and Results	137
3.3	Discussion	140
4	Conclusion	145
	Discussion	146
1	Is the Milky Way an exceptional galaxy ?	149
2	Could we consider all spiral galaxies at equilibrium ?	152
3	Are dwarf galaxies around the Milky Way dark matter dominated ?	155
4	Gas component should be considered more carefully	157
	Conclusion et perspectives	159
1	Conclusions (English version)	159
2	Conclusions (French version)	160
3	Perspectives	161
	Liste des publications	162
	Bibliographie	163

Liste des figures

1.1	Galaxy classification diagrams	3
1.2	Evolution of Hubble sequence	12
1.3	The Milky Way panorama and its bulge model	18
1.4	The spiral structure of the Milky Way.	20
1.5	MW mass estimates	23
2.1	The Milky Way rotation curve before <i>Gaia</i>	27
2.2	MW RC with constant scale lengths	31
2.3	MW RC with decreasing and increasing scale lengths	32
2.4	MW RC with step decreasing scale lengths	32
2.5	MW RC with step decreasing scale lengths	33
2.6	Disc-like orbit of an outer disk star	34
2.7	High eccentric orbit of an outer disk star	35
2.8	v_ϕ versus v_r for the sample stars from Ou et al. (2024)	36
2.9	Uncertainty in distances of selected stars	37
2.10	<i>H</i> -band magnitude distribution of selected stars	39
2.11	Fraction of stars in each bin with sufficient numbers of visits	39
2.12	Radial distribution of selected stars	40
2.13	Difference in the inferred circular velocity for the truncated exponential models .	41
2.14	Fits of truncated radial density profile	41
2.15	Systematic uncertainties in the circular velocity curve	43
2.16	Re-sampled circular velocity of the Milky Way	45
2.17	Best-fit and maximal mass estimation for RC including the cross term with Einasto profile	46
2.18	Best-fit and maximal mass estimation for RC including the splitting data with Einasto profile	46
2.19	Best-fit mass estimations for RCs with NFW profile	47
2.20	Maximum and average χ^2 probabilities for different baryonic models	47
2.21	Maximal mass fits for baryonic model G2 CM with Einasto mass profile.	48
2.22	Same figure as Figure 2.21 but for baryonic model G2 J.	48
3.1	Optical images of NGC 3521.	79
3.2	Optical and HI images of NGC 3521.	80
3.3	Rotation curves of NGC 3521	81
3.4	Position-velocity diagram from THINGS	82
3.5	Spectra of NGC 3521	84
3.6	Emission-line diagnostic diagram for NGC 3521	85
3.7	M31 Star Formation History	86

3.8	Correction of photometry data of NGC3521	88
3.9	Spectrum-only fit for NGC 3521	89
3.10	pPXF fit for NGC 3521 with spectrum and photometry	90
3.11	Age distribution of the stellar population of NGC 3521	90
3.12	Star formation history of the hydrodynamical simulation	92
3.13	NGC 3521 channel maps	93
3.14	Channel maps of mock HI observation	94
3.15	Comparison of observational HI image with mock HI observation	95
3.16	Comparison of the velocity field from THINGS and simulation	96
3.17	Comparisons of position-velocity diagrams	96
3.18	Rotation curve from mock HI observation	98
3.19	Emission-line diagnostic diagram for selected galaxies	101
3.20	Spectra-only fits of the selected galaxies	102
3.21	Spectra and photometry fits of the selected galaxies	102
3.22	Age distribution of the stellar population of the selected galaxies	103
3.23	Age distribution of the stellar population of the selected galaxies	104
4.1	Census of Milky Way dwarf galaxies	107
4.2	Velocity dispersion profiles observed for 8 classical dSphs.	109
4.3	Dynamical M/L ratio as a function of luminosity for dwarf galaxies	111
4.4	Cumulative distribution of time to reach the pericenter.	112
4.5	Lookback time as a function of binding energy	113
4.6	Histograms of the eccentricity distribution of GCs and dwarfs	115
4.7	Relation of R_{200m} and R_{200c} for Auriga	120
4.8	Example of calculation of infall time for Auriga simulations.	121
4.9	Total velocity versus infall look-back time	122
4.10	Potential of DM particles for Auriga level 3 halo 27.	124
4.11	Relation between infall look-back time and the logarithm of the binding energy. .	125
4.12	Lookback infall time versus binding energy for FIRE2 simulations	130
4.13	Lookback infall time versus binding energy for FIRE2 simulations	131
4.14	Lookback infall time versus binding energy for Auriga simulations	132
4.15	Lookback infall time versus binding energy for Auriga simulations	133
4.16	Morphology of Fornax	136
4.17	Surface density profile of Fornax sample S_0	142
4.18	Surface density profile of Fornax sample S_1	143
4.19	Surface density profile of Fornax sample S_2	144
5.1	Relation between baryonic mass and rotation velocity	147
5.2	Comparison between Einasto and gNFW profile fit	151
5.3	Reduced χ^2 versus virial mass	152
5.4	RC of M31	154

Liste des tableaux

2.1	Measurements of the re-sampled circular velocity of the Milky Way	44
3.1	Selected galaxy sample.	78
3.2	Stellar population synthesis models	87
3.3	Clues of a recent major merger of NGC 3521	99
3.4	Summary of other galaxies	101
4.1	Selected FIRE-2 simulations	118
4.2	Selected Auriga simulations	119
4.3	Best-fit parameters to mass profile for FIRE2 simulation	123
4.4	Best-fitting parameters of different density profiles for Fornax	139

Chapitre 1

Introduction

Contents

1	Introduction	1
2	The Classification of Galaxies	1
3	Formation and Evolution of Galaxies	5
3.1	Cosmological Context	5
3.2	Monolithic Collapse Model	6
3.3	The Hierarchical Merger Model	8
4	Rotation Curve	13
5	Dark Matter	14
6	Milky Way	16
6.1	Structure of the Milky Way	17
6.2	The Milky Way Mass	21
7	Structure of This Dissertation	24

1 Introduction

The vast expanse of stars scattered across the night sky has captivated humanity's imagination for millennia, sparking a profound curiosity about the mysteries of astronomy. Ancient civilizations, each in their own way, sought to unravel the secrets of the heavens. In ancient China, the stars were considered as celestial deities. The most attractive continuous band of light traversing the sky, the *Milky Way*, was referred to as the *Sliver River* and imagined to be a heavenly river created by the Queen Mother to separate *the Cowherd* (Altair) and *the Weaver Girl* (Vega). Greek mythology depicted it as the milk of the goddess Hera, spilled across the sky.

In 1610, Galileo Galilei first realized that this Milky Way is a vast collection of individual stars. By the mid-18th century, to explain its circular distribution across the sky, Immanuel Kant (Kant, 1755) and Thomas Wright (Wright, 1750) proposed that the Galaxy must be a stellar disk and that our Solar System is merely one component within that disk. Kant further expanded upon this idea by suggesting that if our galaxy were finite, the faint, diffuse *elliptical nebulae* observed could represent distant, disk-like systems similar to the Milky Way, but located far beyond its bounds. He called these objects *island universes*. The true nature of *island universes*, now known as galaxies, became the subject of extensive investigation. Although we now know that many of these objects are either star clusters or gaseous nebulae within the Milky Way, at the time, there was significant debate over whether these nebulae were located within our Galaxy or far beyond its confines. The argument centered on their distances from us and the relative size of the Galaxy. On April 26, 1920, at the National Academy of Sciences in Washington, D.C., Harlow Shapley of the Mount Wilson Observatory and Heber D. Curtis of the Lick Observatory met to argue the nature of the nebulae, which has become known as the *Great Debate* in astronomy. However, neither side provided conclusive evidence to settle the issue at the time.

The debate was finally resolved in 1923 when Edwin Hubble detected Cepheid variable stars in M31 using the 100-inch telescope at Mount Wilson. Hubble (1925) measured the distance to Andromeda as 285 kpc—while this estimate was smaller than the current value of 761 kpc (± 11 kpc, Li et al., 2021b), it was sufficient to demonstrate definitively that the spiral nebulae were *island universes*. This discovery has profoundly deepened our understanding of the Universe, revealing that the Milky Way is but one among numerous galaxies scattered throughout the vast expanse of the universe. Galaxies, the fundamental building blocks of the universe, are gravitationally bound systems comprising stars, gas, dust, and dark matter, and have become a central focus of modern astronomical research.

2 The Classification of Galaxies

Once the extra-galactic nature of the galaxies was established, the next step was to investigate their physical properties. It is necessary to classify them according to their intrinsic characteristics as the first step in understanding any new collection of objects. A well-developed classification system can systematically organize similar objects into connective patterns that promote the development of science from the explanation to the classification itself, akin to the

zoological classification of various species of animals (Sandage, 2005). Early attempts to classify galaxies include the *Messier* (Messier, 1781) and *New General Catalogue of Nebulae and Clusters of Stars* (NGC, Dreyer, 1888) catalogs, which used descriptive notations that consisted of a series of letters denoting brightness, shape, and concentration. Wolf (1908) published a simple system of letters to describe 17 different types of non-galactic nebulae, ranging from amorphous inclined types to patchy, well-developed spirals. This system was widely used by prominent nebulae researchers, such as Reinmuth (1926), for nearly three decades. Edwin Hubble also used this system in his Ph.D. thesis (Hubble, 1917), which focused on measuring the positions of non-galactic nebulae¹. There are similar descriptive classifications like Shapley (1927) and Vorontsov-Vel'Yaminov & Arkhipova (1962, serie of his book). However, these early visual descriptions cannot yet be considered as classification systems in the modern sense, as they lacked the organization of morphological features into a coherent, continuous framework.

A significant advancement in galaxy classification was made in 1920 by John Henry Reynolds (Reynolds, 1920). He measured the bulge-to-disk ratios of five galaxies and arranged them into a sequence of forms that he called as classes I to VII, where the properties of galaxies changed progressively from one class to the next. While this study did not claim to offer a comprehensive classification of galaxies, it marked the beginning of modern galaxy classification systems.

The most famous work was carried out by Hubble between 1922 and 1926. Around the same time, Lundmark (1927) also conducted similar research. Both Hubble and Lundmark divided galaxies into two main types, which they referred to as “galactic” and “non-galactic”, or “elliptical” and “spiral”, borrowing the concept of a “phylum” from biological classification. However, Hubble introduced some critical innovations by establishing a continuous relationship between elliptical and spiral galaxies. He demonstrated a progression among spiral galaxies based on the relative prominence of their bulges and arms, grouping them into adjacent categories. This was a significant departure from Lundmark’s work, which did not incorporate such continuity.

Hubble in words, describes his classification scheme without any diagram as follows: galaxies lacking spiral arms and showing varying degrees of flattening were classified under the “E” (elliptical) forms, with a continuous gradation based on the apparent degree of flattening. He proposed a transitional class, labeled S0, to bridge elliptical and spiral galaxies. Hubble then divided spiral galaxies into two families—barred and non-barred spirals—which were further categorized into three continuous sub-classes: Sa, Sb, and Sc, based on the tightness of their spiral arms and the size of their central bulges, following the classifications first hinted at by Reynolds. Finally, he classified galaxies that did not fit into these categories as irregular (Irr). However, Hubble (1926) published his classification system without referencing Reynolds’ earlier work, which led to criticism from Reynolds. Hubble had planned to revise his classification system further but died before completing it. Allan Sandage later compiled Hubble’s notes into the monumental *Hubble Atlas of Galaxies* (Sandage, 1961), which solidified Hubble’s classification scheme in astronomical research.

The tuning fork diagram of the Hubble sequence might first come from James Jeans, who first summarized Hubble’s classification scheme with a diagram in his book *Astronomy and*

1. Now we know they are galaxies

Cosmogony (Jeans, 1929), as shown in Figure 1.1. By rotating this diagram 90 degrees and adding images of galaxies, one obtains the well-known tuning fork diagram featured in Hubble's book *The Realm of the Nebulae* (Hubble, 1936). Curiously, Hubble did not acknowledge Jeans' contribution in this regard.

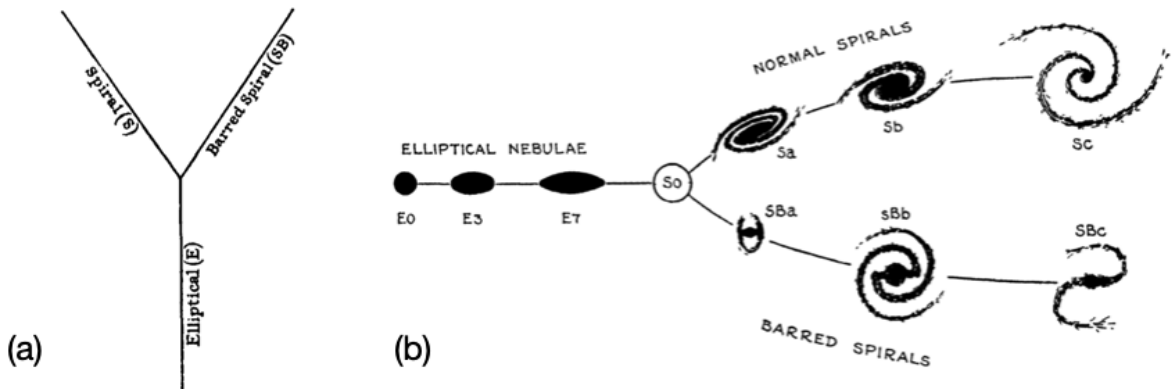


FIGURE 1.1 – Comparison of galaxy classification diagrams. (a) The diagram from James Jeans, as presented in his book *Astronomy and Cosmogony*, which summarized Hubble's classification scheme. (b) The well-known tuning fork diagram from Hubble (1936), as featured in *The Realm of the Nebulae*.

Following this classification system, galaxies are now commonly categorized into four broad classes:

Elliptical galaxies

Elliptical galaxies are characterized by smooth, nearly elliptical isophotes, and their surface brightness generally follows a de Vaucouleurs profile (de Vaucouleurs, 1948). These galaxies contain little to no cool interstellar gas or dust and typically lack a significant stellar disk. The stellar populations in elliptical galaxies are predominantly old, with ages comparable to the universe itself. Due to their minimal gas content, elliptical galaxies are primarily supported by stellar velocity dispersion rather than rotational dynamics.

The physical properties of elliptical galaxies span a wide range. Their total masses (including both baryonic and dark matter) can vary from as little as $10^7 M_\odot$ to more than $10^{13} M_\odot$, and their diameters range from a few tenths of a kiloparsec to several hundred kiloparsecs. The largest elliptical galaxies are among the most massive objects in the universe, while the smallest dwarf ellipticals are comparable in size to typical globular clusters.

Elliptical galaxies are further classified based on their observed ellipticity, defined as $\epsilon = 1 - b/a$, where a and b represent the major and minor axes of the projected ellipse, respectively. The Hubble type of an elliptical galaxy is then denoted as 10ϵ , ranging from E0 for galaxies with nearly spherical star distributions to E7 for those with highly elongated shapes.

Lenticular galaxies

Lenticular galaxies represent an intermediate class between elliptical and spiral galaxies. Together with elliptical galaxies, they are often referred to as *early-type* galaxies. Like elliptical galaxies, lenticular (S0) galaxies exhibit a smooth light distribution without spiral arms or HII regions. However, similar to spiral galaxies, they possess a thin disk and a bulge, though the bulge in lenticular galaxies is more prominent, typically accounting for a larger fraction of the total luminosity, with a bulge-to-total luminosity ratio of $B/T > 0.3$. In some cases, lenticular galaxies may also feature a central bar, and when this is present, they are classified as SB0.

Spiral galaxies

Spiral galaxies, also known as disk galaxies, exhibit a significantly more complex morphology compared to elliptical galaxies. They typically consist of a rotation-supported disk containing spiral arms and a central bulge. Depending on the presence or absence of a bar-like structure within the central bulge, spiral galaxies are further divided into barred spirals (SB) and normal spirals (S). In the earliest types (Sa/SBa, located on the left side of the tuning fork diagram), the bulge can dominate the galaxy's light with a bulge-to-total luminosity ratio of $B/T \lesssim 0.3$. In contrast, in the latest types, the bulge may be almost absent.

The spiral structure is most clearly observed in face-on galaxies, where it is defined primarily by young stars, HII regions, molecular gas, and dust lanes. In edge-on views, spiral galaxies reveal their vertical disk structure, often consisting of two distinct components: a thin disk and a thick disk. The bulge typically follows a de Vaucouleurs surface density profile, whereas the disk is best described by an exponential profile. Furthermore, some spiral galaxies have been observed spheroidal stellar haloes that extend to large radii.

In contrast to elliptical galaxies, spiral galaxies have less variation in their physical properties. For instance, their typical masses range from 10^9 to $10^{12} M_\odot$, and their diameters span from 5 to 100 kpc.

Irregular galaxies

Irregular galaxies typically lack a dominant bulge or a rotationally symmetric disk, displaying no obvious overall symmetry. Instead, their appearance is often irregular and patchy, primarily characterized by a few prominent HII regions. Hubble at first excluded this class from his original sequence due to uncertainty regarding its relationship to other galaxy types. Today, irregular galaxies are generally placed as an extension of spiral galaxies in the classification system. Although irregular galaxies exhibit a wide range of properties, they tend to be relatively small. Their absolute B magnitudes typically range from approximately 13 to 20, with masses between $10^8 M_\odot$ and $10^{10} M_\odot$, and diameters spanning from 1 to 10 kpc. Many irregular galaxies also display noticeable bars, which are frequently off-center.

Hubble originally and mistakenly thought that the tuning fork diagram represented an evolutionary sequence of galaxies. As a result, he referred to galaxies on the left side of the diagram as *early-type* and those on the right as *late*, which are still widely used in current astronomy. However, we can infer the sequence of galaxy evolution by comparing the proportions of different

galaxy types across various redshifts (Chapter 1, Section 3.3).

3 Formation and Evolution of Galaxies

3.1 Cosmological Context

Since galaxies are distributed within the large-scale structure of the Universe and are observed over cosmological time scales, any description of their formation and evolution has to involve cosmology, which describes the properties of space-time on large scales. The development of mathematical models for the universe began even before it was understood that galaxies were truly extragalactic objects. Albert Einstein's theory of general relativity provided the foundation for constructing self-consistent models of the entire universe. In his pursuit of a static universe, which is neither expanded nor contracted, Einstein introduced the cosmological constant into his field equations. In 1922, Alexander Friedmann proposed models based on the assumption of a spatially homogeneous and isotropic universe, exploring both static and expanding solutions (Friedmann, 1922). Independently, Georges Lemaître reached similar conclusions in 1927 (Lemaître, 1927), contributing to the formulation of what is now known as the Friedmann-Lemaître equations.

The discovery of the expansion of the universe occurred even before the *Great Debate* over the nature of nebulae. In 1914, Vesto M. Slipher, working at Lowell Observatory, observed that the spectral lines of most nebulae were redshifted, indicating that these objects were rapidly moving away from Earth (Slipher, 1914). However, the cosmological significance of this discovery was not fully recognized at the time, as the debate over whether these nebulae resided within or beyond the Milky Way was still unresolved. Later, in 1927, in the same work that Lemaître presented the Friedmann-Lemaître equations, Lemaître (1927) also provided observational evidence for a linear relationship between galaxy distances and their recessional velocities. In 1929, Edwin Hubble confirmed this result through his observations of 18 galaxies, demonstrating the same linear correlation (Hubble, 1929):

$$v = H_0 d \quad (1.1)$$

This relationship, is now known as the Hubble-Lemaître law, where H_0 represents the Hubble constant, v is the recessional velocity, and d denotes the distance to the galaxy from the observer.

Since the universe is expanding, it must have been smaller, and therefore denser and hotter in the past. An inevitable conclusion is that the universe would converge to a single point, as a *primeval atom* proposed by Lemaître in 1931 (Lemaître, 1931). This hypothesis was further developed by George Gamow in the 1940s, who proposed that chemical elements were created through thermonuclear reactions in the early universe (e.g., Gamow, 1946, 1948; Alpher et al., 1948). The thermal history of the universe, describing its expansion from an initial dense and hot state, was mockingly referred to as the *Hot Big Bang* by Fred Hoyle, who favored a steady-state cosmology.

The discovery of cosmic microwave background radiation (CMB, Penzias & Wilson, 1965)

provided strong evidence supporting the Big Bang model. Within this framework, Peebles (1966) and Wagoner et al. (1967) performed detailed calculations of primordial nucleosynthesis, which successfully predicted the observed abundances of light elements such as helium, deuterium, and lithium. These results further reinforced the Big Bang theory. With subsequent theoretical advancements, such as the introduction of cosmic inflation and observations of large-scale structures, the Big Bang model evolved into the Lambda-CDM (Λ CDM) model, which is now the most widely accepted cosmological model. The Λ CDM model describes a flat (or nearly flat) universe composed of three major components:

- Dark Energy: $\sim 68\%$ of the energy density, due to the cosmological constant Λ .
- Dark Matter: $\sim 27\%$ of the mass-energy content, due to the "cold" dark matter (CDM).
- Baryonic Matter: $\sim 5\%$ of the remnant component, which stars, galaxies, and other visible structures are made.

In this standard model of cosmology, structures form from small initial perturbations in an otherwise homogeneous and isotropic universe. Inflationary theory suggests that quantum fluctuations in vacuum energy can generate density perturbations during the rapid expansion phase, driven by one or more quantum fields, whose properties are consistent with the observed large-scale structure. The concept of structure formation through gravitational instability originates from Jeans (1902), who demonstrated that the stability of a perturbation depends on the competition between gravity and pressure, a principle later extended to an expanding universe by Gamow & Teller (1939) and Lifshitz (1946).

Density perturbations grow only if they exceed a characteristic length (or mass) scale, now referred to as the Jeans length (or mass), beyond which gravitational forces can overcome pressure gradients. Over-dense regions attract matter, becoming increasingly over-dense as a result. The physical size of such regions expands with time due to the overall expansion of the universe. However, once the perturbation reaches a critical over-density, it decouples from the cosmic expansion and begins to collapse. Dark matter undergoes violent relaxation to form dark matter halos, while gas within these halos flows inward, collapsing into small, high-density cores due to self-gravitation and various cooling mechanisms. These dense cores subsequently give rise to stars, producing the earliest visible fragments of galaxies.

While many aspects of these processes extend beyond the scope of my doctoral study, my primary interest lies in understanding how these primordial fragments evolved into galaxies with the diverse and distinct morphologies that we observe today.

3.2 Monolithic Collapse Model

Given that these over-dense gas regions give rise to stars, it is natural to propose that galaxies also formed from the collapse of gas clouds. An important early attempt to model this process was made by Olin J. Eggen, Donald Lynden-Bell, and Allan R. Sandage in 1962 (Eggen et al., 1962), a model now commonly referred to as the ELS collapse model. This work suggested that the difference between elliptical and spiral galaxies reflects the rate of star formation during the collapse. If most of the gas is converted into stars during the collapse, the process becomes

effectively dissipationless, with the infall motions transformed into the random motions of stars, leading to the formation of an elliptical-like galaxy. Conversely, if the gas remains largely gaseous during the collapse, gravitational energy can be dissipated efficiently through shocks and radiative cooling. The cloud continues to shrink until it is supported by angular momentum, resulting in the formation of a rotationally supported disk galaxy.

With a cosmological interpretation of the CMB, Silk (1968) showed that small-scale oscillations are damped by photon diffusion toward the end of recombination, a process now also referred to as Silk damping. Depending on the matter density and expansion rate of the universe, the characteristic scale of Silk damping falls within the range of $10^{12} - 10^{14} M_{\odot}$. After matter-radiation decoupling, the Jeans mass drops to approximately $10^6 M_{\odot}$, allowing perturbations above this mass scale to grow. Consequently, galaxies are expected to form *top-down*, through the collapse and fragmentation of perturbations larger than the damping scale, a model that parallels the ELS model.

Based on these ideas, Larson (1974, 1975, 1976) conducted the first numerical simulations of galaxy formation. Using near-spherical rotating gas clouds, he confirmed that the timescale of star formation determines whether a system evolves into an elliptical or spiral galaxy. He also emphasized the significance of important processes during galaxy formation. However, his simulations lacked highly flattened elliptical galaxies, and many bright ellipticals show little or no rotation (Bertola & Capaccioli, 1975; Illingworth, 1977).

The angular momentum of disk galaxies in the monolithic collapse framework presents another significant challenge. Efstathiou & Jones (1979) showed that clumps formed through gravitational collapse in a cosmological context typically acquire only about 15% of the angular momentum required for full rotational support. The importance of rotation in a system could be described by the spin parameter:

$$\lambda = \frac{J|E|^{1/2}}{GM^{5/2}} \quad (1.2)$$

where J is the total angular momentum, E is the total energy, M is the total mass, and G is the gravitational constant. Assuming the conservation of mass and angular momentum from the initial gaseous halo to the disk galaxy, the spin parameter of the initial gaseous halo, λ_i , scales as:

$$\lambda = \lambda_i \left(\frac{R}{R_i} \right)^{-1/2} \quad (1.3)$$

To increase the spin parameter from an initial value ~ 0.05 ² to the typical value of ~ 0.425 ³ observed in disk galaxies, a contraction of the gaseous halo R_i/R by a factor of approximately 70 is required. For a galaxy with a mass of $5 \times 10^{10} M_{\odot}$ and a radius of 10 kpc, this implies that the initial gaseous halo would need a radius of roughly 700 kpc, with a free-fall time given by $t_{\text{ff}} = \sqrt{3\pi/32G\rho} \sim 43$ Gyr. This timescale is significantly longer than the age of the Universe, ruling out the possibility that disk galaxies could have formed solely from gas clouds with spin parameters predicted by tidal torque theory.

2. For example, Barnes & Efstathiou (1987) used cosmological simulations to estimate the median spin parameter as $\lambda_{\text{med}} = 0.05$.

3. Assuming an isolated, exponential, virialized disk

3.3 The Hierarchical Merger Model

In the same year that the CMB was discovered, Peebles (1965) studied the effect of isotropic background radiation on the early evolution of matter leading to galaxy formation under isothermal initial conditions. He found that the Jeans gravitational instability (Lifshitz, 1946; Gamow, 1948) could result in the formation of bound systems of gas clouds with masses in the range of $10^5 - 10^7 M_\odot$, depending on the estimated present matter density. This work was the first to propose that galaxies could form through the accretion of smaller gas clouds, a process now known as the *bottom-up* hierarchical clustering scenario.

In 1972, Toomre & Toomre (1972) used simple numerical simulations to demonstrate that some of the extraordinary structures observed in peculiar galaxies, such as extended tidal tails, could be produced by tidal interactions between two spiral galaxies. Based on the observed frequency of galaxies exhibiting such signatures of interactions, and their estimate of the timescale over which tidal tails remain visible, they proposed that most elliptical galaxies could be remnants of mergers. Although their simulation assumed that all galaxies initially form as disks and that elliptical galaxies are the product of mergers between pre-existing galaxies, this work is considered one of the earliest attempts at modeling hierarchical galaxy formation.

By the late 1970s, the discovery of flat rotation curves indicated the presence of dark matter, leading to the consideration of its indispensable role in galaxy formation. White & Rees (1978) proposed a two-stage theory for galaxy formation: dark matter halos form first through a bottom-up hierarchical process of mergers, while the luminous content of galaxies emerges from the cooling and condensation of gas within the potential wells created by these dark matter halos.

In a cold⁴ DM-dominated universe, massive structures like dark matter halos are expected to grow hierarchically. Numerous studies have used both analytical methods and N-body simulations to investigate the properties of dark matter halos, focusing on aspects such as progenitor mass distributions (Bond et al., 1991), merger histories (Lacey & Cole, 1993), spatial clustering (Mo & White, 1996), density profiles (Navarro et al., 1997), halo shapes (e.g., Jing & Suto, 2002), substructure (Moore et al., 1998; Klypin et al., 1999), and angular momentum distributions (Warren et al., 1992; Bullock et al., 2001). Numerical simulations consistently predict that the merger rate of dark matter halos increases rapidly with redshift, scaling approximately as $\sim (1+z)^{2-3}$. However, the theoretical prediction of the galaxy merger rate remains highly uncertain (Jogee et al., 2008; Bertone & Conselice, 2009; López-Sanjuan et al., 2009; Hopkins et al., 2010; Lotz et al., 2011).

From a simulation perspective, following the work of Toomre & Toomre (1972), subsequent simulations (e.g., Toomre, 1977; Gerhard, 1981; Farouki & Shapiro, 1982; Negroponte & White, 1983; Barnes, 1988) showed that major mergers between two galaxies disrupt pre-existing stellar disks, leading to the formation of elliptical galaxies. For example, Toth & Ostriker (1992) studied the thinness and coldness of spiral galaxies' disks in the case of infall of satellite systems. Through numerical simulations and theoretical analysis, they concluded that galaxy mergers in the Λ CDM model produce galaxies with thicker disks than those observed in spiral galaxies.

4. Explanation in Chapter 1, Section 5

These simulations have led to the widespread belief that major mergers result in the formation of elliptical galaxies. However, their simulations lacked the gas component that dominated the galaxy in the early universe. The formation of spiral galaxies is still considered to occur through the dissipational collapse of gas clouds with initial angular momentum.

With the introduction of dark matter in galaxy formation models, it is considered that the radiative cooling of gas within dark matter halos is highly efficient, allowing the gas to radiate away its binding energy and contract, driving it toward a state of minimal energy. In the absence of interactions with other mass components, the gas conserves its angular momentum and forms a disk galaxy. Fall & Efstathiou (1980) developed a model of disk formation within dark matter halos, incorporating the angular momentum expected from tidal torques, which leads to the formation of flat rotation curves. Efstathiou & Silk (1983) further suggested that cooled gas could settle into a rotation-supported disk of the observed scale within a fraction of the Hubble time in an extended halo. However, many challenges remain in simulating the formation and evolution of spiral galaxies. For instance, the behavior of gas, such as collapse, accretion, and ejection, cannot be accurately simulated by N-body simulations, even though gas is the most important component in the early universe.

The first three-dimensional hydrodynamical simulations of galaxy formation incorporating dark matter were conducted in the early 1990s (Katz & Gunn, 1991; Katz, 1992). These studies used smoothed-particle hydrodynamics (SPH) techniques, independently developed by Lucy (1977) and Gingold & Monaghan (1977), which track the motion of individual mass elements. Katz's work modeled the collapse of a uniformly rotating, initially expanding spherical system composed of 90% dark matter and 10% gas, incorporating small-scale perturbations at levels predicted by the CDM model. The simulations reproduced systems resembling spiral galaxies, showing flat rotation curves and exponential surface density profiles. They argued that more than 50% of the disk's original angular momentum is transferred to the DM halo, and efficient cooling prevents gas from heating to the virial temperature. However, the resulting disks were more compact than observed spiral galaxies with excessively high rotation velocities, because too many baryons settled into the disks.

Further cosmological simulations with higher resolution confirmed this issue (Navarro & Benz, 1991; Navarro & White, 1994), revealing that a significant fraction of the baryons' angular momentum is transferred to dark matter through dynamical friction and gravitational torques, leading to too many baryons being locked in galaxies. As a result, disk sizes were approximately an order of magnitude smaller than those observed (Navarro et al., 1995; Navarro & Steinmetz, 1997; Sommer-Larsen et al., 1999). This issue became known as the *angular momentum catastrophe*.

The angular momentum catastrophe is often linked to the *overcooling* problem in CDM-based models (White & Rees, 1978; White & Frenk, 1991; Balogh et al., 2001), with some researchers suggesting that the treatment of feedback associated with star formation was inadequate. Strong feedback processes, such as supernovae, could prevent gas from cooling in small regions, keeping it hot and distributed similarly to dark matter. This would reduce the angular momentum transfer from gas to dark matter, allowing for the formation of more extended disks (Navarro &

Benz, 1991; Brook et al., 2004).

While modifications incorporating stronger feedback mechanisms led to significant changes in the results (e.g., Navarro & White, 1993; Sommer-Larsen et al., 1999; Thacker & Couchman, 2000; Robertson et al., 2004; Okamoto et al., 2005), they often resulted in cosmological simulations producing stars concentrated in low angular momentum bulges, making it difficult for disks to form (Katz et al., 1996; Fukugita et al., 1998; Balogh et al., 2001; Kereš et al., 2005). Other attempts to resolve the issue, such as increasing simulation resolution or exploring warm dark matter models, also proved insufficient.

More recently, simulations have made significant progress in reproducing spiral galaxies by incorporating strong feedback effects from massive stars, supernovae, and active galactic nuclei (AGN) (e.g., Stinson et al., 2010; Agertz et al., 2011; Hopkins et al., 2011; Agertz et al., 2013; Hopkins et al., 2014; Schaye et al., 2015; Nelson et al., 2015; Agertz & Kravtsov, 2015; Pillepich et al., 2018; Nelson et al., 2019). Such strong feedback can drive gas outflows from galaxies, reducing the amount of gas available for star formation and preventing gas from cooling and collapsing into central regions. These outflows can even blow gas out of galaxies, enriching the circumgalactic medium with metals (Governato et al., 2010; Brook et al., 2012; Marinacci et al., 2014; Christensen et al., 2016). Several large radio galaxies are reported, the modeled black hole jet pairs could extend over $5 - 7$ Mpc (e.g., Willis et al., 1974; Machalski et al., 2008; Oei et al., 2024). However, the significance of the observation and model still needs to be confirmed.

On the other hand, observations also indicate that galaxy mergers play a crucial role in the evolution of galaxies. Using the Hubble Space Telescope, Le Fèvre et al. (2000) studied 285 galaxy images from HST, with redshifts provided by the CFRS and LDSS surveys. They found that the merger fraction increases with redshift as $\propto (1 + z)^{2.7 \pm 0.6}$, concluding that galaxy mergers significantly contribute to the evolution of both the luminosity function and luminosity density of the Universe up to $z \sim 1$. The IMAGES-II survey (Neichel et al., 2008) demonstrated that most rotating galaxies (80%) exhibit spiral morphologies, whereas the majority (90%) of galaxies with anomalous kinematics display peculiar morphologies. Hammer et al. (2009) analyzed a subsample of 33 IMAGES starbursts in the CDFS-GOODS field, combining morphological data from the HST with high-quality kinematics (velocity fields and 2D velocity dispersion maps), and found that half of the present-day spirals were in merger phases at $z_{\text{median}} = 0.65$. This suggests that most, if not all, of these galaxies were shaped during gas-rich mergers at earlier epochs, with the mergers occurring approximately 1 Gyr ago.

Delgado-Serrano et al. (2010) compared the evolution of galaxies within the Hubble sequence over 6 Gyr by selecting samples of nearby galaxies from the SDSS and distant galaxies from the GOODS survey. They found that early-type (E/S0) galaxy populations, which constitute about 20% of galaxies in the local Universe, show no evidence of number evolution. Instead, nearly all observed evolution results from the transformation of peculiar galaxies into regular spiral galaxies over time. In the local Universe, spiral galaxies dominate, representing $\sim 70\%$ of the population, as shown in [Figure 1.2](#). However, 6 Gyr ago, the fraction of regular spiral galaxies was 2.3 times lower, a change that is precisely offset by a fivefold increase of peculiar galaxies. After evaluating all possible mechanisms of galaxy evolution, they concluded that only major

mergers could account for the features of peculiar galaxies, which indicates that the formation of regular spiral galaxies is likely driven by major mergers.

Recent simulations (e.g., Springel & Hernquist, 2005; Robertson et al., 2006; Aumer et al., 2014; Athanassoula et al., 2016; Tapia et al., 2017; Eliche-Moral et al., 2018; Sauvaget et al., 2018; Hammer et al., 2018a; Peschken et al., 2020) have demonstrated that major mergers of galaxies with mass ratios of 1:4 can result in disk galaxies. The gas component is key to this transformation during major mergers. In such scenarios, the bulge and thick disk of the galaxy are formed from pre-existing stars in the progenitor galaxies. The gas is accreted to the center of the merger remnant during the merger, redistributed, and forming new stars, which constitute the thin disk. If the gas fraction is sufficient (approximately 50%), the re-formed disk can become the dominant component in the reshaped galaxy. This process is known as the disk rebuilding scenario (Hammer et al., 2005, 2009). On the other hand, minor mergers (mass ratios less than 1:4) are insufficient to reproduce the observed properties of spiral galaxies, including their angular momentum (Bournaud et al., 2007; Stewart et al., 2009; Lackner et al., 2012).

From Figure 1.2 and the disk rebuilding scenario, we can infer that approximately half of the present-day spiral galaxies underwent a major merger around 6 Gyr ago. This insight is crucial because if most spiral galaxies formed through major mergers within the last 6 Gyr, the equilibrium of baryonic components at the edges of the stellar and gas disks needs to be reconsidered. For instance, measurements of velocity or velocity dispersion are essential for determining mass, offering an additional method to mass-to-light ratio estimates. The significant difference between the dynamical mass, derived from dynamical tracers, and the baryonic mass, inferred from the mass-to-light ratio in the outer regions of galaxies, raises an important problem, often called the missing mass problem, which is often attributed to the presence of dark matter.

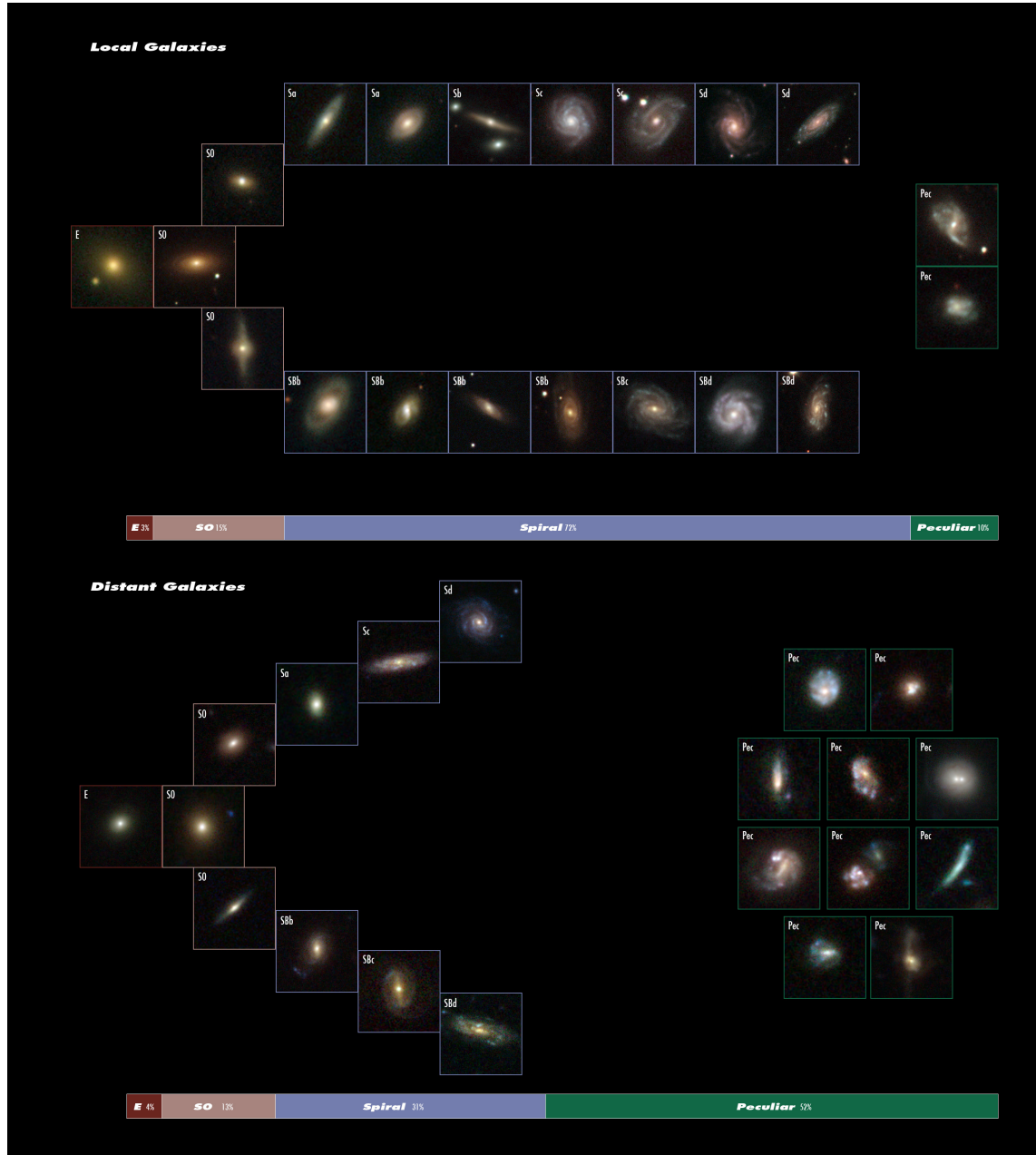


FIGURE 1.2 – Comparison of present-day Hubble sequence from the local sample and past Hubble sequence from distant galaxies. This figure is adapted from Delgado-Serrano et al. (2010).

4 Rotation Curve

The discovery of galactic rotation dates back to 1914, when Slipher (1914) detected inclined absorption lines in the nuclear spectra of Andromeda Galaxy (M31) and the Sombrero galaxy, and Wolf (1914) observed inclined lines in the nuclear spectrum of M81. The success of Newtonian gravity within the solar system led to the assumption that, under classical dynamical principles, specifically that galaxies are in dynamical equilibrium, it should be possible to infer the mass distribution of galaxies from their rotation curves (RCs), which represent the circular velocity profiles of stars and gas as a function of their distances from the galactic center.

In 1925, Lundmark (1925) was amongst the first to identify the flat behavior of RCs in disk galaxies. Through optical spectroscopy, Babcock (1939), followed by Mayall (1951), reported that the RC of M31 exhibited no decline out to 20 kpc from the center. They concluded that the stellar mass-to-light ratio would need to increase radially—up to $62 M_{\odot}/L_{\odot}$ in the outskirts—to reproduce the observed rotation curve. However, Schwarzschild (1954) reanalyzed M31 RC using a constant mass-to-light ratio and found that the dynamical mass inferred from the rotation curve was consistent with the luminous mass. Later, de Vaucouleurs (1959) studied the RCs of eight galaxies, concluding that after reaching a maximum, the rotation velocity decreases with distance from the center and asymptotically approaches a Keplerian decline. These findings led many astronomers to initially dismiss the peculiar rotation curves identified by Babcock, Oort, and Mayall.

Burbidge et al. (1959) were the first to derive a RC by observing the H α and [N II] emission lines from HII regions within spiral galaxies. However, their measurements were confined to the inner regions of galaxies, where the rotation curve is dominated by the bulge and inner disk. The revolution took place in the 1970s. Vera Rubin and Kent Ford used an image tube spectrograph developed in the last decade to perform spectroscopic observations of the M31. The observations of the M31 rotation curve (Rubin & Ford, 1970) were consistent with the radio measurements obtained previously by Roberts (1966). Subsequently, Rubin et al. (1978) published RCs for ten high-luminosity spiral galaxies based on optical spectra, revealing that these curves remained flat out to the outermost measured radii.

In spiral galaxies, gas disks tend to be more extended than stellar disks. Consequently, measuring the RC of the gas disk allows the gravitational potential of the galaxy to be probed at much larger radii (Roberts, 1975). The neutral hydrogen emission line at 21 cm (HI observation) was first predicted by van de Hulst (1945) and later observed by Ewen & Purcell (1951). The first RC based on the HI observation was derived by van de Hulst et al. (1957) for M31, extending measurements up to $2^{\circ}5$ from the center. The most renowned work on HI RCs is that of Albert Bosma. His Ph.D. thesis (Bosma, 1978) included radio observations of the velocity fields and corresponding RCs for 25 galaxies. Bosma's work (Bosma, 1978, 1981) provided convincing evidence that the majority of these galaxies exhibited flat RCs extending to the outermost observed radii (van der Kruit & Bosma, 1978; Trimble, 1987; Ashman, 1992; Persic & Salucci, 1997; Sofue & Rubin, 2001), far beyond the optical size of the galaxies. The dynamical mass inferred from these flat RCs was significantly larger than the baryonic mass derived from mass-

to-light ratios, introducing the so-called *missing mass* problem. This discrepancy has led to the widespread acceptance of the existence of dark matter halos surrounding spiral galaxies.

To derive the circular velocity from the line-of-sight (LOS) velocity, v_{LOS} , the primary assumption is that the gas components are moving in circular orbits. Based on this assumption, various methods, such as tilted-ring fitting (Begeman et al., 1991; Walter et al., 2008), can be used to correct for the position angle (P.A.) and inclination (i), allowing for the derivation of the circular velocity. The circular motion of the gas components implies that the gas disk, and thus the spiral galaxy, is in dynamical equilibrium. This assumption has long been accepted, because spiral galaxies are believed to have avoided major mergers, while minor mergers are not considered significant enough to substantially affect the kinematics of the disk.

However, the assumption of dynamical equilibrium in spiral galaxies has been challenged by recent observations and simulations (Chapter 1, Section 3.3). It has been found that, on average, half of the spiral galaxies have undergone a major merger approximately 6 Gyr ago (Hammer et al., 2009; Delgado-Serrano et al., 2010). According to the disk rebuilding scenario, after a major merger, the gas is accreted from the merger remnants and redistributed from the inside out. Gnedin & Ostriker (1999) estimated that 3-5 orbits are required for the gas or stars to virialize within the disk after a significant perturbation. Therefore, it is crucial to test whether the gas disk at large radii is truly in dynamical equilibrium. If not, the total velocity of the gas at these large radii may either dominate or be absent from the LOS velocity, potentially leading to an overestimation or underestimation of the circular velocity, and consequently, the inferred mass.

Several other tracers can be used to derive the circular velocity in galaxies. For example, the rotational transition lines of carbon monoxide (CO) (e.g., Young et al., 1995; Sofue, 1996; Nishiyama & Nakai, 1998; Sakamoto et al., 1999), maser lines (e.g., Lindqvist et al., 1992; Izumiura et al., 1995, 1999), and planetary nebulae (e.g., Jacoby et al., 1990; Hui et al., 1995), among others. However, these methods are generally restricted to the inner regions of galaxies and are not suitable for probing the total mass of a galaxy. For this reason, these tracers are not analyzed in this thesis.

5 Dark Matter

The concept of dark matter was proposed long before the discovery of the flat RC. In 1933, Fritz Zwicky observed that the velocity dispersion (VD) of galaxies in the Coma Cluster was much higher than anticipated (Zwicky, 1933). Using the virial theorem to the estimated cluster's mass, he calculated a theoretical VD of approximately 80 km/s, which was far lower than the observed value of around 1000 km/s. Zwicky concluded that dark matter is present in much greater amounts than luminous matter. A few years later, in 1936, Sinclair Smith conducted a similar study of the Virgo Cluster. Assuming the outer galaxies were in circular orbits around the cluster, Smith estimated the cluster's total mass to be $10^{14} M_{\odot}$. Dividing this by the roughly 500 observed galaxies, he derived an average mass per galaxy of $2 \times 10^{11} M_{\odot}$, which was significantly higher than Hubble's earlier estimate of $10^9 M_{\odot}$ based on stellar mass-to-light ratios.

Astronomers subsequently debated whether galaxy clusters are in equilibrium, a condition necessary for the application of the virial theorem. On the other hand, some scientists suggested that the missing mass could be attributed to an intergalactic medium (IGM), consisting of hot gas distributed between galaxies (Turnrose & Rood, 1970). However, studies of X-ray emissions from galaxy clusters by Penzias (1961) and Meekins et al. (1971) revealed that the mass of hot intracluster gas was insufficient to account for the high mass-to-light ratios observed in these systems. Other exotic explanations, such as massive collapsed objects (Van den Bergh, 1969), HI snowballs (Peebles, 1971), and M8 dwarf stars (Tarter & Silk, 1974), were also ruled out by measurements of primordial light element abundances (Bertone & Hooper, 2018). In summary, the dark matter hypothesis was neither universally accepted nor dismissed at the time. There was a growing consensus that additional information was required to fully understand the mass distribution in galaxy clusters (Neyman et al., 1961).

Clowe et al. (2006) observed that in the Bullet Cluster, a merging system of two galaxy clusters, the mass distribution does not align with the distribution of hot gas observed in X-ray data. The mass distribution, which followed the distribution of galaxies, was inferred from weak gravitational lensing, the deflection of light from background galaxies due to the mass distribution of the clusters. The hot X-ray emitting gas, which constitutes the majority of the baryonic mass in the clusters, is separated from the inferred mass. This separation was interpreted as evidence for the existence of dark matter. However, the collision between the two clusters represents a highly violent event, meaning the system is far from dynamical equilibrium. As a result, interpreting the mass distribution using weak gravitational lensing and galaxy distributions in such a merging system is challenging. Additionally, the irregular morphology of many distant galaxies further complicates the modeling of weak gravitational lensing in such studies.

The most compelling evidence for dark matter came from the discovery of flat rotation curves in spiral galaxies ([Chapter 1, Section 4](#)). Einasto et al. (1974) and Ostriker et al. (1974) had already highlighted that galaxy masses had been underestimated by nearly an order of magnitude, referencing the flat rotation curves observed by Rogstad & Shostak (1972) and Roberts & Rots (1973). Later in the 1970s, after the observations of flat rotation curves by Rubin et al. (1978) and Bosma (1978), Faber & Gallagher (1979) conducted a comprehensive review of the *missing mass* problem, and concluded that the existence of a significant amount of unseen mass in the Universe is very robust by evaluating standardized mass-to-light ratios.

Cosmological observations also require the presence of dark matter. For instance, the third peak of the observed Cosmic Microwave Background (CMB) power spectrum and the amplitude of baryonic acoustic oscillations (BAO, Eisenstein et al., 2005) can only be reproduced with the inclusion of dark matter. This dark matter is considered to be *cold*, meaning it decoupled from photons while baryons were still coupled with them. Cold dark matter (CDM) begins to form structures, and after recombination, baryons fall into the potential wells created by dark matter, leading to the hierarchical model of structure formation. With the addition of dark energy (Λ), the Λ CDM model has become widely accepted as the standard cosmological model.

Modified Newtonian Dynamics

In 1983, Mordehai Milgrom proposed Modified Newtonian Dynamics (MOND, Milgrom, 1983a) as an alternative to dark matter (DM) for explaining the flat rotation curves (RCs) (Milgrom, 1983b) and the velocity dispersion (VD) in galaxy clusters (Milgrom, 1983c). The idea behind MOND is relatively straightforward: Newtonian dynamics may need modification at low accelerations, since the centripetal acceleration of stars in a galaxy is on the order of $\sim 10^{-10} \text{ m s}^{-2}$, which is several orders of magnitude smaller than the accelerations typically tested within the solar system. Milgrom (1983a) hypothesized an approximate weak-field limit at low accelerations, where $g \ll a_0$, given by:

$$g = \sqrt{g_N a_0}, \quad (1.4)$$

where $g = |\mathbf{g}|$ represents the true gravitational acceleration, $g_N = |\mathbf{g}_N|$ is the Newtonian acceleration, and a_0 is the acceleration constant.

However, the original MOND formalism does not conserve momentum, angular momentum, or energy, and it is inconsistent with general relativity. Over the past four decades, significant efforts have been made to address these issues. For example, Bekenstein & Milgrom (1984) proposed the aquadratic Lagrangian theory (AQUAL), which conserves momentum, angular momentum, and energy, while also respecting the weak equivalence principle. Later, Bekenstein (2004) introduced the tensor-vector-scalar gravity (TeVeS) theory, which provided a relativistic framework for MOND and addressed gravitational lensing. On the observational side, MOND is credited with predicting the baryonic Tully-Fisher relation (McGaugh et al., 2000). However, as noted by Bertone & Hooper (2018), the formalism of MOND has come at the cost of simplicity and economy, and several observations remain unexplained, such as the dynamical mass of galaxy clusters, the third acoustic peak of the CMB, and the large-scale structure of the Universe (Famaey & McGaugh, 2012). As a result, MOND is not widely accepted within the astronomical community. In this thesis, I will continue to work within the framework of Newtonian dynamics and the dark matter paradigm.

6 Milky Way

Studies of the Milky Way are the cornerstone of modern astrophysics, providing the foundation for understanding the formation and evolution of galaxies across cosmic time. Although our position within the Milky Way and the effects of dust extinction limit our ability to observe it globally as we do with external galaxies, the Milky Way offers a unique opportunity to study fully resolved stellar populations and other constituents in unprecedented detail. This makes it invaluable for gaining insights into our Galaxy's present-day structure and dynamics, offering information that is difficult to obtain from other galaxies.

The Milky Way is one of the two dominant members of the Local Group, a low-mass system comprising a loosely bound collection of spiral and dwarf galaxies located in a low-density filament on the outskirts of the Virgo Supercluster. The other major member of the Local Group is the Andromeda Galaxy (M31), located approximately 760 kpc from the Milky Way, making it

the nearest massive spiral galaxy. Studies using the *Hubble Space Telescope* (HST) have shown that M31 is currently moving toward the Milky Way (Cox & Loeb, 2008; Sohn et al., 2012; van der Marel et al., 2012). Recent large surveys, such as the Pan-Andromeda Archaeological Survey (Ibata et al., 2014), the Panchromatic Hubble Andromeda Treasury (PHAT) (Gilbert et al., 2009), and the Spectroscopic and Photometric Landscape of Andromeda’s Stellar Halo survey (Dalcanton et al., 2012), have revealed significant differences between M31 and the Milky Way. For instance, M31 has a more massive bulge and a thicker disk, while its halo is remarkable for many stellar streams (Ibata et al., 2014), including the Giant Stream (Ibata et al., 2001). Many studies have proposed that M31 experienced a major merger in its past (Courteau et al., 2014). Numerical simulations have successfully reproduced many of M31 observed structures, such as the Giant Stream, the 10 kpc ring, and the bulge, suggesting that these features formed during a major merger 2–3 Gyr ago (Hammer et al., 2010, 2018a).

The Milky Way is considered a relatively quiet galaxy (Hammer et al., 2007). Classified as an SBbc-type galaxy, it exhibits declining global star formation rates (SFR) of approximately $1 - 2 M_{\odot} \text{ yr}^{-1}$ (Licquia & Newman, 2015), and its nuclear activity is low. Comparing the Milky Way to other similar spiral galaxies based on the Tully-Fisher relation and angular momentum, Hammer et al. (2007) found it to be systematically offset by about 1σ . According to the disk rebuilding scenario, Hammer et al. (2007) suggested that the Milky Way’s distinct properties are the result of its quiet evolutionary history. This is further supported by the discovery that its last major merger, Gaia-Sausage-Enceladus, occurred approximately 8–10 Gyr ago (Belokurov et al., 2018; Haywood et al., 2018; Helmi et al., 2018).

6.1 Structure of the Milky Way

The Milky Way stellar component is composed of a bulge, thin and thick stellar disks, and a halo (Bland-Hawthorn & Gerhard, 2016). Additionally, the MW contains gas and dust components. Surrounding the Milky Way within a radius of 300 kpc are approximately 50 dwarf galaxies (Li et al., 2021a), more than 150 globular clusters (Piatti et al., 2019), and numerous stellar streams (Ibata et al., 2021), with the most prominent being the Large and Small Magellanic Clouds (LMC and SMC). Both the LMC and SMC are currently undergoing their first infall (Kallivayalil et al., 2006; Piatek et al., 2008). Wang et al. (2019a) used hydrodynamical simulations to reproduce many of the observed properties of the Magellanic Clouds (MCs), suggesting that the Galactic hot gaseous halo, also known as the circumgalactic medium (CGM, Tumlinson et al., 2017), is stripping the MCs via ram-pressure during their first infall. The CGM is also considered a potential solution to the galaxy quenching process and the missing baryon problem. However, the distribution and total mass of this hot gas remain uncertain (Anderson & Bregman, 2010; Miller & Bregman, 2013).

Many of the dwarf galaxies have been observed to align along a plane perpendicular to the MW disk, known as the Vast Polar Structure (VPOS, Kroupa et al., 2005; Pawłowski et al., 2012). The VPOS exhibits not only spatial alignment but also significant kinematic correlation. Using *Gaia* EDR3, Li et al. (2021a) found that at least 20–29 dwarf galaxies have orbital poles aligned

with the VPOS normal vector. Similar satellite planes have also been discovered around other galaxies (Ibata et al., 2013; Müller et al., 2018). This spatial and kinematic alignment challenges theoretical predictions of isotropy and uncorrelated satellite sub-halo systems, presenting an unresolved tension with the Λ CDM paradigm, known as the Planes of Satellite Galaxies Problem. Hammer et al. (2023) explored the relationship between binding energy and infall lookback time for the Bulge, Gaia-Sausage-Enceladus (GSE), Sagittarius (Sgr) globular clusters (GCs), and dwarf galaxies. The study suggested that most dwarf galaxies are undergoing their first infall, where ram-pressure strips their gas, leading to the observed large velocity dispersions (Chapter 4, Section 1.3).



FIGURE 1.3 – *Left panel:* The Milky Way panorama by Serge Brunier (ESO)⁵. *Right panels:* Projections of the Galactic box/peanut (b/p) bulge and long bar reconstructed from near-IR (NIR) star counts. *Top right:* Inner Galaxy as seen from the Sun. *Bottom right:* Projection of the best-fitting red clump giant star count model as seen from the North Galactic Pole. Right panels are adapted from Wegg et al. (2015).

The Galactic bulge is considered to be a structure formed through early mergers during the formation of the MW. This is supported by the old ages of bulge stars, as inferred from color-magnitude diagrams (Ortolani et al., 1995; Clarkson et al., 2008), near-infrared luminosity measurements (Weiland et al., 1994; Binney et al., 1997), and stellar count maps (Skrutskie et al., 2006). Several studies have identified the boxy/peanut-shaped bar structure of the bulge (McWilliam & Zoccali, 2010; Nataf et al., 2010), as illustrated in Figure 1.3. The boxy/peanut isophotal shape of the Milky Way bulge, when viewed edge-on from the Sun’s position, suggests that the MW contains a pseudo-bulge that likely evolved from a bar. Wegg & Gerhard (2013), using red clump giants from the VVV survey (Minniti et al., 2010), revealed an eightfold triaxial symmetry within the bulge, primarily composed of a bar with dimensions of $2.2 \times 1.4 \times 1.2$ kpc.

The stellar mass of the bulge can be estimated through either photometric or dynamical models. Dwek et al. (1995) used COBE near-infrared (NIR) luminosity data combined with a Salpeter initial mass function (IMF) to estimate a bulge mass of $1.3 \times 10^{10} M_\odot$. In contrast, Licquia & Newman (2015) found a significantly higher value of $2 \times 10^{11} M_\odot$ using a Kroupa IMF. Bissantz et al. (2003) modeled gas dynamics based on the deprojected COBE NIR luminosity distribution from Bissantz & Gerhard (2002) and derived a mass of $1.85 \times 10^{10} M_\odot$, a result

consistent with Portail et al. (2015), who used made-to-measure dynamical models fitted to the combined VVV red clump giant (RCG) star density and BRAVA kinematics.

The Galactic Center (GC), located within the bulge, was first identified through the discovery of Sgr A by radio astronomers (Piddington & Minnett, 1951). Its distinct radio emission properties and precise alignment with the dynamical center of the inner rotating HI disk (Oort & Rougoor, 1960) led the International Astronomical Union (IAU) to officially designate Sgr A as the center of the Milky Way. Later, Balick & Brown (1974) discovered the unresolved source Sgr A*, which is now known to coincide with the location of the Milky Way's supermassive black hole (SMBH), with a mass of $4.297 \times 10^6 M_\odot$ (Gravity Collaboration et al., 2023).

The motion of the Sun within the Milky Way (MW) is a key parameter for deriving the motion of other stars. The distance of the Sun from the Galactic Center (GC) was first estimated by Harlow Shapley in 1918 (Shapley, 1918), who used the distribution of globular clusters to determine the Sun's position in the MW, estimating it to be 15 kpc from the GC. Reid et al. (2014), using VLBI parallax measurements of masers, refined the distance to 8.34 ± 0.16 kpc. More recently, GRAVITY Collaboration et al. (2019) estimated the distance to the GC to be 8.178 ± 0.031 kpc based on the orbits of stars around the supermassive black hole (SMBH). The Sun is also located slightly above the disk, at a height of approximately 25 pc (Jurić et al., 2008). It moves within the disk with a peculiar velocity relative to the local standard of rest (LSR) of $U_\odot = 11.1 \text{ km s}^{-1}$, $V_\odot = 12.24 \text{ km s}^{-1}$, and $W_\odot = 7.25 \text{ km s}^{-1}$ (Schönrich et al., 2010). The Sun's tangential velocity relative to the GC, as determined from the proper motion of Sgr A*, is $v_{\tan, \odot} = 248 \pm 3 \text{ km s}^{-1}$ (Reid & Brunthaler, 2004; Reid, 2008).

Significant structures exist within the Milky Way's disk, including spiral arms and a warp. Reid et al. (2019), using very long baseline interferometry observations to map the positions and motions of masers, proposed a four-arm model for the Milky Way. This structure is relatively uncommon among spiral galaxies and contrasts with the two major arms revealed by Churchwell et al. (2009). The Sun is located near, but not within, one of these spiral features known as the Orion-Cygnus arm, or simply the Orion arm, as depicted in Figure 1.4. Although dust extinction hinders direct observation of the MW spiral structure, the 3D distribution of stars can still be reconstructed using infrared observations, even toward the Galactic Center. Figure 1.4 shows the spiral structure of the Milky Way, derived from more than 800,000 images captured by NASA's *Spitzer* Space Telescope⁶. Based on observations of RGB stars, astronomers have been able to reconstruct the Milky Way's spiral arm structure.

The Milky Way's stellar disk can be divided into two components: the thin and thick disks. Following a major merger, most of the pre-existing stellar populations tend to form the thick disk, while the gas component is accreted and redistributed, leading to the birth of stars and the formation of the thin disk. Therefore, stars in the thick disk are generally older compared to those in the thin disk. The thin disk is the dominant component of the Milky Way, whereas the thick disk is distinguished by its unique chemical properties (Bensby et al., 2014; Hawkins et al., 2015; Masseron & Gilmore, 2015). The total stellar mass of the disk is estimated to be $4 \pm 1 \times 10^{10} M_\odot$ (Bovy & Rix, 2013; Piffl et al., 2014; Binney & Piffl, 2015).

6. <https://science.nasa.gov/resource/the-milky-way-galaxy/>

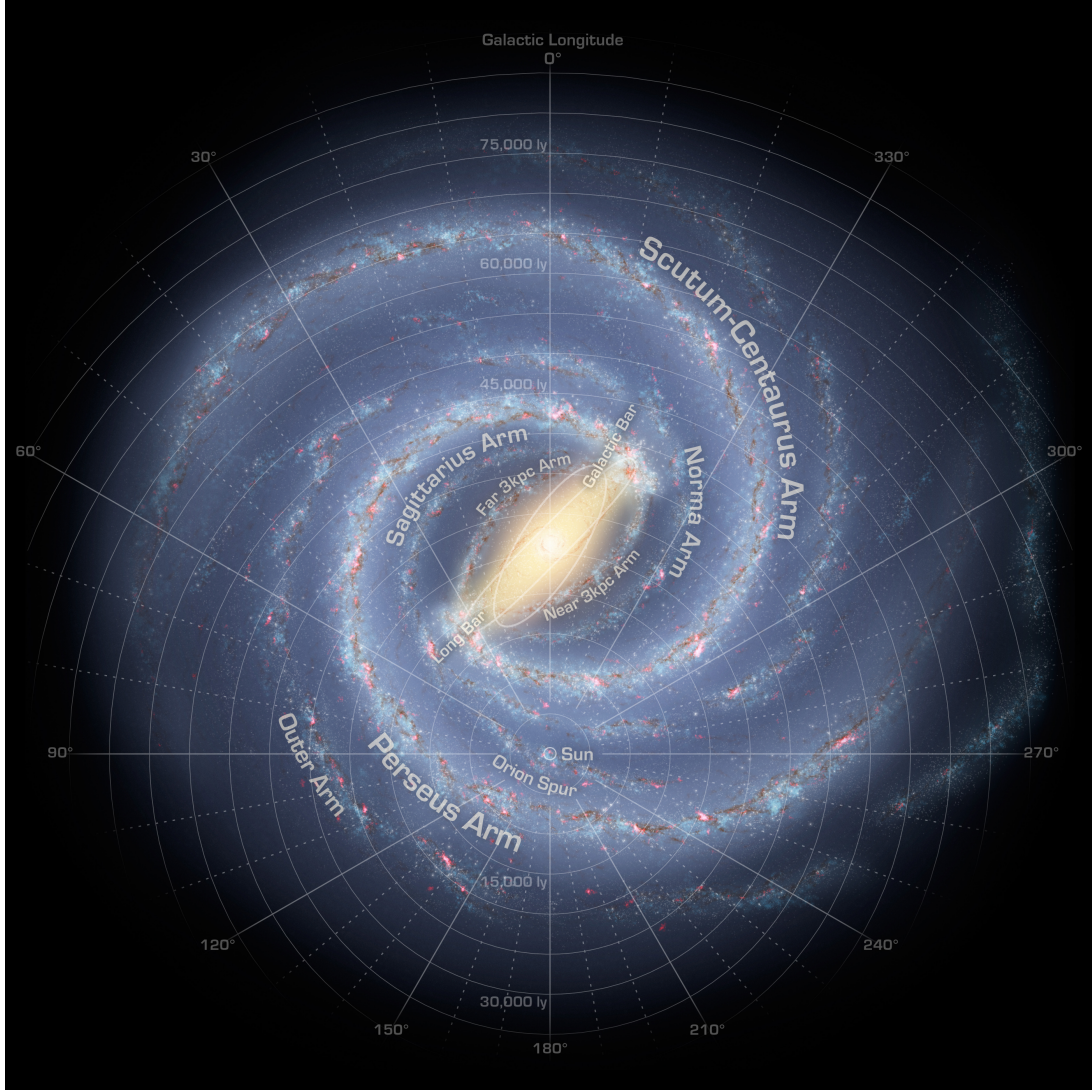


FIGURE 1.4 – The spiral structure of the Milky Way.

Similar to external galaxies, an exponential profile can be used to model the density distribution of the Milky Way's stellar disks. Jurić et al. (2008), using SDSS data of late M dwarfs with $1.0 < r - i < 1.4$, fitted both the thin and thick disk components, finding scale heights of approximately 300 pc for the thin disk and 900 pc for the thick disk, with 20% uncertainties. These results are consistent with previous studies (Schmidt, 1963; Siegel et al., 2002). For the scale length, Jurić et al. (2008) determined values of 2.6 kpc and 3.6 kpc for the thin and thick disks, respectively, with a local thick-to-thin disk density normalization of 0.12. Bovy et al. (2012a) concluded that scale lengths vary with stellar populations, ranging from 2 kpc in the inner disk (older populations) to 3 kpc or more at $R = 12$ kpc (younger populations). Wang et al. (2018), using RGB stars from LAMOST DR3, found that the disk density profile follows a three-segment structure with scale lengths of 2.12 ± 0.26 kpc, 1.18 ± 0.08 kpc, and 2.72 kpc for $R < 11$ kpc, $11 \leq R \leq 14$ kpc, and $R > 14$ kpc, respectively.

The MW warp was first detected in neutral hydrogen gas by Kerr (1957), and subsequent

studies identified the warp in the stellar disk as well (Drimmel & Spergel, 2001; López-Corredoira et al., 2002b; Momany et al., 2006; Poggio et al., 2018). The origin of the warp remains a subject of debate (Bailin, 2003; Shen & Sellwood, 2006; Weinberg & Blitz, 2006; Wang et al., 2020b). Sauvaget et al. (2018), using N-body/SPH simulations, suggested that the warp could be a natural remnant of a gas-rich major merger, potentially persisting for several billion years. Similarly, Deng et al. (2024) employed a gas-rich merger simulation to reproduce nearly all observed features of the warp, suggesting that it might be the remnant of the MW last major merger.

The Milky Way's stellar halo contains about 1% of its total stellar mass. Halo stars exhibit large random motions, minimal rotation, and a spheroidal to spherical spatial distribution. Some studies suggest that these stars originated from small accreted galaxies that were tidally disrupted by the Milky Way gravitational field (Ibata et al., 1997; Belokurov et al., 2006a; Schlaufman et al., 2009). Due to the long dynamical timescales of such minor mergers, remnants of these accretion events are still observable today in the form of stellar streams within the halo (Ibata et al., 1994; Majewski et al., 2004; Grillmair, 2006), serving as a fossil record of the Milky Way accretion history (Helmi, 2008; De Lucia, 2012; Belokurov, 2013).

6.2 The Milky Way Mass

Accurate estimate of the MW mass is essential for determining the distribution of dark matter, the gravitational potential, and the overall structure of the Galaxy. It also influences our understanding of satellite galaxies, the MW interactions with nearby galaxies, and the stability of its disk. Furthermore, the MW mass provides critical context for comparing our Galaxy with others, aiding in the study of galaxy formation and evolution on a cosmological scale. Therefore, precise measurement and modeling of the MW mass are fundamental for advancing our understanding of the Galaxy, other galaxies, and the Universe.

Compared to distant galaxies, the distances and velocities of individual stars in the MW disk and halo can be measured more directly and accurately, as we are embedded within the MW and much closer to these objects. The observed dynamics of luminous tracers, such as stars, dwarf galaxies, globular clusters, maser sources, and tidal streams, provide valuable information about the underlying MW potential. It is important to note, however, that measuring the distances of HI clouds is nearly impossible, which is why HI observations are typically not used to derive the MW circular velocity, unlike in other spiral galaxies. With a well-constructed model that describes their dynamics or phase-space distributions within a realistic potential profile, it is possible to constrain the mass distribution of the MW.

When discussing the total mass of the MW, it is crucial to clearly define the boundaries of the MW, as these limits are still difficult to establish. Additionally, some DM profiles, such as the NFW profile (Navarro et al., 1997), do not have a finite mass. A commonly used definition is the virial mass, which is the total mass enclosed within a radius, R_{200} , where the average density is 200 times the critical density of the universe. In some studies, other multiples (Δ) of the critical density or matter density are used to define the cutoff for the DM distribution,

leading to the use of terms like R_Δ . Furthermore, different DM profiles can yield varying results, as they exhibit different slopes in the outer regions of the halo.

Different methods use tracers that cover different ranges, and usually cannot reach the virial radius. Therefore, most studies have to extrapolate the mass distribution out to the virial radius, which is usually much larger than the region explored by the tracers and the result is dependent on the model used. Assuming circular orbits, stars are used to constrain the mass distribution based on the LOS velocity measurements. However, the lack of proper motion measurements before *Gaia* leads to uncertainties in the mass estimation.

Dwarf galaxies are also used to constrain the MW mass. However, recent observations and simulations suggest that most of the MW dwarf galaxies are newcomers, which is in tension with the previous understanding of long-lived satellites. The mass estimation based on the dwarf galaxies will be biased if the assumption of long-lived satellites is incorrect ([Chapter 4, Section 1.4](#)).

Another constraint on the MW mass comes from the estimation of the total mass of the Local Group, known as *the timing argument* (Kahn & Woltjer, 1959). This method is based on the assumption that the combined masses of M31 and the MW must be sufficient to overcome universal expansion, thereby explaining their present-day kinematics (van der Marel et al., 2012). However, the recent major merger of M31, which occurred 2–3 Gyr ago (Hammer et al., 2018a), may have significantly affected its proper motion, introducing uncertainties in the mass estimation.

[Figure 1.5](#) presents a summary of measured virial masses for the Milky Way from various studies (Wang et al., 2020a). Most estimates place the MW mass within the range of $0.8 – 1.5 \times 10^{11} M_\odot$.

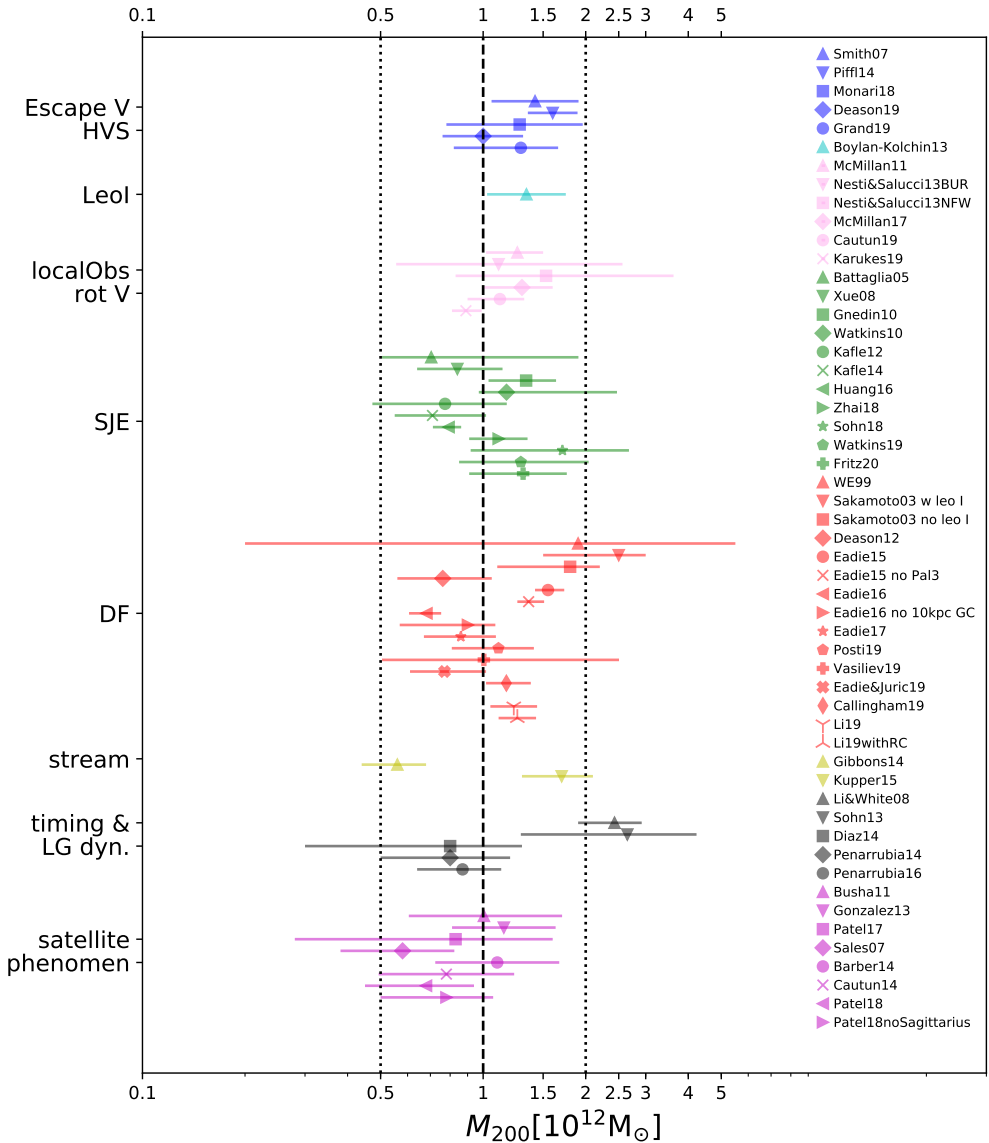


FIGURE 1.5 – Literature compilation of inferred virial masses for the MW. Classes of methods are marked in different colors. Measurements have been converted to M_{200} , assuming NFW profiles. The vertical dashed line presents $1 \times 10^{12} M_\odot$, and two vertical dotted lines are at $0.5 \times 10^{12} M_\odot$ and $2 \times 10^{12} M_\odot$. This figure is adapted from Wang et al. (2020a).

7 Structure of This Dissertation

The rotation curve is one of the most reliable tools for probing the dynamical mass of galaxies. However, with advancements in understanding galaxy evolution and accurate observations, the fundamental assumption that spiral galaxies are in equilibrium when deriving the rotation curve has begun to be questioned. In this dissertation, I analyze observational data from both the Milky Way and nearby galaxies. For nearby galaxies, I compare them with simulations to assess the radius on which we can accurately derive the rotation curve and estimate mass distribution.

Dwarf galaxies were considered the most dark matter-dominated systems in the Universe. However, recent observations suggest that many of them may be newcomers to the Milky Way, challenging the earlier understanding of them as long-lived satellites. In this dissertation, I will also present my studies on dwarf galaxies and the comparison of observational data with different cosmological simulations.

Specifically, this dissertation is organized as follows:

In Chapter 2, I present my first article, focusing on the estimation of the MW dynamical mass using its rotation curve from *Gaia DR2* (Eilers et al., 2019). I then use *Gaia DR3* to derive an updated MW rotation curve and estimate its mass, discussing the discovery of the Keplerian decline in the MW rotation curve and its implications for dark matter distribution.

In Chapter 3, I present my studies of nearby galaxies, introducing the galaxy sample, explaining the methods used to determine the timing of their last major mergers, and comparing these results with gas-rich major merger simulations. I discuss the impact of major mergers on the rotation curve and mass distribution of galaxies.

In Chapter 4, I explore my work on dwarf galaxies, outlining the cosmological simulations employed and comparing the results with observational data.

Finally, I will discuss the overall findings of this dissertation, conclude them, and discuss future work.

Chapitre 2

Milky Way rotation curve and mass estimation

Contents

1	Introduction	26
1.1	Milky Way rotation curves before <i>Gaia</i>	26
1.2	Revolution of <i>Gaia</i>	27
2	Milky Way mass based on the rotation curve from <i>Gaia DR2</i>	28
2.1	Subsequent summary of Paper I	28
3	Milky Way rotation curve from <i>Gaia DR3</i>	29
3.1	Subsequent summary of Paper II	29
3.2	Discussion about Paper II	30
4	A further analysis of the Milky Way rotation curve	35
4.1	Introduction	35
4.2	Methodology	37
4.3	Rotation curve and maximal mass estimation	43
4.4	Discussion	47
4.5	Conclusion	49
Appendix A:	Which Milky Way masses are consistent with the slightly declining 5-25 kpc rotation curve? (Paper I)	50
Appendix B:	Detection of the Keplerian decline in the Milky Way rotation curve (Paper II)	60

1 Introduction

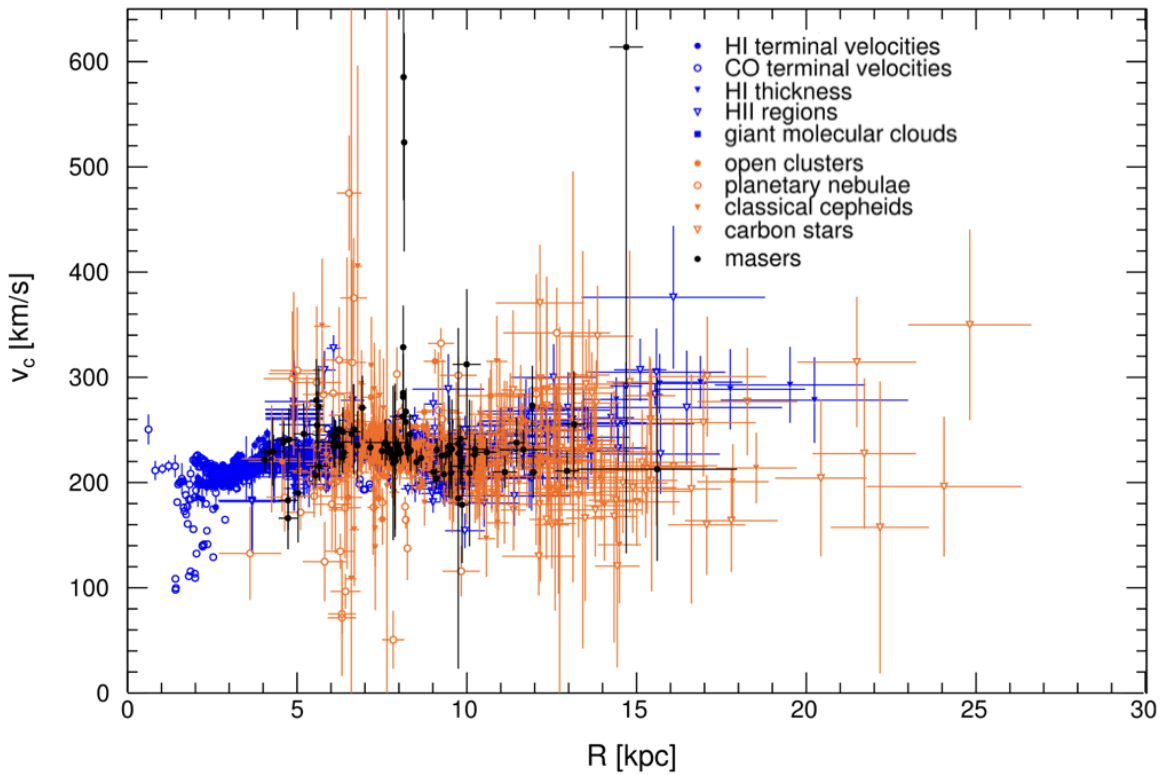
The study of the Milky Way (MW) is fundamental to modern astrophysics. As our home Galaxy, it offers a vast amount of observational data. With the accumulation of data from all-sky surveys across various wavelengths, such as 2MASS, SDSS, and *Gaia*, billions of stars have been cataloged with precise photometric magnitudes and colors in optical and infrared wavelengths. Additionally, many of these stars have been observed with high-quality spectroscopic data, providing radial velocities, distances, and detailed elemental abundances. This extensive dataset enables astronomers to probe the formation and evolutionary processes of the MW from its most fundamental components: the stars.

One application of this wealth of data is the estimation of the initial mass function (IMF), which plays a crucial role in understanding stellar populations and the chemical evolution of galaxies. Kinematic and chemical studies of MW stars, combined with age and spatial distribution analyses, suggest that the stellar halo and thick disk likely formed from pre-existing stars during a major merger event approximately 8-10 Gyr ago. This event, known as the Gaia-Sausage-Enceladus merger, has been widely studied (Belokurov et al., 2018; Haywood et al., 2018; Helmi et al., 2018). In contrast, the thin disk is considered to have formed from gas that was redistributed during this period based on the disk rebuilding scenario. Consequently, research on the MW not only deepens our knowledge of the Galaxy but also provides a crucial framework for understanding the structure and evolution of other galaxies.

1.1 Milky Way rotation curves before *Gaia*

The most precise method for determining the mass distribution within a galaxy is typically through the analysis of its rotation curve (RC) (Sofue & Rubin, 2001). However, our position within the disk of the Milky Way (MW) makes it challenging to obtain a comprehensive, global view of the Galaxy. Fortunately, the relatively quiescent evolutionary history of the MW allows for the assumption that the disk is in equilibrium. This equilibrium enables the derivation of the MW RC using local observations. Early efforts to measure the inner RC relied heavily on terminal velocities of neutral hydrogen (HI) and carbon monoxide (CO) gases (Burton & Gordon, 1978; Clemens, 1985; Fich et al., 1989). For the outer regions of the Galaxy, RCs were determined by combining optical distance measurements of OB stars (Blitz, 1979; Demers & Battinelli, 2007). Additionally, the HI thickness method was employed to measure the rotation across the entire disk (Merrifield, 1992; Honma & Sofue, 1997).

However, accurately determining gas distances remains challenging, introducing significant uncertainties into the derived RC. The motion of stars in the infrared (IR) was first used to estimate the mass distribution in the innermost regions of the Galactic Center (GC) (Lindqvist et al., 1992). With the increasing availability of line-of-sight (LOS) velocity measurements of stars, several studies have used these data to derive the RC, assuming that stars move in circular orbits (e.g., Huang et al., 2016). Nevertheless, the selected stars may have eccentric orbits, which cannot always be confirmed, leading to RCs with significant uncertainties and fluctuations, particularly at larger radii. Although some studies have employed stellar proper motions to

FIGURE 2.1 – The Milky Way rotation curve before *Gaia*

derive the RC (Honma et al., 2012; Reid et al., 2014), these approaches are also limited by large proper motion uncertainties and the relatively small sample sizes available. Consequently, RCs often exhibit considerable uncertainty overall.

As a result, the MW RC before *Gaia* was considered almost the worst¹ RC compared to those of other spiral galaxies, as shown in Figure 2.1. Beyond 5 kpc, the discrepancies could reach up to ~ 200 km/s. Despite these limitations, earlier studies used this rotation curve to estimate the MW mass, often adopting the NFW profile (Navarro et al., 1997) and extrapolating to a virial radius of approximately 200–300 kpc. These studies typically estimated the total mass of the MW to be in the range of $\sim 1 - 2 \times 10^{12} M_{\odot}$ (Bovy et al., 2012b; Sofue, 2013, 2015; Huang et al., 2016).

1.2 Revolution of *Gaia*

The *Gaia* mission, operated by the European Space Agency, is a groundbreaking space observatory launched in December 2013. Its primary goal is to create the most precise and comprehensive 3D map of the Milky Way, enabling the derivation of the spatial distribution, kinematics, chemical abundances, and various other physical properties of stars within our galaxy.

The revolution came with its second data release (DR2) in 2018. *Gaia* DR2 provided radial

1. It could be argued that RCs of other spiral galaxies are typically derived only from H α (and/or other emission lines) in the inner regions and HI in the outer regions.

velocity measurements (median values across multiple epochs) for more than 7.2 million stars, with mean G magnitudes ranging from approximately 4 to 13, alongside detailed positional data, motions on the sky, and parallaxes. This extensive dataset enabled the derivation of the MW RC with unprecedented precision by using the highly accurate proper motion and parallax measurements of individual stars. It leads to 2 MW RCs published in 2019: Eilers et al. (2019) and Mróz et al. (2019).

Eilers et al. (2019) selected 23 129 red giant branch stars (RGBs) to derive the rotation curve. They adopted a data-driven approach, combining spectroscopic data from APOGEE DR14 with photometric data from *Gaia* DR2, 2MASS, and WISE to calculate precise spectrophotometric parallaxes, yielding highly accurate distance estimates. Using the Jeans equation, they corrected for asymmetric drift and derived the circular velocity. In addition, they conducted a comprehensive analysis of systematic uncertainties, which were significantly smaller compared to previous rotation curves. Their results revealed a slightly declining rotation curve, with a linear fit indicating a slope of -1.7 ± 0.1 km/s/kpc. Beyond ~ 19 kpc, the curve shows a steep decline, although the authors did not investigate this further, possibly due to the larger uncertainties in that region. By applying the NFW profile, they estimated the dark matter mass of the Milky Way to be $7.25 \times 10^{11} M_{\odot}$.

Mróz et al. (2019) utilized 832 Cepheids to derive the MW RCs. Based on distance measurements provided by Skowron et al. (2019), they assumed several velocity models as functions of radius to calculate the circular velocity of the Cepheids. Their results also indicated a declining rotation curve, with a small gradient of -1.34 ± 0.21 km/s/kpc. They argued that this slope contrasts with the expected Keplerian decline, however, their RCs were limited to a radius of 20 kpc.

With the most accurate MW RC, we can estimate the MW mass using various dark matter density profiles. This has led to my first article (Jiao et al., 2021, hereafter referred to as Paper I). With the data from *Gaia* DR3, the MW rotation curve can be derived with even greater accuracy and extended to larger radii, which has resulted in my second article (Jiao et al., 2023, hereafter referred to as Paper II).

2 Milky Way mass based on the rotation curve from *Gaia* DR2

The paper is published on *Astronomy & Astrophysics* and is available at <https://doi.org/10.1051/0004-6361/202141058>. The paper also can be found in the Appendix A.

2.1 Subsequent summary of Paper I

In paper I, we employed χ^2 method to fit the MW RC derived by Eilers et al. (2019) based on *Gaia* DR2 with NFW, generalized NFW, and Einasto DM density profiles. Our analysis revealed that the NFW and gNFW profiles tend to narrow the total mass range, potentially introducing a methodological bias, particularly against lower MW mass estimates. In contrast, the Einasto profile provided a better fit to the slightly declining RC by allowing for a varying outer DM

density slope. While the Einasto profile results in a larger range of MW mass estimates, it suggests that the best-fit mass could be as low as $2.6 \times 10^{11} M_{\odot}$. This is significantly lower than previous estimates of approximately $1 \times 10^{12} M_{\odot}$ (Bovy et al., 2012b; Sofue, 2013, 2015; Huang et al., 2016; Eilers et al., 2019; Cautun et al., 2020; Karukes et al., 2020).

Karukes et al. (2020) applied the Einasto profile to fit the MW RCs and obtained a smaller total mass estimate of $5.01 \times 10^{11} M_{\odot}$, compared to $8.91 \times 10^{11} M_{\odot}$ from the NFW profile. They argue that the slight decline in the RC causes the extrapolated DM distribution in the Einasto profile to transition from a cored structure in the inner region to a flatter mass profile (with a steeper density gradient) in the outer regions, which contrasts with the NFW profile when using the MCMC method. This transition leads to a lower total mass estimate.

They interpreted this difference arising from the Einasto profile as a systematic uncertainty resulting from DM profile selection. They still used the gNFW and Burkert profiles to estimate the MW mass, as the Burkert profile produced a value similar to that of the gNFW profile. Both the NFW and Burkert profiles, however, are too shallow ($\rho \propto r^{-3}$) at large radii, and their virial masses are extrapolated out to 190 kpc. Therefore, it is not surprising that these profiles yield similar mass estimates. Despite the uncertainties in the RC beyond 21 kpc being significant, the use of the Einasto profile to represent systematic uncertainty, however, may introduce bias into the MW mass estimation.

3 Milky Way rotation curve from *Gaia* DR3

The paper is published on *Astronomy & Astrophysics* and is available at <https://doi.org/10.1051/0004-6361/202347513>. The paper also can be found in the Appendix B.

3.1 Subsequent summary of Paper II

The most significant finding of Paper II is the detection of a Keplerian decline in the MW RC. Since the flat behavior of RCs has long been regarded as significant evidence for the existence of DM, it is unsurprising that this discovery has attracted considerable attention both within the astronomical community and beyond. As a result, we have been invited by several research institutions to present this finding. Additionally, the result has been featured multiple times in public media, including *The Times*², *ScientificAmerican*³, *PHYSORG*⁴.

The first reaction to this paper often centers on the implication that the result suggests the absence of DM. Therefore, I must emphasize once again that under the current model of baryonic matter distribution in the MW, which includes stars, cold gas, and dust, the baryonic mass alone cannot account for the total dynamical mass indicated by the RC and its Keplerian decline. Therefore, DM is still required to reconcile this discrepancy. This conclusion, however, introduces additional challenges:

2. <https://www.thetimes.com/uk/science/article/milky-way-a-fifth-as-heavy-as-previous-thought-7j27xjvqq>

3. <https://www.scientificamerican.com/article/the-milky-way-may-be-missing-a-trillion-suns-orth-of-mass/>

4. <https://phys.org/news/2023-09-revisited-mass-milky-smaller-cosmology.html>

First, it is at odds with the well-known *missing baryon* problem. The newly estimated ratio of DM to baryonic mass within the MW is approximately 2 to 2.5, which is significantly lower than the ratio of around 5 predicted by the Λ CDM model for the Universe. Previous estimates for galaxies yielded much higher ratios, and have been associated to the *missing baryon* problem. If the Keplerian decline is confirmed, it would imply that, even without introducing additional baryonic matter, the baryonic content within the Milky Way is higher than what cosmological models predict. This would effectively shift the missing baryon problem into an *excess baryon* problem.

Second, dwarf galaxies have long been regarded as satellites of the Milky Way. However, if the MW mass is constrained by the Keplerian decline, some of these galaxies may no longer be classified as MW satellites (Hammer et al., 2024). This would necessitate a reassessment of the properties and classification of dwarf galaxies (see details in Chapter 4, Section 1.3).

Hot gas has long been considered as a potential solution to the missing baryon problem. By adding the mass of hot baryons to the visible mass of the MW, Nicastro et al. (2016) estimated the total baryonic mass within 300 kpc to be between $0.8 \times 10^{11} M_\odot$ and $4 \times 10^{11} M_\odot$. However, within 20 kpc, their estimated baryonic mass is less than $0.8 \times 10^{11} M_\odot$, still insufficient to account for the total dynamical mass of approximately $2 \times 10^{11} M_\odot$ implied by the Keplerian decline. This leaves around 60% of the mass unaccounted for. New observations of MW hot gas, such as those from the eROSITA mission, are crucial for providing more accurate estimates of the hot baryon mass.

This result has also been used to test the modified Newtonian dynamics (MOND) theory (e.g., Chan, 2024; Coquery & Blanchard, 2024). The Keplerian decline in the MW RC is in tension with MOND, which predicts a flat⁵ RC at large radii. Additionally, this low-mass MW model has been compared with the high-mass estimate proposed by Cautun et al. (2020), which suggests a mass of approximately $1 \times 10^{12} M_\odot$, to test for the presence of primordial black holes (PBHs) in the MW halo. The results are consistent with the absence of PBHs as DM in the MW.

3.2 Discussion about Paper II

Given that Keplerian decline is in tension with many current astrophysical studies, numerous researchers have thoroughly reviewed our results and provided valuable comments and feedback.

3.2.1 Systematic uncertainties

In Paper II, we followed the approach of Eilers et al. (2019) in estimating the systematic uncertainties for the rotation curve. However, the systematic uncertainties were likely overestimated, as Eilers et al. (2019) accounted for both the neglected cross-term and the effects of splitting the data. These two factors, however, both relate to the asymmetric drift in the Milky Way disk and should not be considered separately, leading to an overestimation of the uncertainties. This, in turn, resulted in artificially low χ^2 values during the fitting process. As

5. Or at least the decrease cannot be Keplerian.

Paul McMillan pointed out on his X account (formerly Twitter), the fits appeared to be too good. We think that one of the reasons for this discrepancy is the overestimation of systematic uncertainties in previous methods and we address this problem in Chapter 2, Section 4.2.3.

3.2.2 First tests on varying scale length of the MW disk

The scale length of the MW disk is a crucial parameter for deriving the RC using the Jeans equation. While most studies adopt a scale length of 2.5-3 kpc (Jurić et al., 2008; Bland-Hawthorn & Gerhard, 2016), some research suggests that the MW may have a variable scale length (Lian et al., 2024; Wang et al., 2018). Therefore, it is important to investigate how different scale lengths impact the RC.

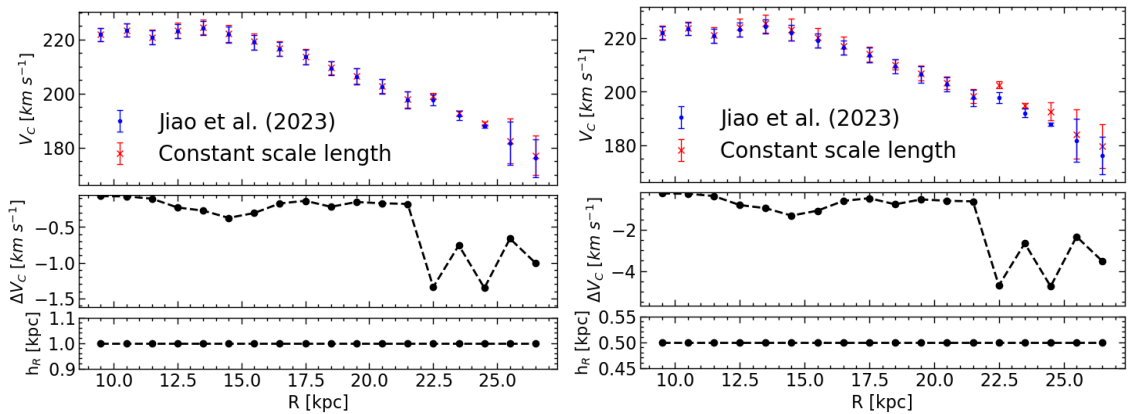


FIGURE 2.2 – The Milky Way rotation curve (RC) with different disk scale lengths. The blue points with error bars represent the RC from Jiao et al. (2023). The red crosses with error bars show the RC using different scale lengths compared to those adopted by Jiao et al. (2023, $h_R = 2.5$ kpc). The middle panel in each figure presents the residuals of the RC, while the bottom panel in each figure shows the tested disk scale lengths.

In this study, we used data from Wang et al. (2023) to derive the MW RCs with varying scale lengths and compare them with the RC from Paper II. According to the Jeans equation, a smaller scale length results in a higher circular velocity. First, we tested scale lengths of 1 kpc and 0.5 kpc, as shown in Figure 2.2. We find that the RC at large radii is sensitive to scale length, with smaller disk scale lengths increasing the contribution of radial velocity to the circular velocity. However, the difference compared to previous studies is not significant, as the radial velocity estimated by Wang et al. (2023) is relatively small. This may be due to the MW disk being in a state of equilibrium. As a result, applying the LIM method to all stars reduces the contribution of radial velocity. To produce a flat RC, a much smaller scale length would be required.

Therefore, we tested a linear variation in scale length from 2.5 to 0.1 kpc. The resulting RC still exhibits a decline in the inner region (within 20 kpc) while flattening at larger radii, as shown in Figure 2.3. As a control, we also tested a variation in scale length from 2.5 to 7.5 kpc, which confirmed that the choice of scale length does not affect the Keplerian decline observed in the RC.

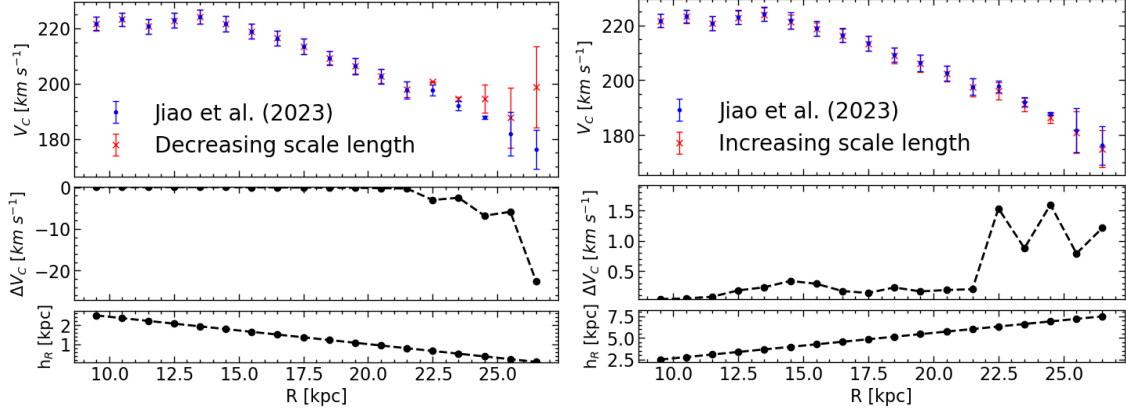


FIGURE 2.3 – Same as Figure 2.2, but with decreasing (left panel) and increasing (right panel) scale length.

Gary Mamon (private communication) used MW-like simulations from TNG50 to compare the RC derived from the Jeans equation with the true RC obtained from the potential. He found that the Jeans equation could introduce a bias toward a Keplerian decline at large radii, potentially due to the assumption of a purely exponential disk. To further test this, we examined a step-decreasing exponential disk model using two examples from TNG50: (I) with inner and outer scale lengths of $h_{R,\text{inner}} = 7.0$ kpc and $h_{R,\text{outer}} = 4.0$ kpc, and (II) with $h_{R,\text{inner}} = 3.4$ kpc and $h_{R,\text{outer}} = 2.9$ kpc, both transitioning at 12 kpc. Similar to previous tests, the RC showed almost no changes as shown in Figure 2.4. Additionally, we tested a broken exponential disk with a transition at 12 kpc, using an inner scale length of 2.5 kpc and outer scale length ratios of 2 and 5. These results confirmed that a smaller scale length corresponds to a higher velocity. Given that the radial velocity in Ou et al. (2024) is relatively larger, selecting an appropriate scale length is crucial when deriving the MW RC (see Chapter 2, Section 4.2.2).

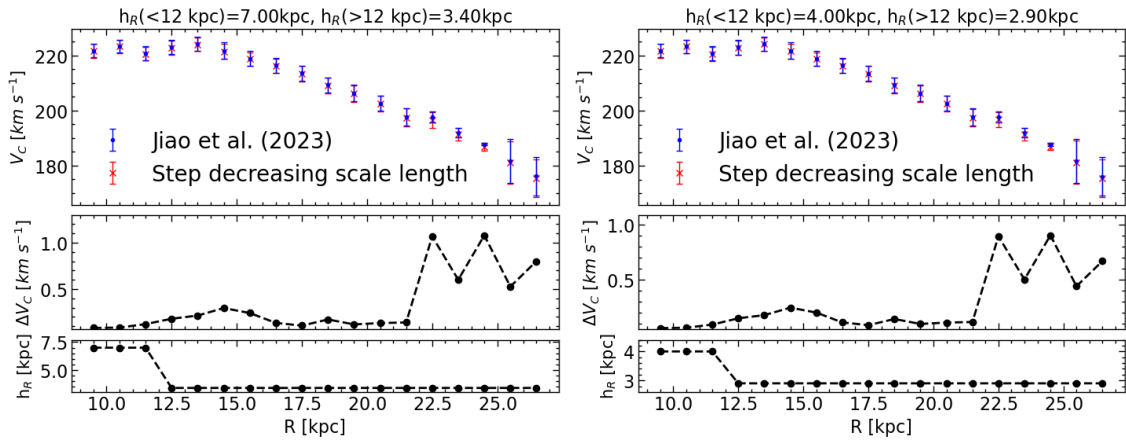


FIGURE 2.4 – Same as Figure 2.2, but with step decreasing scale lengths.

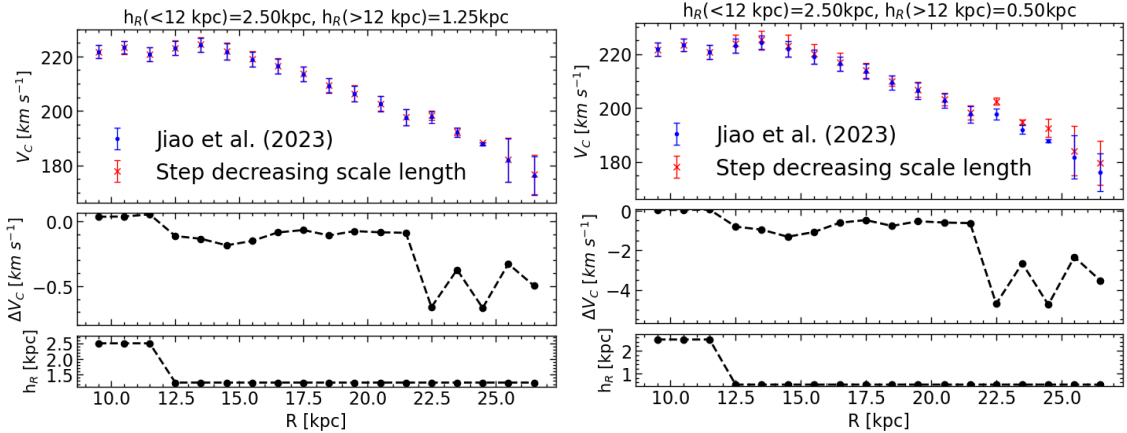


FIGURE 2.5 – Same as Figure 2.2, but with step decreasing scale length.

3.2.3 Is the MW disk out of equilibrium?

Interactions between the MW, the MCs, and Sgr have been proposed to potentially disrupt the dynamical equilibrium of the Galactic disk at larger radii (Laporte et al., 2018; Vasiliev et al., 2021; Koop et al., 2024). However, these studies are prone to overestimating the masses of these galaxies. For instance, the displacement of the MW halo relative to its disk caused by the influence of the LMC has been used to estimate the mass ratio between the MW and LMC with reasonable accuracy (Conroy et al., 2021; Erkal et al., 2021). However, assuming a more massive MW model as a prior can lead to an overestimation of the LMC mass. In addition, many simulations neglect the gas component, which plays a crucial role in the evolution of dwarf galaxies (Hammer et al., 2023, 2024; Wang et al., 2024). Using hydrodynamical simulations, Wang et al. (2019a) were able to reproduce several key features of the MCs, such as the dual filamentary structure in the HI stream, through a ram-pressure and collision model. Their simulations suggest that LMC mass up to $2 \times 10^{10} M_{\odot}$ can be accommodated, but exclude masses exceeding $10^{11} M_{\odot}$.

The presence of the Galactic warp has also been suggested as an indication that the Galactic disk is not in dynamical equilibrium. Ibata et al. (2024) used the RC from Eilers et al. (2019), limited to within 15 kpc, to fit the MW mass, because they argued that the observed decline in the RC at larger radii could be attributed to the warp. However, Philippe Amram (private communication) estimated that for the warp to reproduce the RC derived from the mass profile of Ibata et al. (2024), it would require an inclination larger than 20 degrees beyond 20 kpc⁶ when correcting the RC from Eilers et al. (2019). This estimation contradicts observations, where the MW warp is typically measured to have an inclination of less than 10 degrees. Thus, the warp is unlikely to account for the significant decrease in the MW RC at large radii.

Several mechanisms have been proposed to explain the existence of the Galactic warp, such as interactions with satellite galaxies (e.g., López-Corredoira et al., 2002a; Bailin, 2003; Weinberg & Blitz, 2006), bending instabilities and self-excited or internally driven warps in the disk (Revaz & Pfenniger, 2004; Sellwood & Debattista, 2022). However, since warps are commonly observed

6. And 40 degrees at 25 kpc.

in spiral galaxies (Reshetnikov & Combes, 1998; Sánchez-Saavedra et al., 2003), it is possible that the MW warp represents a more fundamental aspect of spiral galaxy evolution, potentially originating from gas-rich major mergers. Sauvaget et al. (2018), using N-body/SPH simulations, proposed that warps could naturally result from gas-rich major mergers, persisting for several billion years. Particularly, Deng et al. (2024) employed gas-rich merger simulations to reproduce nearly all the observed features of the Galactic warp, suggesting it might be a remnant of the MW last major merger, possibly related to the GSE event. Therefore, we propose that the Galactic warp may be a structure in (quasi-)equilibrium, implying that RCs derived from stellar kinematics using the Jeans equation are unlikely to be significantly affected. A more detailed study of the warp's dynamics is needed to fully understand its role in the evolution of galaxies.

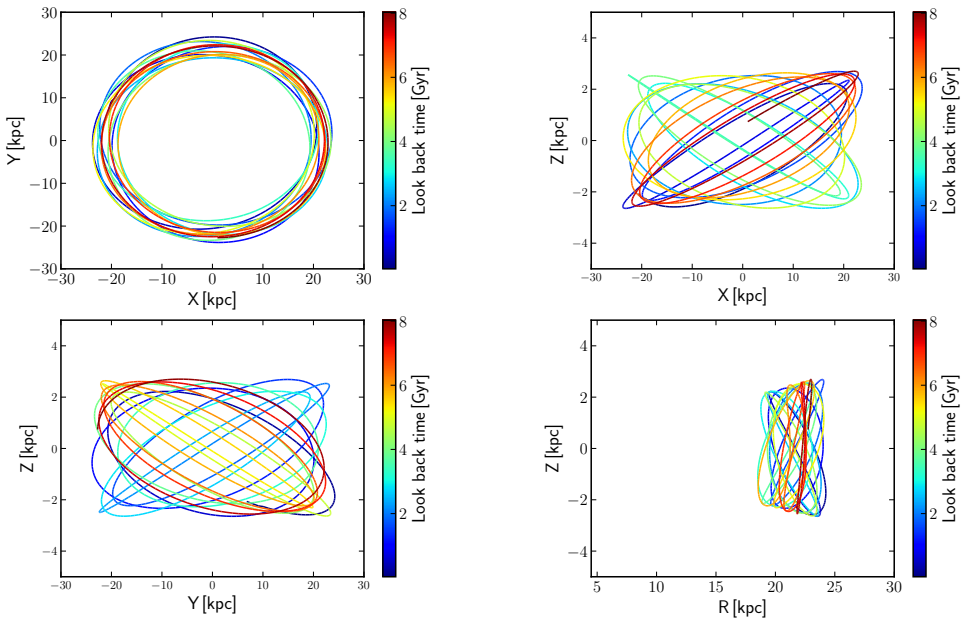


FIGURE 2.6 – Projections of an outer disk star, GaiaDR3 244707655774974464, with a disc-like orbit in the X-Y (top-left), X-Z (top-right), Y-Z (bottom-left), and R-Z (bottom-right) planes. The orbit is color-coded by the look-back time. The majority of the outer sample (244 stars) exhibits these very similar orbits. This figure is adapted from Ou et al. (2024).

Furthermore, beyond 20 kpc, almost all disk stars used to derive the RC in the study of Ou et al. (2024) follow circular orbits, as shown in Figure 2.6. Only three stars in their sample exhibit highly eccentric orbits, one of which is highlighted in Figure 2.7. Chrobáková et al. (2020), using N-body simulations, demonstrated that the Jeans equation can provide a reasonable approximation of the system if the amplitude of radial velocity is much smaller than the azimuthal component. Based on the outermost RC data from Ou et al. (2024), which shows a velocity of 170 km s^{-1} at a radius of 27 kpc, a star would have completed approximately nine orbits if the GSE event occurred 9 Gyr ago. This suggests that if the MW disk has not been significantly disturbed by recent interactions, the disk stars should be in equilibrium. As a result, the RC derived from these disk stars remains reliable.

Stacy McGaugh (private communication) raised concerns regarding the MW RC beyond 20

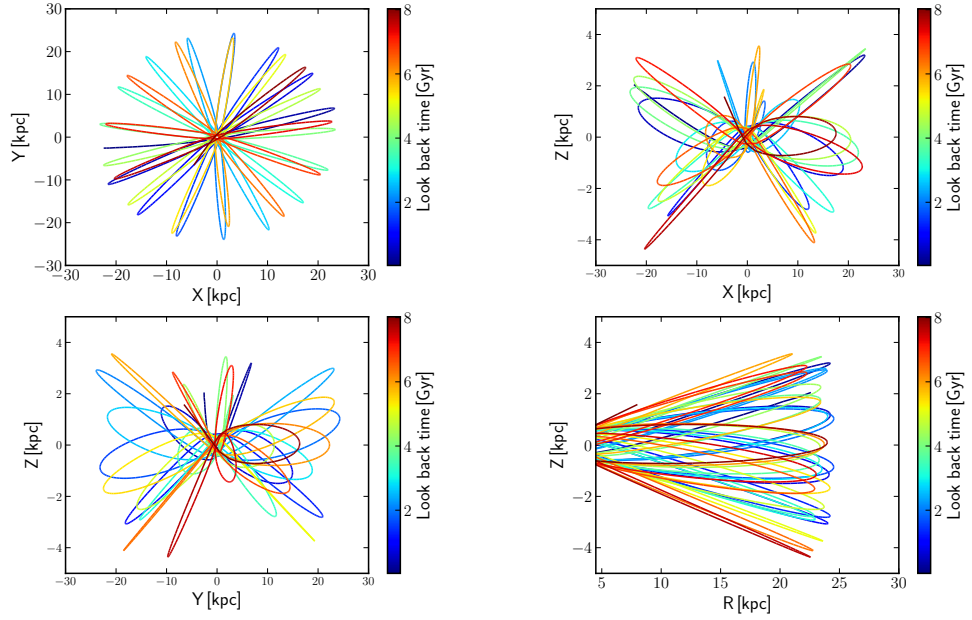


FIGURE 2.7 – Projections of an outer disc star, GaiaDR3 3382839632449159040, with a highly eccentric orbit in the X-Y (top-left), X-Z (top-right), Y-Z (bottom-left), and R-Z (bottom-right) planes. The orbit is color-coded by the look-back time. Only three out of the 244 outer sample stars present such an orbit. This figure is adapted from Ou et al. (2024).

kpc, as shown in Wang et al. (2023, Figure 8). Specifically, the radial velocity profile of stars within 1 kpc of the Galactic plane displays notable differences when compared to stars within heights of 3 or 5 kpc. We think this may reflect the presence of dynamical structures above and below the Galactic plane, which prompted us to include this factor when estimating the systematic uncertainties in the MW RC (see Section 4.2.3).

Additionally, Wang et al. (2023) divided the stars into smaller regions and applied Lucy’s inversion method (Lucy, 1974, LIM,) to derive the 6D parameters of each cell using all available stars. The inclusion of all disk stars may also be contributing to the discrepancies in the radial velocity profile observed at different heights. However, the LIM is a statistical deconvolution method, which prevents the accurate recovery of the true 6D parameters for individual stars, thereby limiting further analysis due to data degeneracy. To address these issues, we will use the RGB data from Ou et al. (2024) for resampling and recalculating the RC, providing a more accurate estimate of the systematic uncertainties (see Chapter 2, Section 4).

4 A further analysis of the Milky Way rotation curve

4.1 Introduction

As presented in Paper II, the Keplerian decline observed in the MW RC, along with its relatively low dynamical mass, raises important questions about its cosmological context. First, the baryonic component (stars, dust, and neutral gas) comprises approximately $0.6 \times 10^{11} M_{\odot}$, which accounts for nearly 30% of the total dynamical mass ($2.06 \times 10^{11} M_{\odot}$; Paper II). This

fraction is considerably larger than what is typically observed in other galaxies (around one-tenth) and the Universe as a whole (roughly one-sixth). Second, the MW RC shows a distinct Keplerian decline, in contrast to the flat RCs commonly seen in other spiral galaxies. Notably, this decline occurs around the optical disk radius (17 kpc), implying that the MW is more compact in both size and mass than previously assumed.

Despite these findings, few studies have rigorously assessed the maximum MW mass that remains consistent with *Gaia* DR3 RCs, factoring in a comprehensive error analysis. For instance, Ou et al. (2024) performed a detailed evaluation of potential sources for systematic uncertainties, following Eilers et al. (2019), yet did not account for these when modeling their RC. Incorporating all the systematic uncertainties identified by Eilers et al. (2019) would lead to a significant overestimation of them, yielding a MW mass range between 2 and $8 \times 10^{11} M_\odot$, which is comparable to values derived from *Gaia* DR2 data (Paper I). To refine this estimate, a careful re-evaluation of systematic uncertainties is critical, as it has broad implications for research on dark matter, the MW disk, and its dwarf galaxy population.

In this section, we use the stellar sample from Ou et al. (2024) to assess the robustness and accuracy of the MW RC derived from *Gaia* DR3 data. Section 4.2 provides a re-analysis of the star sample, and accounts for systematic uncertainties. Section 4.3 provides the RC and the fittings for determining the maximum possible MW mass. In Section 4.4, we compare our findings on the MW maximum mass with earlier estimates.

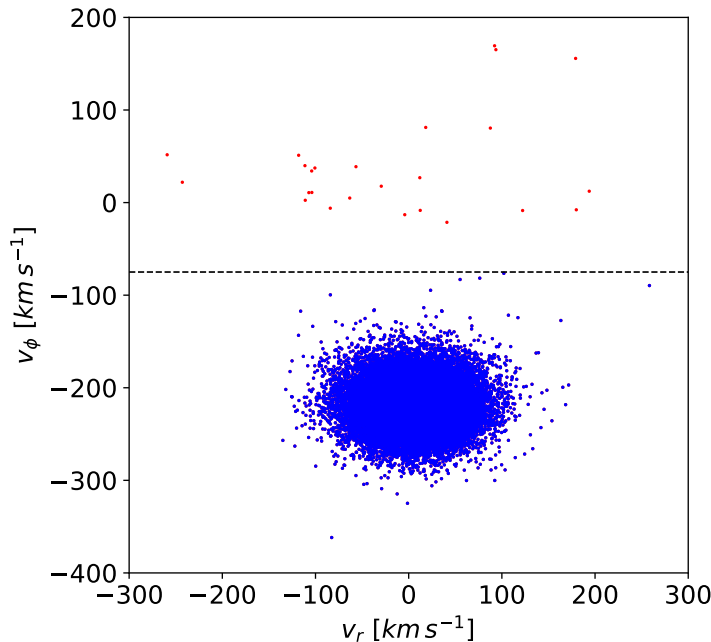


FIGURE 2.8 – Tangential (azimuthal) velocity v_ϕ versus radial velocity v_r for the star sample from Ou et al. (2024). Stars above the horizontal dashed line at $v_\phi = -75 \text{ km s}^{-1}$ have excessively small or inverted tangential velocities and are excluded from the revised sample.

4.2 Methodology

4.2.1 Resampling the data from Ou et al. (2024)

We used the data sample from Ou et al. (2024), who follow the methodology of Eilers et al. (2019). Their data samples employ a linear model that combines spectroscopic data from APOGEE with photometric measurements to estimate spectrophotometric parallaxes for Red Giant Branch (RGB) stars (Hogg et al., 2019). Additionally, we applied an extra criterion to the Ou et al. (2024) sample, selecting stars with $v_\phi < -75 \text{ km s}^{-1}$ to exclude those that might not be in dynamical equilibrium, as shown in Figure 2.8. This selection reduced the sample to 33 327 stars⁷.

However, the RC from Ou et al. (2024) is sampled using 37 radial bins, which may not be entirely independent. For example, in the R_{GC} range of 10 to 23 kpc, the bin width is 0.5 kpc, whereas the uncertainty in distance estimates from spectrophotometric parallaxes can reach up to 1 kpc, as illustrated in Figure 2.9. Posti (2022) also argued that assuming independent velocity data points in RC fits leads to biased parameter constraints and unrealistically small uncertainties on the predicted velocity profile. Oman & Riley (2024) applied the method proposed by Posti (2022) and confirmed that this correlation could lead to an overestimation of the mass by approximately 50%. To address this, we adopt a bin width of 1 kpc within the 10–23 kpc range, thereby reducing contamination between adjacent bins due to distance uncertainties. For star samples beyond 23 kpc, we adjust the bin size to ensure a minimum of 36 stars per bin, providing sufficient sampling for the outer RC while minimizing bias.

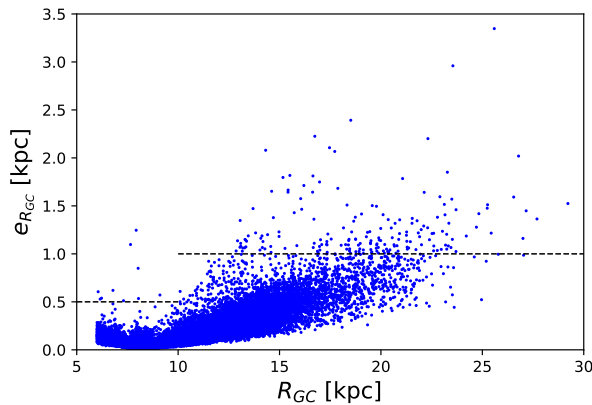


FIGURE 2.9 – Uncertainty in distances from the Galactic center as a function of distance. The red horizontal lines indicate the bin widths adopted for distances below and above 10 kpc, respectively.

4.2.2 Scale length estimation

The scale length is associated with the ν term in the Jeans equation, which represents the density distribution of the tracer population. In this study, we followed the selection criteria of

⁷. Following the selection criteria in Ou et al. (2024) only, our star sample includes 33 352 stars, 17 stars more than their final sample of 33 335 stars.

Eilers et al. (2019) and Ou et al. (2024), specifically choosing stars with $0 \leq \log(g) \leq 2.2$ and $[\alpha/\text{Fe}] < 0.12$. These tracers are upper RGB stars with low α -element abundances. Such stars are more dynamically virialized and experience less asymmetric drift than other populations (Eilers et al., 2019), making them well-suited for dynamical studies and Jeans modeling. Their luminosities allow for more precise measurements of velocity and position, making them ideal for deriving the MW RC through the Jeans equation. Therefore, accurately estimating their density distribution is essential for obtaining a reliable MW RC.

Assuming that the stars in the sample follow the same distribution as the MW disk, previous studies typically adopt a single exponential profile when deriving the Jeans equation. Wang et al. (2023) and Jiao et al. (2023) used an exponential radial profile for the tracer population, with a scale length of $h_R = 2.5$ kpc. This value aligns well with the estimate from Jurić et al. (2008), who analyzed a large sample of M dwarfs from the SDSS photometric survey and reported a scale length of 2.6 kpc for the thin disk. In contrast, Eilers et al. (2019) and Ou et al. (2024) used a slightly larger scale length of $h_R = 3$ kpc (Bland-Hawthorn & Gerhard, 2016).

Wang et al. (2018) used RGB stars from LAMOST DR3 to study the MW disk out to 19 kpc and identified breaks in the radial profile at approximately $R \sim 11$ kpc and $R \sim 14$ kpc. Their analysis divided the radial density profile into three regions, with scale lengths of 2.12 kpc for $R < 11$ kpc, 1.18 kpc for $11 \leq R \leq 14$ kpc, and 2.72 kpc for $R > 14$ kpc. Similarly, Lian et al. (2024), using APOGEE data to model the MW surface luminosity density, concluded that the MW disk cannot be described by a single exponential profile. Furthermore, Koop et al. (2024) suggested that a truncated MW disk at around 20 kpc could help to obtain a flat RC at larger radii. Kroupa et al. (2024) also argued that the Keplerian decline observed in the MW RC could be due to a break in the MW disk occurring at about 17 kpc.

Given that the MW disk stellar distribution, particularly at large radii, remains in debate, previous studies have also estimated the systematic uncertainties associated with the density distribution. Paper II, as well as Eilers et al. (2019) and Ou et al. (2024), accounted for a 1 kpc uncertainty in the scale length and considered a power-law density profile instead of an exponential profile as part of the systematic uncertainty analysis. Zhou et al. (2023) adopted a smaller uncertainty of 0.23 kpc. Despite this difference, all of these studies agree that scale length uncertainty is the dominant contributor to total systematic uncertainty. This dominance could lead to an overestimation of the overall systematic uncertainty. Consequently, the use of a 1 kpc uncertainty in the scale length, along with the consideration of a power-law profile, tends to drive the systematic uncertainty for RC within $R < 22$ kpc.

However, since we applied the Jeans equation to a small sample of RGB stars for deriving the RC, selecting a representative and relatively complete sub-sample with correction of selection bias could allow us to estimate the density distribution of the tracer population directly. This would be a crucial step in calculating the circular velocity and could potentially eliminate the need to rely on pre-existing estimates of the MW disk density profile. By doing so, we would reduce the associated systematic uncertainties, i.e., those related to the scale length and density profile, leading to a more accurate estimation of RC and systematic uncertainties.

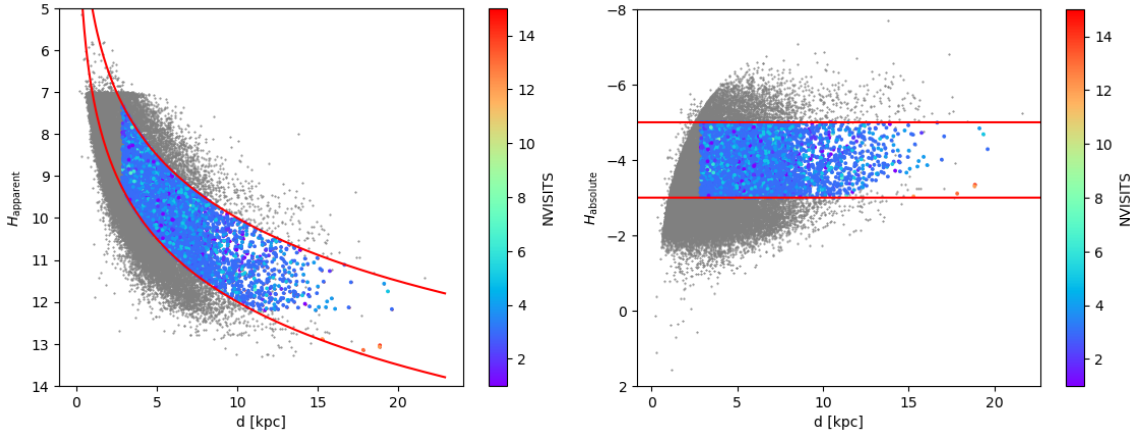


FIGURE 2.10 – H -band magnitude (Left panel: apparent magnitude, right panel: absolute magnitude) as a function of heliocentric distance for the stars from Ou et al. (2024) (gray points). The rainbow-colored points represent the selected stars used to calculate the scale length. The red solid lines indicate absolute magnitudes of -3 and -5.

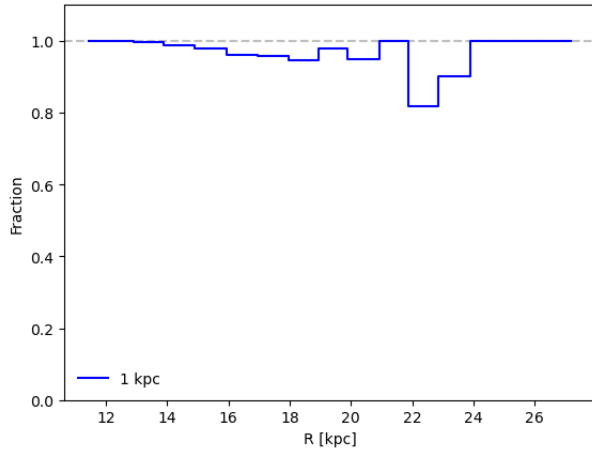


FIGURE 2.11 – Fraction of stars in each 1-kpc bin that their numbers of visits larger than the requirement of H magnitude limit of APOGEE

Selection criteria of star sample for scale length estimation

The targets in the APOGEE main survey are selected from candidates based on their $(J-K)_0$ color and H magnitude in the 2MASS Point Source Catalogue. In each field, a group of stars with the same number of observational visits is referred to as a ‘cohort’. For a single field, there can be up to three cohorts, each corresponding to a different range of H magnitudes, which in turn correspond to varying depths of observation. The exact H magnitude range used for target selection depends on the specific field and the number of visits assigned to each cohort.

To derive the scale length of the star sample and test its completeness, we selected a sub-sample of stars with EXTRATARG==0, ensuring their number of visits corresponds to the H magnitude limits. This restricts the galactocentric distance of our sample to greater than 11 kpc (with heliocentric distances $\gtrsim 3$ kpc), as shown in Figure 2.10. In Figure 2.11, we show the

fraction of stars for which the number of visits exceeds the required limits. Only one 1-kpc bin at $R = 22$ kpc has a fraction lower than 0.9 (still above 0.8), indicating that the sub-sample is relatively complete.

Fittings for the disk scale length

Figure 2.12 presents the radial distribution of the number density of stars selected from Ou et al. (2024). We assume that the uncertainties in the density estimates follow a Poisson distribution. To avoid the issue of a limited number of stars in the outer regions, we adopt a bin width of 2 kpc for radii beyond $R = 24$ kpc, compared to the 1-kpc binning employed for smaller radii in the left panel. The uncertainties in the scale length are estimated by ensuring that all error bars in the density distribution are accounted for. Since the stars at larger radii are selected across different disk vertical heights ($|z|$), we employ volume density to test the scale length.

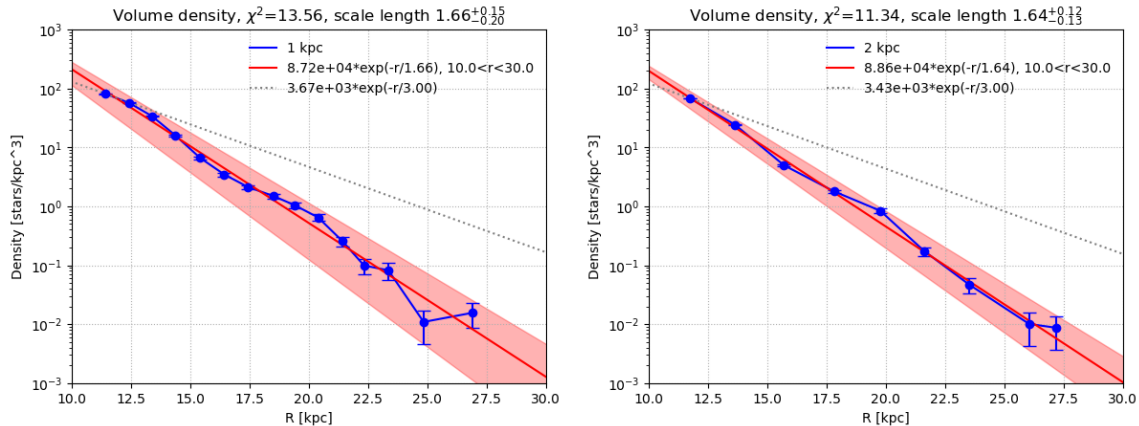


FIGURE 2.12 – Radial distribution of selected stars using 1-kpc bins (left panel) and 2-kpc bins (right panel). We assumed the uncertainties in the density estimates follow a Poisson distribution. The red solid line represents the best-fit using an exponential density profile. The red shaded region corresponds to the uncertainty in the exponential fit, which was adjusted to include all data points and error bars. Note that the last two data points in the left panel use 2-kpc bins to ensure an adequate number of stars. The gray dotted line represents an exponential profile normalized to the first point, with a scale length of 3 kpc.

The density distribution decreases smoothly from 11 to 27 kpc, and this trend is well-represented by an exponential profile. This indicates that the density profile, ν , in the Jeans equation is relatively well-constrained. Consequently, the previously estimated systematic uncertainties due to the assumed ± 1 kpc variation in the disk scale length are likely overestimated. Additionally, there is no significant evidence of systematics arising from a possible shift from an exponential disk to a power-law profile, as demonstrated in Figure 2.12. Based on this analysis, we estimate the scale length to be 1.65 ± 0.2 kpc.

Is the MW disk truncated?

Koop et al. (2024) argued that the largest source of uncertainty and possibly bias at larger radii might come from the density profile of the tracer population, particularly if affected by truncation. They investigated a truncated disk density profile, $\nu_n = \nu \exp(-R^n/R_{\max}^n)$, where ν represents an exponential profile. Their analysis found that circular velocity could be underestimated by up to $\sim 10 \text{ km s}^{-1}$ at 30 kpc for $n = 2$ and as much as $\sim 45 \text{ km s}^{-1}$ for $n = 4$, as illustrated in Figure 2.13. Changes in the scale length and density profile can indeed have a significant impact on the results obtained from the Jeans equation. To ensure an accurate estimate of the scale length used in the Jeans equation for deriving the RC, we selected a relatively complete sub-sample of stars and carefully estimated the disk scale length.

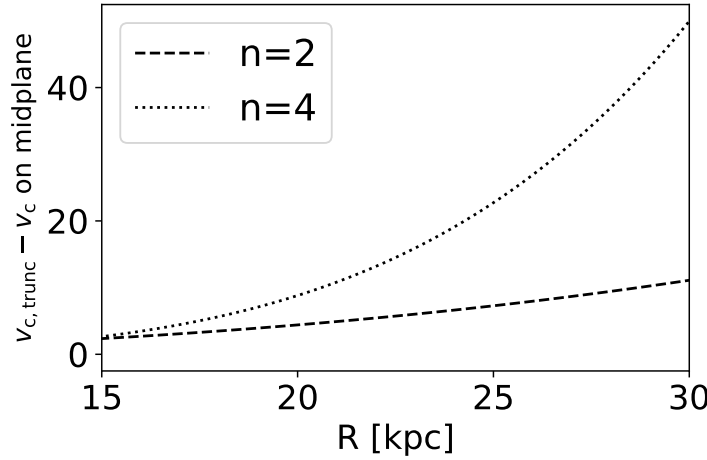


FIGURE 2.13 – Difference in the inferred circular velocity for the truncated exponential models compared to an exponential disk with $n=2$ and 4. This figure is adapted from Koop et al. (2024).

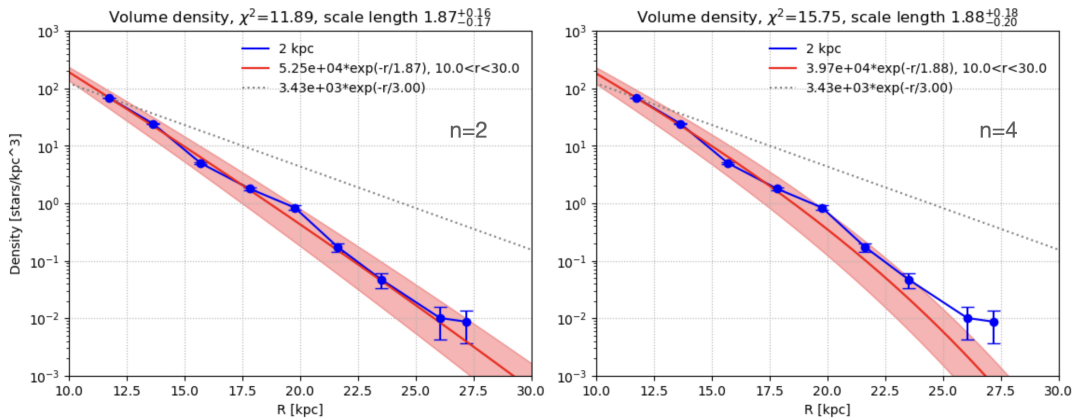


FIGURE 2.14 – Fits of truncated radial density profile (left panel: $n=2$; right panel: $n=4$) of distribution of selected stars with 2-kpc width bin. Others are the same as Figure 2.12.

In Figure 2.14, we present the estimated radial density profile of selected stars using 2-kpc bins. For the case of $n = 2$, the fit is reasonable, although the last two points show an upward trend, which is also observed in the 1-kpc bin width density profile in Figure 2.12. On the other hand, within the radius where we derive the RC, the difference between the exponential

and $n = 2$ truncated density profiles is only about 4 km s^{-1} at $R = 20 \text{ kpc}$. This difference is insufficient to explain the Keplerian decline of the MW RC beyond 19 kpc. Moreover, it is clear that the $n = 4$ case does not align with the density profile of the Galactic disk. Therefore, the Keplerian decline of the MW RC cannot be attributed to uncertainties linked to the density profile of the Galactic disk. In Section 3.2.2, we also tested various scale lengths and found that only an unrealistically small scale length, approaching *zero*, could reproduce a flat RC. Therefore, a truncated disk scenario might not be a plausible explanation for the observed declining RC.

4.2.3 Systematic uncertainties

Following previous studies, a robust estimation of systematic uncertainties is essential (Eilers et al., 2019; Jiao et al., 2023; Wang et al., 2023; Zhou et al., 2023). We analyzed the radial distribution of the disk RGB stars (Figure 2.12), which demonstrates that changing the disk scale length by 1 kpc or assuming a power-law profile instead of an exponential disk is not justified within this radial range. Additionally, we account for uncertainties in both the Sun's position and the motion of Sgr A* to further refine our estimates.

In order to estimate the impact of different dynamical features above and below the MW disk (Gaia Collaboration et al., 2021b; Koop et al., 2024) on the estimation of the rotation curve, we also split the data sample into two disjoint sub-samples: one above the Galactic plane ($z > 0 \text{ kpc}$) and the other below ($z < 0 \text{ kpc}$). The asymmetric drift can be estimated either by the neglected cross-term or by splitting the data samples along the anticenter direction. Adding the systematic uncertainties together would result in an overestimation of systematics, because they are mostly redundant. Therefore, we consider two scenarios for the total systematic uncertainty, as presented in Figure 2.15. The difference between the two cases lies in whether the neglected terms are included or if the data sample is split (Paper I). The systematics associated with including the neglected terms are slightly smaller in the outskirts, which may be attributed to the complex dynamical structures of the disk at larger radii that cannot be easily corrected.

The total systematic uncertainties are indicated by the black solid lines in Figure 2.15, which is obtained from the quadratic sum of all systematic uncertainties assuming that the errors are all Gaussian. Then the total uncertainties of RC correspond to the quadratic sum of statistical errors with systematic uncertainties.

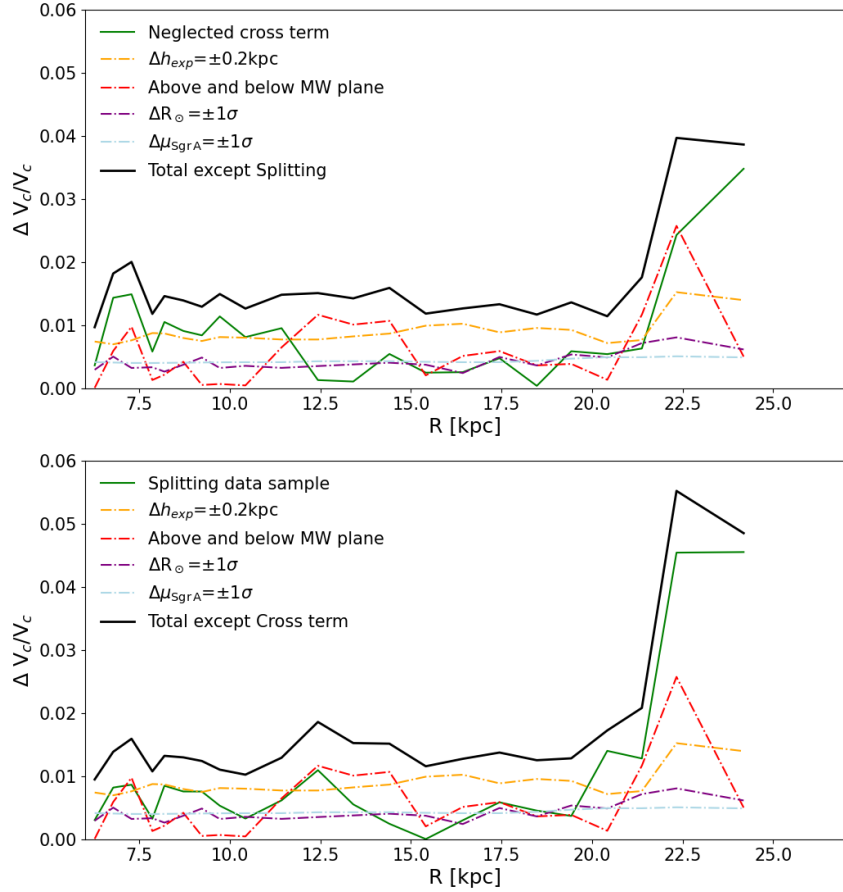


FIGURE 2.15 – Summary of potential systematic uncertainties in the circular velocity curve. We consistently account for the uncertainties in the scale length (0.2 kpc), the Sun’s position, the motion of Sgr A*, and the differences between regions above and below the Galactic plane. In the top panel, we include the neglected terms, while in the bottom panel, we present the results using the split data sample estimation.

4.3 Rotation curve and maximal mass estimation

The RC measurements are reported in Table 2.1. In Figure 2.16, we present the RC with re-estimated uncertainties. Note that because of the decrease of the scale length, from 3 kpc (Eilers et al., 2019; Ou et al., 2024) to 1.65 kpc, the circular velocities slightly increase. The two sets of errorbars correspond to the two scenarios of total systematic uncertainty, as detailed in Figure 2.15.

In Figure 2.17, we present the best-fit and maximal mass estimates for the MW RC based on the Ou et al. (2024) data, using the Einasto profile. Systematic uncertainties were calculated as the quadratic sum of statistical errors and systematics, including the neglected cross-term. Different lines represent the contributions of various components. The left panel shows the best-fit model, while the right panel illustrates the maximal mass fit, offset by 1σ from the best fit.

TABLE 2.1 – Measurements of the re-sampled circular velocity of the Milky Way.

R kpc	V_c km s $^{-1}$	$\sigma_{v_c,\text{cross}}^+$ km s $^{-1}$	$\sigma_{v_c,\text{cross}}^-$ km s $^{-1}$	$\sigma_{v_c,\text{split}}^+$ km s $^{-1}$	$\sigma_{v_c,\text{split}}^-$ km s $^{-1}$
6.27	236.66	2.48	2.50	2.44	2.45
6.78	236.89	4.40	4.47	3.41	3.49
7.28	238.76	4.84	4.87	3.88	3.92
7.86	241.04	2.89	2.90	2.65	2.65
8.19	239.72	3.53	3.53	3.20	3.20
8.71	237.33	3.35	3.35	3.13	3.13
9.23	236.11	3.09	3.07	2.97	2.95
9.72	235.25	3.53	3.54	2.62	2.64
10.43	234.61	2.97	2.97	2.41	2.41
11.43	232.85	3.46	3.46	3.02	3.02
12.43	231.92	3.51	3.51	4.32	4.32
13.41	230.00	3.29	3.29	3.51	3.52
14.41	227.45	3.64	3.65	3.47	3.48
15.41	226.72	2.73	2.74	2.67	2.68
16.43	225.66	2.98	2.98	3.00	3.00
17.44	223.91	3.11	3.09	3.20	3.18
18.48	220.17	2.75	2.70	2.93	2.88
19.43	213.71	3.08	3.04	2.92	2.88
20.42	205.38	2.84	2.75	3.89	3.82
21.38	207.00	4.02	4.20	4.64	4.79
22.33	211.05	8.68	8.65	11.87	11.85
24.19	198.63	8.01	8.18	9.90	10.04

The columns are the radius R , circular velocity V_c , the systematic uncertainties that include the neglected cross-term in the Jeans equation $\sigma_{v_c,\text{cross}}^+$, $\sigma_{v_c,\text{cross}}^-$, and the systematic uncertainties that account for the effect of splitting data sample $\sigma_{v_c,\text{split}}^+$, $\sigma_{v_c,\text{split}}^-$.

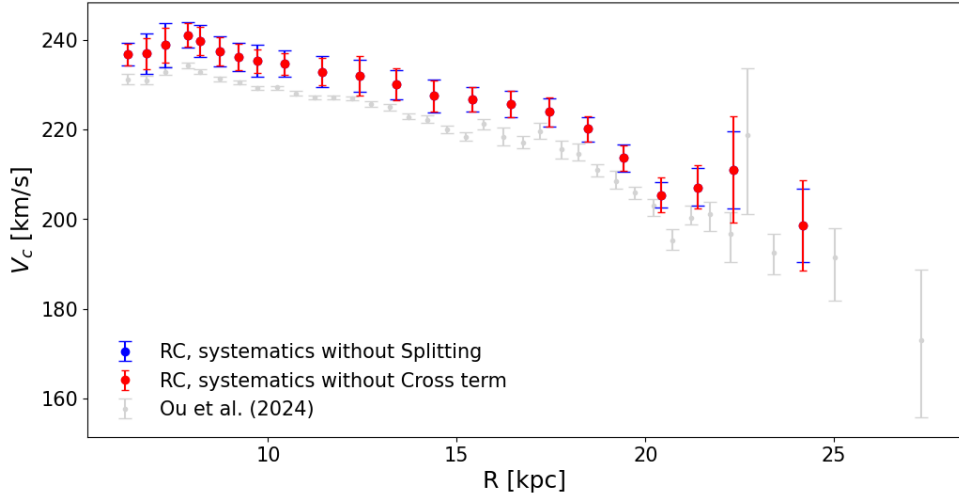


FIGURE 2.16 – Re-sampled circular velocity of the Milky Way with re-estimated uncertainties. The two sets of error bars correspond to the two scenarios of total systematic uncertainty, as shown in Figure 2.15. The re-sampled circular velocity is slightly larger than the original RC from Ou et al. (2024) due to the decrease in the scale length from 3 kpc to 1.65 kpc.

The χ^2 probability is defined as (Paper I):

$$P\left(\frac{\chi^2}{2}, \frac{N-\nu}{2}\right) = \frac{\gamma\left(\frac{N-\nu}{2}, \frac{\chi^2}{2}\right)}{\Gamma\left(\frac{N-\nu}{2}\right)} \quad (2.1)$$

where N is the number of independent observed velocity points in the RC and ν represents the degrees of freedom. The offset of 1σ is defined as $P(\chi^2) \approx 0.16$, indicating a confidence level where the probability corresponds to one standard deviation from the best-fit model.

The best-fit total mass of the MW is estimated to be $2.48 \times 10^{11} M_\odot$ at $R = 118.60$ kpc, consistent with the results from Ou et al. (2024). However, the maximal mass is calculated to be $4.14 \times 10^{11} M_\odot$ at $R = 146.50$ kpc, which is notably higher than Ou et al. (2024)'s estimate of $2.49 \times 10^{11} M_\odot$. This discrepancy may stem from the different treatments of systematic uncertainties, as Ou et al. (2024) did not account for systematics in their mass estimate, potentially leading to an underestimation of the maximal MW mass.

By including systematic uncertainties that account for the effects of splitting data samples, we find a slightly higher MW mass compared to previous estimates: $2.56 \times 10^{11} M_\odot$ at $R = 120.27$ kpc for the best fit and $5.6 \times 10^{11} M_\odot$ at $R = 164.48$ kpc for the maximal mass, as shown in Figure 2.18. This outcome aligns with the systematic uncertainties, where the splitting data sample scenario results in slightly larger uncertainties than those produced by the cross term, as shown in Figure 2.15.

We also applied the NFW profile to fit the optimized RCs, as shown in Figure 2.19. The best-fit total MW mass is estimated to be $8.91 \times 10^{11} M_\odot$ at $R = 194.99$ kpc for the splitting data case and $8.39 \times 10^{11} M_\odot$ at $R = 190.82$ kpc for the cross term case. It is important to note that, with both the Einasto and NFW profiles, an excessively shallow profile can lead to unrealistically

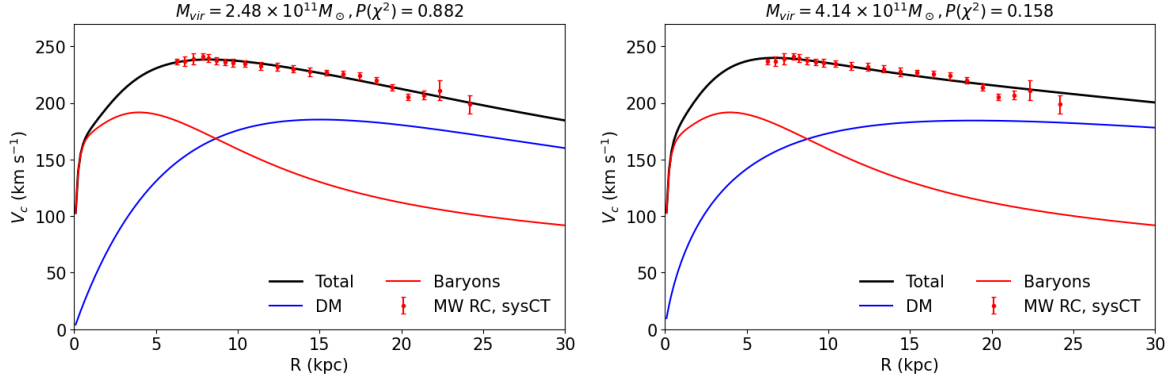


FIGURE 2.17 – Best-fit and maximal mass estimations for the optimized MW RC (red points) based on Ou et al. (2024) data, with error bars calculated as the quadratic sum of statistical errors and systematics, including the neglected cross term. The red lines represent the baryonic components, the blue lines show the velocity contribution from the Einasto profile, and the black lines present the total velocity fit. The left panel displays the best fit of the MW RC, while the right panel shows the maximal mass fit that is offset by 1σ from the best fit.

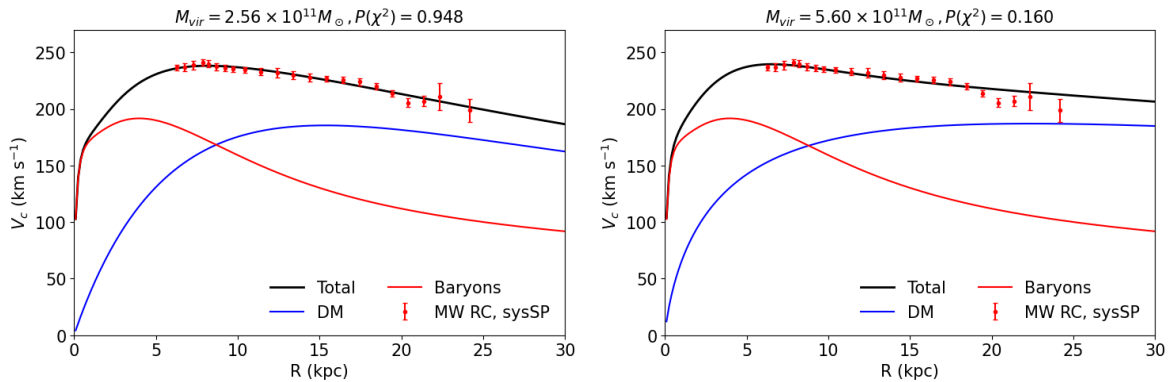


FIGURE 2.18 – Same as Figure 2.17, but the systematic uncertainties are estimated by including the effect of splitting the data sample.

high mass estimates; however, we constrain the fits to be consistent with the mass-concentration relation described by Dutton & Macciò (2014). The best fits using the NFW profile also show low χ^2 probabilities, which is in line with the gNFW fit from Ou et al. (2024). Given the steep decline in the MW RC, the NFW (or gNFW) profile proves too shallow to adequately fit the data, as demonstrated in Figure 2.19, where it fails to capture the rapid decrease in the RCs, particularly at larger radii.

In summary, we estimate the best-fit MW mass to be $2.52 \times 10^{11} M_\odot$ at $R \sim 120$ kpc and the maximal mass to be $5.6 \times 10^{11} M_\odot$ at $R = 164.48$ kpc, based on an average of results from two systematic approaches using the Einasto profile for the best-fit model and only splitting data effect for the maximal mass. This best-fit value is consistent with the MW mass estimates from Ou et al. (2024) and Jiao et al. (2023). However, the best-fit NFW profile yields a significantly higher MW mass of $8.75 \times 10^{11} M_\odot$ at $R \sim 190$ kpc, which aligns with the findings of Eilers et al. (2019), who also applied the NFW profile to the MW RC. This mass estimate, however, exceeds

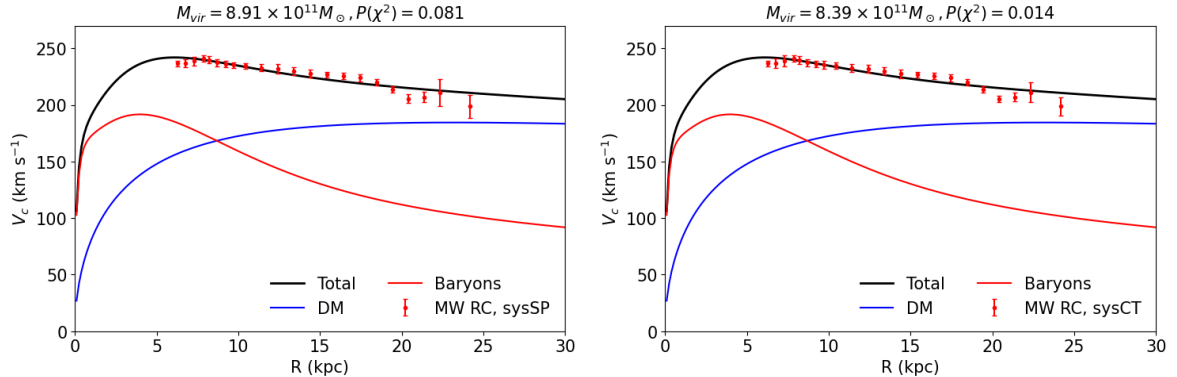


FIGURE 2.19 – Best-fit mass estimations for the optimized MW RCs based on Ou et al. (2024) data and NFW profile for the DM, with error bars calculated as the quadratic sum of statistical errors and systematics, including the splitting data effect (left panel) and the neglected cross term (right panel). Other symbols are the same as in Figure 2.17.

the value obtained by Ou et al. (2024) using the gNFW profile, indicating that the NFW profile may overestimate the MW mass.

4.4 Discussion

4.4.1 Compare with MW mass based on Gaia DR2

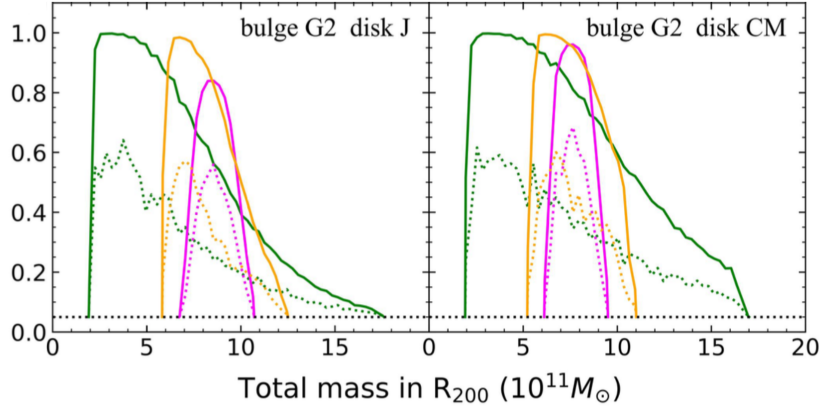


FIGURE 2.20 – Maximum (solid lines) and average (dotted lines) χ^2 probabilities for different baryonic models fitted to the MW RC from Eilers et al. (2019). The model names are labeled in each panel, with mass predictions from the Einasto, NFW, and gNFW profiles shown in green, magenta, and orange, respectively. The horizontal dotted line indicates the χ^2 probability threshold of 0.05, below which a model is considered unable to fit the MW RC. This figure is adapted from Paper I.

In this study, we also estimated the maximal MW mass at the 1σ uncertainty (χ^2) to provide an upper limit. Using the Einasto profile, the upper mass limit is $4.14 \times 10^{11} M_\odot$ and $5.6 \times 10^{11} M_\odot$ for the two cases of systematics. To compare these results with those derived from *Gaia* DR2, we applied two additional baryonic models, G2 J and G2 CM, both of which yield a reasonable

baryonic mass of approximately $6 \times 10^{10} M_{\odot}$ and a broad MW mass range for the Einasto profile at 1σ uncertainty. The maximal MW mass estimates are $1.4 \times 10^{12} M_{\odot}$ and $1.6 \times 10^{12} M_{\odot}$ for G2 J and G2 CM, respectively, as presented in Figure 2.20.

However, the maximal MW mass derived from *Gaia* DR3, ranging from approximately 4.5 to $6.8 \times 10^{11} M_{\odot}$ at $R \sim 150\text{kpc}$ as shown in Figures 2.21 and 2.22, is significantly smaller than that estimated from *Gaia* DR2, which is approximately $15 \times 10^{11} M_{\odot}$ (Paper I). This discrepancy is attributed to: (i) the overestimation of systematic uncertainties in the *Gaia* DR2 analysis, (ii) the more precise proper motion and parallax measurements available in *Gaia* DR3, and (iii) the inclusion of a larger sample of stars in our study, which allows for a more accurate determination of the MW mass.

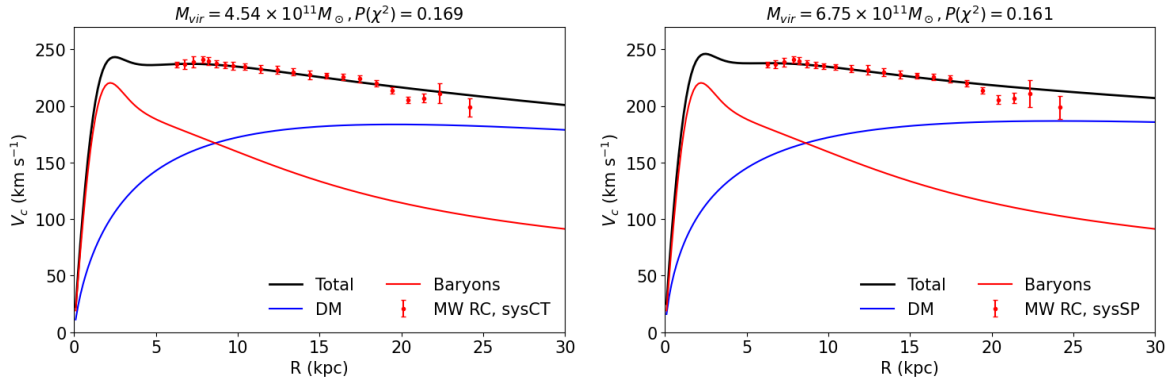


FIGURE 2.21 – Maximal mass fits for baryonic model G2 CM with Einasto mass profile. The left panel is for the case of neglected cross term and the right panel is for the case of splitting data sample. Others are the same as Figure 2.17.

4.4.2 Keplerian decline

Paper II was the first to detect a Keplerian decline in the MW RC, a deviation from the flat RCs typically observed in most spiral galaxies. This decline begins around 17 kpc, near the edge of the optical disk, and continues out to 27 kpc, where the most distant stars in the sample are located. Understanding why the MW is the only spiral galaxy showing this type of RC is

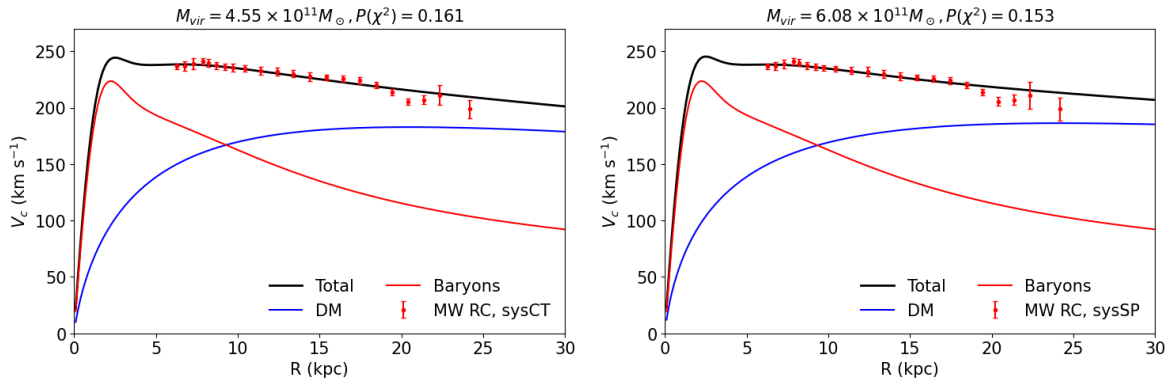


FIGURE 2.22 – Same figure as Figure 2.21 but for baryonic model G2 J.

essential for understanding the formation and evolution of spiral galaxies, or the potential biases in the data analysis.

One of the unique characteristics of the MW is that its last major merger occurred in the ancient past. Based on *Gaia* data, its last major merger, GSE, took place about 9-10 Gyr ago (Belokurov et al., 2018; Haywood et al., 2018; Helmi et al., 2018). Consequently, even stars as far as 30 kpc from the Galactic center have had sufficient time to complete 5-6 orbital cycles, allowing them to reach dynamical equilibrium (Gnedin & Ostriker, 1999). In contrast, most spiral galaxies experienced their last major mergers approximately 6 Gyr ago on average, meaning that gas and stars in their outer disks may not have fully reached equilibrium. If the asymmetrical features in the Galactic disk are related to the GSE merger, we could not attribute the Keplerian decline in the MW RC to such asymmetries in the Galactic disk.

Another possible explanation is methodological. Using *Gaia* data, we can accurately determine the 3D positions and 3D velocities of stars, allowing us to predict both their past and future orbits. In our study, for example, we specifically selected stars whose circular velocities dominate over the radial and vertical velocity components, ensuring the circularity and stability of their orbits. In contrast, for other spiral galaxies, observational data is much more limited—typically providing only two spatial coordinates and the line-of-sight velocity. This constraint makes it challenging to apply a comprehensive dynamical model as accurate as what we can achieve with the MW RC.

However, to derive a representative RC, we required that bins at larger radii contain at least 36 stars, which reduced the number of RC data points in the outer regions. This limitation complicates a comprehensive assessment of the significance of the Keplerian decline. Based on a rough estimate, the RC between 17 and 21 kpc appears consistent with a Keplerian decline, but beyond 21 kpc, the RC trends upward for two data points before declining again at the final point. A similar rise is observed in the RC from Ou et al. (2024) at 23 kpc, which may be due to the small number of stars in the outer regions that have large radial velocities.

Additionally, our analysis is restricted to the anticenter direction, covering only 60 degrees, limiting our ability to fully explore the dynamical features of the Galactic disk. Future data at larger radii from *Gaia* or other surveys will be essential for deriving a more accurate RC and further assessing the significance of the Keplerian decline.

4.5 Conclusion

In this section, we used the data from Ou et al. (2024) to re-estimate the MW RC and its associated systematic uncertainties. These uncertainties were evaluated by considering the effects of splitting the data sample or the neglected cross-term in the Jeans equation. Since these two approaches address the same potential asymmetrical features related to radial and vertical velocities in different directions, we did not apply both simultaneously in our analysis. We think that these two approaches effectively address the issue of overestimating uncertainties. This approach resulted in an optimized MW RC with two distinct systematic estimates, as shown in Figure 2.15.

Our analysis indicates a best-fit MW mass of $2.52 \times 10^{11} M_{\odot}$, with a maximal mass of $5.6 \times 10^{11} M_{\odot}$ at the 1σ uncertainty level. This best-fit value aligns well with the MW mass estimates provided by Ou et al. (2024) and Jiao et al. (2023). The maximal mass estimate could be useful for studies of the interaction between the MW and nearby dwarf galaxies.

Given the upper limit on the MW mass, the baryonic fraction is estimated to be approximately 0.12, which is consistent with typical values observed in disk galaxies, around 0.1. However, the upper limit fits tend to underestimate the dark matter (DM) contribution in the inner regions and overestimate it in the outer regions, leading to a shallower Einasto profile at larger radii, resembling that of the NFW profile. As shown in Figures 2.17 and 2.18, the maximal mass fits are systematically smaller than the data between 10 and 19 kpc, while they exceed the data beyond 19 kpc.

We also compared the MW mass derived from *Gaia* DR3 data with that from *Gaia* DR2, finding that the maximal mass estimates based on *Gaia* DR3 are significantly smaller, reflecting the considerable improvements in *Gaia* DR3 measurements. Additionally, the rebinned data resulted in fewer RC data points beyond 20 kpc compared to previous studies. Therefore, future data at larger radii will be crucial for refining the RC and evaluating the significance of the observed Keplerian decline.

Appendix A: Which Milky Way masses are consistent with the slightly declining 5-25 kpc rotation curve? (Paper I)

Which Milky Way masses are consistent with the slightly declining 5–25 kpc rotation curve?

Y. Jiao¹, F. Hammer¹, J. L. Wang², and Y. B. Yang¹

¹ GEPI, Observatoire de Paris, Université PSL, CNRS, Place Jules Janssen, 92195 Meudon, France
e-mail: francois.hammer@obspm.fr

² CAS Key Laboratory of Optical Astronomy, National Astronomical Observatories, Beijing 100101, PR China

Received 12 April 2021 / Accepted 1 July 2021

ABSTRACT

Context. Discoveries of extended rotation curves have suggested that spiral galaxy halos contain dark matter. This has led to many studies that estimated the total mass of the Galaxy, mostly using the Navarro, Frenk, and White (NFW) density profile.

Aims. We determine the effect that the choice of the dark matter profile has on the predicted values of extrapolated total masses.

Methods. We considered a recently reported Milky Way (MW) rotation curve, first because of its unprecedented accuracy, and second because the Galactic disk appears to be least affected by past major mergers that have fully reshaped the initial disk.

Results. We find that the use of an NFW profile (or its generalized form, gNFW) to calculate the dark-matter contribution to the MW rotation curve generates apparently inconsistent results such as an increase in baryonic mass that leads to an increase in dark matter mass. Furthermore, we find that NFW and gNFW profiles narrow the total mass range, leading to a possible methodological bias particularly against low MW masses. Using the Einasto profile, which is better suited to represent cold dark matter halos, we finally found that the slightly decreasing rotation curve of the MW favors a total mass that can be as low as $2.6 \times 10^{11} M_{\odot}$, disregarding any other dynamical tracers farther out in the MW. This is inconsistent with values higher than $18 \times 10^{11} M_{\odot}$ for any type of cold dark matter halo profiles under the assumption that stars and gas do not affect the predicted dark matter distribution in the MW.

Conclusions. This methodological paper encourages the use of the Einasto profile to characterize rotation curves with the aim of evaluating their total masses.

Key words. Galaxy: kinematics and dynamics – Galaxy: structure – dark matter – methods: numerical

1. Introduction

Gaia DR2 provided accurate stellar proper motions to calculate the circular velocity curve of the Milky Way (MW) up to 25 kpc (Eilers et al. 2019; Mróz et al. 2019). The result was based on a thorough analysis of a very large sample of 26 000 RGB stars in the MW disk (Eilers et al. 2019), resulting in a slightly but robustly determined decrease in circular velocity from 5 to 25 kpc. While Eilers et al. (2019, see also Hogg et al. 2019) used spectrophotometric distances in their analysis, their finding was confirmed by Mróz et al. (2019) using 773 Classical Cepheids with precise distances. Subsequent analyses of these rotation curves (RCs) have led to a total MW mass near or well below $10^{12} M_{\odot}$ (Eilers et al. 2019; de Salas et al. 2019; Grand et al. 2019; Karukes et al. 2020). Karukes et al. (2020) have used a considerable number of baryonic matter distributions to derive the overall mass distribution, while the de Salas et al. (2019) have accounted for very large error bars after cumulating all the systematics described in details by Eilers et al. (2019).

The accuracy of the MW RC also allows testing different mass profiles for the dark matter (DM) distribution in the MW halo. Recent studies have shown that the three-parameter Einasto profile (Einasto 1965, see also Retana-Montenegro et al. 2012) provides a better description of the CDM halo density profile than the NFW profile (Navarro et al. 2004, 2010; Gao et al. 2008), and it is even than the three-parameter generalized gNFW (Klypin et al. 2016).

We propose to test the Einasto and NFW (Navarro et al. 1997) density profiles and their effect on the total mass

estimates when spiral rotation curves are fit. We consider the MW RC because of its unprecedented accuracy, and also because the history of the MW is likely quiescent when compared to other spirals (Hammer et al. 2007) because the last MW major merger occurred ~ 10 Gyr ago, as has recently been confirmed based on the resulting debris identified by *Gaia* DR1 (Belokurov et al. 2018) and as will soon be confirmed by *Gaia* DR2 (Haywood et al. 2018; Helmi et al. 2018).

In Sect. 2 we present our proposed treatment of the error bars for the Eilers et al. (2019) RC, and then describe the choice and mathematical descriptions of the baryon and DM models. In Sect. 3 we compare the χ^2 probability distribution for DM represented by the NFW or Einasto profiles. In Sect. 4 we discuss which mass range is consistent with the combined constraints provided by the fit of the MW RC and by adopting DM halo profiles from the cold dark matter (CDM) theory.

2. Methods

2.1. Rotation curve and error bars

Eilers et al. (2019) provided a thorough analysis of the possible systematic errors that may affect the MW RC and summarized (see their Fig. 4) four different types of systematics. The first type includes the neglected term in their Jeans equation (see their Eq. (3)), which is a cross-term made by the vertical density gradient of the product of the radial and vertical velocities. This term is found to be small but not negligible at large distances. For example, Mackereth et al. (2019) showed

that vertical velocities are higher for young stars, which is expected because the gaseous disk is likely affected by (former) gas infall. This may affect the derived RC because Eilers et al. (2019) selected relatively young stars (<4 Gyr) for the MW RC in order to avoid asymmetric drift effects.

However, the effect is expected to be smaller (<5 km s⁻¹ at 12 kpc) than the RC amplitude. The second possible systematics is empirical, and it is an estimate of the error variations with radius after splitting the sample into two parts. We consider here only the first type of systematics because it likely includes the second.

Adding to this, Eilers et al. (2019) considered a third category of systematics with a quite different nature because it proportionally applies in the same way to all RC points. It is revealed by the three almost horizontal lines in Fig. 4 of Eilers et al. (2019). This last category of systematics includes the effect of changing the distance of the Sun to the Galactic center, the proper motion of the latter, and it can be extended to the change in scale length. These uncertainties have to be applied to the derived mass as a whole after the fitting analysis. Added together, they correspond to an additional systematic uncertainty of ~2% on the velocity scale and ~4% on the mass scale. We note in agreement with Christina Eilers (Eilers, priv. comm.) that summing all the errors of Fig. 4 of Eilers et al. (2019) (as it has been done by de Salas et al. 2019) would strongly overestimate the error bars (see the discussion above), which dilutes the significance of the MW RC.

In the following we adopt the same parameters for the position of the Sun and for the solar velocity as Eilers et al. (2019). Karukes et al. (2020) have shown that the choice of the solar velocity may significantly affect the determination of its mass, while it has been considered determined at a 2–3% level by Eilers et al. (2019).

2.2. Milky Way baryonic mass models

The contribution of the baryonic components to the MW mass or RC is still uncertain, and this may well affect the determination of the DM distribution. Following Karukes et al. (2020), we adopt here a large number of models from the literature to describe the MW baryonic component, as described below. The baryonic component and its distribution in the bulge, disk, thick disk, gas, and even halo gas is still debated (see the review by Bland-Hawthorn & Gerhard 2016), and some modeling also introduces an ionized gas component (Cautun et al. 2020). The basic idea is to cope with uncertainties on baryons by using a very large grid of possible models, although we are aware that some baryons models may not be fully consistent with other important constraints from vertical dynamics of the disk stars (Bovy & Rix 2013) or from microlensing (Wegg et al. 2016).

Pouliasis et al. (2017) generated a new axisymmetric model (Model I) including a spherical bulge and a thin and thick disk. This model satisfies a number of observational constraints: stellar densities at the solar vicinity, thin- and thick-disk scale lengths and heights, and the absolute value of the perpendicular force K_z as a function of distance to the Galactic center. Although the disk is made of a thin and a thick disk, the associated density profiles are both described by a Miyamoto–Nagai profile (Eq. (1)). Pouliasis et al. (2017) concluded that Model I supersedes the axisymmetric model (Model A&S) proposed by Allen & Santillan (1991) because there is growing evidence for a strong thick-disk component and because the bulge is less prominent and less classical than assumed in Model A&S. Model A&S

Table 1. Parameters for Model I, Model A&S, and Model S.

Parameter	Model I	Model A&S	Model S
$M_{\text{bulge}} (10^{10} M_{\odot})$	1.067	1.406	2.5
$M_{\text{thin}} (10^{10} M_{\odot})$	3.944	8.561	11.2
$M_{\text{thick}} (10^{10} M_{\odot})$	3.944	—	—
$a_{\text{thin}} (\text{kpc})$	5.3	5.3178	5.73
$a_{\text{thick}} (\text{kpc})$	2.6	—	—
$b_{\text{bulge}} (\text{kpc})$	0.3	0.3873	0.87
$b_{\text{thin}} (\text{kpc})$	0.25	0.25	—
$b_{\text{thick}} (\text{kpc})$	0.8	—	—

consists of a stellar thin disk with a Miyamoto–Nagai profile (Miyamoto & Nagai 1975) and a central bulge with a Plummer profile (Binney & Tremaine 2011). The description of the bulge and disks for both Model I and Model A&S is expressed in the form (Pouliasis et al. 2017) for (R, z) cylindrical coordinates,

$$\rho_{\text{thin}}(R, z) = \frac{b_{\text{thin}}^2 M_{\text{thin}}}{4\pi} \times \frac{\left(R^2 a_{\text{thin}} + 3(z^2 + b_{\text{thin}}^2)^{1/2}\right) \left(a_{\text{thin}} + (z^2 + b_{\text{thin}}^2)^{1/2}\right)^2}{\left(R^2 + [a_{\text{thin}} + (z^2 + b_{\text{thin}}^2)^{1/2}]^2\right)^{5/2} (z^2 + b_{\text{thin}}^2)^{3/2}} \quad (1)$$

$$\rho_{\text{bulge}}(r) = \frac{3b_{\text{bulge}}^2 M_{\text{bulge}}}{4\pi (r^2 + b_{\text{bulge}}^2)^{5/2}}, \quad (2)$$

where $r = \sqrt{R^2 + z^2}$, and M_{thin} , M_{thick} , M_{bulge} , a_{thin} , a_{thick} , b_{thin} , b_{thick} , b_{bulge} are the disks and bulge mass and scale constants, respectively (see Table 1).

Sofue (2015) presented a model (Model S) of the MW by attempting to fit a ‘grand rotation curve’, which defines the combination of the actual rotation curves (up to 20–25 kpc) with estimates based on orbital motions of objects beyond 25 kpc in the MW halo, e.g., distant globular clusters. The bulge was approximated by a de Vaucouleurs profile (de Vaucouleurs 1958). We chose to adopt a Plummer profile (Eq. (2)) for the bulge, and the disk was assumed to follow an exponentially thin density profile. The surface mass density of the disk is expressed as (Sofue 2015)

$$\Sigma_d(R) = \Sigma_0 \exp(-R/a_{\text{thin}}), \quad (3)$$

where Σ_0 is the central value and a_{thin} is the scale radius (see Table 1). This model provides the highest baryonic mass when compared to other models in the literature (see Fig. 1). Nevertheless, we consider it useful for testing the effect of an extremely high baryonic mass for the MW disk and bulge.

A great addition to our choices of baryonic components was presented by Iocco et al. (2015), and they allowed several possible combinations of models for the bulge and the disk. For the bulge we chose the two triaxial mass density distributions E2 and G2 presented by Stanek et al. (1997),

$$\text{E2 : } \rho_{\text{bulge}}(x, y, z) = \rho_0 e^{-r_1} \quad (4)$$

$$\text{G2 : } \rho_{\text{bulge}}(x, y, z) = \rho_0 e^{-r_2^2/2}, \quad (5)$$

with

$$r_1^2 = \frac{x^2}{x_b^2} + \frac{y^2}{y_b^2} + \frac{z^2}{z_b^2}, \quad r_2^4 = \left(\frac{x^2}{x_b^2} + \frac{y^2}{y_b^2}\right)^2 + \frac{z^4}{z_b^4}, \quad (6)$$

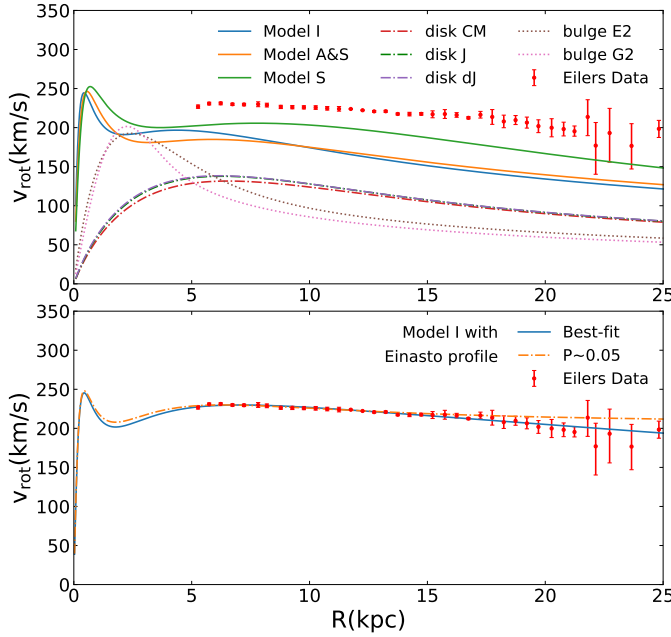


Fig. 1. Top: contribution to the rotation curve of different baryonic models and model components. Red points indicate the rotation curve of the Milky Way from Eilers et al. (2019). The error bars are estimated by bootstrapping and include the systematic uncertainties from the neglected term (see text). Bottom: fit of the rotation curve by the best-fit model (solid blue curve, total mass of $2.8 \times 10^{11} M_{\odot}$), and with the most massive MW model for which the χ^2 probability reaches $P = 0.05$ (dash-dotted orange line, total mass of $18 \times 10^{11} M_{\odot}$), both associated with the baryonic distribution from model I of Pouliasis et al. (2017).

Table 2. Parameters for bulge E2 and bulge G2.

Parameter	Bulge E2	Bulge G2
$M_{\text{bulge}} (10^{10} M_{\odot})$	2.41	2.12
x_b (kpc)	0.899	1.239
y_b (kpc)	0.386	0.609
z_b (kpc)	0.250	0.438

where (x, y, z) are the coordinates along the major, intermediate, and minor axes. For the thin and thick disks, we adopted a double exponential of the three models (CM from Calchi Novati & Mancini 2011, DJ from de Jong et al. 2010 and J from Jurić et al. 2008) as described below (see Table 3):

$$\text{CM : } \rho(R, z) = \Sigma_{\text{thin}} \left(\frac{1}{2H_1} \exp \left(-\frac{R}{L_1} - \frac{z}{H_1} \right) + f_{\text{thick}} \frac{1}{2H_2} \exp \left(-\frac{R}{L_2} - \frac{z}{H_2} \right) \right) \quad (7)$$

$$\text{J, DJ : } \rho(R, z) = \rho_{\text{thin}, \odot} \left(e^{R_{\odot}/L_1} \exp \left(-\frac{R}{L_1} - \frac{z}{H_1} \right) + f_{\text{thick}} e^{R_{\odot}/L_2} \exp \left(-\frac{R}{L_2} - \frac{z}{H_2} \right) \right). \quad (8)$$

In decreasing order of baryonic mass, Model S, Model A&S, and then Model I assume significantly higher mass baryonic components than the six combinations of bulge (G2, E2) and disk (CM, DJ, J), which is illustrated by Fig. 1 or by comparing Table 1 with Tables 2 and 3.

Table 3. Parameters of disk CM J and DJ.

Parameter	Disk CM	Disk J	Disk DJ
$M_{\text{thin}} (10^{10} M_{\odot})$	3.11	3.17	3.33
$M_{\text{thick}} (10^{10} M_{\odot})$	0.82	0.90	0.78
L_1 (kpc)	2.75	2.6	2.6
L_2 (kpc)	4.1	3.6	4.1
H_1 (kpc)	0.25	0.3	0.25
H_2 (kpc)	0.75	0.9	0.75

2.3. Milky Way dark matter models

We considered the NFW and Einasto profiles to describe the density profiles of DM halos in spherical coordinates (r). The generalized NFW profile (gNFW, see Zhao 1996) can be expressed as in de Salas et al. (2019),

$$\rho(r) = \frac{\rho_0}{(r/r_0)^{\gamma}(1+r/r_0)^{3-\gamma}}, \quad (9)$$

where r_0 is the scale radius, and ρ_0 is the characteristic dark matter density. For $\gamma = 1$, the profile becomes the NFW profile (Navarro et al. 1997) for which we investigate which parameters are able to fit the MW RC, after letting the two NFW parameters, r_0 and $m_{\text{NFW}} = 4 \pi \rho_0 r_0^3$, vary from 2 to 100 kpc and from 1 to $50 \times 10^{11} M_{\odot}$, respectively. For the gNFW profile we let the additional parameter, γ , vary from 0.1 to 3 (see also Karukes et al. 2020). For each tested mass configuration, we verified later that the investigated parameter space was sufficiently large to avoid having missed any solution.

Using the Retana-Montenegro et al. (2012) mathematical framework, the Einasto profile can be written as

$$\rho(r) = \rho_0 \exp \left[- \left(\frac{r}{h} \right)^{1/n} \right], \quad (10)$$

where n can determine how fast the density decreases with r . To determine which models are able to fit the MW RC, we let the three Einasto parameters, $b_E = 3 \times n$, $h_{\text{red}} = h^{1/n}$, and $m_E = 4 \pi \rho_0 h^3 n \Gamma(b_E)$, vary from 3 to 30, 0.05 to 3 and from 1 to $50 \times 10^{11} M_{\odot}$, respectively. For each tested mass configuration, we verified later that the investigated parameter space was sufficiently large to avoid any missing solution.

In order to determine a non-indefinite total MW mass, the DM halo mass has to be limited by the virial radius, R_{vir} , which enclosed M_{vir} , which is the virial mass. We define the virial radius as the radius of the sphere for which the average dark matter density equals 200 times the critical density of the Universe ρ_{cr} . We adopted a critical density of $\rho_{\text{cr}} = 1.34 \times 10^{-7} M_{\odot} \text{ pc}^{-3}$, which comes from Hinshaw et al. (2013). With this definition, the relation between virial radius and virial mass is

$$M_{\text{vir}} = 200 \times \frac{4\pi}{3} \rho_{\text{cr}} R_{\text{vir}}^3. \quad (11)$$

3. Results

3.1. Deriving the total MW mass and χ^2 probability

The total MW potential can be obtained through the Poisson equation,

$$\nabla^2 \Phi_{\text{tot}} = 4\pi G \sum_i \rho_i, \quad (12)$$

after adding all the different MW mass components. The theoretical estimate of the circular velocity is derived at different disk radii (R) from the potential Φ_{tot} of the Galaxy through

$$v_c^2(R) = R \frac{\partial \Phi_{\text{tot}}}{\partial R} \Big|_{z \approx 0}. \quad (13)$$

We applied the χ^2 method to fit the RC and calculate its associated probability, for which we tested an extremely large parameter space. The χ^2 was calculated by the sum at each disk radius R_i ,

$$\chi^2 = \sum_i^N \frac{(v_{\text{mod},i} - v_{\text{obs},i})^2}{\sigma_i^2}, \quad (14)$$

where v_{mod} is the modeled circular velocity for the cumulative baryons + DM profiles, v_{obs} is the observed circular velocity, and σ_{stat} is the statistical uncertainty of the measurement so that $\sigma_{\text{stat},i} = (\sigma_{v_{\text{obs},i}}^+ + \sigma_{v_{\text{obs},i}}^-)/2$, to which we added the systematic uncertainty $\sigma_{\text{sys},i}$ to calculate σ_i (see Sect. 2.1 and the table in Appendix A). Hence the χ^2 probability can be expressed as

$$\text{Prob}\left(\frac{\chi^2}{2}, \frac{N-\nu}{2}\right) = \frac{\gamma\left(\frac{N-\nu}{2}, \frac{\chi^2}{2}\right)}{\Gamma\left(\frac{N-\nu}{2}\right)}, \quad (15)$$

where N is the number of independent observed velocity points in the Eilers et al. (2019) RC, and ν is the number of degrees of freedom.

To fit the MW RC, we investigated a very large parameter space, allowing for the total MW mass from 1 to $50 \times 10^{11} M_\odot$, for instance. In Fig. 2 each point $(P(\chi^2), M_{\text{tot}})$ represents an investigated baryon + DM model. The top panels of Fig. 2 present the χ^2 probability for the Model I baryon profile (Pouliasis et al. 2017) when associated with either the Einasto (left), the NFW (middle), or the gNFW (right) profiles. The first profile shows that high χ^2 probabilities are reached for low MW masses. In contrast, there is no similar trend for the NFW profile, which selects a narrow range of MW masses to fit the RC. The situation is improved with the gNFW, although it does not recover the whole range of masses and especially misses total masses below $5 \times 10^{11} M_\odot$. The bottom panels present the same for model S, for which the probabilities are very low when associated either with the Einasto or the NFW DM profiles. Examination of the RC fit shows that the baryonic mass is so high that its radial profile is setting up most of the expected RC (see also Fig. 1), leading to differences with the observed RC at almost every radius. This is expected because model S is clearly at odds for the MW; its disk plus bulge mass is higher than that of M31, while half this value is more likely (see, e.g., Hammer et al. 2007).

The two panels in the middle row of Fig. 2 compare the results when the bulge is changed from G2 (top) to E2 (bottom), both added to disk J. The first shows a similar behavior as Model I associated with either Einasto or NFW DM profiles. When we used the Einasto profile for the DM, we found that increasing the bulge mass by 15% (from G2 to E2) is sufficient to exclude high values of the total mass of the MW. This is expected because when the baryonic mass is increased, a smaller amount of DM mass is available to reproduce the MW RC. Moreover, a too large bulge may limit the number of possible solutions that can fit the RC at low radii. However, for the NFW profile we find that a bulge mass increase from G2 to E2 is sufficient to prevent an efficient reproduction of the MW RC, providing very low χ^2 values. We also find that the associated total (and DM) masses are higher

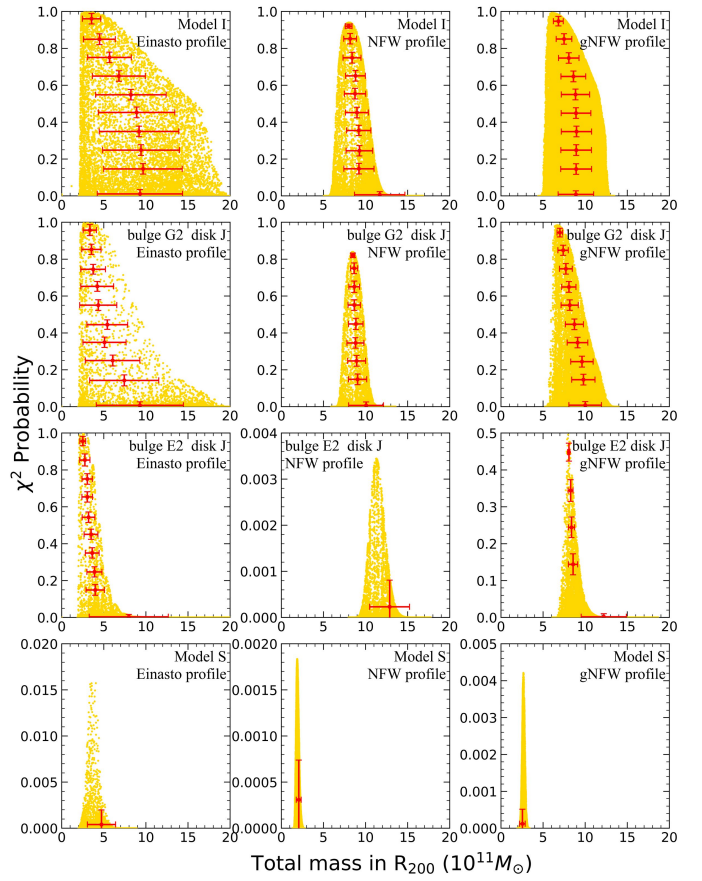


Fig. 2. χ^2 probability associated with the combination of different baryonic models with Einasto, NFW, or gNFW mass profiles for the DM. From top to bottom, we show Model I, bulge G2+disk J, bulge E2+disk J, and model S. The red points and error bars are the average and 1σ uncertainties.

than the mass for the G2 bulge, which disagrees with our expectations. We note that these two properties disappear when the three-parameter gNFW model is used, which might be because for $\gamma < 1$, this profile is less cuspy and is therefore less affected by changes in bulge mass.

The above motivates us to investigate further why adding an additional baryonic mass could lead to an increase of the DM mass when the latter is modeled by the NFW density profile. We tested the effect of changing the amount of baryonic mass on the NFW DM mass. We considered a range of baryonic masses scaled on the mass of Model I, with scale factors f varying from 0.85 to 1.15. For $f = 0.85, 1$, and 1.15 , this confirmed that by increasing the baryonic mass, the NFW DM model leads to a significant increase in DM mass from $5.9, 7.2$, and $10.7 \times 10^{11} M_\odot$, respectively. This is an unexpected behavior because the DM role is to compensate for the lack of baryonic mass when a given RC is fit. Our first explanation was to relate this to the two-parameter nature of the NFW profile. However, a similar (although less pronounced) behavior affects the gNFW profile. For $f = 0.85, 1$, and 1.15 , the gNFW DM model also leads to an increase in DM mass from $4.8, 5.25$, and $7.1 \times 10^{11} M_\odot$, respectively. This suggests the following mechanism: for an increasing baryonic mass, the NFW DM scale radius (r_0 , see Eq. (9)) has to increase to dilute the DM mass from 5 to 25 kpc (the latest point of the RC). Because outer density slope of the NFW and gNFW is almost constant and shallow (-3) at large radii, this automatically leads to increasing DM masses. This indicates a possible

methodological problem of using the NFW (or gNFW) to fit the RC as and to estimate the mass of a galaxy from it.

3.2. Systematics due to the NFW and gNFW when the total mass is estimated

To evaluate the differences between Einasto and NFW DM density profiles in fitting the MW RC, we need to ensure that our method does not depend on the initial conditions. In particular, the parameter grid might affect our results because Fig. 2 shows that the three-parameter space (Einasto or gNFW) might be more difficult to be populated than the two-parameter space (NFW). We further performed for each model a combination of several Monte Carlo simulations that also accounted for the variance due to the RC error bars, which are assumed to follow a Gaussian distribution, in order to fill the high-probability space in the $(P(\chi^2), M_{\text{tot}})$ plane as much as possible.

The solid lines in Fig. 3 identify the envelop for each baryonic + DM model, which is defined as being the highest χ^2 probability calculated in mass slices with sizes of $0.3 \times 10^{11} M_{\odot}$. We assume that only χ^2 probabilities higher than 0.05 correspond to a good fit of the RC, which we verified after examining the latter. For comparison, Fig. 3 also shows the averaged probabilities.

Figure 3 shows that for all baryonic models, a narrower range of total masses is found for the MW when an NFW or gNFW instead of a Einasto profile is adopted for the DM. Conversely, using the Einasto profile suffices to sample most of the points generated by the NFW profile in the $(P(\chi^2), M_{\text{tot}})$ plane. We find that the total mass solutions based on the NFW and gNFW profiles are often included in those from the Einasto profile, while using an NFW does not match the highest χ^2 probabilities found by the Einasto model (compare the peaks of the solid magenta and green lines). However, in the case of a massive bulge (E2, especially when associated with disk J), the three-parameter gNFW may sample total MW mass values that cannot be reached by the Einasto model.

Table 4 gives the estimated total masses based on the minimum χ^2 values (best fit, highest probabilities) or on averaging the χ^2 probabilities in each mass slice (average). As in Fig. 3, the rows are sorted from high- to low-mass baryonic models. This indicates that the best fit of the MW RC for all baryonic models, except for A&S, are unavoidably related to low total masses (from 2.3 to $3.3 \times 10^{11} M_{\odot}$) if a Einasto profile is chosen for the DM. Conversely, adopting an NFW (or gNFW) profile for the DM leads to much higher total mass values by a factor of 2 to 4.

Of the models we studied, Model A&S possesses the second highest baryonic mass, close to $10^{11} M_{\odot}$, and we investigated why the behavior it shows is so different from that of other baryonic models, especially Model I. In addition to baryonic masses that differ by 11%, the main difference between the two models is the presence of a thick disk incorporating half the disk mass in Model I, with a scale length that is half that of the thin disk of Models I and A&S. By modifying the thick-disk scale length of Model I to a higher value, we find that this suffices to provide a similar behavior to Model A&S for the normalized cumulative probabilities of both NFW and Einasto DM profiles. As previously noted for model S, this suggests that an extended and relatively massive baryonic disk determines a significant part of the RC shape.

Considering the averaged total masses slightly improves the similarities between predictions based on NFW and Einasto DM mass profiles. This is true for Models A&S and I, which lead to almost consistent NFW and Einasto values of the total masses. However, for lighter baryonic models, the NFW profile for DM

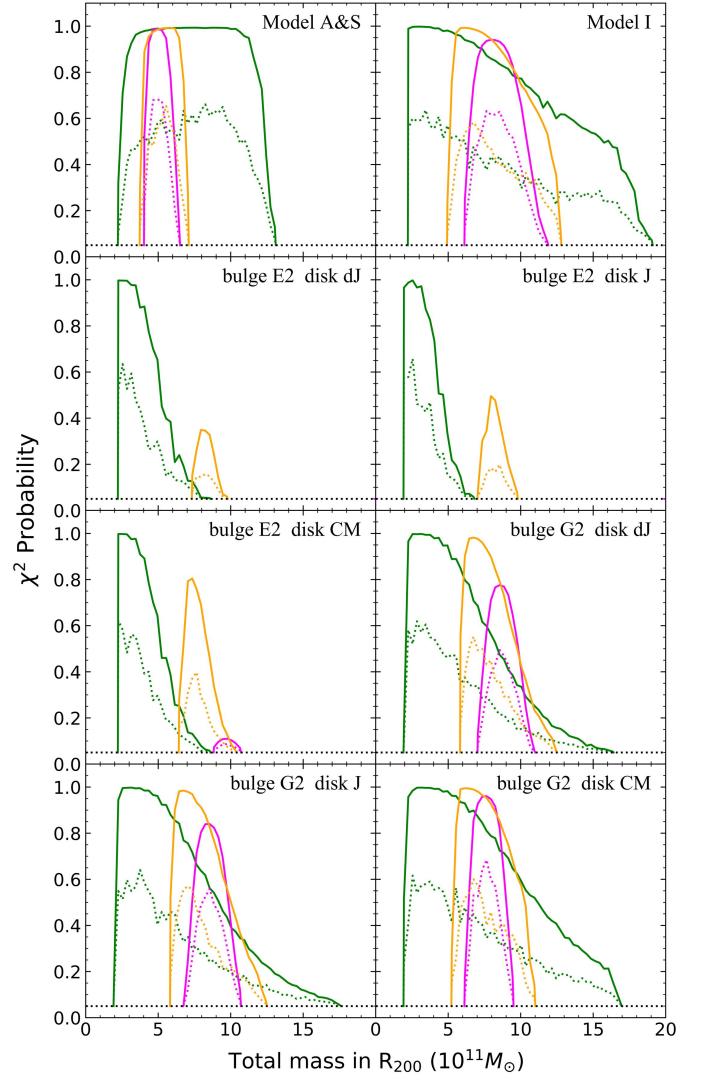


Fig. 3. Maximum (solid lines) and averaged (dotted lines) χ^2 probabilities for the different baryonic models. Model names are labeled in each panel, with Einasto, NFW, and gNFW mass predictions in green, magenta, and orange, respectively. The two panels associated with baryonic model E2+dJ and E2+J show no histogram for the NFW because this density profile fails to reproduce the MW RC. The horizontal dotted lines indicate the χ^2 probability limit of 0.05 below which a model is found to be unable to fit the MW RC.

still leads to a mass that is higher by factors from 1.5 to 3 when compared to that resulting from the Einasto profile. The NFW (and to a lesser extent, the gNFW) profile appears to preferentially select a narrow range of total masses, excluding in particular the low-mass values that are favored when the Einasto profile is used.

4. Discussion

4.1. Limitations of this study and comparison with other works

The goal of this paper is mostly methodological, that is, we search for the range of total MW masses that reproduces the MW RC, and then evaluate which mass density profile is the most suitable for estimating the DM mass. We focus on the rotation curve provided by *Gaia* DR2 alone (Eilers et al. 2019;

Table 4. Mass and χ^2 probabilities for Einasto, NFW, and gNFW DM density profiles.

Baryon model	M_{bar}	M_{tot} Einasto best fit	R_{200} Einasto best fit	M_{tot} Einasto average	M_{tot} NFW best fit	R_{200} NFW best fit	M_{tot} NFW average	M_{tot} gNFW best fit	R_{200} gNFW best fit	M_{tot} gNFW average
S	1.370	—	—	—	—	—	—	—	—	—
A&S	0.997	$7.36^{+3.11}_{-2.85}$	$186.22^{+20.07}_{-40.21}$	$7.20^{+2.24}_{-2.34}$	$4.93^{+1.03}_{-0.54}$	$151, 17^{+14.04}_{-12.30}$	$5.13^{+0.66}_{-0.60}$	$5.83^{+0.95}_{-0.66}$	$161.92^{+15.02}_{-12.13}$	$5.26^{+0.74}_{-0.66}$
I	0.896	$2.77^{+6.13}_{-0.29}$	$134.48^{+70.29}_{-9.12}$	$6.56^{+4.70}_{-3.12}$	$8.02^{+2.49}_{-0.97}$	$184.26^{+24.45}_{-13.59}$	$8.66^{+1.48}_{-1.45}$	$6.15^{+3.09}_{-0.76}$	$166.44^{+30.60}_{-13.34}$	$8.23^{+1.82}_{-1.61}$
E2 dJ	0.652	$2.37^{+1.03}_{-0.23}$	$127.63^{+17.75}_{-10.13}$	$3.01^{+0.70}_{-0.46}$	—	—	—	$7.93^{+0.85}_{-0.70}$	$186.47^{+8.52}_{-13.45}$	$8.42^{+0.68}_{-0.65}$
E2 J	0.648	$2.56^{+1.60}_{-0.13}$	$130.99^{+17.78}_{-14.46}$	$3.13^{+0.93}_{-0.82}$	—	—	—	$7.97^{+1.09}_{-0.74}$	$186.79^{+9.92}_{-14.62}$	$8.51^{+0.79}_{-0.75}$
E2 CM	0.634	$2.41^{+1.30}_{-0.75}$	$128.34^{+18.66}_{-18.43}$	$3.59^{+1.01}_{-0.81}$	$9.68^{+1.45}_{-0.51}$	$200.24^{+9.77}_{-14.37}$	$9.72^{+0.80}_{-0.89}$	$7.44^{+1.48}_{-0.61}$	$182.41^{+15.54}_{-11.74}$	$8.08^{+0.94}_{-0.93}$
G2 dJ	0.623	$3.08^{+3.72}_{-0.10}$	$139.3^{+48.34}_{-7.93}$	$4.10^{+2.40}_{-1.40}$	$8.58^{+1.30}_{-1.11}$	$192.00^{+10.12}_{-18.24}$	$9.01^{+1.06}_{-1.07}$	$6.82^{+2.20}_{-0.86}$	$176.89^{+20.79}_{-14.63}$	$8.26^{+1.47}_{-1.23}$
G2 J	0.619	$3.11^{+4.68}_{-0.14}$	$139.82^{+58.41}_{-6.41}$	$4.46^{+3.04}_{-1.61}$	$8.41^{+1.25}_{-1.30}$	$190.64^{+12.75}_{-16.62}$	$8.76^{+0.93}_{-1.09}$	$6.70^{+2.79}_{-0.74}$	$175.79^{+26.47}_{-13.41}$	$8.57^{+1.62}_{-1.53}$
G2 CM	0.605	$3.29^{+4.80}_{-0.28}$	$142.39^{+59.48}_{-10.11}$	$5.69^{+3.95}_{-2.49}$	$7.53^{+1.18}_{-0.93}$	$183.45^{+12.61}_{-14.05}$	$7.82^{+0.82}_{-0.89}$	$6.19^{+2.32}_{-0.58}$	$170.99^{+23.49}_{-11.31}$	$7.60^{+1.36}_{-1.19}$

Notes. Models and associated baryonic mass (first and second columns), and estimated total mass using χ^2 probabilities for Einasto, NFW, and gNFW DM density profiles (third to eighth columns, all masses are given in units of $10^{11} M_\odot$). The total mass and mass ranges are evaluated using the minimum χ^2 (best fit, Cols. 3 and 5) and by weighting the total masses by their χ^2 probabilities (average, Cols. 4 and 6), together with associated 1σ uncertainties. Uncertainties also account for systematics related to the Galactic distance and its motion, as well as to change in scale length ($\sim 4\%$ on masses, see Sect. 2.1), which have been added to the quoted error bars in this table.

(Mróz et al. 2019) because its accuracy is several times better than those of any former studies (see Fig. 3 of Eilers et al. 2019). This is also because disk stars correspond to dynamical points that are well anchored in the stellar disk, which is assumed to be well in equilibrium with the MW potential. In this context, our study broadens the recent work of de Salas et al. (2019) and Karukes et al. (2020) because here we consider a wider range of baryonic matter models of the MW to fit the *Gaia* DR2 RC¹. Our resulting total masses for the baryonic Model I are indeed quite similar to the values in Table 2 of de Salas et al. (2019), thus confirming that using Einasto profile will predict significantly lower total MW masses than when NFW or gNFW profiles are used. Small differences between the two works are probably due to the different schemes in interpreting the systematics of the Eilers et al. (2019) RC. We also retrieved similar results by Karukes et al. (2020), who also studied the effect of changing the DM density profile. While it goes in the same direction (the Einasto profile predicts lower total masses than the gNFW), their results have not been applied on the accurate *Gaia* DR2 MW RC, which prevents a detailed comparison.

We are aware that using the RC up to 25 kpc to constrain the mass density profile of the MW is a limited exercise because it needs to be extrapolated to larger radii (see Fig. 4). Extrapolations of the total mass from a rotation curve is incorrect, although it has been used very often in the literature either for giant spirals such as the MW (see, e.g., Eilers et al. 2019 and references therein) or for dwarfs (see, e.g., Read et al. 2016). Other works used different mass tracers such as globular clusters (Vasiliev 2019), massive and very bright stars (Deason et al. 2021), or dSph galaxies assumed to be satellites of the MW (Callingham et al. 2019). These methods have the advantage of sampling objects much farther out in the MW halo, although their virial equilibrium with the MW potential is less guaranteed than for rotating disk stars (Eilers et al. 2019). A warp and flare that occur at radii larger than 12 kpc may also limit our study, especially in the outer disk. However, the effect is possibly limited for our χ^2 fitting because the error bars are very large in

¹ The study of Karukes et al. (2020) is not principally based on the *Gaia* DR2 RC, except in their Sect. 5.1, in which they favored a similarly low MW mass as in our work (see also their Fig. 8).

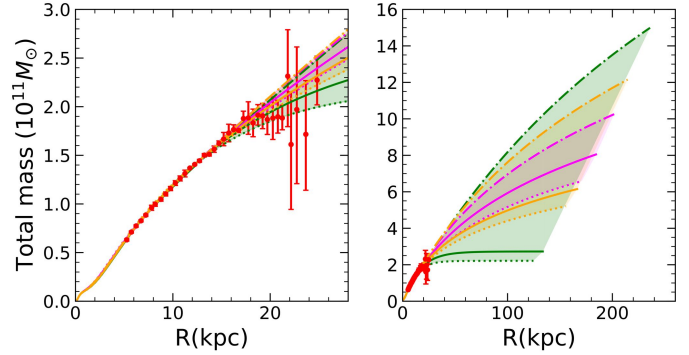


Fig. 4. Mass model derived from the MW RC (left panel) and extrapolated to larger radii (right panel), using Model I for the MW baryonic mass. The best-fit low- and high-mass models are shown as solid, dotted, and dash-dotted lines from Einasto (green), NFW (magenta), and gNFW (orange) models, respectively. Areas showing the possible mass ranges are shaded using the same color code. This shows how the NFW and gNFW bias the mass determination from RCs.

the outer disk because they account for the action of the vertical component (see Sect. 2.1 and Mackereth et al. 2019).

There are two other limitations of our study. The first is linked to the adoption of a spherical halo, although constraints on the dark matter halo shape in the Milky Way are still weak (see Read 2014). The second limitation is linked to our choice of initial (flat) priors for DM halo profiles, and this might alter the validity of our results. We compared our initial halos with the Dutton & Macciò (2014) CDM simulations, in particular, through the relation between concentration and total mass (M200). Our very broad range of parameters encompasses all the Dutton & Macciò (2014, see Fig. 3 of Udrescu et al. 2019) values in the range of $10^{11}\text{--}10^{12.5} M_\odot$ and in the $(c, M200)$ plane. The solutions that fit the MW rotation curve are also well within the range of halos simulated by Dutton & Macciò (2014).

Interestingly, our mass boundaries for the χ^2 fitting of the MW RC encompass all these values using other mass tracers. The question remains which mass density profile is the most suitable to properly evaluate the DM contribution to the MW RC. During the submission of this paper, a study by

[Cautun et al. \(2020\)](#) was published. They provide a detailed analysis of the effect of baryons on the DM profile. It results in a contracted halo in the spatial region in which the RC is determined. While the total mass is assumed to be consistent within the error bars with the [Callingham et al. \(2019\)](#) value ($M_{\text{tot}} = 1.17 \pm 0.18 \times 10^{12} M_{\odot}$), [Cautun et al. \(2020\)](#) succeeded to fit the MW RC that provided most of the constraints, given its accuracy. Together with our study, this leads us to three important remarks:

- When the MW RC alone is used as a constraint, we find that the Einasto mass density profile leads to the largest range of MW total masses that can reproduce its RC, while both NFW and gNFW profiles lead to a narrow mass range, in particular, by excluding total mass ($M_{200} = M_{\text{tot}}$) values lower than $\sim 5 \times 10^{11} M_{\odot}$.
- The contracted halo density profile might be difficult to reproduce by NFW or by gNFW profiles ([Cautun et al. 2020](#)), while it is part of the solutions of this paper using an Einasto profile combined with the baryonic model of [Cautun et al. \(2020\)](#) (see Fig. 5).
- We find that both NFW and gNFW profiles provide total masses that increase with baryonic masses (see rows four to nine in Table 4), which contradicts expectations that the DM compensates for a lack of mass from baryons in a galaxy. This contradicts the Einasto predictions, according to which the DM mass is higher when the assumed baryonic mass is lower.

It might have been envisioned that these limitations of the NFW profile are related to its two-parameter nature, but this seems to be ruled out by the (almost) similar behavior of the three-parameter gNFW profile. Alternatively, this might be attributed to the density profile of the models in the outskirts. Both have an analytical form that imposes a constant slope of the density profile reaching -3 at large distances, leading to an enclosed mass value that does not converge because it increases as the logarithm of the radius. Investigations by [Nesti & Salucci \(2013\)](#) of the internal $r < 5$ kpc MW kinematics showed that a cusp-like NFW (or gNFW for $\gamma > 0$) profile may also experience some difficulties when combined to baryonic mass.

4.2. Can the MW has a total mass as low as $2.6 \times 10^{11} M_{\odot}$?

The Einasto profile fit of the RC points toward low total mass values for the MW (see Table 4, Figs. 2 and 3), disregarding any other dynamical tracers farther out in the Milky Way. However, the main result of this paper is provided by the combination of RC fitting with either an Einasto or NFW profile for the MW DM halo, leading to a range of the total MW mass of between 2.5 to $18 \times 10^{11} M_{\odot}$ (see Figs. 1–4). This range is consistent with many studies, including that based on other mass indicators, although they generally disagree with our lowest mass range. Figure 6 compares the orbital energy of globular clusters (GCs) from [Vasiliev \(2019\)](#) with that expected from the most likely (total mass: $2.6 \times 10^{11} M_{\odot}$) and the highest (total mass: $15 \times 10^{11} M_{\odot}$) MW mass model that could reproduce the MW RC when combining Model I for baryons and the Einasto profile for DM. Both are consistent with the scenario that GCs are gravitationally bounded to the MW except for one, Pyxis, which appears to disagree significantly for the lighter model. However, the Pyxis eccentric orbit, metallicity, and age indicate an extra-galactic origin of Pyxis ([Fritz et al. 2017](#)). This indicates that in absence of other precise mass indicators from 25 to 70 kpc, it may be premature to conclude on the total MW mass value from $2.6 \times 10^{11} M_{\odot}$ and $R_{200} = 135$ kpc (χ^2 probability = 0.999)

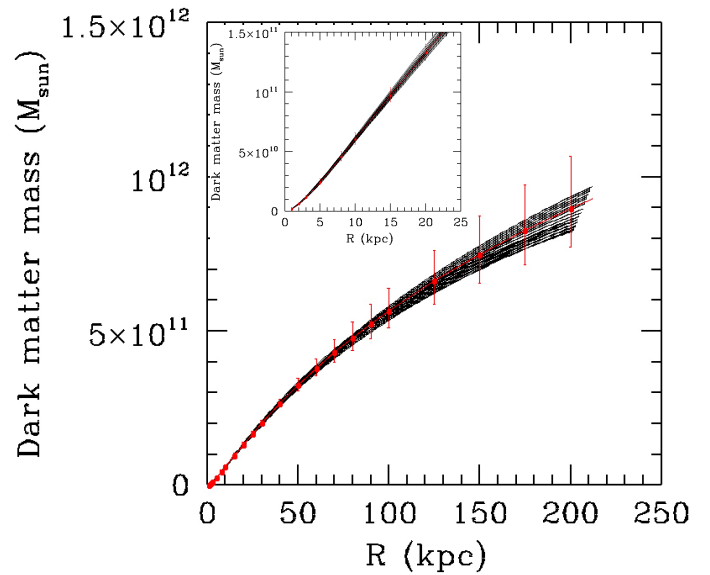


Fig. 5. Dark-matter enclosed mass vs. radius for the mass profile of the contracted halo of [Cautun et al. \(2020\)](#), from which points and error bars are given in red. When the same baryon content is assumed, the black curves show the result from 24 Einasto models that fit both the RC and the contracted halo. The total mass are very similar within a few percent, and the only small difference is that R_{200} ranges from 200 to 213 kpc instead of 218 kpc for the contracted halo of [Cautun et al. \(2020\)](#). The inset shows a zoom of the mass distribution below 25 kpc to show the similarity of the Einasto DM and the contracted halo near the range of radii of the RC.

to $15 \times 10^{11} M_{\odot}$ and $R_{200} = 236$ kpc (χ^2 probability = 0.35), and even $18 \times 10^{11} M_{\odot}$ with a χ^2 probability = 0.05.

We remark that a low value for the MW mass would have considerable consequences on the orbits of many dSph galaxies, for instance. For example, [Boylan-Kolchin et al. \(2013\)](#) convincingly showed that an MW mass significantly higher than $10^{12} M_{\odot}$ is necessary to bound Leo I. Using the [Boylan-Kolchin et al. \(2013\)](#) phase space plot, [Hammer et al. \(2020\)](#) showed that *Gaia* DR2 orbits might indicate a passage more recent than 4 Gyr ago for many dSphs, assuming a total mass of $8.66 \times 10^{11} M_{\odot}$ for the MW ([Eilers et al. 2019](#)). Because MW dSphs also have a peculiar planar alignment ([Pawlowski et al. 2014](#)), [Deason et al. \(2021\)](#) opted to use halo stars. After a thorough analysis of the possible recent accretions based on phase-space diagrams, they derived a total mass within 100 kpc of $6.07 \times 10^{11} M_{\odot}$ ², with which they associated systematics up to $1.2 \times 10^{11} M_{\odot}$. This is only marginally consistent with a very low MW mass and makes a future study of *Gaia* EDR3 results promising that combines the MW RC and GC motions (Wang et al., in prep.).

5. Summary

Rotation curves are major tools for determining the dynamical mass distribution in the Milky Way and spiral galaxies ([Sofue 2013](#)). They are also historically at the root for the requirement of DM in galactic halos ([Bosma 1978; Rubin et al. 1980](#)), especially when they have been derived from the HI gas, which often extends far beyond the optical disk. Since the end of the 70s, many estimates of the DM content in many spiral galaxies were

² We do not discuss their extrapolation to $11.6 \times 10^{11} M_{\odot}$ for the total MW mass because it depends on the NFW profile that was assumed.

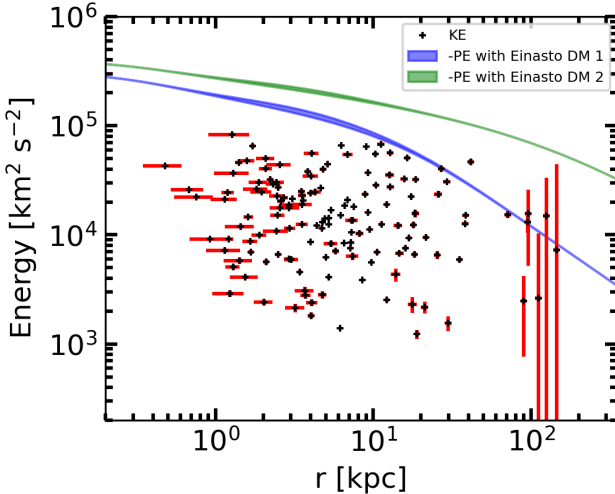


Fig. 6. Kinetic energy (KE) of the GCs from Vasiliev (2019) (crosses with red error bars) compared to the blue and green thick lines that indicate the potential energy (PE, absolute values) expected from the most likely and the heaviest Einasto model when associated to Model I for baryons, respectively. Error bars have been estimated with Monte Carlo randomly sampling by considering the errors in distance and radial velocity, as well as errors in proper motion and their covariance. The (small) thickness of the potential lines is due to the presence of the axisymmetric disk component.

derived, generally through extrapolations of the observed rotation curves of spiral galaxies.

We have tested the most frequently used density profile to perform numerous analyses of galaxy RCs, namely the NFW density profile (Navarro et al. 1997), and its generalization to three parameters, the gNFW profile. We considered the MW RC because it is one of the most accurately determined RCs (Eilers et al. 2019), and also because the MW has not had a major merger since ~ 10 Gyr (Hammer et al. 2007; Helmi 2020). This supports the idea that its disk is dynamically virialized to at least 30 kpc because Gnedin & Ostriker (1999) showed that it takes more than three dynamical times for a system to virialize after a perturbation.

In contrast to the NFW (or gNFW) profile for DM, the three-parameter Einasto profile (Einasto 1965, see also Retana-Montenegro et al. 2012) may account for many types of outer slopes, and it provides a much better fit of the simulated DM properties (Dutton & Macciò 2014, and references therein), including for the physically motivated contracted halo (Cautun et al. 2020). It also shows consistent results that can fit the MW RC with most combinations of baryonic mass models, generating a plausible wide range of possible total masses (see Figs. 2–4).

Methodological problems due to the use of a too analytically constrained density model may affect the current estimates of the MW mass such as were reported by Eilers et al. (2019). Perhaps this also applies to the numerous galaxies for which the RC has been analyzed. Other galaxy RCs have yet to be analyzed using a three-parameter density model for the DM as we did here, although see Chemin et al. (2011) for their promising results. These future investigations should focus first on galaxies that did not experience a recent major merger during which most of the disk was resettled or rebuilt (Hammer et al. 2005, 2009; Hopkins et al. 2009). For example, an event like this might complicate the interpretation of the M31 RC, whose recent major merger 2–3 Gyr ago has had a more serious impact (see

Hammer et al. 2018) than that of the Sagittarius passage near the MW. The Sagittarius passage is thought to have created vertical waves within the MW disk, although this is still disputed (see Bennett & Bovy 2021, and references therein), while the recent merger in M31 has completely destroyed the thin disk of M31 for stars with ages older than 2 Gyr (see the modeling by Hammer et al. 2018, which reproduced the anomalous age-velocity dispersion discovered by Dorman et al. 2015). In addition, it is also possible that other two-parameter models are affected in a similar manner, for instance, the isothermal model, which renders comparisons of the validity of these profiles for fitting RCs somewhat obsolete.

Using the Einasto profile, we find that the MW mass is mostly constrained by its slightly declining RC, which leads to higher χ^2 probabilities for low-mass values (i.e., slightly below $3 \times 10^{11} M_\odot$) for the MW, although less probable higher values up to $18 \times 10^{11} M_\odot$ cannot be excluded. This causes a revision of the available total mass range of the MW down to values that can be as low as $2.6 \times 10^{11} M_\odot$, which are also consistent with the kinetic energy distribution of globular clusters. Further improvements of the accuracy of the MW RC will be invaluable to support or reject these low total masses. They would be invaluable in particular for determining precise orbits for the MW dSphs, for which, given the *Gaia* EDR3 precision, most uncertainties now come from our insufficient knowledge of the total MW mass.

Acknowledgements. We are very grateful for the useful and insightful discussions with Christina Eilers about the MW RC and the treatment of the systematics. We warmly thank Piercarlo Bonifacio for his careful advices and comments on the manuscript, and also Frederic Arenou and Carine Babusiaux for their contributions in the meetings during which the methodology of the paper has been adopted. We are acknowledging the support of the International Research Program Tianguan led by the French CNRS and the Chinese NAOC and Yunnan University.

References

- Allen, C., & Santillan, A. 1991, *Rev. Mex. Astron. Astrofis.*, **22**, 255
- Belokurov, V., Erkal, D., Evans, N. W., Koposov, S. E., & Deason, A. J. 2018, *MNRAS*, **478**, 611
- Bennett, M., & Bovy, J. 2021, *MNRAS*, **503**, 376
- Binney, J., & Tremaine, S. 2011, *Galactic Dynamics* (Princeton: Princeton University Press)
- Bland-Hawthorn, J., & Gerhard, O. 2016, *ARA&A*, **54**, 529
- Bosma, A. 1978, PhD Thesis, Groningen University, The Netherlands
- Bovy, J., & Rix, H.-W. 2013, *ApJ*, **779**, 115
- Boylan-Kolchin, M., Bullock, J. S., Sohn, S. T., Besla, G., & van der Marel, R. P. 2013, *ApJ*, **768**, 140
- Calchi Novati, S., & Mancini, L. 2011, *MNRAS*, **416**, 1292
- Callingham, T. M., Cautun, M., Deason, A. J., et al. 2019, *MNRAS*, **484**, 5453
- Cautun, M., Benítez-Llambay, A., Deason, A. J., et al. 2020, *MNRAS*, **494**, 4291
- Chemin, L., de Blok, W. J. G., & Mamon, G. A. 2011, *AJ*, **142**, 109
- Deason, A. J., Erkal, D., Belokurov, V., et al. 2021, *MNRAS*, **501**, 5964
- de Jong, J. T. A., Yanny, B., Rix, H.-W., et al. 2010, *ApJ*, **714**, 663
- de Salas, P. F., Malhan, K., Freese, K., Hattori, K., & Valluri, M. 2019, *JCAP*, **2019**, 037
- de Vaucouleurs, G. 1958, *ApJ*, **128**, 465
- Dorman, C. E., Guhathakurta, P., Seth, A. C., et al. 2015, *ApJ*, **803**, 24
- Dutton, A. A., & Macciò, A. V. 2014, *MNRAS*, **441**, 3359
- Eilers, A.-C., Hogg, D. W., Rix, H.-W., & Ness, M. K. 2019, *ApJ*, **871**, 120
- Einasto, J. 1965, *Trudy Astrofizicheskogo Instituta Alma-Ata*, **5**, 87
- Fritz, T. K., Linden, S. T., Zivick, P., et al. 2017, *ApJ*, **840**, 30
- Gao, L., Navarro, J. F., Cole, S., et al. 2008, *MNRAS*, **387**, 536
- Gnedin, O. Y., & Ostriker, J. P. 1999, *ApJ*, **513**, 626
- Grand, R. J. J., Deason, A. J., White, S. D. M., et al. 2019, *MNRAS*, **487**, L72
- Hammer, F., Flores, H., Elbaz, D., et al. 2005, *A&A*, **430**, 115
- Hammer, F., Puech, M., Chemin, L., Flores, H., & Lehnert, M. D. 2007, *ApJ*, **662**, 322
- Hammer, F., Flores, H., Puech, M., et al. 2009, *A&A*, **507**, 1313
- Hammer, F., Yang, Y., Arenou, F., et al. 2018, *ApJ*, **860**, 76
- Hammer, F., Yang, Y., Arenou, F., et al. 2020, *ApJ*, **892**, 3

- Haywood, M., Di Matteo, P., Lehnert, M. D., et al. 2018, [ApJ](#), **863**, 113
 Helmi, A. 2020, [ARA&A](#), **58**, 205
 Helmi, A., Babusiaux, C., Koppelman, H. H., et al. 2018, [Nature](#), **563**, 85
 Hinshaw, G., Larson, D., Komatsu, E., et al. 2013, [ApJS](#), **208**, 19
 Hogg, D. W., Eilers, A.-C., & Rix, H.-W. 2019, [AJ](#), **158**, 147
 Hopkins, P. F., Cox, T. J., Younger, J. D., & Hernquist, L. 2009, [ApJ](#), **691**, 1168
 Iocco, F., Pato, M., & Bertone, G. 2015, [Nat. Phys.](#), **11**, 245
 Jurić, M., Ivezić, Ž., Brooks, A., et al. 2008, [ApJ](#), **673**, 864
 Karukes, E. V., Benito, M., Iocco, F., Trotta, R., & Geringer-Sameth, A. 2020, [JCAP](#), **2020**, 033
 Klypin, A., Yepes, G., Gottlöber, S., Prada, F., & Heß, S. 2016, [MNRAS](#), **457**, 4340
 Mackereth, J. T., Bovy, J., Leung, H. W., et al. 2019, [MNRAS](#), **489**, 176
 Miyamoto, M., & Nagai, R. 1975, [PASJ](#), **27**, 533
 Mróz, P., Udalski, A., Skowron, D. M., et al. 2019, [ApJ](#), **870**, L10
 Navarro, J. F., Frenk, C. S., & White, S. D. M. 1997, [ApJ](#), **490**, 493
 Navarro, J. F., Hayashi, E., Power, C., et al. 2004, [MNRAS](#), **349**, 1039
 Navarro, J. F., Ludlow, A., Springel, V., et al. 2010, [MNRAS](#), **402**, 21
 Nesti, F., & Salucci, P. 2013, [JCAP](#), **2013**, 016
 Pawłowski, M. S., Famaey, B., Jerjen, H., et al. 2014, [MNRAS](#), **442**, 2362
 Pouliasis, E., Di Matteo, P., & Haywood, M. 2017, [A&A](#), **598**, A66
 Read, J. I. 2014, [J. Phys. G Nucl. Phys.](#), **41**, 063101
 Read, J. I., Iorio, G., Agertz, O., & Fraternali, F. 2016, [MNRAS](#), **462**, 3628
 Retana-Montenegro, E., van Hese, E., Gentile, G., Baes, M., & Frutos-Alfaro, F. 2012, [A&A](#), **540**, A70
 Rubin, V. C., Ford, W. K., Jr., & Thonnard, N. 1980, [ApJ](#), **238**, 471
 Sofue, Y. 2013, [PASJ](#), **65**, 118
 Sofue, Y. 2015, [PASJ](#), **67**, 75
 Stanek, K. Z., Udalski, A., Szymański, M., et al. 1997, [ApJ](#), **477**, 163
 Udrescu, S. M., Dutton, A. A., Macciò, A. V., & Buck, T. 2019, [MNRAS](#), **482**, 5259
 Vasiliev, E. 2019, [MNRAS](#), **484**, 2832
 Wegg, C., Gerhard, O., & Portail, M. 2016, [MNRAS](#), **463**, 557
 Zhao, H. 1996, [MNRAS](#), **278**, 488

Appendix A: Data of the MW RC and adopted error bars

Table A.1 provides the data for the MW RC given by [Eilers et al. \(2019\)](#), for which they defined the statistical errors ($\sigma_{v_c}^-$ (km s^{-1}) and $\sigma_{v_c}^+$ (km s^{-1})), and to which we added the systematic error (see Sect. 2.1) in the last column as a fraction of the observed velocity, following the definition made in Figure 4 of [Eilers et al. \(2019\)](#).

Table A.1. Data points for the MW RC and adopted error bars.

R (kpc)	v_c (km s^{-1})	$\sigma_{v_c}^-$ (km s^{-1})	$\sigma_{v_c}^+$ (km s^{-1})	$\Delta v_{\text{sys}}/v_c$
5.27	226.83	1.91	1.90	0.0045
5.74	230.80	1.43	1.35	0.0045
6.23	231.20	1.70	1.10	0.0045
6.73	229.88	1.44	1.32	0.002
7.22	229.61	1.37	1.11	0.0045
7.82	229.91	0.92	0.88	0.013
8.19	228.86	0.80	0.67	0.010
8.78	226.50	1.07	0.95	0.008
9.27	226.20	0.72	0.62	0.0088
9.76	225.94	0.42	0.52	0.0088
10.26	225.68	0.44	0.40	0.010
10.75	224.73	0.38	0.41	0.010
11.25	224.02	0.33	0.54	0.013
11.75	223.86	0.40	0.39	0.001
12.25	222.23	0.51	0.37	0.001
12.74	220.77	0.54	0.46	0.0046
13.23	220.92	0.57	0.40	0.0054
13.74	217.47	0.64	0.51	0.0054
14.24	217.31	0.77	0.66	0.010
14.74	217.60	0.65	0.68	0.0072
15.22	217.07	1.06	0.80	0.020
15.74	217.38	0.84	1.07	0.0257
16.24	216.14	1.20	1.48	0.0123
16.74	212.52	1.39	1.43	0.001
17.25	216.41	1.44	1.85	0.0182
17.75	213.70	2.22	1.65	0.0434
18.24	207.89	1.76	1.88	0.0377
18.74	209.60	2.31	2.77	0.0247
19.22	206.45	2.54	2.36	0.032
19.71	201.91	2.99	2.26	0.0385
20.27	199.84	3.15	2.89	0.056
20.78	198.14	3.33	3.37	0.041
21.24	195.30	5.99	6.50	0.010
21.80	213.67	15.38	12.18	0.086
22.14	176.97	28.58	18.57	0.13
22.73	193.11	27.64	19.05	0.13
23.66	176.63	18.67	16.74	0.13
24.82	198.42	6.50	6.12	0.045

Appendix B: Detection of the Keplerian decline in the Milky Way rotation curve (Paper II)

Detection of the Keplerian decline in the Milky Way rotation curve

Yongjun Jiao¹, François Hammer¹, Haifeng Wang², Jianling Wang^{1,3}, Philippe Amram⁴, Laurent Chemin⁵, and Yanbin Yang¹

¹ GEPI, Observatoire de Paris, Paris Sciences et Lettres, CNRS, Place Jules Janssen, 92195 Meudon, France
e-mail: yongjun.jiao@obspm.fr, francois.hammer@obspm.fr

² Centro Ricerche Enrico Fermi, Via Panisperna 89a, 00184 Rome, Italy

³ CAS Key Laboratory of Optical Astronomy, National Astronomical Observatories, Beijing 100101, PR China

⁴ Aix-Marseille Univ., CNRS, CNES, LAM, 38 Rue Frédéric Joliot Curie, 13338 Marseille, France

⁵ Instituto de Astrofísica, Universidad Andres Bello, Fernandez Concha 700, Las Condes, Santiago, RM, Chile

Received 20 July 2023 / Accepted 21 August 2023

ABSTRACT

Our position inside the Galactic disc has previously prevented us from establishing an accurate rotation curve (RC). The advent of *Gaia* and its third data release (*Gaia* DR3) made it possible to specify the RC up to twice the optical radius. We aim to establish a new RC of the Galaxy from the *Gaia* DR3 by drastically reducing systematic uncertainties. Our goal is to provide a new estimate of the mass of the Galaxy. We compared different estimates, established a robust assessment of the systematic uncertainties, and addressed differences in methodologies, particularly regarding distance estimates. We find a sharply decreasing RC for the Milky Way; the decrease in velocity between 19.5 and 26.5 kpc is approximately 30 km s^{-1} . We identify, for the first time, a Keplerian decline of the RC, starting at ~ 19 kpc and ending at ~ 26.5 kpc from the Galaxy centre, while a flat RC is rejected with a significance of 3σ . The total mass is revised downwards to $2.06^{+0.24}_{-0.13} \times 10^{11} M_\odot$, which is in agreement with the absence of a significant mass increase at radii larger than 19 kpc. We evaluated the upper limit on the total mass by considering the upper values of velocity measurements, which leads to a strict, unsurpassable limit of $5.4 \times 10^{11} M_\odot$.

Key words. Galaxy: kinematics and dynamics – Galaxy: general – Galaxy: stellar content – Galaxy: structure

1. Introduction

Almost a century ago, Lundmark (1925, see their Fig. 4) was amongst the first to identify the flat behaviour of disc-galaxy rotation curves (RCs). From optical spectroscopy, Babcock (1939, then Mayall 1951) reported that the RC of M31 shows no decrease up to 20 kpc from the centre. With a larger sample of galaxies, Rubin et al. (1978) found that several spiral galaxies have a flat RC. The advent of radio astronomy made it possible to probe galaxy rotation beyond the optical disc. The increased sensitivity of radio telescopes allowed Bosma (1978) to obtain the first sample of galaxies observed in the neutral hydrogen line, and he demonstrated that most galaxies show a flat RC. Extended flat RCs of spiral galaxies can be considered as major evidence of the presence of an extended halo of dark matter (DM) surrounding them.

Early RC investigations were made beyond our own Galaxy because our location in it and the extinction prevented straightforward, direct determination of the RC as is possible for nearby external galaxies. HII regions, OB stars, carbon stars, planetary nebulae, and cepheids have been used to trace the rotation of the Galaxy. As reviewed by Schmidt (1965), before the early 1960s, the outer RC was thought to be Keplerian, and from the late 1960s until today, evidence has been found to show that its outer curve is rather flat, albeit with significant uncertainties. Therefore, the Galaxy must contain large amounts of dark matter. However, it is interesting to note that the RC collected by Sofue et al. (2009) is, despite huge uncertainties, consistent with a decreasing RC from ~ 15 to ~ 23 kpc.

A revolution in this area came with *Gaia*, whose proper motion measurements have allowed 3D velocity measurements. Pioneering efforts to establish the Milky Way (MW) RC with *Gaia* DR2 were made by Eilers et al. (2019), who used spectrophotometric parallax distances from Hogg et al. (2019) for a set of more than 20 000 red giant branch (RGB) stars. Eilers et al. (2019) provided by far the most accurate RC for the MW, a success confirmed by Mróz et al. (2019) on the basis of a small sample of variable stars that nevertheless led to very accurate distance estimates.

The MW has been found to have an exceptionally quiet merger history, evidenced by its rather pristine halo and small angular momentum when compared to other spiral galaxies (Hammer et al. 2007, and references therein). This was confirmed by the discovery of its last major merger, Gaia–Sausage–Enceladus (GSE, 8–10 Gyr ago, Belokurov et al. 2018; Haywood et al. 2018; Helmi et al. 2018), which was identified from the angular momentum signatures of residual stars in the halo. Because most spiral galaxies underwent their last major merger more recently (~ 6 Gyr ago, Hammer et al. 2009; Puech et al. 2012), the MW disc may be less affected by the large-scale motions expected following such a major event. This would make the MW one of the most appropriate targets for deriving a RC, assuming equilibrium conditions. It has been argued that a minor merger, such as the infall of Sagittarius (Sgr) 4–6 Gyr ago, could have perturbed the MW outer disc, providing a possible explanation for the warp (Bailin 2003) and the observed vertical oscillations (Laporte et al. 2018). Being at first passage, the Large Magellanic Cloud

(LMC) may have affected the MW disc location with respect to its halo (Conroy et al. 2021; Erkal et al. 2021), but is unlikely to have affected its internal dynamics or morphology (Laporte et al. 2018).

Gaia DR3 (Gaia Collaboration 2023b) has provided improved parallaxes and proper motions, whose systematic uncertainties are smaller by a factor of 2 when compared to those of *Gaia* DR2 (Lindegren et al. 2021a,b). Gaia Collaboration (2023a, hereafter D23) measured a robust RC of the MW out to $R = 14$ kpc from the 3D velocity space of a clean sample of OB stars and another sample of RGB stars using *Gaia* DR3 data. This was followed by three studies investigating the outer MW RC (Wang et al. 2023a; Zhou et al. 2023; Ou et al. 2023), which used different star samples and methodologies. Wang et al. (2023a) derived distances from the *Gaia* parallaxes (π) of a very large number of stars for which there are also radial velocities from *Gaia* DR3. These latter authors implemented a Lucy's inversion method (LIM; Lucy 1974), from which they populated 6D phase space cells ($l, b, \pi, V_r, \mu_\alpha^*, \mu_\delta$). These authors then determined the average values of the velocity components and their dispersions, which were tested and shown to provide reliable results. Ou et al. (2023) followed a technique similar to that of Eilers et al. (2019), namely using spectrophotometric distances to establish the RC of over 30 000 RGB stars. A similar approach was adopted by Zhou et al. (2023), although their distances were estimated using different priors.

Figure 1 compares the three corresponding RCs; they show many consistencies, except in the inner (where Wang et al. 2023a have lower velocities) and outer (where Zhou et al. 2023 have higher velocities) parts. This latter discrepancy should significantly affect the estimation of the dynamical mass¹ of the MW. The goal of the present paper is to verify whether these differences can be attributed to different methodologies in order to establish the MW RC and to determine the dynamical mass of our Galaxy from *Gaia* DR3. In Sect. 2, we describe the Jeans equation, and show how we derive the systematic uncertainties for the Wang et al. (2023a) RC using a method similar to that of Eilers et al. (2019) and to that of Ou et al. (2023). In Sect. 3, we show the approach we take to determine the MW dynamical mass using a set of models including baryonic and DM components. In Sect. 4, we show that the three RCs can be reconciled together, providing a sharp velocity drop at large radii, and we provide the MW dynamical mass range and its uncertainty. In Sect. 5, we describe the limitations of our estimates, and compare them to estimates based on other tracers. We also test whether or not we can detect the Keplerian decline of the MW RC.

2. Methods: RC determination and associated uncertainties

2.1. The RC derived from Jeans equation

Assuming an axisymmetric MW potential and a disc at equilibrium, Wang et al. (2023a) used the Jeans equation (Binney & Tremaine 2008, Eq. (4.222a)) to measure the circular velocity curve:

$$\frac{\partial \nu \langle V_R \rangle}{\partial t} + \frac{\partial \nu \langle V_R^2 \rangle}{\partial R} + \frac{\partial \nu \langle V_R V_z \rangle}{\partial z} + \nu \left(\frac{\langle V_R^2 \rangle - \langle V_\phi^2 \rangle}{R} + \frac{\partial \Phi}{\partial R} \right) = 0, \quad (1)$$

¹ In the following, we use the term dynamical (or total) mass, (M_{dyn}), to refer to the sum of the baryonic and dark matter masses. This latter is also referred to as the virial dark-matter mass (M_{vir}) inside the virial radius, above which no additional mass is expected.

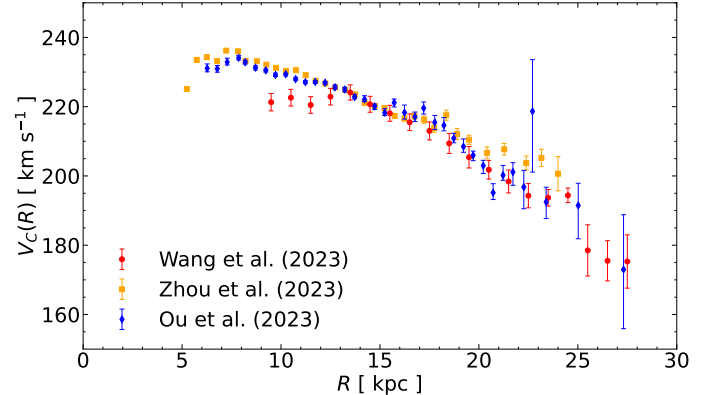


Fig. 1. Comparison of the three different measurements of the MW RC based on *Gaia* DR3.

where ν denotes the matter density distribution. By assuming a steady state, a disc that is symmetric about its equator ($\partial\nu/\partial z = 0$ at $z = 0$), and an exponential radial profile of the tracer population with a scale length of $h_R = 2.5$ kpc (Jurić et al. 2008), the circular velocity curve can be derived using $R(\partial\Phi/\partial R) = V_c^2$ in Eq. (1):

$$V_c^2 = \langle V_\phi^2 \rangle + \frac{R - h_R}{h_R} \langle V_R^2 \rangle - R \frac{\partial \langle V_R^2 \rangle}{\partial R} - R \frac{\partial \langle V_R V_z \rangle}{\partial z}. \quad (2)$$

For the three velocity components, we apply:

$$\langle V_X^2 \rangle = \langle V_X \rangle^2 + \sigma_{\langle V_X \rangle}^2, \quad (3)$$

where X presents R, ϕ , and z , respectively.

Concerning the RC of Wang et al. (2023a), we adjusted the bin size to improve the calculation within each bin. Specifically, we calculated $\langle V_\phi^2 \rangle$ and $\langle V_R^2 \rangle$ using the same 1 kpc width bins as was done by Wang et al. (2023a). However, we derived the gradient term $\partial \langle V_R^2 \rangle / \partial R$ after centring the 1 kpc bin width around each data point. Figure 2 shows that the slightly modified RC is consistent with that of Wang et al. (2023a) within 22 kpc, which means that systematic uncertainties associated with the choice of the bin size and position are very small. The largest modification is for the point at $R = 24.5$ kpc, whose velocity amplitude decreases by 8 km s^{-1} . However, this velocity is more consistent with the decreasing slope of the RC between 13 and 23 kpc. Data beyond 27.5 kpc are lacking (within a height of 3 kpc, i.e. $|z| < 3$ kpc), and so we do not derive the last point at $R = 27.5$ kpc.

We derived the RC and the associated systematic uncertainties within the height of 3 kpc, i.e., $|z| < 3$ kpc, which provides the most extended RC in Wang et al. (2023a). The cross term $\partial \langle V_R V_z \rangle / \partial z$ was also neglected in the calculations of several previous works (e.g. Eilers et al. 2019; Wang et al. 2023a) because it is generally considered to be two to three orders of magnitude smaller than the remaining terms at many radii. This term is further analysed in Sect. 2.2.1.

2.2. Systematic uncertainties

The MW has various and complex dynamical structures, which implies that the assumptions of the time-independent gravitational potential and of a smooth density distribution are rough approximations of the true dynamics. For example, the observed velocity field in our Galaxy has been found to have asymmetrical motions with significant gradients in all velocity components

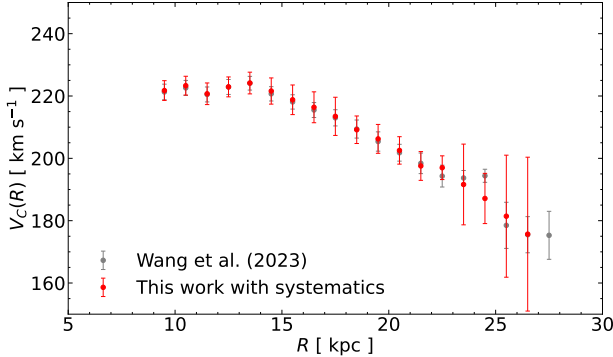


Fig. 2. Comparison of the RC of this work with that of Wang et al. (2023a). Red points and error bars represent the RC measurement with adjusted bin sizes and systematic uncertainties at a vertical height of $|z| < 3$ kpc. Grey points and error bars present previous findings from Wang et al. (2023a) without systematic uncertainties.

(D23) because of various gravitational influences, such as those of the bar, bulge, and spiral arms, or because of the tidal interaction with the Sagittarius dwarf galaxy (Bailin 2003). It is crucial to estimate the systematic uncertainties brought to the circular velocity curve from the data. Wang et al. (2023a) derived the kinematic maps of different velocity components from *Gaia* DR3 up to 30 kpc. However, the perturbations due to the radial velocity component are sufficiently small, which justifies the use of the time-independent Jeans equation.

2.2.1. The neglected cross-term

The vertical gradient of the cross-term $\langle V_R V_z \rangle$ is usually considered negligible within about 20 kpc. As we consider the RC out to 27 kpc, the largest contribution to the systematic uncertainty of the circular velocity comes from the neglected cross-term in the Jeans equation at large radii. Figure 3 shows the map of this cross-term on the projection of the Galactic (R, z) plane, which suggests significant variations of the cross-term with radius. The red dotted curve of Fig. 4 presents the corresponding contribution to systematic uncertainties. This term causes systematic uncertainties of smaller than 2% below 23 kpc, and of up to $\sim 8\%$ at 25.5 kpc. It should not be neglected at large radii. In addition, we also limited the analysis to a narrower Galactic plane, that is $|z| < 2$ kpc. In this case, systematic uncertainties from this term are smaller than 5% within 25 kpc.

2.2.2. Disc scale length

Another contribution to the systematic uncertainty that cannot be ignored is the unknown density profile of the tracer population, particularly in the outer disc. Our calculation assumes an exponential density profile with a scale length of $h_R = 2.5$ kpc. Following Eilers et al. (2019), we vary this scale length, that is, $\Delta h_R = \pm 1$ kpc, and this causes systematic uncertainties at the $\sim 1\%$ level, which are represented in Fig. 4 by an orange-dashed line.

2.2.3. Disc radial-density profile

The functional form chosen for the density profile can also lead to systematic uncertainties. We therefore applied a power-law density profile instead, for which we chose an index of $\alpha = -2.25$, which has the same slope as the exponential function

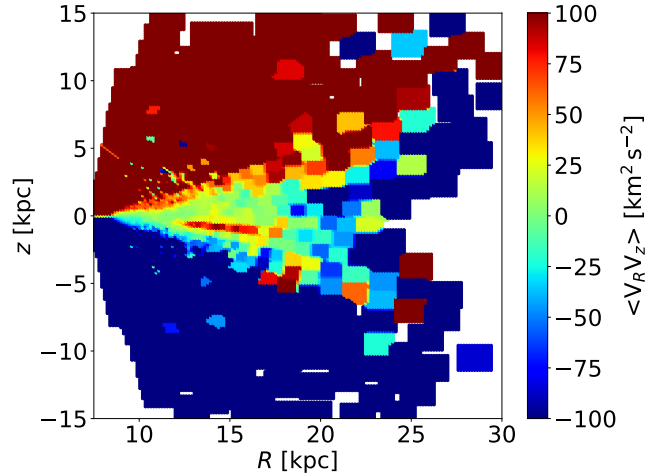


Fig. 3. Cross-term $\langle V_R V_z \rangle$ using LIM in the Galactic (R, z) plane.

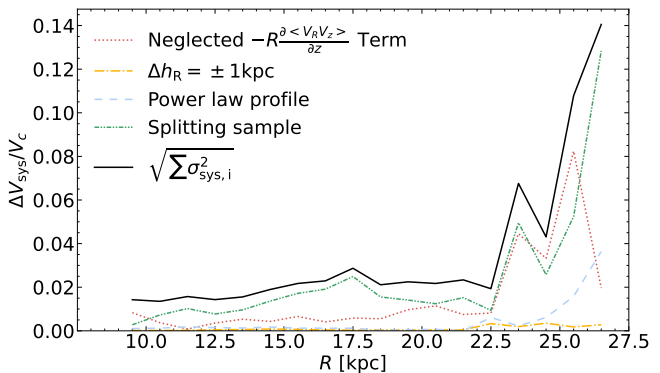


Fig. 4. Summary of potential systematic uncertainties in the circular velocity curve at a vertical height of $|z| < 3$ kpc. We estimate systematic uncertainties arising from the neglected cross-term (see the red-dotted line), from varying the exponential scale length of the density profile (orange-dashed line), from passing from an exponential to a power law (blue-dashed line) with an index $\alpha = -2.25$, and finally after splitting the sample into two parts (green-dotted line). The total systematic uncertainty (black-solid line) is at the 2% level up to $R = 22.5$ kpc, and then increases at larger radii.

at the Sun's location. This leads to a systematic error of less than 4% (blue-dashed line in Fig. 4).

2.2.4. Splitting data sample

In order to estimate global systematic uncertainties arising from the data sample of different azimuthal ranges, we divided the data sample into two subsamples selected within $160^\circ \leq l \leq 180^\circ$ and $180^\circ \leq l \leq 200^\circ$, respectively. We calculated the average of the velocity difference between these two subsamples and the total sample. We present this systematic contribution in Fig. 4 with a green-dotted line. The systematic uncertainty due to the data sample is smaller than 2% within 22 kpc. At large radii, it is comparable to the systematic uncertainties associated with the neglected cross-term.

2.2.5. Total uncertainties including systematics

The total relative systematic uncertainties are indicated by the black-solid line of Fig. 4, which is obtained from the quadratic

Table 1. Parameters of bulge, see more details in Sect. 3.1.

Parameter	Bulge E	Bulge G	Bulge B2
$M_{\text{bulge}} (10^{10} M_{\odot})$	1.962	1.639	1.550
x_b (kpc)	0.899	1.239	0.700 ^(a)
y_b (kpc)	0.386	0.609	–
z_b (kpc)	0.250	0.438	–

Notes. ^(a)Value of r_b in Eq. (7).

Table 2. Parameters of disk, see more details in Sect. 3.1.

Parameter	Disk CM	Disk J	Disk dJ	Disk B2
$M_{\text{thin}} (10^{10} M_{\odot})$	3.11	3.17	3.33	3.65
$M_{\text{thick}} (10^{10} M_{\odot})$	0.82	0.90	0.78	–
L_{thin} (kpc)	2.75	2.60	2.60	2.35
L_{thick} (kpc)	4.10	3.60	4.10	–
H_{thin} (kpc)	0.25	0.30	0.25	0.14
H_{thick} (kpc)	0.75	0.90	0.75	–

sum of all systematic uncertainties assuming that the errors are all Gaussian:

$$\sigma_{\text{sys}}^2 = \sigma_{\text{Cross Term}}^2 + \sigma_{\text{Scale Length}}^2 + \sigma_{\text{Density Profile}}^2 + \sigma_{\text{Splitting Sample}}^2. \quad (4)$$

This total has been adopted to calculate error bars in Fig. 2. The latter (see red vertical error bars) corresponds to the quadratic sum of statistical errors with systematic uncertainties.

However, we note that the systematic uncertainty due to the neglected cross-term and that obtained after splitting the sample into two parts follow the same trend (compare the red-dotted with the green-dashed line in Fig. 4). A quite similar trend may be identified in Fig. 5 of Ou et al. (2023). This leads us to suspect that systematic uncertainties are overestimated by both studies.

3. Methods: MW mass models

3.1. Varying baryonic models for bulge and disc

The contribution of the baryonic components to the MW mass is still uncertain, and this may affect the determination of the DM distribution (Karukes et al. 2020; Jiao et al. 2021). The basic idea is to cope with uncertainties in baryons by using a very large grid of possible models. However, we are aware that some baryonic models may not be fully consistent with other important constraints from the vertical dynamics of the disc stars (Bovy & Rix 2013) or from microlensing (Wegg et al. 2016).

To verify how the baryonic mass distribution may affect the RC, we followed Jiao et al. (2021) in considering several possible combinations of models for the bulge and the disc presented by Iocco et al. (2015), all with baryonic mass smaller than $7 \times 10^{11} M_{\odot}$ ². In addition, we also considered the baryonic model B2 from de Salas et al. (2019), which includes neutral gas and dust components, and was used by Ou et al. (2023). Two triaxial density profiles E (Exponential-type) and G (Gaussian-type) for the bulge from Stanek et al. (1997) can be expressed as:

$$\begin{aligned} \text{E: } \rho_{\text{bulge}}(x, y, z) &= \rho_0 e^{-r} \\ \text{G: } \rho_{\text{bulge}}(x, y, z) &= \rho_0 e^{-r^2/2} \end{aligned} \quad (5)$$

² We notice that Model I of Pouliasis et al. (2017) used by Eilers et al. (2019) and Jiao et al. (2021) overestimates the bulge mass (Paola di Matteo, priv. comm.).

with:

$$r^2 = \frac{x^2}{x_b^2} + \frac{y^2}{y_b^2} + \frac{z^2}{z_b^2}, \quad (6)$$

where (x, y, z) are the coordinates along the major, intermediate, and minor axes. The bulge of B2 is modelled with a Hernquist potential:

$$\Phi(r) = -\frac{GM}{r + r_b}. \quad (7)$$

For the disc component, we adopted a double exponential as described below:

$$\rho(R, z) = \rho_0 \exp\left(-\frac{R}{L} - \frac{z}{H}\right), \quad (8)$$

where $\rho_0 = M/(4\pi HL^2)$ is the normalisation, M is the corresponding disc mass, and L and H are the disc scale length and height, respectively. Three-disc models (CM from Calchi Novati & Mancini 2011, dJ from de Jong et al. 2010 and J from Jurić et al. 2008) contain thin and thick discs. Model B2 possesses only a thin disc. The dust component and the gas distribution of B2 are also modelled as double exponential profiles (Eq. 8).

Tables 1 and 2 provide the various parameters adopted to represent the bulge and the disc of the MW.

3.2. Dark matter model for the halo

The Einasto profile (Einasto 1965; Retana-Montenegro et al. 2012) is widely used to describe the distributions of stellar light and of the mass of dark matter in galaxies, whose density is defined as:

$$\rho(r) = \rho_0 \exp\left[-\left(\frac{r}{h}\right)^{1/n}\right], \quad (9)$$

where n is the Einasto index, which can determine how fast the density decreases with r . Several studies (e.g. Chemin et al. 2011; Jiao et al. 2021) have shown that the Einasto profile gives a significantly better fit to the RCs when compared to the Navarro, Frenk & White profile (NFW; Navarro et al. 1997). In particular, Jiao et al. (2021) found that the three-parameter Einasto profile may account for a larger range of outer slopes and generate a plausible wide mass range. This is also supported by Ou et al. (2023) and Sylos Labini et al. (2023), who found the NFW profile unsuitable for reproducing the external slope of the MW RC. Therefore, the present study focuses on a spherical Einasto profile for modelling the MW RC.

Constraints on the shape of the dark matter halo in the Milky Way are weak and no consistent picture has yet emerged. However, at 20 kpc scales, Küpper et al. (2015) and Koposov et al. (2010) determined the flattening of the dark halo to be $q_z = 0.95 \pm 0.15$, that is, almost spherical. In the inner regions of the MW, the disc and bulge dominate the RC in that they contribute $\sim 85\%$ of the rotational velocity and $\sim 70\%$ of the rotational support at 2.2 disc scale lengths, i.e., where the disc velocities are maximal and therefore the disc is maximal (Sackett 1997). The wide variety of baryonic models used in this study allows us to test the hypothesis of the maximum disc and to resolve the debate over the core or cusp nature of the dark halo of our galaxy. It also allows us to test the NFW halo, which in any case cannot fit a decreasing RC.

The optical diameter of an external galaxy is often defined using the D_{25} isophote. This limit has been used to estimate the radius of the MW to 13.4 kpc (e.g. Goodwin et al. 1998). In the following, we obtain a radius that is almost twice as large.

Table 3. Measurements of the Circular Velocity of the Milky Way.

R [kpc]	V_c [km s $^{-1}$]	σ_{V_c} [km s $^{-1}$]
9.5	221.75	3.17
10.5	223.32	3.02
11.5	220.72	3.47
12.5	222.92	3.19
13.5	224.16	3.48
14.5	221.60	4.20
15.5	218.79	4.75
16.5	216.38	4.96
17.5	213.48	6.13
18.5	209.17	4.42
19.5	206.25	4.63
20.5	202.54	4.40
21.5	197.56	4.62
22.5	197.00	3.81
23.5	191.62	12.95
24.5	187.12	8.06
25.5	181.44	19.58
26.5	175.68	24.68

4. Results

4.1. Measurement of the rotation curve and comparison with Ou et al. (2023)

We report our final circular velocity in Table 3. Figure 5 shows our final circular velocity curve and one of our best fits with $n = 0.43$, $h = 11.41$ kpc, and $\rho_0 = 0.01992 M_\odot \text{ pc}^{-3}$ (see first line of Table 4). In our study, as well as in Ou et al. (2023), error bars account for systematic uncertainties. For $R \geq 13$ kpc, the two RCs are in reasonably good agreement except for one point at about 23 kpc (see Fig. 1). We suspect that this discrepancy is caused by the disagreement over the radial velocity component at $R \sim 23$ kpc, for which the top panel of Fig. 3 of Ou et al. (2023) shows a large deviation on $\sqrt{\langle v_R^2 \rangle}$. In the range of $R = 9\text{--}13$ kpc, our RC points are slightly lower than those of Ou et al. (2023), which is discussed in Appendix A.

The largest discrepancy between the RC of this paper and that of Ou et al. (2023) is perhaps related to the amplitude of the error bars, which are larger in this latter study (compare Fig. 4 with Fig. 5 of Ou et al. 2023).

Both RCs show a significant decline with increasing radius, which can be well approximated by a linear function (see Fig. 2):

$$V_c(R) = V(R_\odot) + \beta(R - R_\odot), \quad (10)$$

where R_\odot is the distance between the Sun and the Galactic centre³. We find that the slope of our declining RC is $\beta = -(2.18 \pm 0.23) \text{ km s}^{-1} \text{ kpc}^{-1}$, which is similar to the value of $\beta = -(2.22 \pm 0.20) \text{ km s}^{-1} \text{ kpc}^{-1}$ obtained by Ou et al. (2023)⁴.

Wang et al. (2023a) also split the Galactic region into two, one with galactic latitude $b > 0^\circ$ and the other with $b < 0^\circ$ (or

³ We note that $R_\odot = 8.34$ kpc for this RC and 8.178 kpc for RC of Ou et al. (2023).

⁴ In the present study, we accounted for the systematic uncertainties of Ou et al. (2023, see their Fig. 5) when deriving parameters from the corresponding RC. The values that cannot be seen in their Fig. 5 have been chosen to be 0.14.

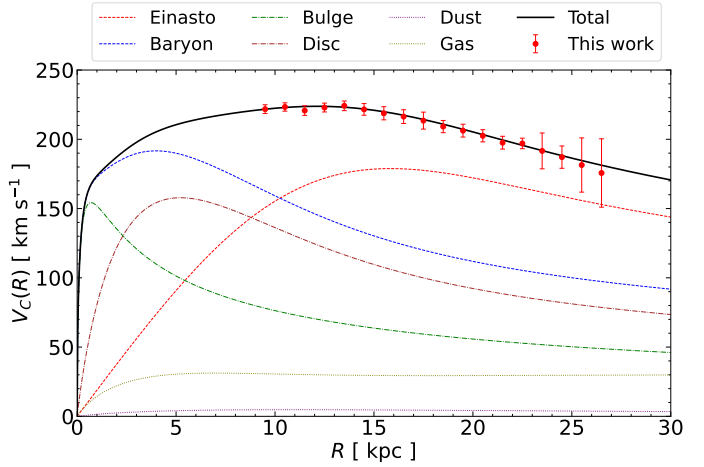


Fig. 5. Circular velocity of the Milky Way. The red data points are the measurements computed in this work; error bars include systematic uncertainties. The black solid line represents the sum of the baryonic and dark matter components: the baryonic model B2 (blue-dashed line), including its decomposition into baryonic components (bulge, disc, gas, and dust) and the best fit of the Einasto dark matter profile (red-dashed line).

one with $z > 0$ kpc and the other with $z < 0$ kpc) and found an uncertainty on the slope of RC of $\sim 20\%$.

4.2. Comparison with Zhou et al. (2023)

Figure 1 shows that the RC from Zhou et al. (2023) indicates larger velocities at the MW disc outskirts. In Appendix B, we compare the distances adopted by the present study to those adopted in other estimates (see Fig. B.1), which leads us to suspect that the distances by Zhou et al. (2023) are overestimated. After correcting for this, it appears that the Zhou et al. (2023) RC is consistent with both the RC of the present study and that from Ou et al. (2023). We also notice that Zhou et al. (2023) did not consider the impact of the cross-term when analysing systematic uncertainties. For consistency, we have not considered this study in the following.

4.3. Estimated range for the dynamical mass of the Milky Way

Using a Bayesian analysis, one can determine the posterior distribution of the model parameters based on the given data. In the present study, we applied the Markov chain Monte Carlo (MCMC) affine invariant sampler EMCEE⁵ (Foreman-Mackey et al. 2013) to test the parameter space of the Einasto profile using flat priors; that is, $M_0 = 4\pi h^3 \rho_0$, h , and $1/n$, from 10^{10} to $10^{14} M_\odot$, from 0 to 20, and from 0 to 5, respectively. Following previous studies, the sum of the logarithm of the likelihood for the observed RC can be derived as:

$$\ln \mathcal{L} = -\frac{1}{2} \sum_i \left(\frac{v_{\text{mod},i} - v_{\text{obs},i}}{\sigma_i} \right)^2 \quad (11)$$

where the summation i is done over all the data points, v_{mod} is the theoretical circular velocity from the MW models, v_{obs} is the measured circular velocity, and σ is the statistical uncertainty of the measurement (see Sect. 2.2).

⁵ <https://github.com/dfm/emcee>

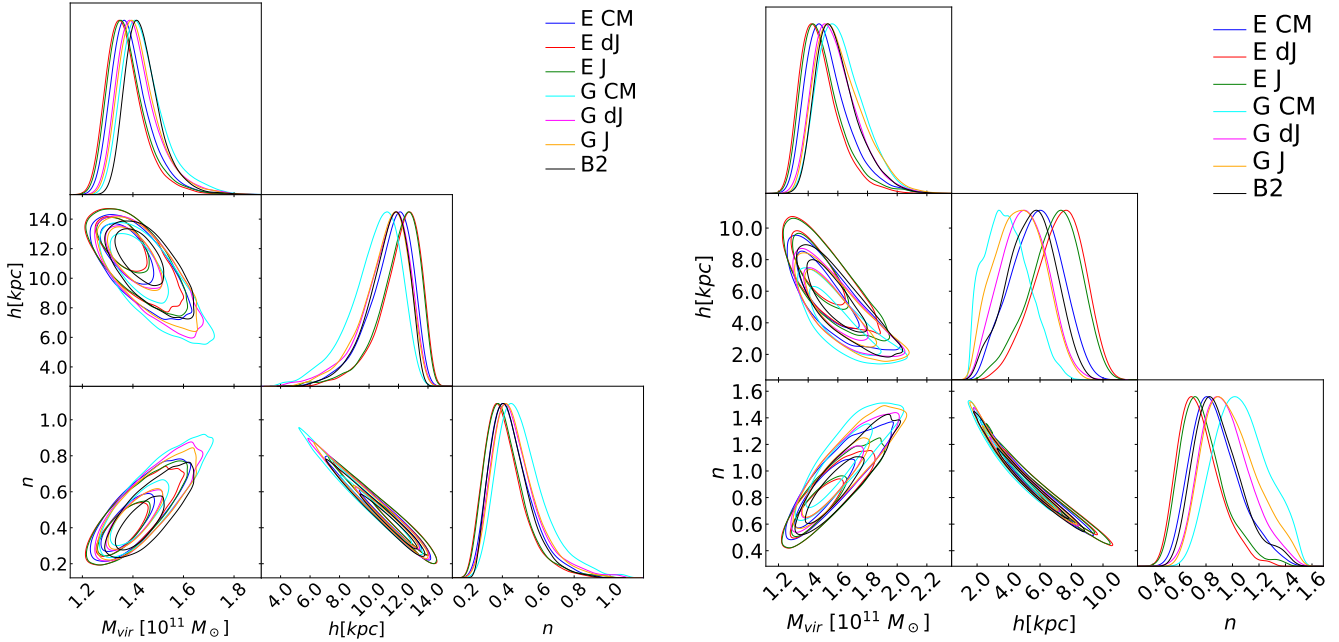


Fig. 6. MCMC tests of Einasto dark matter parameters with several baryonic models (represented by coloured lines) for our RC (right panel) and that of Ou et al. (2023) RC.

In the present study, we extrapolated the DM halo to the virial radius, denoted as R_{vir} , which encloses the virial or the DM contribution to the dynamical mass, M_{vir} . The virial radius is defined as the radius of a sphere within which the average density of dark matter is equal to 200 times the critical density of the Universe ρ_{cr} . Here, we adopted a critical density of $\rho_{\text{cr}} = 1.34 \times 10^{-7} M_{\odot} \text{ pc}^{-3}$ (Hinshaw et al. 2013).

In order to properly estimate the dynamical mass, we investigated various baryonic models, as described in Sect. 3.1. The posterior distributions for both RC fits with different baryonic models are given in Fig. 6. We note that we converted the parameters of the virial DM mass M_{vir} , scale length h , and Einasto index n .

We calculated the dynamical mass as the sum of the baryonic mass and the DM halo virial mass. Results are presented in Table 4. We find a MW dynamical mass of $1.99^{+0.09}_{-0.06} \times 10^{11} M_{\odot}$ at $R_{\text{vir}} = 121.03^{+1.80}_{-1.23} \text{ kpc}$ from the present work, which can be compared to the dynamical mass of $2.13^{+0.17}_{-0.12} \times 10^{11} M_{\odot}$ at $123.80^{+3.21}_{-2.37} \text{ kpc}$ using the RC of Ou et al. (2023). The local DM density is found in the range of 0.011 to $0.012 M_{\odot} \text{ pc}^{-3}$ (0.418 – $0.456 \text{ GeV cm}^{-3}$) for both RCs with different baryonic models. One may question the significance of such small error bars, given the fact that they lead to only very small values for the MW dynamical mass. On one hand, this is assuming that each point (and associated error bars) of the RC has been determined independently from the others, which is the underlying assumption of the MCMC method. This is likely true for the RC points, but not necessarily for the error bars, which may have led to an underestimation of the error bars on dynamical mass. On the other hand, error bars account for systematic uncertainties, and the latter may have been overestimated, as shown in Sect. 2.2.5.

We performed another test to evaluate the error bars of the MW dynamical mass. To this end, we arbitrarily replaced all the points of our RC by values provided by their upper error bars. By fitting these points with different baryonic models, we obtain dynamical masses ranging from 2.44 to $2.53 \times 10^{11} M_{\odot}$.

The latter value would correspond to an absolute upper limit for the MW dynamical mass. However, Fig. 7 shows that Ou et al. (2023) RC points have larger error bars than in our study. Performing the same exercise with these values, one would find total mass values from 3.8 to $5.4 \times 10^{11} M_{\odot}$. We consider the latter value as an absolute upper limit on the MW dynamical mass.

5. Discussion

5.1. The impact of asymmetric drift on the rotation curve measurement

We calculated the asymmetric drift following Eqs. (4.225), (4.227), and (4.228) (Strömberg's equation) in Binney & Tremaine (2008), and it could impact RCs. D23 provided velocities for RGB and OB stars that were not corrected for the asymmetric drift. Figure 7 compares the corresponding RCs to ours and that of Ou et al. (2023). This comparison shows that the non-corrected RGBs (magenta triangles) from D23 lag the corrected curves (see blue and red dots), which clearly illustrates the necessity of the asymmetric drift correction. OB stars (green triangles) are rotating faster, and as they rotate closer to the circular velocity, this would imply that both the correction in our study and that in Ou et al. (2023) are sufficient, at least for radii of greater than 10 kpc.

However, our correction does not seem entirely sufficient for $R < 10$ kpc, perhaps because of the unknown shape of the true density profile of the MW. This might also mean that the decrease in this region is even steeper than shown by the red and blue points. In the future, extending the very young star rotation curve towards inner disc regions, as well as to larger radii, may provide evidence supporting the decrease in the MW RC, and in particular might help to better determine the radius at which the decrease occurs.

Concerning systematic uncertainties introduced by the asymmetric drift, Ou et al. (2023, see their Fig. 5) showed that beyond 22 kpc, the asymmetric drift can contribute to relative systematic uncertainties at the level of 15%, which might cause the

Table 4. Estimated MW dynamical mass and associated Einasto profile parameters for the RC of the present work (TW) and for that of Ou et al. (2023, O23).

Baryon model	M_{bar} [$10^{11} M_{\odot}$]	M_{dyn} [$10^{11} M_{\odot}$]		M_0 [$10^{11} M_{\odot}$]		h [kpc]		n	
		TW	O23	TW	O23	TW	O23	TW	O23
B2	0.616	$2.05^{+0.08}_{-0.06}$	$2.19^{+0.17}_{-0.12}$	$3.72^{+0.45}_{-0.70}$	$1.23^{+0.63}_{-0.58}$	$11.41^{+1.15}_{-1.62}$	$5.5^{+1.46}_{-1.56}$	$0.43^{+0.12}_{-0.09}$	$0.87^{+0.20}_{-0.15}$
E dJ	0.607	$1.97^{+0.09}_{-0.06}$	$2.07^{+0.15}_{-0.11}$	$3.72^{+0.36}_{-0.63}$	$1.82^{+0.64}_{-0.72}$	$12.30^{+1.10}_{-1.63}$	$7.3^{+1.46}_{-1.74}$	$0.40^{+0.13}_{-0.09}$	$0.73^{+0.18}_{-0.14}$
E J	0.603	$1.97^{+0.09}_{-0.06}$	$2.08^{+0.16}_{-0.11}$	$3.72^{+0.36}_{-0.70}$	$1.70^{+0.65}_{-0.72}$	$12.21^{+1.12}_{-1.68}$	$7.03^{+1.49}_{-1.79}$	$0.40^{+0.13}_{-0.09}$	$0.76^{+0.19}_{-0.14}$
E CM	0.589	$1.97^{+0.09}_{-0.06}$	$2.10^{+0.17}_{-0.12}$	$3.55^{+0.43}_{-0.73}$	$1.26^{+0.69}_{-0.61}$	$11.63^{+1.20}_{-1.77}$	$5.81^{+1.58}_{-1.71}$	$0.43^{+0.14}_{-0.10}$	$0.85^{+0.21}_{-0.16}$
G dJ	0.575	$1.98^{+0.09}_{-0.07}$	$2.14^{+0.17}_{-0.12}$	$3.47^{+0.51}_{-0.78}$	$1.02^{+0.64}_{-0.52}$	$11.34^{+1.28}_{-1.86}$	$4.99^{+1.52}_{-1.54}$	$0.45^{+0.15}_{-0.10}$	$0.94^{+0.21}_{-0.17}$
G J	0.571	$1.98^{+0.09}_{-0.06}$	$2.15^{+0.19}_{-0.13}$	$3.39^{+0.50}_{-0.76}$	$0.89^{+0.62}_{-0.51}$	$11.29^{+1.26}_{-1.82}$	$4.72^{+1.60}_{-1.64}$	$0.45^{+0.14}_{-0.10}$	$0.97^{+0.24}_{-0.18}$
G CM	0.557	$1.99^{+0.10}_{-0.07}$	$2.16^{+0.18}_{-0.13}$	$3.31^{+0.58}_{-0.91}$	$0.64^{+0.56}_{-0.38}$	$10.63^{+1.40}_{-2.01}$	$3.85^{+1.52}_{-1.35}$	$0.49^{+0.16}_{-0.11}$	$1.06^{+0.23}_{-0.19}$
Average		$1.99^{+0.09}_{-0.06}$	$2.13^{+0.17}_{-0.12}$						

peculiar point around 23 kpc. Figure 8 of Wang et al. (2023a) shows that the declining slope is shared for stars selected at different heights, for which differences are most likely caused by the asymmetric drift effect. Points near and above $R = 24$ kpc might also be affected by the asymmetric drift systematic errors, which is similar to the findings of Ou et al. (2023) for their RC.

5.2. Does the Milky Way warp have a significant impact on the rotation curve measurement?

The MW has a warped disc. Observations show that the MW disc is flat out to roughly the Solar Circle, where it then bends upwards and downwards in the northern and southern hemispheres. The amplitude of the warp clearly increases with radius and varies with azimuthal angle. The position and kinematics of the Galactic warp also depend on the stellar populations (Poggio et al. 2018; Wang et al. 2020; Chrobáková et al. 2020a; Li et al. 2023).

Wang et al. (2020) analysed the stellar warp of different stellar populations by combining LAMOST DR4 and *Gaia* DR2. These authors concluded that the Galactic warp might not be caused by the gravitational interaction scenarios but by the gas infall process, and gravitational interactions such as that due to the Sgr passages are also addressed.

On the other hand, there has been no major merger in the MW for between 9 and 10 Gyr, which corresponds to the GSE event, as described in Sect. 1. Interactions with nearby dwarfs or satellites are not expected to have a great impact on disc stability, though Sgr passages near the disc edge have been suggested to have affected or even possibly formed the warp (Bailin 2003). Even in the latter case, if the Sgr main interaction with the disc occurred more than 5 Gyr ago, it is likely that the MW disc is in relative equilibrium (quasi-equilibrium within 30 kpc)⁶ with some oscillations. Those oscillating asymmetries on either side of the galactic plane are called corrugations. From a sample of 40 nearby low-inclination disc galaxies, Urrejola-Mora et al. (2022) identified that 20% of the galaxies exhibit vertically perturbed galactic discs, which could be described by corrugations. One of the most famous corrugations in the MW is

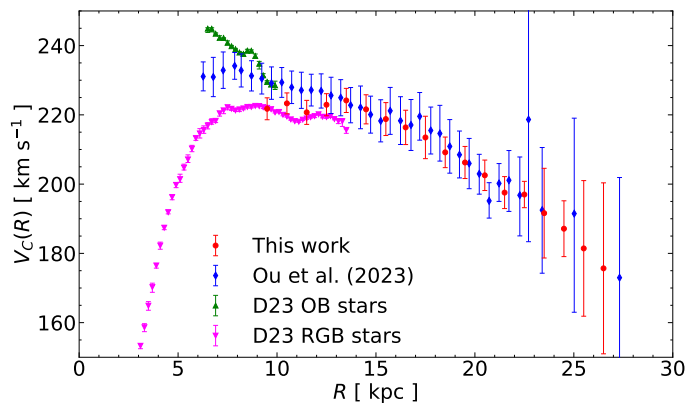


Fig. 7. Circular velocity of the Milky Way. The red (blue) data points are the measurements computed in the present work (and in Ou et al. 2023), with error bars including systematic uncertainties. These are compared with data points from D23 (OB: magenta triangles, and RGB: green triangles, stars) that have not been corrected for asymmetric drift.

the Monoceros Ring located at low Galactic latitudes. Although this is more likely to be explained by disc flaring (Wang et al. 2018; Bergemann et al. 2018), scenarios of a perturbed disc by an ancient disrupted dwarf galaxy have also been proposed (Conn et al. 2007, 2012; Johnston et al. 2017). Corrugations start from the Sun and at least four ripples are seen in the disc outskirts (Newberg et al. 2002; Ibata et al. 2003; Xu et al. 2015); these blur our representation of a flat disc and can produce wiggles in the RC that are different from those due to spiral arms.

Chrobáková et al. (2020b) used *N*-body simulations and found that the Jeans equation could provide a reasonable approximation to the system dynamics if the amplitude of the radial velocity component is significantly smaller than the azimuthal one. It is possible to assume an axisymmetric steady disc to measure the RC globally using the Jeans equation. In Fig. 1 (see Appendix A), we also compared the RC with different limits for the vertical heights and they show good consistency even in the outer disc. The warp could affect spatial and velocity measurements, and especially the vertical velocities, which are expected to be its main kinematic signature. In order to measure the effect of the vertical velocity, we analysed the neglected cross-term

⁶ At 30 kpc, a star rotating at 170 km s^{-1} would have the time to make 4.5 orbits, i.e. a sufficiently large number to consider the system to be at equilibrium (Gnedin & Ostriker 1999).

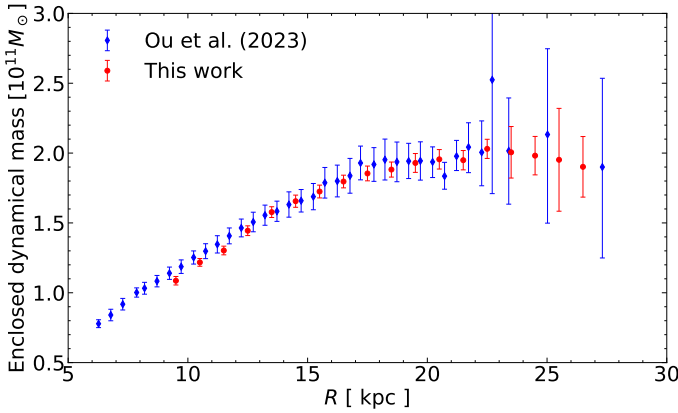


Fig. 8. Enclosed dynamical mass of the MW as a function of radius.

$\langle V_R V_z \rangle$ in detail (see Sect. 2.2.1). We also note that Wang et al. (2023a) applied LIM to the full *Gaia* DR3 data set with different stellar populations, which helps to reduce the warp impact because we know that the warp is much stronger for young populations.

5.3. Have we reached the Keplerian decline of the Milky Way rotation curve?

Our RC measurements based on *Gaia* DR3 (as well as that from Ou et al. 2023) demonstrate its significant decline. Additionally, the slope of the declining RC is steeper compared to the previous studies (Eilers et al. 2019; Mróz et al. 2019) based on *Gaia* DR2. This also implies that the increase in cumulative mass at larger radii is minimal. We apply an approximate conversion from the measured circular velocity to the enclosed dynamical mass using the following relation:

$$M_{\text{dyn},i} = \frac{v_{\text{circ},i}^2 R_i}{G}, \quad (12)$$

where G is the gravitational constant and $v_{\text{circ},i}$ is the circular velocity at each radius R_i . The conversion is not accurate in a non-spherical potential but the difference is very small at large radii, where the spherical DM component dominates (see Fig. 5). By applying Eq. (12), we determined that beyond $R > 19$ kpc, the enclosed mass barely varies (see Fig. 8), remaining within 1.9 to $2.0 \times 10^{11} M_\odot$, which is remarkably close to our estimate made at a significantly larger radius (see Table 4). The small decay of enclosed dynamical mass at large radii ($R > 23$ kpc) in Fig. 8 cannot be physical. However, given that the amplitude of the decay is much smaller than the error bars, it has no incidence on the validity of this work.

Given that the RC drops faster at large radii and because of the agreement between enclosed and virial masses, we conducted a test to assess whether or not the MW RC has reached a Keplerian decline beyond $R > 19$ kpc. In Fig. 9, we compare the Keplerian decline using the same enclosed mass at each radius beyond $R > 19$ kpc, which helps us to verify whether or not the MW RC at the outskirts can be fitted this way. Figure 9 displays the best fit for a Keplerian decline to the RCs from our measurement (top panel) and that of Ou et al. (2023, bottom panel), respectively. At large radii, this fits well with the two estimated RCs, suggesting that stellar rotation at the outskirts follows a Keplerian decline, which implies that the enclosed mass within a certain radius is sufficient to account for the observed velocities, without requiring an increase in mass at

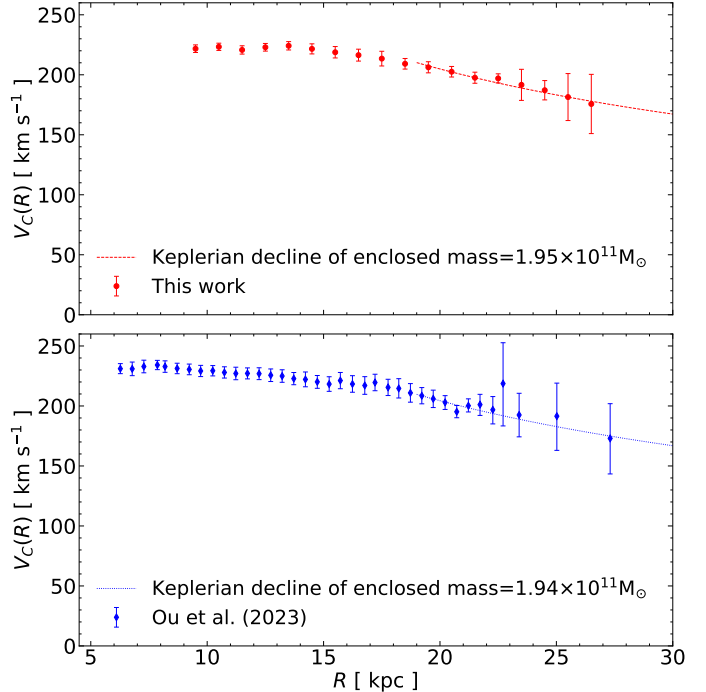


Fig. 9. Rotation curve with the best fit of the Keplerian decline for our RC measurement (top panel) and that from Ou et al. (2023, bottom panel).

larger radii. Interestingly, we find a consistent enclosed mass for the Keplerian decline in both RC measurements, which amounts to approximately $1.95 \times 10^{11} M_\odot$.

In order to further test for the presence of a Keplerian decline at large radii, we assumed a circular velocity profile following:

$$V(R) = AR^\gamma, \quad (13)$$

where A is an amplitude parameter, and γ is the exponential slope of the outer RC. The posterior distributions are presented in Fig. 10. By sampling γ using a flat prior between -10 and 5 , we found that the slope γ beyond $R > 19$ kpc is $-0.47^{+0.15}_{-0.15}$ and $-0.56^{+0.23}_{-0.22}$ for the RC of this work and that of Ou et al. (2023), respectively. This suggests that the MW RC is consistent with a Keplerian decline ($\gamma = -0.5$) at large radii, while a flat RC is rejected at a 3σ significance level (see green arrows in Fig. 10).

5.4. Comparison of the MW dynamical mass with that based on different mass tracers

The RC of the Milky Way is the most accurate tracer for estimating the enclosed dynamical mass within a range of approximately 30 kpc, because rotating stars in the disc are likely at equilibrium with the total potential associated with the enclosed dynamical mass. We note that our dynamical mass estimate is primarily constrained by the RC within the range of $R = 9$ – 27 kpc and is then extrapolated to the virial radius. The extrapolation is unlikely to bring an additional mass component, because the MW RC seems to follow a Keplerian decline at large radii.

Other estimates derived from stellar streams (Vasiliev et al. 2021; Koposov et al. 2023), globular clusters (Eadie & Jurić 2019; Posti & Helmi 2019), the Magellanic Cloud (Correa Magnus & Vasiliev 2022), or dwarf galaxies (Cautun et al. 2020; Li et al. 2020; Slizewski et al. 2022) provide virial masses

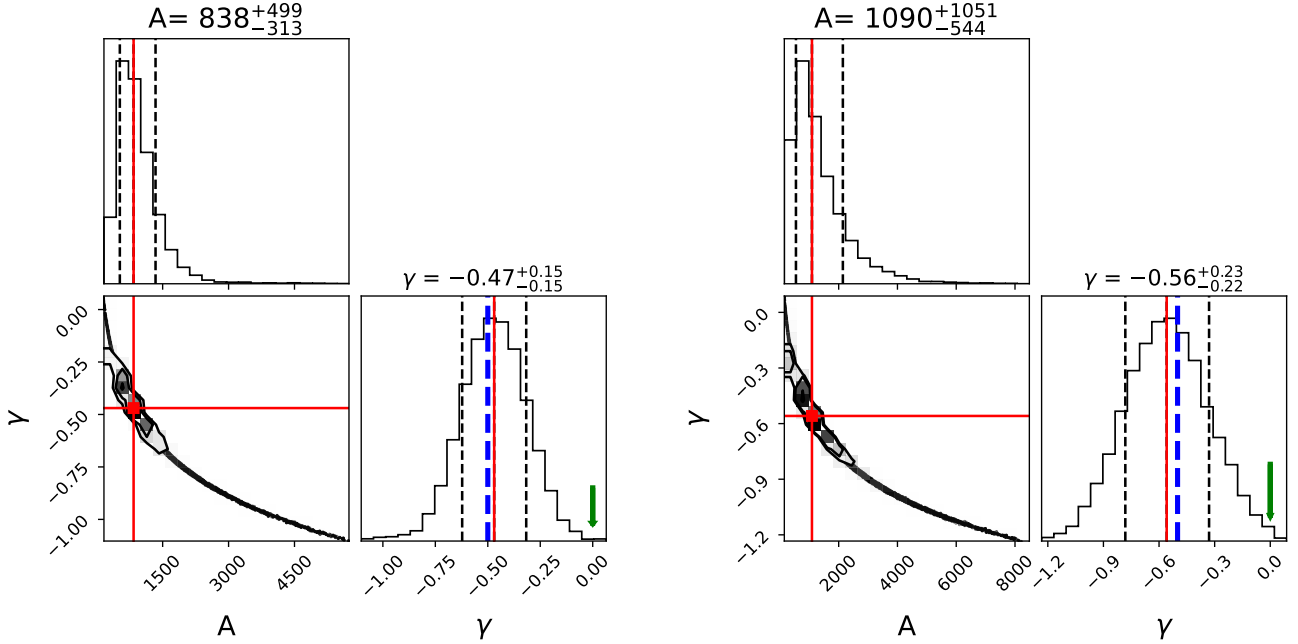


Fig. 10. Posterior distributions for the parameters A and γ . We show fits to the RC of this work (left panel) and to that of Ou et al. (2023, right panel) including systematics uncertainties. Histograms of parameters A and γ correspond to the maximum density distribution. Red solid lines represent the median of the posterior distributions. Black dashed lines correspond to 1σ uncertainty. Blue dashed lines correspond to the slope of the Keplerian decline, $n = -0.5$. Green arrows indicate the slope of a flat RC ($n = 0$).

ranging from 7 to $11 \times 10^{11} M_\odot$ at about 150 to 250 kpc. Our predicted virial mass from the MW RC is then considerably lower than these previous estimates.

However, the findings of recent studies of the orbital histories of halo inhabitants may challenge our previous understanding. Hammer et al. (2023) found that most dwarf galaxies are relative newcomers. This is due to the expected linear relationship between infall times and the logarithm of the total orbital energy (Rocha et al. 2012). As dwarf-galaxy orbital energies are larger than those of former events such as the GSE and the Sgr infall, they likely entered the MW halo less than 3 Gyr ago. Moreover, Li et al. (2021) found that the dwarf galaxies are highly concentrated near their pericentre. Consequently, the assumption of virial equilibrium for dwarf-galaxy orbital motions is likely invalid, and it is not surprising that one finds very large mass values when using these orbital motions as mass tracers for the MW. This is well illustrated by Boylan-Kolchin et al. (2013) who showed that assuming Leo I as a bound satellite would lead to a significant overestimate of the MW mass.

After using both globular clusters and the MW RC from *Gaia* DR2, Wang et al. (2022b) found that excluding Crater and Pyxis, which possess large amounts of orbital energy, leads to a decrease in the MW mass estimate from $5.73^{+0.76}_{-0.58} \times 10^{11} M_\odot$ to $5.36^{+0.81}_{-0.68} \times 10^{11} M_\odot$ when assuming an Einasto profile.

These recent findings highlight the fact that our understanding of the MW structure is changing. They also emphasise the need to verify whether or not various tracers have their orbital velocity in equilibrium with the MW potential in order to avoid systematic overestimates of the total mass.

5.5. Is our Galaxy exceptional or is its rotation curve related to the *Gaia* methodology used to recover it?

We investigated the literature on searching for declining spiral galaxy RCs to find out whether or not some of them

may show a Keplerian decline. In reviewing galaxy discs, van der Kruit & Freeman (2011) mentioned that none spiral galaxies show a decline in their RCs, which can be associated with a cut-off in the mass distribution, so that in no case has the RC been traced to the limit of the dark matter distribution. In their analysis of well-studied spirals from the THINGS project, de Blok et al. (2008) found that a declining RC such as that of M 81 is likely caused by galaxy interactions.

Noordermeer et al. (2007, see also Zobnina & Zasov 2020) specifically studied spirals with a declining RC and found no RCs with a fully Keplerian decline in the outer regions, indicating that we have not yet reached the point where the mass density becomes negligible, except perhaps for UGC 4458 (NGC 2599). However, the latter shows a bright UV nucleus that may be active, and its disc morphology also appears quite different from that of the MW. Dicaire et al. (2008) identified NGC 7793 as a possible candidate for exhibiting a Keplerian decline; its DM content is surprisingly low for a dwarf galaxy, and is smaller than that of stars at all radii.

The MW may indeed be relatively exceptional if it is the only isolated grand-design spiral showing a Keplerian decline in its RC, which is consistent with a possible cut-off of its mass distribution. One might wonder whether or not this declining RC is related to its four-arm structure discovered by Georgelin & Georgelin (1976). Four-armed spirals are rare in nearby Milky Way-type galaxies, although galaxies with two arms frequently exhibit bifurcations resulting in several arm segments, which could also be the case for the Milky Way.

Alternatively, our Galaxy may be exceptional due to its relatively quiet past history (Hammer et al. 2007; Belokurov et al. 2018; Haywood et al. 2018), having experienced no major merger for ~ 9 Gyr. We must also consider the possibility that the methodology used by *Gaia* to recover its full 6D space-velocity parameters for very large numbers of stars may be a contributing factor to the exceptional nature of the RC we obtain based on

these data; it certainly contrasts with the less constrained RC of external galaxies.

6. Conclusions

Gaia DR3 has led to significant progress in our capacity to estimate the MW RC when compared to *Gaia* DR2. Three different studies have derived the RC of the MW: One used the whole and very large *Gaia* DR3 catalogue with distances estimated from parallaxes, and then averaged into specific 6D cells using LIM (Wang et al. 2023a). The second (Ou et al. 2023) is based on a smaller number of RGB stars (33 335), for which distances are estimated from spectrophotometry. The third (Zhou et al. 2023) is based on 58 000 bright RGB stars, and in the present study we re-evaluated their distance estimates, rendering their RC consistent with that of the two other studies.

Here, we carried out a full analysis of the systematic uncertainties that can affect the Wang et al. (2023a) study. We then compared the different RCs from *Gaia* DR3, and find that they have consistent rotational velocity values from 9 to 27 kpc. This indicates a robust and significant decline of the MW RC, with a slope of $\beta = -(2.18 \pm 0.23) \text{ km s}^{-1} \text{ kpc}^{-1}$, which is based on combining the very similar slopes from this study and that from Ou et al. (2023). The decrease in velocity between 19.5 and 26.5 kpc is approximately 30 km s^{-1} .

The estimated MW dynamical mass is consistent with $1.99_{-0.06}^{+0.09} \times 10^{11} M_\odot$ at $121.03_{-1.23}^{+1.80}$ kpc (from the RC of this study) and with $2.13_{-0.12}^{+0.17} \times 10^{11} M_\odot$ at $123.80_{-2.37}^{+3.21}$ kpc (from the RC of Ou et al. 2023, respectively)⁷. The relatively small size of the error bars is perhaps a result of the assumption that the two RC points and their associated error bars were independently determined.

Consequently, the ratio of DM to baryonic mass is only a factor of about 3, instead of a factor of approximately 6 from Λ CDM (Planck Collaboration VI 2020), which suggests that baryons are not missing in our Galaxy. A small dynamical mass for the MW may also impact mass estimations for the LMC, which is mostly constrained by its ratio to that of the MW; for example, when studying the induced sloshing of the Galactic halo (Erkal et al. 2021; Conroy et al. 2021). If the total MW mass is as small as $2.06 \times 10^{11} M_\odot$, the LMC total mass would be from 2 to $3 \times 10^{10} M_\odot$. Interestingly, the latter value is consistent with the modelling of the Magellanic Stream through ram pressure as shown by Hammer et al. (2015) and Wang et al. (2019, see also LMC mass predictions from Wang et al. 2022a), which would resolve the numerous difficulties in reproducing it with tidal tail models (Besla et al. 2012; Lucchini et al. 2020, 2021).

We conclude that the MW RC cannot be consistent with a flat RC at a significance of 3σ , and that our findings suggest a Keplerian decline occurring at radii of greater than 19 kpc. The Keplerian decline indicates the point where the mass density becomes negligible (Zobnina & Zasov 2020). Some spiral galaxies present a declining RC, but at large radii they appear to flatten out, meaning that their RC has not been traced to the outermost extent of the dark matter distribution (de Blok et al. 2008; van der Kruit & Freeman 2011). This contrasts with the MW, whose accretion history (Hammer et al. 2023, and references therein) shows no major merger for 8 to 10 Gyr, while half of the spiral galaxies underwent their last major merger more recently (Hammer et al. 2005, 2009; Puech et al. 2012). It would

be interesting to study the impact of relatively recent assembly events on the RC at the outskirts of spiral galaxies.

In many respects, a Keplerian decline for the MW RC may appear quite exceptional. This could be due to the extraordinarily quiet history of our Galaxy, or to the very different methodology used by *Gaia* to calculate its kinematics compared to that used to study external galaxies.

Acknowledgements. We thank the anonymous referee for their comments and suggestions. Y.-J.J. acknowledges financial support from the China Scholarship Council (CSC) No. 202108070090. J.-L.W. is also grateful to be supported by the CSC No. 202210740004. L.C. acknowledges the Chilean Agencia Nacional de Investigación y Desarrollo through the grant Fondecyt Regular 1210992. We are grateful to Chrobáková Žofia, López-Corredoira Martín and Francesco Sylos Labini for their invaluable assistance in producing the datasets and tests of Wang et al. (2023a). We thank Yang Huang for sharing their data from Zhou et al. (2023). We are grateful for the support of the International Research Program Tianguan, which is an agreement between the CNRS in France, NAOC, IHEP, and the Yunnan Univ. in China. The data underlying this article will be shared on request to the corresponding author.

References

- Babcock, H. W. 1939, *Lick Obs. Bull.*, **498**, 41
- Bailin, J. 2003, *ApJ*, **583**, L79
- Belokurov, V., Erkal, D., Evans, N. W., Koposov, S. E., & Deason, A. J. 2018, *MNRAS*, **478**, 611
- Bergemann, M., Sesar, B., Cohen, J. G., et al. 2018, *Nature*, **555**, 334
- Besla, G., Kallivayalil, N., Hernquist, L., et al. 2012, *MNRAS*, **421**, 2109
- Binney, J., & Tremaine, S. 2008, *Galactic Dynamics: Second Edition* (Princeton: Princeton University Press)
- Bosma, A. 1978, PhD Thesis, University of Groningen, The Netherlands
- Bovy, J., & Rix, H.-W. 2013, *ApJ*, **779**, 115
- Boylan-Kolchin, M., Bullock, J. S., Sohn, S. T., Besla, G., & van der Marel, R. P. 2013, *ApJ*, **768**, 140
- Calchi Novati, S., & Mancini, L. 2011, *MNRAS*, **416**, 1292
- Cautun, M., Benítez-Llambay, A., Deason, A. J., et al. 2020, *MNRAS*, **494**, 4291
- Chemin, L., de Blok, W. J. G., & Mamon, G. A. 2011, *AJ*, **142**, 109
- Chrobáková, Ž., Nagy, R., & López-Corredoira, M. 2020a, *A&A*, **637**, A96
- Chrobáková, Ž., López-Corredoira, M., Sylos Labini, F., Wang, H. F., & Nagy, R. 2020b, *A&A*, **642**, A95
- Conn, B. C., Lane, R. R., Lewis, G. F., et al. 2007, *MNRAS*, **376**, 939
- Conn, B. C., Noël, N. E. D., Rix, H.-W., et al. 2012, *ApJ*, **754**, 101
- Conroy, C., Naidu, R. P., Garavito-Camargo, N., et al. 2021, *Nature*, **592**, 534
- Correa Magnus, L., & Vasiliev, E. 2022, *MNRAS*, **511**, 2610
- de Blok, W. J. G., Walter, F., Brinks, E., et al. 2008, *AJ*, **136**, 2648
- de Jong, J. T. A., Yanny, B., Rix, H.-W., et al. 2010, *ApJ*, **714**, 663
- de Salas, P. F., Malhan, K., Freese, K., Hattori, K., & Valluri, M. 2019, *JCAP*, **2019**, 037
- Dicaire, I., Carignan, C., Amram, P., et al. 2008, *AJ*, **135**, 2038
- Eadie, G., & Jurić, M. 2019, *ApJ*, **875**, 159
- Eilers, A.-C., Hogg, D. W., Rix, H.-W., & Ness, M. K. 2019, *ApJ*, **871**, 120
- Einasto, J. 1965, *Trudy Astrofizicheskogo Instituta Alma-Ata*, **5**, 87
- Erkal, D., Deason, A. J., Belokurov, V., et al. 2021, *MNRAS*, **506**, 2677
- Foreman-Mackey, D., Hogg, D. W., Lang, D., & Goodman, J. 2013, *PASP*, **125**, 306
- Gaia Collaboration (Drimmel, R., et al.) 2023a, *A&A*, **674**, A37
- Gaia Collaboration (Vallenari, A., et al.) 2023b, *A&A*, **674**, A1
- Georgelin, Y. M., & Georgelin, Y. P. 1976, *A&A*, **49**, 57
- Gnedin, O. Y., & Ostriker, J. P. 1999, *ApJ*, **513**, 626
- Goodwin, S. P., Gribbin, J., & Hendry, M. A. 1998, *The Observatory*, **118**, 201
- Hammer, F., Flores, H., Elbaz, D., et al. 2005, *A&A*, **430**, 115
- Hammer, F., Puech, M., Chemin, L., Flores, H., & Lehnert, M. D. 2007, *ApJ*, **662**, 322
- Hammer, F., Flores, H., Puech, M., et al. 2009, *A&A*, **507**, 1313
- Hammer, F., Yang, Y. B., Flores, H., Puech, M., & Fouquet, S. 2015, *ApJ*, **813**, 110
- Hammer, F., Li, H., Mamon, G. A., et al. 2023, *MNRAS*, **519**, 5059
- Haywood, M., Di Matteo, P., Lehnert, M. D., et al. 2018, *ApJ*, **863**, 113
- Helmi, A., Babusiaux, C., Koppelman, H. H., et al. 2018, *Nature*, **563**, 85
- Hinshaw, G., Larson, D., Komatsu, E., et al. 2013, *ApJS*, **208**, 19
- Hogg, D. W., Eilers, A.-C., & Rix, H.-W. 2019, *AJ*, **158**, 147
- Ibata, R. A., Irwin, M. J., Lewis, G. F., Ferguson, A. M. N., & Tanvir, N. 2003, *MNRAS*, **340**, L21

⁷ We note that the two estimates are very similar and the average value would be $2.06_{-0.13}^{+0.24} \times 10^{11} M_\odot$.

- Iocco, F., Pato, M., & Bertone, G. 2015, *Nat. Phys.*, **11**, 245
- Jiao, Y., Hammer, F., Wang, J. L., & Yang, Y. B. 2021, *A&A*, **654**, A25
- Johnston, K. V., Price-Whelan, A. M., Bergemann, M., et al. 2017, *Galaxies*, **5**, 44
- Jurić, M., Ivezić, Ž., Brooks, A., et al. 2008, *ApJ*, **673**, 864
- Karukes, E. V., Benito, M., Iocco, F., Trotta, R., & Geringer-Sameth, A. 2020, *JCAP*, **2020**, 033
- Koposov, S. E., Rix, H.-W., & Hogg, D. W. 2010, *ApJ*, **712**, 260
- Koposov, S. E., Erkal, D., Li, T. S., et al. 2023, *MNRAS*, **521**, 4936
- Küpper, A. H. W., Balbinot, E., Bonaca, A., et al. 2015, *ApJ*, **803**, 80
- Laporte, C. F. P., Johnston, K. V., Gómez, F. A., Garavito-Camargo, N., & Besla, G. 2018, *MNRAS*, **481**, 286
- Li, Z.-Z., Qian, Y.-Z., Han, J., et al. 2020, *ApJ*, **894**, 10
- Li, H., Hammer, F., Babusiaux, C., et al. 2021, *ApJ*, **916**, 8
- Li, X., Wang, H.-F., Luo, Y.-P., et al. 2023, *ApJ*, **943**, 88
- Lindgren, L., Bastian, U., Biermann, M., et al. 2021a, *A&A*, **649**, A4
- Lindgren, L., Klioner, S. A., Hernández, J., et al. 2021b, *A&A*, **649**, A2
- Lucchini, S., D’Onghia, E., Fox, A. J., et al. 2020, *Nature*, **585**, 203
- Lucchini, S., D’Onghia, E., & Fox, A. J. 2021, *ApJ*, **921**, L36
- Lucy, L. B. 1974, *AJ*, **79**, 745
- Lundmark, K. 1925, *MNRAS*, **85**, 865
- Mayall, N. U. 1951, *Pub. Mich. Obs.*, **10**, 19
- Mróz, P., Udalski, A., Skowron, D. M., et al. 2019, *ApJ*, **870**, L10
- Navarro, J. F., Frenk, C. S., & White, S. D. M. 1997, *ApJ*, **490**, 493
- Newberg, H. J., Yanny, B., Rockosi, C., et al. 2002, *ApJ*, **569**, 245
- Noordermeer, E., van der Hulst, J. M., Sancisi, R., Swaters, R. S., & van Albada, T. S. 2007, *MNRAS*, **376**, 1513
- Ou, X., Eilers, A. C., Necib, L., & Frebel, A. 2023, ArXiv e-prints [arXiv:2303.12838]
- Planck Collaboration VI. 2020, *A&A*, **641**, A6
- Poggio, E., Drimmel, R., Lattanzi, M. G., et al. 2018, *MNRAS*, **481**, L21
- Posti, L., & Helmi, A. 2019, *A&A*, **621**, A56
- Pouliasis, E., Di Matteo, P., & Haywood, M. 2017, *A&A*, **598**, A66
- Puech, M., Hammer, F., Hopkins, P. F., et al. 2012, *ApJ*, **753**, 128
- Queiroz, A. B. A., Anders, F., Chiappini, C., et al. 2023, *A&A*, **673**, A155
- Retana-Montenegro, E., van Hese, E., Gentile, G., Baes, M., & Frutos-Alfaro, F. 2012, *A&A*, **540**, A70
- Rocha, M., Peter, A. H. G., & Bullock, J. 2012, *MNRAS*, **425**, 231
- Rubin, V. C., Ford, W. K., Jr., & Thonnard, N. 1978, *ApJ*, **225**, L107
- Sackett, P. D. 1997, *ApJ*, **483**, 103
- Schmidt, M. 1965, in *Galactic Structure*, eds. A. Blaauw, & M. Schmidt (Chicago: University of Chicago Press), 513
- Slizewski, A., Dufresne, X., Murdock, K., et al. 2022, *ApJ*, **924**, 131
- Sofue, Y., Honma, M., & Omodaka, T. 2009, *PASJ*, **61**, 227
- Stanek, K. Z., Udalski, A., Szymański, M., et al. 1997, *ApJ*, **477**, 163
- Sylos Labini, F., Chrobáková, Ž., Capuzzo-Dolcetta, R., & López-Corredoira, M. 2023, *ApJ*, **945**, 3
- Urrejola-Mora, C., Gómez, F. A., Torres-Flores, S., et al. 2022, *ApJ*, **935**, 20
- van der Kruit, P. C., & Freeman, K. C. 2011, *ARA&A*, **49**, 301
- Vasiliev, E., Belokurov, V., & Erkal, D. 2021, *MNRAS*, **501**, 2279
- Wang, J., Shi, J., Pan, K., et al. 2016, *MNRAS*, **460**, 3179
- Wang, H.-F., Liu, C., Xu, Y., Wan, J.-C., & Deng, L. 2018, *MNRAS*, **478**, 3367
- Wang, J., Hammer, F., Yang, Y., et al. 2019, *MNRAS*, **486**, 5907
- Wang, H. F., López-Corredoira, M., Huang, Y., et al. 2020, *ApJ*, **897**, 119
- Wang, J., Hammer, F., & Yang, Y. 2022a, *MNRAS*, **515**, 940
- Wang, J., Hammer, F., & Yang, Y. 2022b, *MNRAS*, **510**, 2242
- Wang, H.-F., Chrobáková, Ž., López-Corredoira, M., & Sylos Labini, F. 2023a, *ApJ*, **942**, 12
- Wang, J., Cao, Z., Huang, Y., & Yuan, H. 2023b, *Res. Astron. Astrophys.*, **23**, 025020
- Wegg, C., Gerhard, O., & Portail, M. 2016, *MNRAS*, **463**, 557
- Xu, Y., Newberg, H. J., Carlin, J. L., et al. 2015, *ApJ*, **801**, 105
- Zhou, Y., Li, X., Huang, Y., & Zhang, H. 2023, *ApJ*, **946**, 73
- Zobnina, D. I., & Zasov, A. V. 2020, *Astron. Rep.*, **64**, 295

Appendix A: The impact of the z selection on the RC between 9 and 13 kpc

Figure A.1 indicates that by limiting the Wang et al. (2023a) data to $|z| < 1$ kpc, their RC from 9 to 13 kpc becomes consistent with that of Ou et al. (2023).

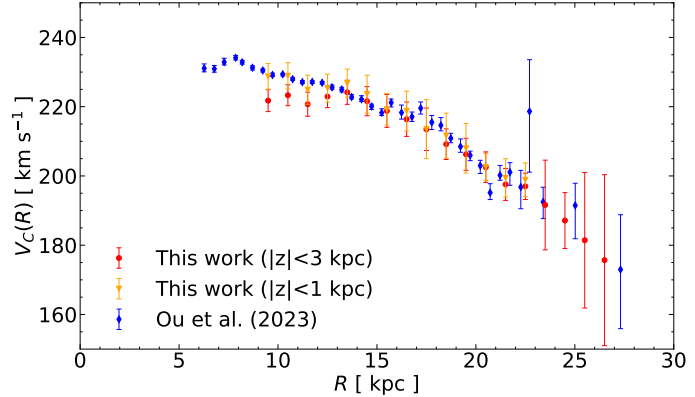


Fig. A.1. Comparison of the RC using different selections in the vertical direction.

Appendix B: Comparison of distance estimates

Figure B.1 compares the distance estimates by Zhou et al. (2023) with those of three different methods on the APOGEE data. One is a modified version of Wang et al. (2016), in which *Gaia* EDR3 parallax has been incorporated as a prior to constrain stellar distances as described in Wang et al. (2023b). Other distance estimates are from Hogg et al. (2019), which were used by Eilers et al. 2019), and from the results of StarHorse

(Queiroz et al. 2023). This comparison shows that Zhou et al. (2023) always overestimate distances for $R > 10$ kpc stars. To evaluate the consequences of such a bias, Figure B.2 provides a very rough analysis by correcting each Zhou et al. (2023) RC point accordingly, which suffices to reconcile their RC with those from this study and from Ou et al. (2023). However, a better analysis, where the distances are corrected for individual stars, is still needed.

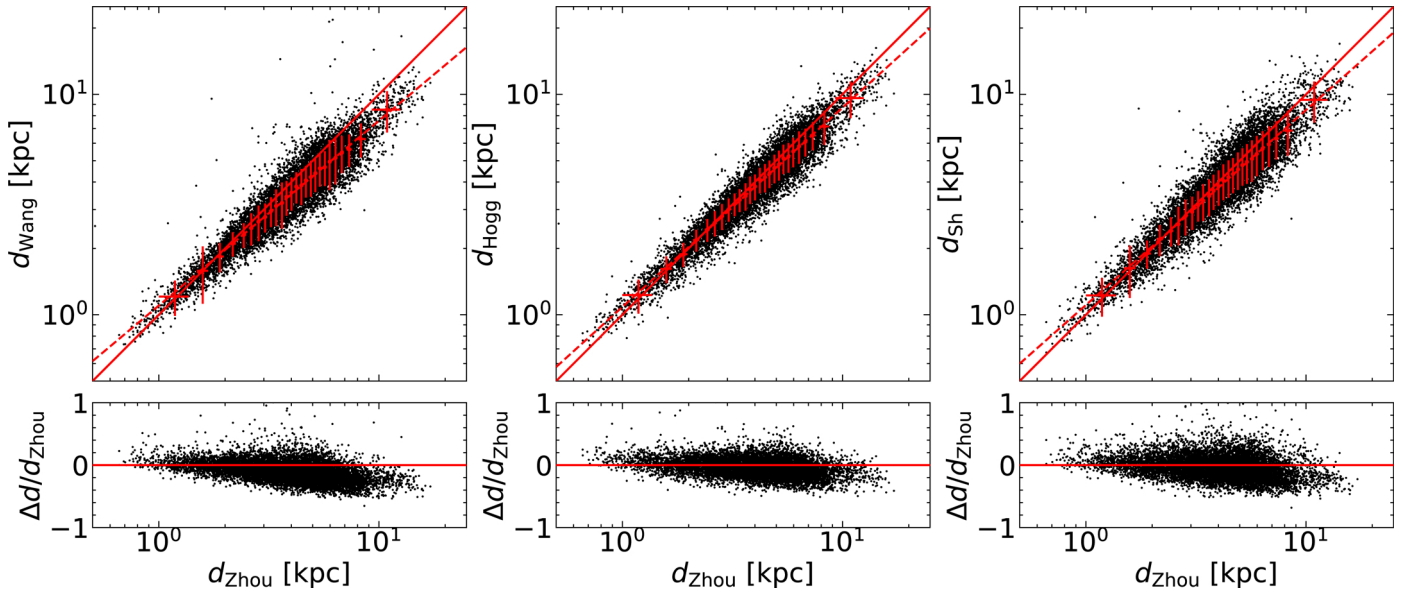


Fig. B.1. Comparison of distance estimates made by Zhou et al. (2023) to those made by Wang et al. (2016), Hogg et al. (2019), and StarHorse (Queiroz et al. 2023) in the top panels, respectively. The solid line presents a one-to-one correspondence. The dashed line presents the best linear fit on the logarithmic scale. Red points and error bars indicate the median and standard deviation per 400 data points. The ratios $\Delta d/d_{\text{zhou}}$ are shown in the bottom panels.

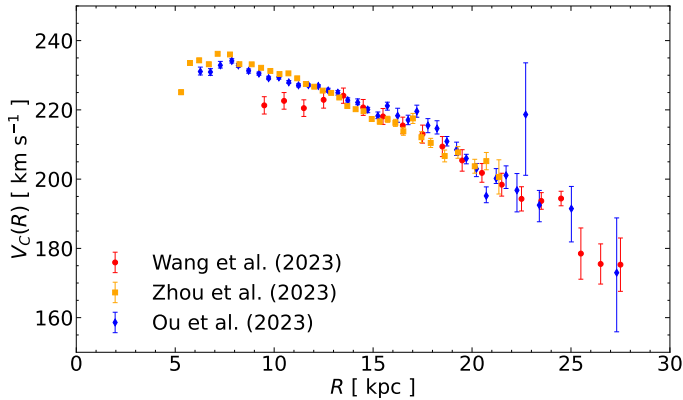


Fig. B.2. Comparison of RCs after a rough correction of the distance applied to the points from Zhou et al. (2023, see text).

Chapitre 3

Nearby Spiral Galaxies

Contents

1	Introduction	75
2	Galaxy sample	76
3	Studies of NGC 3521	79
3.1	Morphology of NGC 3521	79
3.2	Kinematics	81
3.3	Ionized properties of NGC 3521	83
3.4	Stellar population of NGC 3521	85
4	Hydrodynamical simulations	91
4.1	Comparison of HI observation	91
4.2	Comparison of position-velocity diagram	95
4.3	Analysis of rotation curve from mock HI observation	96
5	Discussion	98
5.1	Could we consider NGC 3521 experienced a recent major merger?	98
5.2	Other galaxies	100

1 Introduction

By modeling and analyzing H α (and other emission lines) and H I observation with sufficient spatial resolution from nearby galaxies, it is possible to derive the rotation curves (RCs) for both the inner and outer regions of these galaxies. The flat RCs observed in spiral galaxies have long been considered one of the most convincing evidence for the presence of dark matter (DM). However, with the data release from the *Gaia* mission, the RC of the MW has exhibited a distinct decline. Eilers et al. (2019) and Mróz et al. (2019), using data from *Gaia* DR2, reported a slightly declining RC for the MW. This finding has been confirmed by subsequent studies based on *Gaia* DR3 data (Wang et al., 2023; Zhou et al., 2023; Jiao et al., 2023; Ou et al., 2024). Moreover, Jiao et al. (2023) proposed that the MW RC beyond 19 kpc follows a Keplerian decline. This apparent inconsistency prompted me to reconsider the validity of the flat RCs observed in spiral galaxies.

Most spiral galaxies experienced their last major mergers on average 6 Gyr ago (Chapter 1, Section 3.3). Since stars or gas typically require 3-5 orbits to reach virial equilibrium after a significant perturbation (Gnedin & Ostriker, 1999), it becomes essential to examine the impact of a recent major merger on the RCs of nearby spiral galaxies. For example, the last major merger in the MW, Gaia-Sausage-Enceladus (GSE), occurred approximately 8-10 Gyr ago (Belokurov et al., 2018; Haywood et al., 2018; Helmi et al., 2018). Consequently, even the outskirts of the MW disk may have already reached equilibrium. In contrast, M31 experienced a more recent major merger, approximately 2-3 Gyr ago (Hammer et al., 2018a). Given the 3-5 orbit timescale, only the stars and gas within about 20 kpc of M31 are likely to have reached equilibrium, while the outer disk may still be in the process of virializing. This process could explain the flat or even rising behavior observed in the M31 RC beyond 20 kpc (Corbelli et al., 2010; Chemin et al., 2011).

To derive the circular velocity at large radii using three-dimensional coordinates, i.e., the line-of-sight (LOS) velocity and its projection on the sky, it is necessary to assume that the gas is in equilibrium and follows circular motion. By applying corrections for position angle (P.A.) and inclination (i), the circular velocity can be obtained from the LOS velocity. However, non-circular motions may arise due to the most recent major merger, potentially leading to biases in the derived circular velocities. In this chapter, we investigate the influence of recent major mergers on the RCs of nearby galaxies. Section 2 introduces the galaxy sample, with NGC 3521 serving as the primary example in the main text, while additional galaxies are discussed in the appendix. In Section 3, I present the morphological and kinematic characteristics of NGC 3521, along with the approach used to estimate the timing of its last major merger. Section 4 compares our results with hydrodynamical simulations. Finally, in Section 5, I discuss the implications of our results.

2 Galaxy sample

The SPARC (*Spitzer* Photometry and Accurate Rotation Curves, Lelli et al., 2016) database includes 175 late-type galaxies that cover a broad range of surface brightness (4 dex) and luminosity (5 dex). Their luminosity profiles are well characterized by *Spitzer* photometry at 3.6 μm . Stellar population synthesis (SPS) models indicate that the mass-to-light ratio (γ_*) remains relatively constant across different star formation histories in the near-infrared bands (e.g., McGaugh & Schombert, 2014; Meidt et al., 2014). As a result, the stellar mass distributions can be accurately derived using *Spitzer* data, offering a robust method for addressing the disc-halo degeneracy. The combination of a wide range of galaxy luminosities, *Spitzer* near-infrared photometry, RCs, and the relatively large sample size makes SPARC an ideal resource for studying the properties of DM haloes and their relationships with galactic disks

The SPARC database does not provide new H I observations. In some cases, it incorporates relatively older data, leading to lower spatial resolution compared to more recent observations at large radii. Lelli et al. (2016) noted that RCs derived from THINGS (The H I Nearby Galaxy Survey, de Blok et al., 2008) and LITTLE-THINGS (Local Irregulars That Trace Luminosity Extremes-The H I Nearby Galaxy Survey, Oh et al., 2015) exhibit numerous small-scale bumps and wiggles, which are less apparent in other RC datasets. These small-scale variations are unlikely to trace the smooth, axisymmetric gravitational potential and may instead result from non-circular motions, such as streaming along spiral arms (e.g., Khoperskov & Bertin, 2015). By contrast, SPARC RCs tend to be smoother, often displaying large-scale features that correspond directly to features in the surface brightness profile. They argued that SPARC database aligns with Renzo's rule (Sancisi, 2004), which states: "For any feature in the luminosity profile, there is a corresponding feature in the RC, and vice versa."

However, the small-scale wiggles and bumps may correspond to non-equilibrium structures, which can arise not only from minor perturbations but also from remnants of the most recent major merger. To supplement the H I RC data, we also used the THINGS database (Walter et al., 2008), which contains high spatial resolution H I observations for 34 nearby galaxies. These galaxies were observed using the Very Large Array (VLA) in its B, C, and D configurations. The H I data, along with detailed descriptions of the data reduction process, have been thoroughly documented in previous publications from the THINGS series (see, e.g., Walter et al., 2008).

We selected 9 galaxies from the SPARC and THINGS databases based on the following criteria: (1) the galaxy's inclination angle is greater than 30 degrees, (2) H I data are available from the THINGS database, and (3) the galaxy has a quality flag of 1 in the SPARC database. The selected galaxies are NGC 2403, NGC 2841, NGC 2903, NGC 3198, NGC 3521, NGC 5055, NGC 6946, NGC 7331, and NGC 7793. The H I data for these galaxies are sourced from the THINGS database. A summary of the selected galaxy sample is presented in [Table 3.1](#).

The luminosities of the selected galaxies are derived from *Spitzer* photometry at 3.6 μm , as provided by the SPARC database. The half-light radii are also taken from the SPARC database, based on their 3.6 μm data. Distances to the galaxies are taken from the Cosmicflows-4 catalog (Tully et al., 2023). Stellar mass distributions are calculated using Spitzer 3.6 μm photometry,

while the hi masses are obtained from the THINGS database. The star formation rates (SFRs) are estimated using the total infrared luminosity (TIR) from the KINGFISH survey (Key Insights on Nearby Galaxies: a Far-Infrared Survey with Herschel [Kennicutt et al., 2011](#)), following the calibration reviewed by [Kennicutt & Evans \(2012\)](#).

Galaxy	Classification	R.A.	Dec	D	i	M_{stellar}	M_{H_2}	\mathbf{R}_{half}	$\mathbf{L}_{[3.6 \mu\text{m}]}$	SFR
		hh mm ss.s	dd mm ss.s	Mpc	deg	$10^9 M_{\odot}$	$10^9 M_{\odot}$	kpc	$10^9 L_{\odot}$	$M_{\odot} \text{yr}^{-1}$
NGC 2403	SF	07 36 51.1	+65 36 02.9	3.13	63.00	5.02	2.58	2.16	10.04	0.85
NGC 2841	AGN/LINER	09 22 02.6	+50 58 35.4	14.66	76.00	94.06	8.58	5.51	188.12	1.87
NGC 2903	SF	09 32 10.1	+21 30 04.3	8.97	66.00	40.93	4.35	4.54	81.86	1.49
NGC 3198	SF	10 19 55.0	+45 32 58.9	13.36	73.00	19.14	10.17	5.84	38.28	1.49
NGC 3521	AGN	11 05 48.6	-00 02 09.2	12.56	75.00	42.42	8.02	2.45	84.84	4.71
NGC 5055	AGN/LINER	13 15 49.2	+42 01 45.3	8.83	55.00	76.46	9.1	4.18	152.92	2.97
NGC 6946	SF	20 34 52.2	+60 09 14.4	6.95	38.00	33.08	4.15	4.20	66.17	4.71
NGC 7331	AGN	22 37 04.1	+34 24 56.5	14.51	75.00	125.32	9.13	3.99	250.63	7.46
NGC 7793	SF	23 57 49.7	-32 35 27.9	3.39	47.00	3.53	0.89	2.19	7.05	0.30

TABLE 3.1 – Selected galaxy sample.

3 Studies of NGC 3521

3.1 Morphology of NGC 3521

3.1.1 Optical images

In Figure 3.1, we present two optical images of NGC 3521. The left panel shows an image captured by Eric W. Benson using a small telescope, processed by Dietmar Hager, and featured in the *Astronomy Picture of the Day* on April 2, 2021¹. The right panel displays an optical image from Martínez-Delgado et al. (2010), obtained with the primary survey camera at the Black Bird Observatory, with a total exposure time of 495 minutes. In the left panel, the green triangle highlights a triangular structure near the edge of the disk, which appears as a ring or tail-like feature projected on the sky, with no counterpart on the opposite side. This feature is also visible in the right panel as an elongated structure in the same location. However, on the opposite side of the disk, a faint diffuse structure is noticeable near the lower portion. Both images reveal an almost ellipsoidal stellar cloud enveloping the disk, suggesting the presence of a broad stellar thick disk.

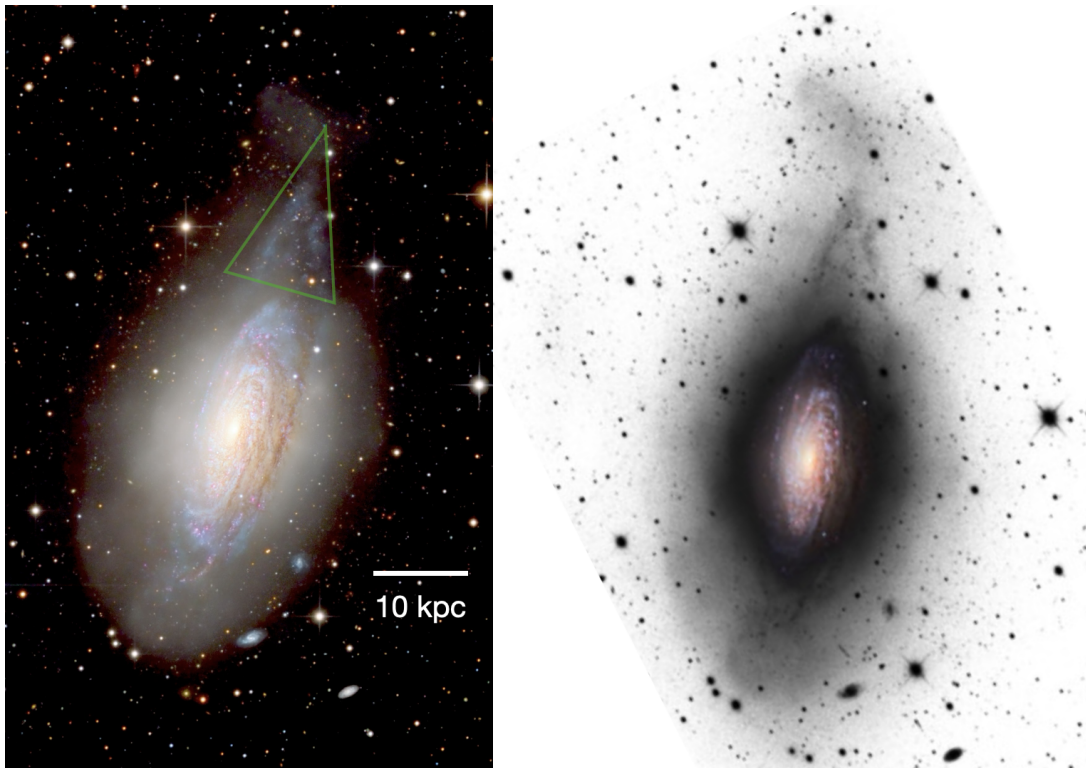


FIGURE 3.1 – Optical images of NGC 3521. The left panel shows an optical image taken by amateur astronomer Eric W. Benson using a small telescope, processed by Dietmar Hager (details in *Astronomy Picture of the Day*, April 2, 2021). The right panel presents an optical image from Martínez-Delgado et al. (2010). The green triangle highlights a triangular structure near the edge of the disk, which appears to be a ring or tail-like feature projected on the sky and is not visible on the opposite side.

1. <https://apod.nasa.gov/apod/ap210402.html>

3.1.2 HI images

In Figure 3.2, we compare the optical image with the H I image of NGC 3521 from the THINGS database. The left panel displays the same optical image as in Figure 3.1, while the right panel shows the H I image from THINGS. The red solid ellipse (radius of 300 arcsec) roughly marks the edge of the optical disk. The dashed line indicates the major axis of the galaxy (THINGS). The asymmetrical triangular structure observed at the top of the disk in the optical image is also visible in the H I image. However, the H I image reveals a long tail-like structure at the bottom of the disk, extending well beyond the optical disk. This structure presents from approximately 22.35 kpc from the galactic center to the observational edge around 51 kpc. The broad, thick stellar disk seen in the optical images is not detectable in the H I image. Additionally, the H I data reveal asymmetry in the outer regions of the gas disk, extending beyond the 300 arcsec elliptical boundary.

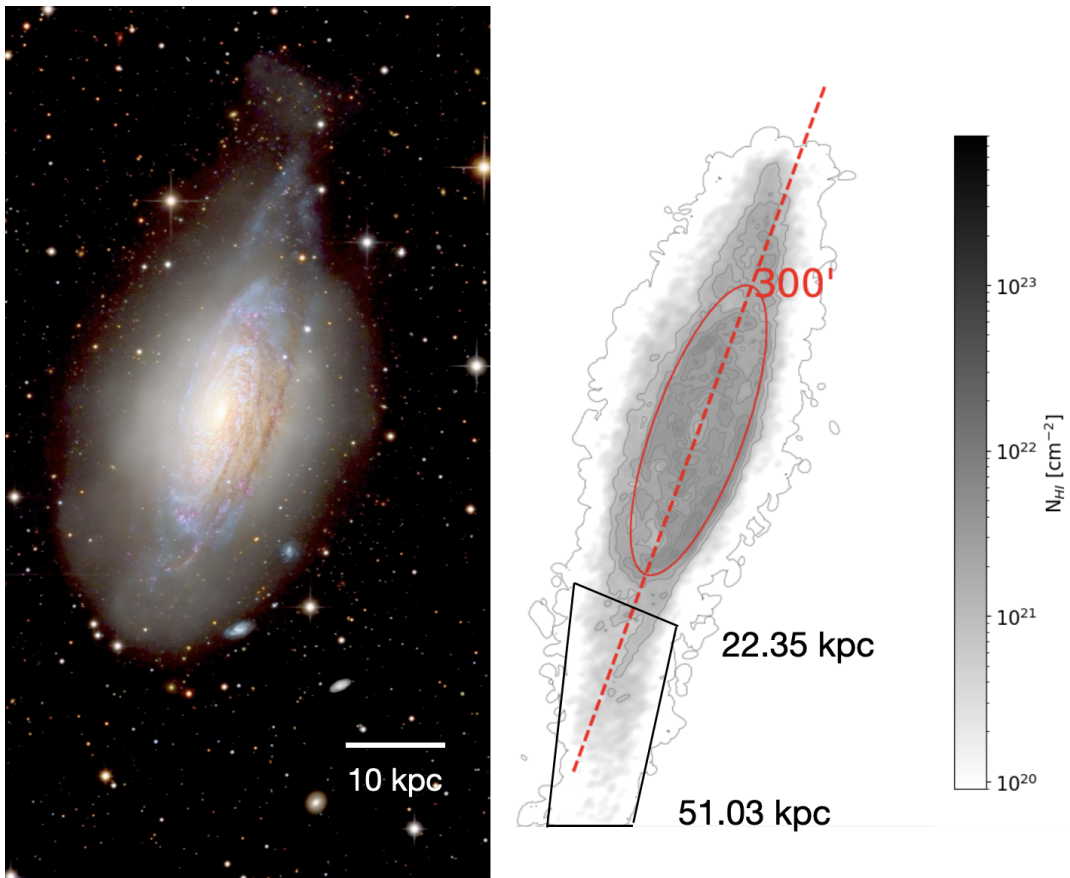


FIGURE 3.2 – Optical and HI images of NGC 3521. The left panel shows the same optical image as in Figure 3.1, while the right panel presents an H I image from the THINGS database. The red solid ellipse (radius of 300 arcsec) approximately marks the edge of the optical disk, and the dashed line represents the major axis of the galaxy. The black quadrilateral highlights a tail structure at the bottom of the disk in the H I image, extending farther than what is visible in the optical images. The values indicate the distance from the galaxy center to the edge of this structure as indicated by the quadrilateral.

3.2 Kinematics

3.2.1 Rotation curve of NGC 3521

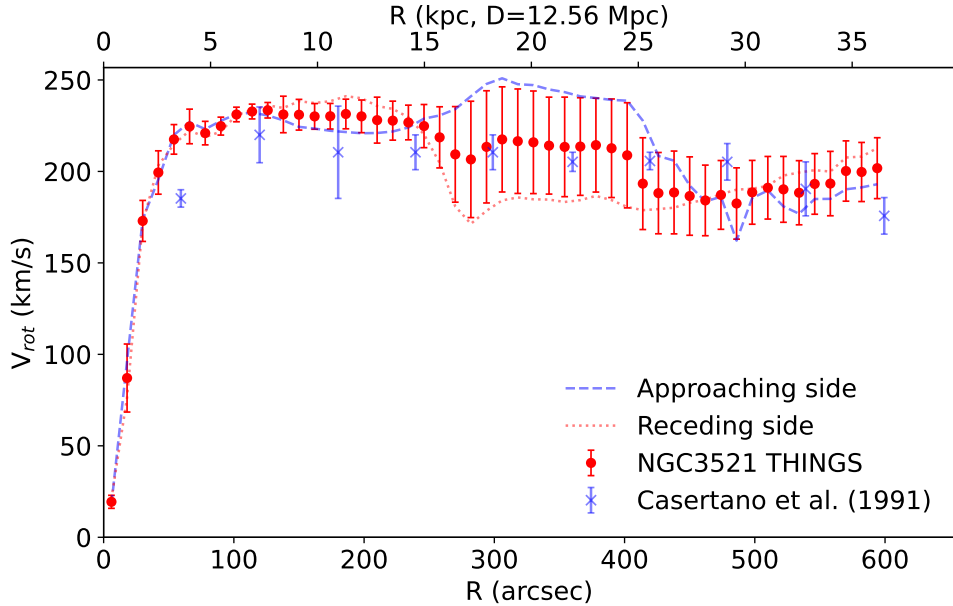


FIGURE 3.3 – Rotation curves of NGC 3521. The red points with error bars represent the derived circular velocity and associated uncertainties from THINGS. The blue dashed line shows the circular velocity on the approaching side of the galaxy, while the red dotted line represents the circular velocity on the receding side. The blue crosses indicate the rotation curve derived by Casertano & van Gorkom (1991).

The RC of NGC 3521 (red points and error bars in Figure 3.3) shows the first wiggle at approximately 300 arcsec, followed by a flat region extending to around 400 arcsec. After a second decline at 400 arcsec, the curve remains flat up to 500 arcsec, after which there is a slight increase. Casertano & van Gorkom (1991) presented an earlier RC of NGC 3521 using VLA H I observations, proposing one of the first reported instances of a genuinely declining H I RC in a spiral galaxy. This decline occurs at a radius of approximately 500 arcsec. de Blok et al. (2008) argued that this discrepancy is unlikely to result from differences in the position angle or inclination. Their analysis tested a 5° variation in inclination from an initial value of $i = 75^\circ$ and found it only produced a 2% or $\sim 4 \text{ km s}^{-1}$ change in velocity, which falls far short of the $\sim 30 \text{ km s}^{-1}$ difference needed to reconcile the RC of Casertano & van Gorkom (1991) with that of THINGS. They concluded that although the RC in the outer regions is lower than in the inner parts, there is no evidence of a steep decline or negative gradient in outer velocities as proposed by Casertano & van Gorkom (1991).

One of the most striking features in the RC is the significant discrepancy between the approaching and receding sides, as shown by the blue dashed line and red dotted line in Figure 3.3. The first major difference occurs between radii of 150 and 250 arcsec, with a velocity discrepancy of nearly 20 km s^{-1} . However, a much larger velocity discrepancy, around 80 km s^{-1} , is observed between 270 and 450 arcsec. This substantial difference also contributes to the significant uncer-

tainties in the THINGS RC. A gas disk in dynamical equilibrium should not exhibit such a large velocity difference between its two sides, which amounts to roughly 40% of the circular velocity. If this discrepancy cannot be attributed to observational or data processing errors, it raises the possibility that the gas disk may not be in dynamical equilibrium. Interestingly, when comparing this to the solid elliptical ring in Figure 3.2, the discrepancy aligns with the asymmetric region seen in the H I observations, starting at the edge of the optical stellar disk (around 300 arcsec).

3.2.2 Position-velocity diagram of NGC 3521

Figure 3.4 displays the position-velocity diagram of NGC 3521 along the major axis, derived from the THINGS H I data cube (de Blok et al., 2008). The slice thickness is equivalent to one pixel (1.5 arcsec). The systemic velocity of NGC 3521, 803.5 km s^{-1} , is indicated by the dashed horizontal line, while the galaxy's center is marked by the vertical dashed line. The overplotted curve represents the projected rotation curve onto the average major axis, accounting for the radial variations in position angle (P.A.) and inclination (i).

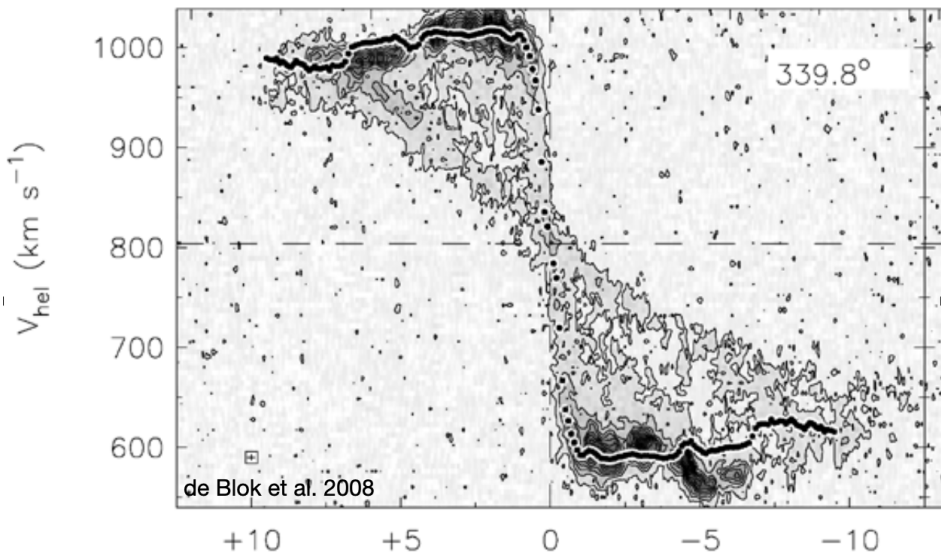


FIGURE 3.4 – Position-velocity diagram along the major axis of NGC 3521 from THINGS observations, with a slice thickness of $1''.5$ (1 pixel). The dashed horizontal line represents the systemic velocity of NGC 3521, while the vertical dashed line marks the galaxy's center. The overplotted points show the rotation curve projected onto the average major axis, incorporating the derived radial variations of P.A. and inclination (i). The spatial and velocity resolutions are indicated by the cross enclosed in the rectangle in the bottom-left corner. This figure is adapted from de Blok et al. (2008).

The position-velocity diagram also shows the asymmetric features between the approaching and receding sides. On the left side (receding side), the observational data reveal a slight decline, with the contours lying above the RC in the inner region and below it in the outer part. On the right side (approaching side), after a relatively flat part, there is a distinct second increase, resulting in a significant difference between the approaching and receding sides of the RC. Besides, the contours fall below the RC in the inner region and rise above it in the outer region,

opposite to what is observed on the receding side. This asymmetry in the position-velocity diagram is consistent with the morphological features and the RC variations observed on both sides of the galaxy.

3.3 Ionized properties of NGC 3521

To classify the ionized properties of the selected galaxies, we utilized the Baldwin, Phillips & Terlevich (BPT, Baldwin et al., 1981) diagram, based on emission line fluxes from the spectra presented by Moustakas et al. (2010). The optical spectra were obtained between 2001 and 2006 using the Bok 2.3-meter telescope on Kitt Peak and the CTIO 1.5-meter telescope. Moustakas et al. (2010) employed the long-slit drift-scanning technique pioneered by Kennicutt (1992). One-dimensional spectra were extracted using a $2''.5 \times 2''.5$ (or $2''.5 \times 3''.0$ for the CTIO spectra) aperture for the nuclear region and a $20'' \times 20''$ aperture for the circumnuclear region. Radial strip spectra were extracted over a $(0.55 \times D_{25}) \times \Delta_{\text{scan}}$ arcsec 2 rectangular region, where D_{25} is the major-axis diameter of each galaxy and Δ_{scan} is $56''$ ($55''$ in some cases), representing the drift-scan length perpendicular to the slit. The total exposure times for the radial strip, circumnuclear, and nuclear spectra ranged from 20-60 minutes, 10-30 minutes, and 5-10 minutes, respectively, typically split into two or more exposures to facilitate cosmic ray identification.

The data reduction process involved several steps, including overscan and bias subtraction, flat-fielding, correction for varying illumination patterns, and sky subtraction, following the methods described by Moustakas & Kennicutt (2006). The *relative* spectrophotometric accuracy across the full spectral range is $\lesssim \pm 5\%$ (Moustakas et al., 2010). Finally, all spectra were corrected for foreground Galactic reddening using the extinction law of O'Donnell (1994) and the dust map from Schlegel et al. (1998), assuming $R_V \equiv A_V/E(B-V) = 3.1$.

Moustakas et al. (2010) used high-resolution stellar population synthesis (SPS) models to accurately separate the stellar continuum of a galaxy from its integrated emission-line spectrum, allowing the emission-line strengths to be analyzed without the systematic effects of Balmer and metal-line absorption. They achieved a pure emission-line spectrum, and corrected self-consistently for stellar absorption, by subtracting the best-fitting stellar continuum from the observed data. Each spectrum was fitted using SPS models from Bruzual & Charlot (2003, hereafter BC03), assuming the Chabrier (2003) initial mass function (IMF) between 0.1 and $100 M_\odot$. The stellar continuum was modeled as a non-negative linear combination of 10 BC03 models with ages ranging from 5 Myr to 13 Gyr, and three metallicities: $Z = 0.004, 0.02$, and 0.05 . Moustakas et al. (2010) verified that variations in their model assumptions had no significant impact on the measured emission-line strengths. In this study, we utilized the optical emission-line equivalent widths measured by Moustakas et al. (2010) to classify the ionized properties of the selected galaxies.

An example spectrum of NGC 3521 is shown in Figure 3.5, presenting the reduced one-dimensional spectra in units of $\text{erg s}^{-1} \text{cm}^{-2} \text{\AA}^{-1}$ versus rest-frame wavelength in Å. The observed data are plotted in gray, with the best-fitting stellar continuum model overlaid in black. The right panel also includes an optical image from the Digitized Sky Survey (DSS), illustrating

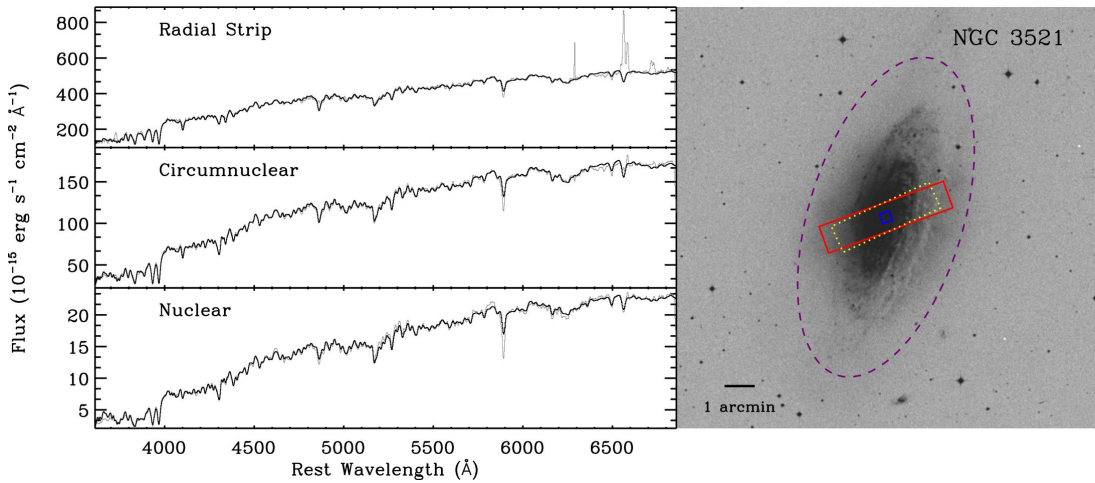


FIGURE 3.5 – Spectra of NGC 3521 from Moustakas et al. (2010). The left panels plot the nuclear, circumnuclear, and radial-strip spectra optical spectra of NGC 3521; the observed spectra are shown in grey and the best-fitting stellar continuum fit is overplotted in black. The right panels show the size of the circumnuclear (blue square) and radial-strip (red rectangle) spectroscopic apertures, overlaid on an optical DSS image of NGC 3521. The dashed purple ellipse indicates the optical extent of the galaxy, and the dotted yellow rectangle shows the spatial coverage of the *Spitzer*/IRS radial-strip long-low spectrum obtained as part of SINGS.

how the spectroscopic aperture compares to the optical extent of the galaxy (indicated by the *dashed purple ellipse*). The size of the spectroscopic aperture corresponding to the radial-strip and circumnuclear spectra is represented by the red rectangle and blue square, respectively. The dotted yellow rectangle shows the spatial coverage of the corresponding *Spitzer*/IRS long-low spectrum obtained as part of the SINGS survey, where there was at least double coverage in both spectral orders (Smith et al., 2007). A mismatch exists between the orientation angle of the IRS and optical radial-strip spectra. This difference arises because many of the optical spectra were obtained before the IRS spectra had been observed or even scheduled.

In Figure 3.6, we present the classification of the ionized properties of NGC 3521. The diagram plots $[\text{N II}] \lambda 6584/\text{H}\alpha$ versus $[\text{O III}] \lambda 5007/\text{H}\beta$, using the emission-line diagnostic diagram to classify galaxies. The classification curves from Kewley et al. (2001) and Kauffmann et al. (2003) are used to separate galaxies into star-forming (SF), active galactic nuclei (AGN), and composite SF/AGN regions. Additionally, we supplemented the dataset by incorporating data from Moustakas & Kennicutt (2006), which utilized the same observational methods and similar data processing, to account for galaxies lacking measurements in the Moustakas et al. (2010) dataset.

For NGC 3521, the emission-line ratios based on the nuclear and radial-strip spectra from Moustakas & Kennicutt (2006) are shown in Fig. 3.6 with blue and red triangles, respectively. The nuclear spectrum emission-line ratio lacks error bars, as we used the 1σ upper limits, assuming two significant figures, which do not provide uncertainty estimates. The red circle represents the emission-line ratios from the radial-strip spectra of Moustakas et al. (2010). The vertical line indicates the $[\text{N II}]/\text{H}\alpha$ ratio alone, based on the circumnuclear spectrum, due to an

unconstrained [O III]/H β ratio, where Moustakas et al. (2010) adopted $\log([\text{N II}]/\text{H}\alpha) = -0.25$ as the boundary between the two classes. The emission-line ratios for NGC 3521 are consistent with an AGN (LINER) classification. The classifications for other galaxies will be presented in Section 5.2.

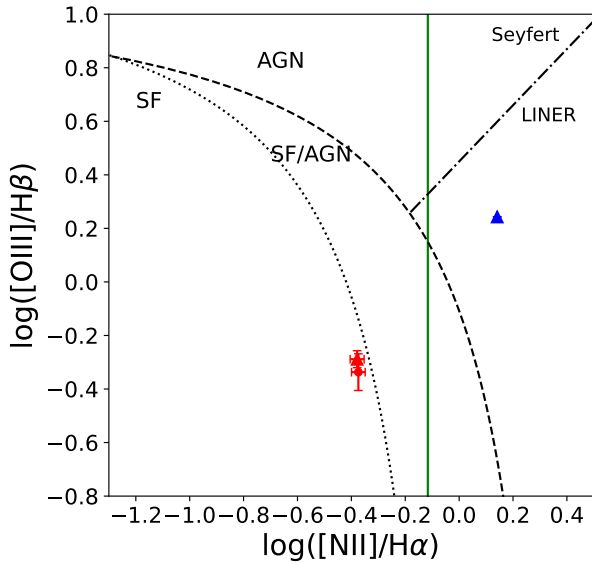


FIGURE 3.6 – Emission-line diagnostic diagram used to separate star-forming (SF) galaxies from active galactic nuclei (AGNs) for NGC 3521. The dotted and dashed lines are the empirical and theoretical boundaries between SF galaxies and AGNs defined by Kauffmann et al. (2003) and Kewley et al. (2001). The dash-dotted line is the Seyfert/LINER division line from Cid Fernandes (2010). The triangle symbols represent the data coming from Moustakas & Kennicutt (2006) and the circle symbols represent the data coming from Moustakas et al. (2010). Emission line ratios based on nuclear and radial-strip spectra using blue and red respectively. The vertical line presents the [N II]/H α ratio alone based on the circumnuclear spectrum because of an unconstrained [O III]/H β ratio, where we adopt $\log([\text{N II}]/\text{H}\alpha) = -0.25$ as the boundary between the two classes.

3.4 Stellar population of NGC 3521

The principal objective of Moustakas et al. (2010) in modeling the underlying stellar continuum was to obtain a pure emission-line spectrum that is self-consistently corrected for stellar absorption, rather than to constrain the star formation history (SFH) or stellar metallicity. However, the SFH is crucial for estimating the epoch of the last major merger in a galaxy. During such merger events, gas is compressed, triggering significant star formation and leading to the birth of new stars.

Hammer et al. (2018a) used simulations of a 4:1 mass ratio major merger that successfully reproduced nearly all of the observed features in M31. Their simulations indicate that the merger occurred approximately 1.8–3 Gyr ago, with a peak in the star formation rate (SFR) coinciding with this merger epoch. In Figure 3.7, the left four panels display the star formation history from five hydrodynamical major merger simulations, measured at 3, 4.7, 7.8, and 14.2 kpc

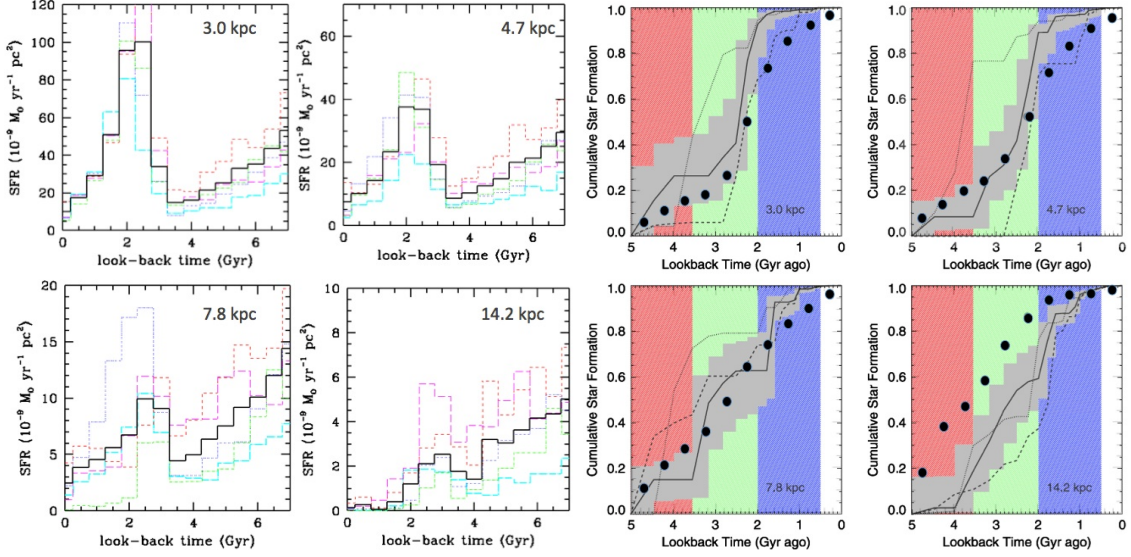


FIGURE 3.7 – Star formation history of five fiducial simulations from Hammer et al. (2018a) (left panels) and cumulative star formation from the models compared to observations by Williams et al. (2015) (right panels). In the left panels, the green (dot-short dash), magenta (long dash), red (short dash), blue (dot), and cyan (dot-long dash) lines represent the five models, while the black solid line shows the average of all models. The peaks in the SFH correspond to the assumed major merger event approximately 2–4 Gyr ago. In the right panels, the solid lines with gray shading illustrate the fits to the Padova models, including total uncertainties. The dashed lines indicate the best fit to the BASTI models, and the dotted lines represent the best-fit for the PARSEC models. The three colored stripes denote the epochs of major merger events. The fits from Williams et al. (2015) are based on observational data, with the solid dots representing the average values from the five models of Hammer et al. (2018a).

along the disc, corresponding to the fields studied by Williams et al. (2015). The dashed lines represent individual models, while the solid lines show the average of all models, emphasizing a star formation episode approximately 2–4 Gyr ago across the entire disc. These SFR peaks are consistent with the estimated timing of M31’s last major merger.

In the right four panels, we compare the cumulative star formation from the simulations with observations of M31 by Williams et al. (2015). Williams et al. (2015) investigated cumulative star formation over the past 5 Gyr at eight different radii along the major axis using color-magnitude diagram (CMD) fitting. The solid lines with gray shading represent the fits to the Padova models, with total uncertainties included. The dashed lines show the best fit to the BASTI models, and the dotted lines correspond to the best fit using the PARSEC models. The three colored stripes highlight the epochs of the three major merger events, providing a temporal comparison between the observational data and the merger-driven star formation episodes identified in the simulations.

It is important to note that Williams et al. (2015) focused their analysis on the star formation history (SFH) of M31 over the past 5 Gyr. While they acknowledged that the color-magnitude diagrams (CMDs) contain a substantial fraction of stars older than 5 Gyr, which were included in the SFH fitting, they excluded these older populations from their primary analysis to focus on

the epoch of interest. Their main objective was not to identify a specific epoch with the highest concentration of stars but rather to determine a period during which star formation rates were notably higher compared to both earlier and later times.

Therefore, by decomposing the stellar population and estimating the age distribution of the stars, we can infer the timing of the last major merger event in the galaxy. By fitting the stellar continuum, we can derive the stellar population of the galaxy and subsequently translate this into a relationship between light or mass fractions as a function of stellar age. This approach allows us to trace the history of star formation and identify periods of heightened star formation activity, which may correspond to significant events like major mergers.

3.4.1 Spectrum and photometry fit of NGC 3521

We fit the spectrum using the χ^2 -minimization algorithm pPXF (Cappellari & Emsellem, 2004; Cappellari, 2017, 2023), which models both the emission lines and the stellar continuum simultaneously. The emission lines are modeled as Gaussians, while the stellar continuum is represented as a non-negative combination of simple stellar population (SSP) spectra across a grid of ages and metallicities. For the SSP spectra, we utilize the E-MILES SPS model templates from Vazdekis et al. (2016), which employ Padova isochrones and assume a Salpeter IMF.

It is important to note that the E-MILES models only include stellar populations older than 63 Myr. To account for younger stellar populations, we supplement the fit with the SPS models used by Cappellari (2023), specifically: (i) the FSPS model (version 3.2, Conroy et al., 2009; Conroy & Gunn, 2010)², and (ii) the GALAXEV model (Bruzual & Charlot, 2003)³. A detailed description of these models can be found in Table 3.2.

TABLE 3.2 – Stellar population synthesis models

Model	Age log(Age)[Gyr]	Metallicity [M/H]
E-MILES	From 7.8 to 10.2, with intervals of 0.1	-1.71, -1.31, -0.71, -0.4, 0.0, 0.22
FSPS	From 6 to 10.2, with intervals of 0.1	-1.75, -1.5, -1.25, -1.0, -0.75, -0.5, -0.25, 0.0, 0.25
GALAXEV	From 6 to 10.2, with intervals of 0.1	-1.74, -0.73, -0.42, 0.0, 0.47

The FSPS and GALAXEV models used the MILES stellar library (Sánchez-Blázquez et al., 2006; Falcón-Barroso et al., 2011) to generate spectra for the optical region (Cappellari, 2023). To avoid introducing bias by relying solely on optical-band spectra, we also incorporated photometric data ranging from the near-ultraviolet (NUV) to the near-infrared bands into our analysis. This included data from GALEX NUV, SDSS *u g r i z*, and 2MASS *J H Ks*, as provided by Dale et al. (2017).

To simultaneously fit spectroscopic and photometric data, the observational data should ideally be measured using the same aperture. In this case, we performed an approximate correction. First, we calculated the average flux of the observed spectrum in the SDSS *g* and *r* bands,

2. Latest public version 3.2: <https://github.com/cconroy20/fsp>

3. <http://www.bruzual.org/bc03/>

and then determined their average ratio compared to the photometric observations from Dale et al. (2017). Using this ratio, we corrected the photometric data across all bands, treating the corrected values as if they were measured with the same aperture as the spectroscopic data.

Figure 3.8 shows an example for correcting photometry data of NGC 3521, where the red squares represent the corrected photometry based on the spectrum, and the blue circles represent the original photometry data.

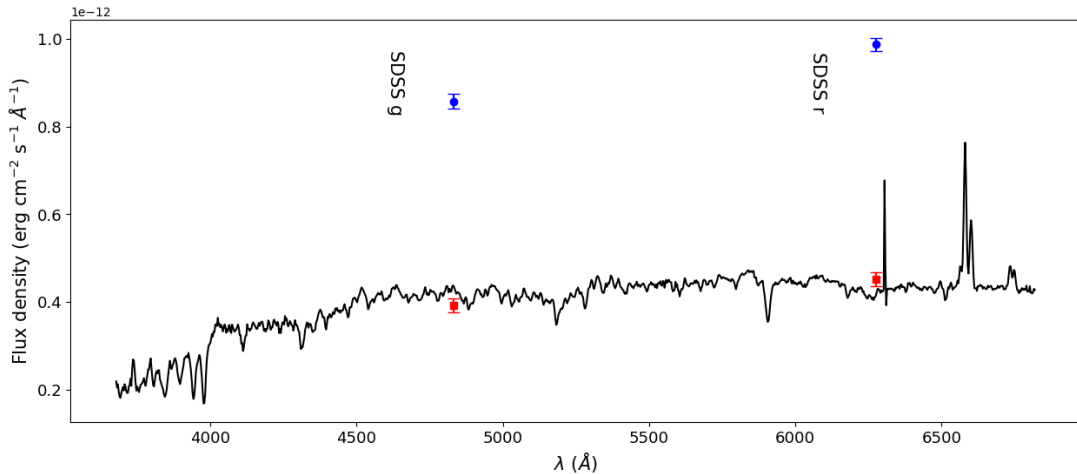


FIGURE 3.8 – Correction of photometry data of NGC3521. The black line is the observed radial-strip spectrum, the blue circles are the photometry data, and the red squares are the corrected photometry data based on the spectrum.

In Figure 3.9, we present the spectrum-only fit of NGC 3521 in the observed wavelength range. The flux has been normalized to the average flux of the spectrum. The gray solid line represents the observed spectrum, the red solid line shows the best pPXF fit, and the green dashed line represents the best-fit stellar continuum. The black peaks correspond to the pPXF fits for the gas emission lines, and the orange points indicate the fit residuals.

Figure 3.10 shows the pPXF fit of NGC 3521, incorporating both the spectrum and photometric data. In this figure, the stellar continuum fit, gas emission lines, and residuals are not shown; instead, the photometric data are displayed as blue points with error bars. The green symbols represent the fitted photometry.

3.4.2 Estimation of last major star formation episode of NGC 3521

Based on the spectral and photometric fits shown in Figures 3.9 and 3.10, we estimated the age distribution of the stellar population in NGC 3521, as displayed in Figure 3.11. We notice a significant fraction of the old stellar population, similar to findings from M31 by Williams et al. (2015). However, considering the logarithmic scale of the horizontal axis, the difference in SFR over time would not be as pronounced when converted to SFR values. As previously mentioned, the goal is to identify a time range during which the SFR was significantly higher compared to both earlier and later epochs.

All fits show a peak in mass fraction between 0.5 and 2.5 Gyr (approximately $10^{8.7} - 10^{9.4}$

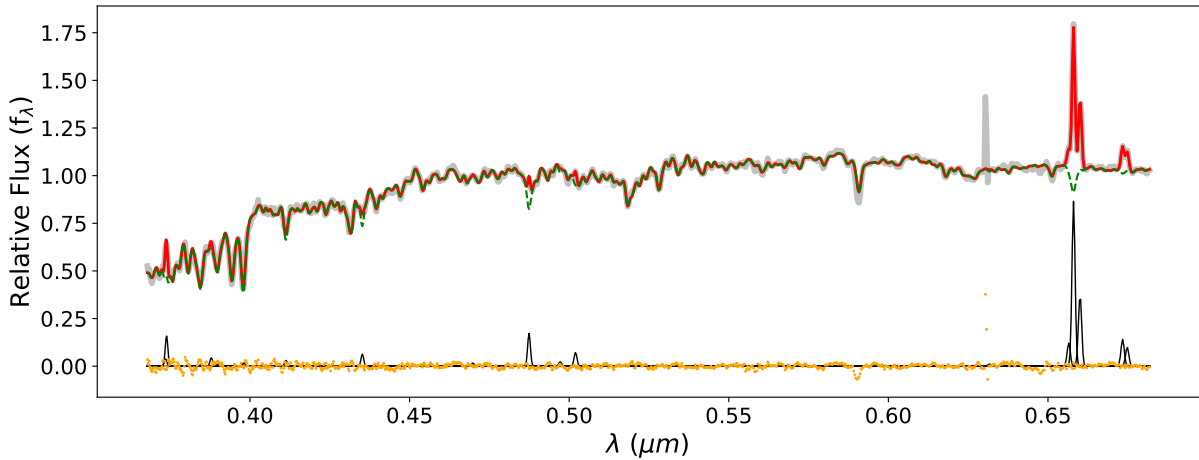


FIGURE 3.9 – The spectrum-only pPXF fit for NGC 3521. The gray solid line represents the observed spectrum, while the red solid line shows the best pPXF fit. The green dashed line represents the best-fit stellar continuum, the black peaks correspond to the pPXF fits for the gas emission lines, and the orange points indicate the fit residuals.

yr). The stellar population around 1 Gyr is approximately 10 times larger than that at around 3 Gyr, which corresponds to a local minimum between the old stellar population and the peak of the mass fraction. This is marked by the vertical dashed line at 3 Gyr, similar to the SFH peak observed in M31 (Figure 3.7). This suggests a significant increase in star formation during this epoch. By drawing an analogy with the case of M31, we estimate that the last major merger of NGC 3521 occurred approximately 1-3 Gyr ago, as indicated by the gap between the old stellar population and the first peak in mass fraction, highlighted by the gray region in Figure 3.11.

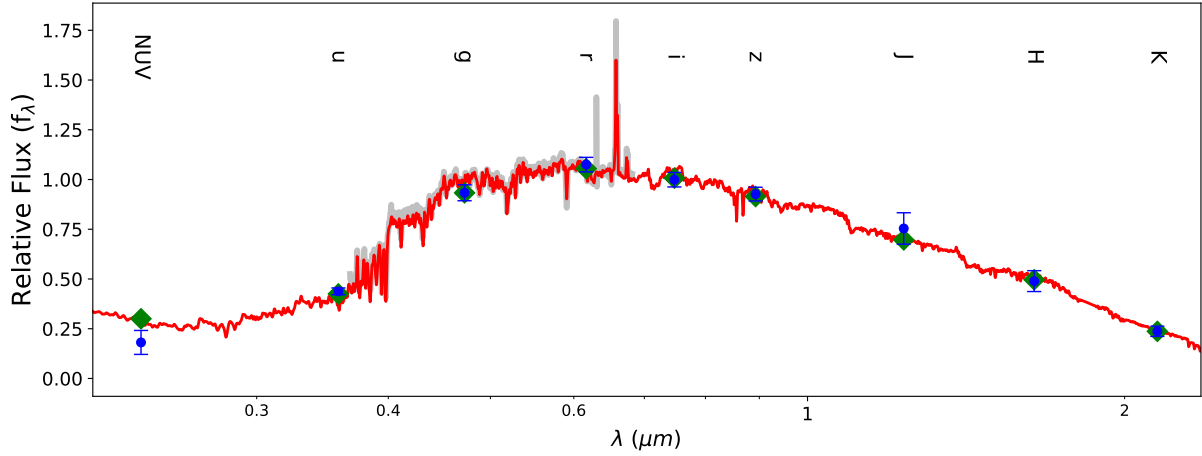


FIGURE 3.10 – The pPXF fit of NGC 3521, incorporating both spectrum and photometry. The gray solid line represents the observed spectrum, while the red solid line denotes the best pPXF fit. The blue points with error bars correspond to the corrected photometry data from Dale et al. (2017), and the green symbols indicate the fitted photometry. The relevant photometric bands are also labeled in the figure.

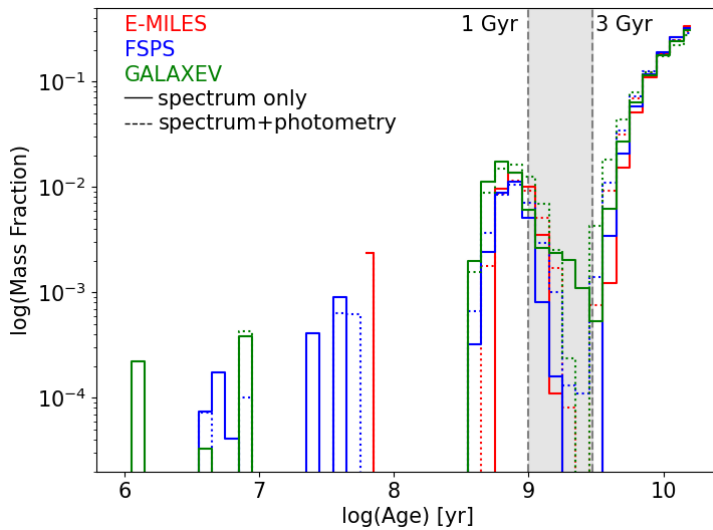


FIGURE 3.11 – The age distribution of the stellar population in NGC 3521. The solid lines represent the mass fraction of stars as a function of age from the spectrum-only fit, while the dashed lines show the estimates from the fit incorporating both spectrum and photometry. Different colors correspond to various SPS models, as labeled in the upper left corner. The gray region indicates the estimated epoch of the last major merger.

4 Hydrodynamical simulations

We used hydrodynamic simulations of major galaxy mergers from Sauvaget et al. (2018) to quantitatively assess the impact of major mergers on the measurement of RCs. Sauvaget et al. (2018) employed a modified version of the public N-body/SPH code GADGET2 (Springel, 2005), with star formation, supernova feedback, and cooling processes modeled following Cox et al. (2006), as implemented by Wang et al. (2012, 2015). Sauvaget et al. (2018) ran a suite of simulations with varying orbital parameters between the two progenitors, building a library of gas-rich major mergers with a mass ratio of 1:4.

We aim to find the best match between the observed features of NGC 3521 and a simulated merger remnant from this library. By deriving mock observational data from the simulations, we can quantitatively analyze any discrepancies between the simulated and observed data, enhancing our understanding of how major mergers influence galaxy observations. This approach will allow us to determine whether a single merger event is sufficient to explain the complex features observed in NGC 3521.

For future studies, comparing specific physical parameters between the simulations and observations could provide a scaling factor to adjust the simulation results to more closely align with the observed galaxy. This scaling factor could be derived from properties such as mass, size, or other relevant physical parameters. Once determined, the scaling factor can be applied to refine the simulation outcomes, bringing them in line with the observed characteristics of NGC 3521. This approach would offer a more accurate representation of the galactic evolutionary history.

Accurately simulating a specific galaxy requires consideration of various parameters involved in galaxy mergers, as demonstrated in the detailed M31 major merger simulations by Hammer et al. (2018a). However, such detailed simulations are beyond the scope of this study and require substantial additional effort. In this section, we select a simulation that approximately reproduces the features of NGC 3521 and roughly tests the impact of a recent major merger on the RC estimations.

4.1 Comparison of HI observation

We use snapshot 210 from the polar prograde-prograde simulation from Sauvaget et al. (2018). Figure 3.12 displays the proportion of newly formed stars, allowing us to estimate that this snapshot corresponds to approximately 1 Gyr after the major merger.

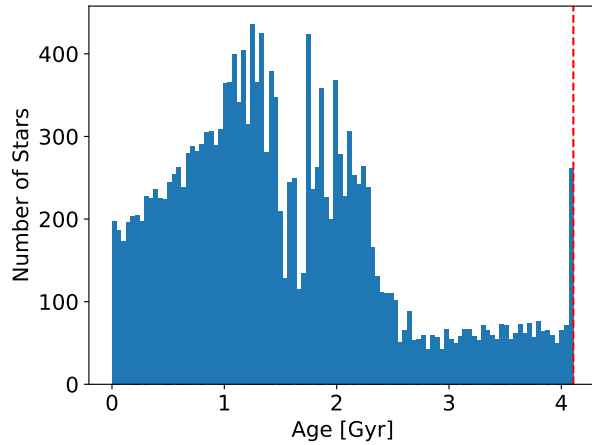


FIGURE 3.12 – Star formation history of the hydrodynamical simulation at snapshot 210. The histogram shows the ages of newly formed stars from gas after the simulation starts. The two peaks correspond to the first (~ 2 Gyr) and second (~ 1.2 Gyr) passages during the major merger. The vertical dashed line indicates the beginning of the simulation. We estimate that this snapshot corresponds to approximately 1 Gyr after the major merger.

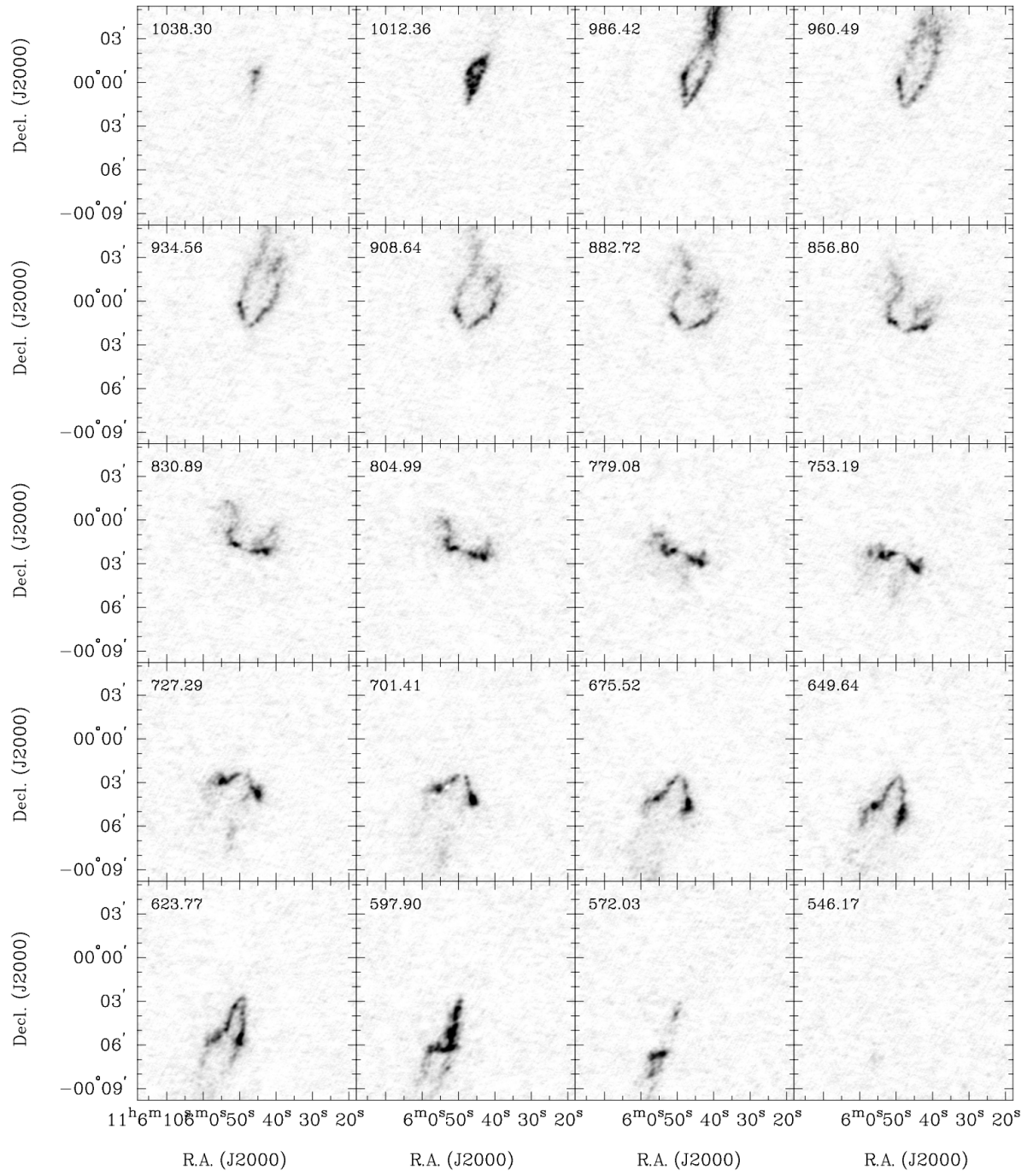


FIGURE 3.13 – Channel maps of NGC 3521. Every fifth channel is shown (channel width: 5.2 km s^{-1}). This figure is adapted from Walter et al. (2008).

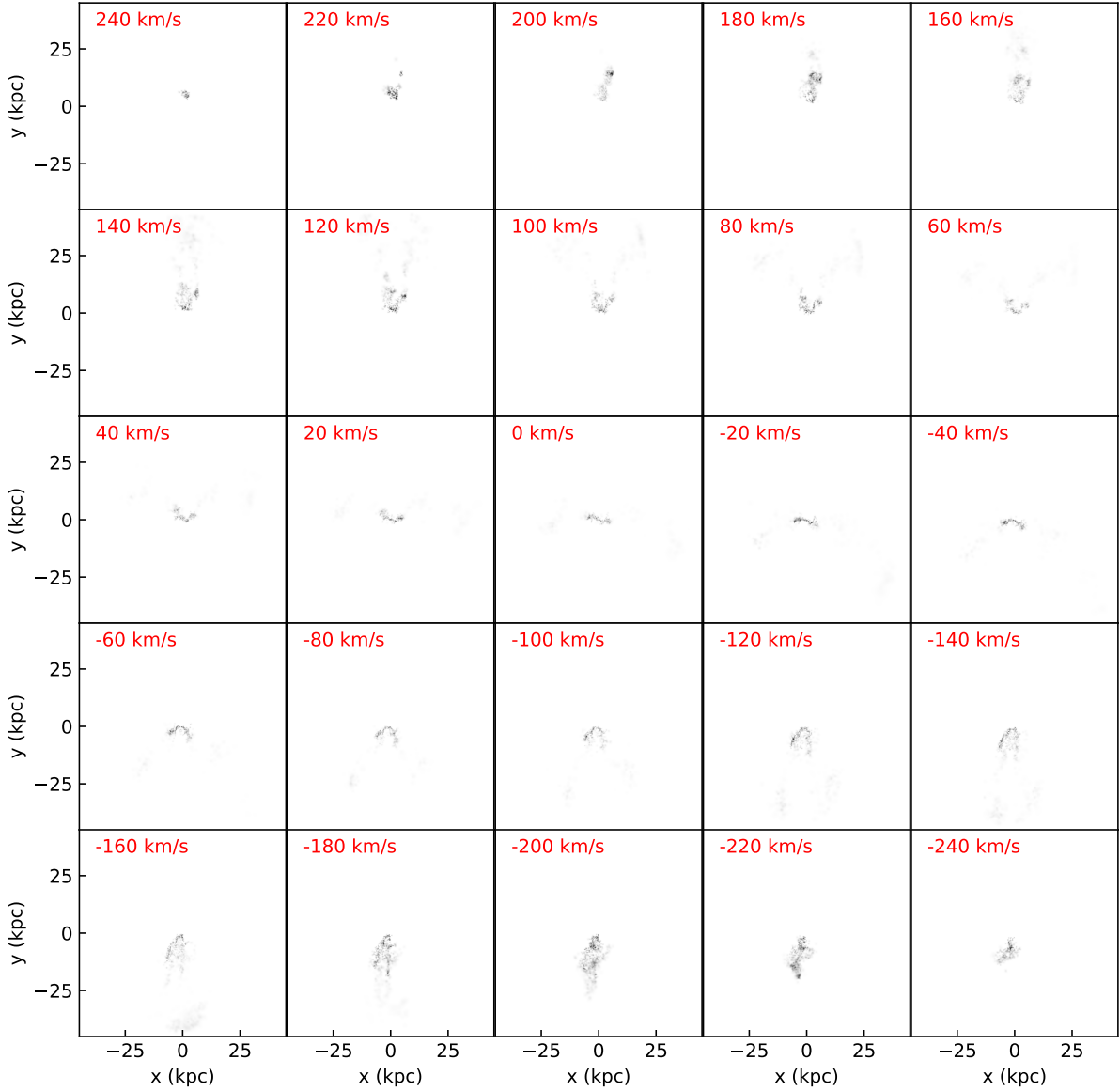


FIGURE 3.14 – Channel maps of the mock HI observation from the simulation. Every fourth channel is presented (channel width: 5 km s^{-1}).

To generate the mock H I observation, we used similar spatial and velocity resolutions. One pixel in the mock data corresponds to 0.08789 kpc, which closely matches the spatial resolution of THINGS for this galaxy, approximately 0.09108 kpc. We assume a Gaussian distribution of gas particles projected onto the sky. The velocity resolution is set to 5 km s^{-1} , which is comparable to the THINGS resolution of 5.2 km s^{-1} . Currently, we have not applied any velocity smoothing along the projected directions. Figure 3.13 presents the channel maps from THINGS, while the mock channel maps are shown in Figure 3.14. Both maps have various asymmetric structures.

Figure 3.15 compares the observed H I data with the assumed mock H I observation. We notice that our simulated gas disk is relatively smaller than the observed one. The triangular structure in the top part of the galaxy may correspond to a warped disk. In the current simulation, there is a gap between the warped disk and the inner disk. Therefore, to better fit the observations,

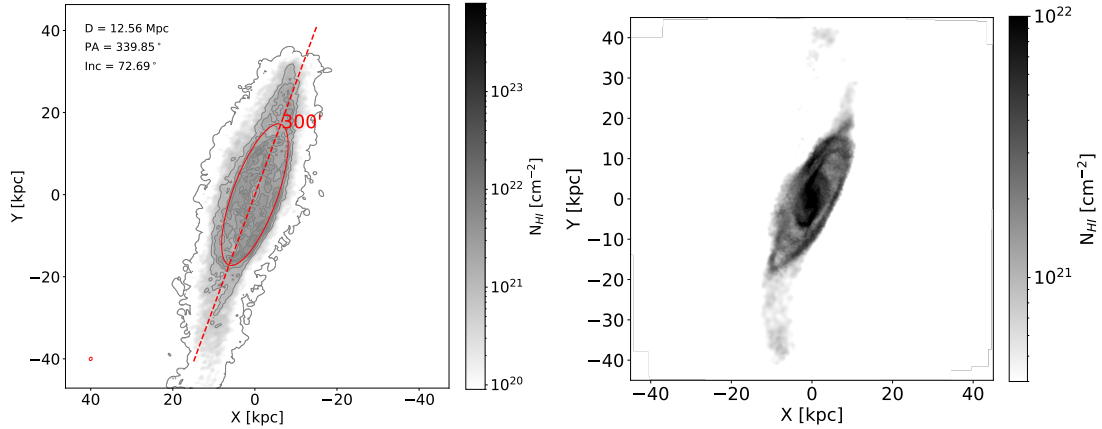


FIGURE 3.15 – Comparison of the observational HI image with the mock HI observation from hydrodynamical simulation. The left panel shows the HI image of NGC 3521 from the THINGS survey, with distance, position angle (P.A.), and inclination noted in the figure. All other details are the same as in Figure 3.2. The right panel displays the mock HI observation from the hydrodynamical simulation. The color bar on the right indicates the HI intensity in cm^{-2} .

we applied a relatively higher value for the lower density limit for gas as shown in the figure. Another notable difference is the direction of the tail in the south, which points in a different direction in the simulation compared to the observation.

Figure 3.16 shows the velocity fields from both the observation and the simulation. In both cases, I have corrected for the corresponding systemic velocities. Since the velocity component has not been smoothed, I did not apply Gaussian fits to determine the velocities for each pixel. Instead, I used a weighted average of the velocities based on the gas density at each given LOS velocity. Future improvements will be velocity smoothing and fitting techniques.

4.2 Comparison of position-velocity diagram

In Figure 3.17, we compare the position-velocity (PV) diagrams along the major axis between the simulation and observations. The left panels show the PV diagram from THINGS with different thicknesses: 1 pixel in the top panel and all data included in the bottom panel. The right panels present the PV diagram from the mock H I data. Since the center of the simulated galaxy is not aligned within a single pixel, I used a thickness of 2 pixels in the top right panel to compare to the observations. Similarly, the bottom right panel used all data from the simulation for a more comprehensive comparison.

The simulated data also show clear asymmetry between the approaching and receding sides, consistent with the features observed in the H I data from THINGS (left panels). In the left panels, the approaching sides are significantly more extended compared to the receding side, corresponding to the long tail on the approaching side. The discontinuities in the maximum velocities on both sides in the top right panel reflect the separation between the inner and outer disk. Achieving a more accurate simulation will require further improvements.

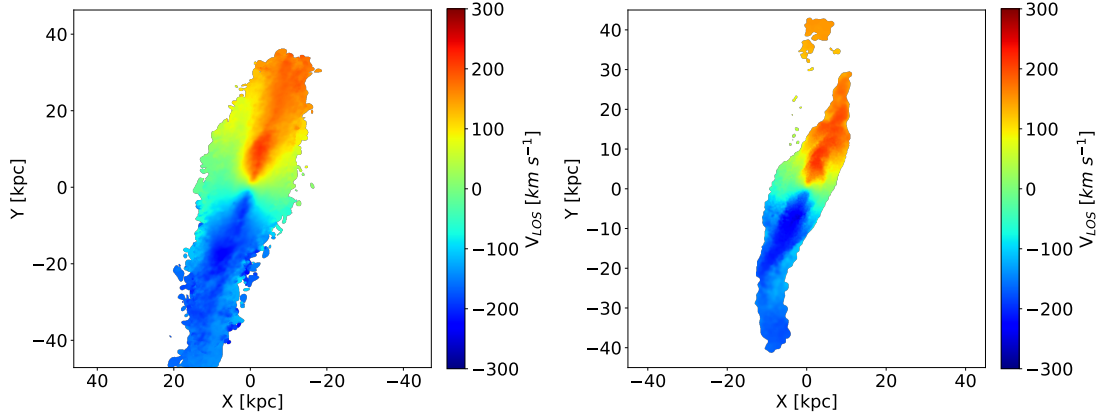


FIGURE 3.16 – Velocity field (moment 1) of NGC 3521 (left panel) and the velocity field of the simulated galaxy (right panel). The colorbars represent the line-of-sight (LOS) velocity. The LOS velocity of NGC 3521 has been corrected for the systemic velocity of 803.5 km s^{-1} from THINGS (de Blok et al., 2008).

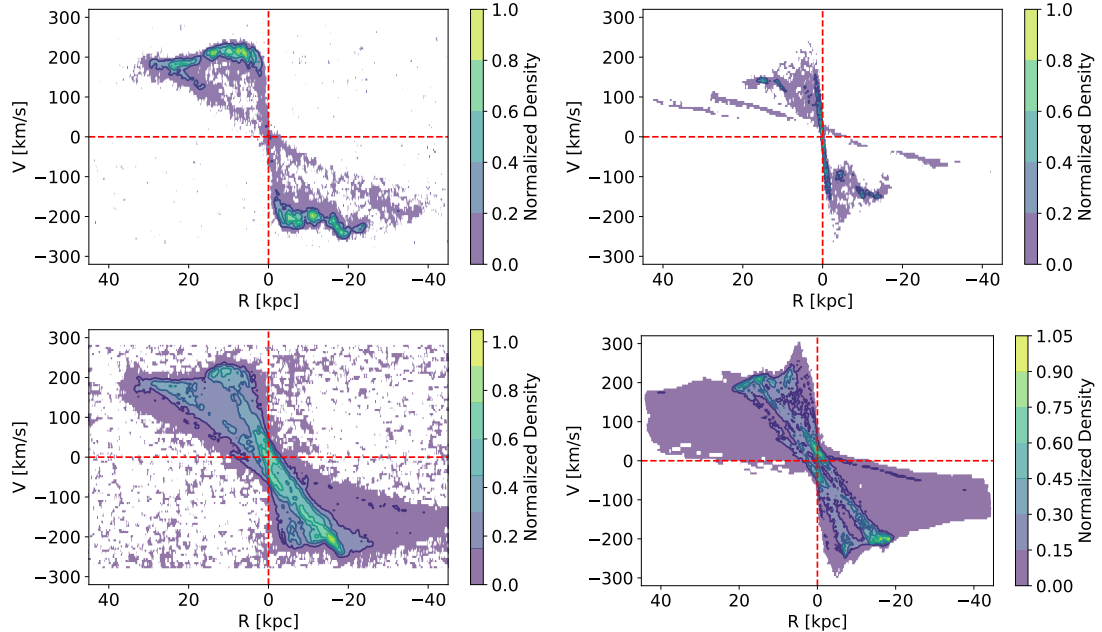


FIGURE 3.17 – Position-velocity (PV) diagram along the major axis from THINGS observation (left panels) and from hydrodynamical simulation (right panels). The top panels show the position-velocity diagram with a slice thickness of 1 pixel ($\sim 0.01 \text{ kpc}$, 2 pixels for the mock HI data), comparable to Figure 3.4. The bottom panels display the PV diagram using all data. The vertical dashed lines indicate the position of the center. All velocities have been corrected by the systemic velocities, therefore the horizontal lines present the systemic velocities of 0 km s^{-1} .

4.3 Analysis of rotation curve from mock HI observation

In Figure 3.18, we compare the derived RC with the *real* RC. The real RC is based on the mass distribution and Newtonian gravity. Due to previous discrepancies between the simulation and observation (Sections 4.1 and 4.2), we focus here on analyzing the derived RC and its corresponding mass distribution.

During the process of deriving the RC, I did not use a tilted ring model with varying P.A. and inclinations. Instead, I used the same angles applied when projecting the galaxy for comparison with the observation. At each radius, the RC was calculated using a weighted average of rotational velocities, weighted by $|\cos(\theta)|$, where θ is the P.A. relative to the receding major axis, measured in the plane of the galaxy.

The first discrepancy occurs in the inner region ($R < 6\text{-}7 \text{ kpc}$), where the derived RC is significantly smaller than the theoretical one. This issue may come from the method used to generate the mock HI velocity field (moment 1) map, which will be improved in future work. Between 15 and 35 kpc, a discrepancy between the approaching and receding sides is observed, similar to what is seen in the RC of NGC 3521. At larger radii, the RC flattens, even increases, displaying the characteristic *flat* RC. Although this simulation does not perfectly reproduce NGC 3521, there are many similarities between the RC from the mock HI data and observations. Both RCs show several bumps, wiggles, and a significant discrepancy between the approaching and receding sides⁴, indicating that the disk may not be in equilibrium.

The RC does not closely trace the mass distribution, suggesting that the RC may not be a reliable mass estimator for galaxies that have recently experienced a major merger. Although the RC underestimates the mass in this case, more reliable methods to generate and handle the simulations will be developed in future work.

4. For NGC 3521, the rotational velocity of the approaching side is initially smaller than that of the receding side, then becomes larger, whereas in the mock RC, the approaching side is always smaller. This suggests that further improvements of the simulation is needed.

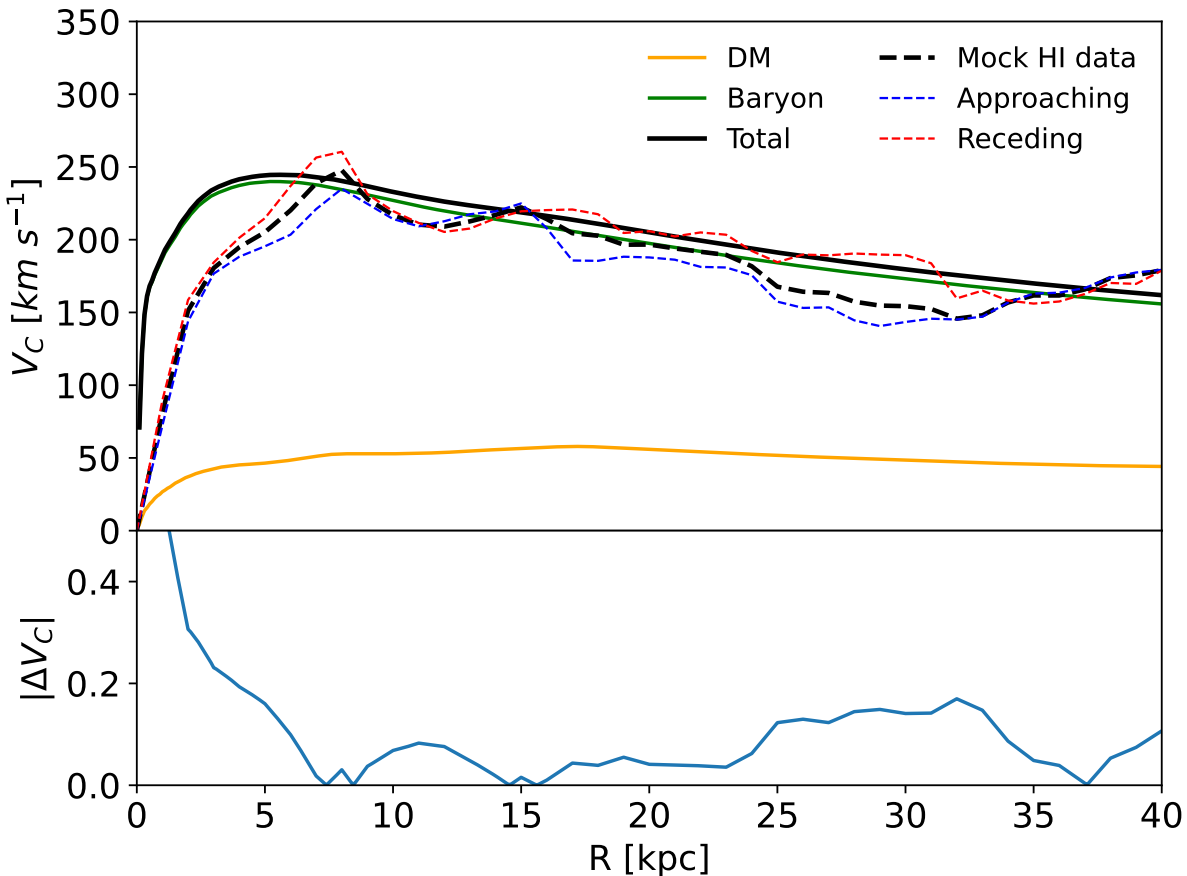


FIGURE 3.18 – Rotation curve (RC) of the mock HI observation from the simulation. **Top panel:** The solid black line represents the estimated rotational velocity based on the total mass distribution from the simulation. The orange and green lines show the contributions of dark matter (DM) and baryonic matter, respectively. The black dashed line indicates the RC derived from the mock HI data. Red and blue lines correspond to the velocities of the receding and approaching sides, respectively. **Bottom panel:** Differences between the RC from the mass distribution and that derived from the mock HI data.

5 Discussion

NGC 3521 is classified as an SABb (late-type) galaxy. McGaugh (2016) suggested that NGC 3521 is the closest structural analogue to the Milky Way (MW), sharing similar luminosity, scale length, and rotation curve characteristics. Pilyugin et al. (2023) further compared the radial oxygen abundance distribution and RC, arguing that NGC 3521 may be the most similar galaxy to the MW. Therefore, a detailed study of NGC 3521 and its comparison with the MW is of great significance for advancing our understanding of the role that major mergers may play in galaxy evolution.

5.1 Could we consider NGC 3521 experienced a recent major merger?

The morphology of NGC 3521 is consistent with the characteristics of galaxies that have undergone a recent major merger. Figure 3.1 reveals a broad, thick stellar disk and asymmetrical

features in the outskirts. The thick disk is likely formed from pre-existing stars, and the merger process contributes to its further thickening. After a major merger, the disk tends to stabilize from the inside out, leading to a symmetric inner disk and an asymmetric outer disk, consistent with the observed features of NGC 3521. The HI observations also show structures similar to those seen in the optical images.

The disk is stabilized from the inside out, therefore the inner disk could be in dynamical equilibrium, while the outer disk may not be. The RC of NGC 3521 displays a significant difference between the approaching and receding sides in the outer regions (Figure 3.3), which is inconsistent with dynamical equilibrium. Additionally, the position-velocity diagram of NGC 3521 (Figure 3.4) shows asymmetric features, further supporting the idea of a recent major merger influencing the dynamics of the galaxy.

During a major merger, gas is compressed, triggering the formation of new stars and resulting in a significant increase in star formation. The star formation history (SFH) of NGC 3521 shows a notable rise in star formation approximately 1-3 Gyr ago (Figure 3.11), which aligns with the hypothesis of a recent major merger.

In Section 4, we compared hydrodynamical simulations of a major merger with observations of NGC 3521. The simulations provide a reasonably⁵ match to both the observed HI data and the position-velocity diagram, suggesting that a single major merger could reproduce the observed structures in NGC 3521. Preliminary analysis of the RC derived from the mock HI data indicates that a recent major merger may also reproduce key characteristics observed in the RC of NGC 3521.

In summary, we propose that NGC 3521 likely experienced a recent major merger. It is important to note that a recent major merger is just one scenario that can explain the observed features. Alternative processes, such as AGN feedback or multiple minor mergers, may also account for these observations. However, a major merger remains the most plausible explanation, offering a comprehensive fit to the data in a single scenario. A brief summary of the evidence supporting a recent major merger in NGC 3521 is presented in Table 3.3.

TABLE 3.3 – Clues of a recent major merger of NGC 3521

	Characteristics	Figure	Major merger
Morphology	Broad thick disk	3.1	In favor
	Asymmetrical disk	3.1, 3.2	In favor
	HI observation	3.2	In favor
Dynamics	RC	3.3	In favor
	Asymmetric feature PV diagram	3.3 3.4	In favor
Stellar population	SFH peak	3.11	In favor

5. Not that bad.

5.2 Other galaxies

A brief summary of the other galaxies is provided in Table 3.4. Currently, I am lacking spectroscopic data for NGC 2903 and photometric data for NGC 2903, NGC 6946, and NGC 7793, which will require further efforts to collect or measure. The BPT diagrams for all⁶ galaxies are shown in Figure 3.19. The spectral-only fits and combined spectral-photometric fits for all galaxies are presented in Figures 3.20 and 3.21, respectively. The associated SFH⁷ estimates are shown in Figures 3.22 and 3.23. In the following, I describe the galaxies that we think could be modeled by recent major mergers.

5.2.1 NGC 2841

NGC 2841 is an Sb spiral galaxy. Our reconstructed stellar population does not indicate a significant star formation episode. Zhang et al. (2018), using the Dragonfly Telephoto Array, explored its stellar disk out to approximately 70 kpc⁸. They identified a warped disk beginning at around 30 kpc, which suggests an interaction between the outskirts of the disk and infall from the circumgalactic medium. We propose that this feature could be explained by a past major merger event.

5.2.2 NGC 5055

NGC 5055 (Messier 63) is an Sbc galaxy with an extended and warped tenuous outer H I disk. Significant tidal streams are observed in its halo (e.g., Martínez-Delgado et al., 2010; Alberts et al., 2011; Chonis et al., 2011; Staudaher et al., 2015; Liu et al., 2024). Its gas disk warp is about 20 degrees. However, most studies suggested that these streams are remnants of accreted satellites or minor mergers. We proposed that this could be explained by a recent major merger.

5.2.3 NGC 6946

NGC 6946 is a late-type spiral galaxy with a relatively small inclination angle, averaging 32.6° (de Blok et al., 2008). Its H I observations reveal numerous structures, such as H I holes and high-velocity gas (Kamphuis & Sancisi, 1993; Boomsma, 2007; de Blok et al., 2008). Aniyan et al. (2021) used high-resolution spectroscopy to identify two kinematically distinct populations of tracers within its disk. Spectrum fitting also indicates a continuous star formation episode. Based on these features, we propose that NGC 6946 may have undergone a recent major merger.

5.2.4 NGC 7331

NGC 7331 is an Sb spiral galaxy with prominent spiral arms. Its stellar population shows a peak around 1 Gyr, which may be associated with a recent major merger. The H I observations reveal an asymmetric structure, including a long tail to the north. Sutter & Fadda (2022)

6. For the galaxies that I have the associated data.

7. Stellar population proportion.

8. 23 times the inner scale length.

reported a significant young stellar population in the spiral arms using [C II] maps. These features are consistent with the effects of a major merger.

TABLE 3.4 – Summary of other galaxies

Galaxy	Morphology	Dynamics	Stellar population	Major merger
NGC 2403	–	–	in favor	–
NGC 2841	in favor	in favor	–	in favor
NGC 2903	–	–	–	–
NGC 3198	–	–	–	–
NGC 3521	in favor	in favor	in favor	in favor
NGC 5055	in favor	in favor	in favor	in favor
NGC 6946	–	–	in favor	–
NGC 7331	in favor	in favor	in favor	in favor
NGC 7793	–	–	–	–

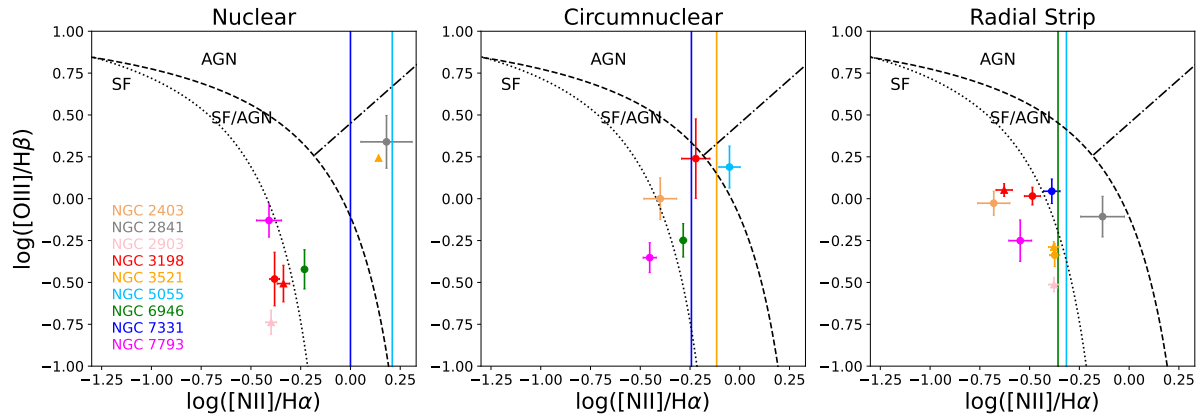


FIGURE 3.19 – Emission-line diagnostic diagram used to separate star-forming (SF) galaxies from active galactic nuclei (AGNs) for all selected galaxies. The dotted and dashed lines are the empirical and theoretical boundaries between SF galaxies and AGNs defined by Kauffmann et al. (2003) and Kewley et al. (2001). The dash-dotted line is the Seyfert/LINER division line from Cid Fernandes (2010). The triangle symbols represent the data coming from Moustakas & Kennicutt (2006) and the circle symbols represent the data coming from Moustakas et al. (2010). The vertical line presents the [N II]/H α ratio alone because of an unconstrained [O III]/H β ratio, where we adopt $\log([N II]/H\alpha) = -0.25$ as the boundary between the two classes. Different colors represent different galaxies as labeled in the first panel.

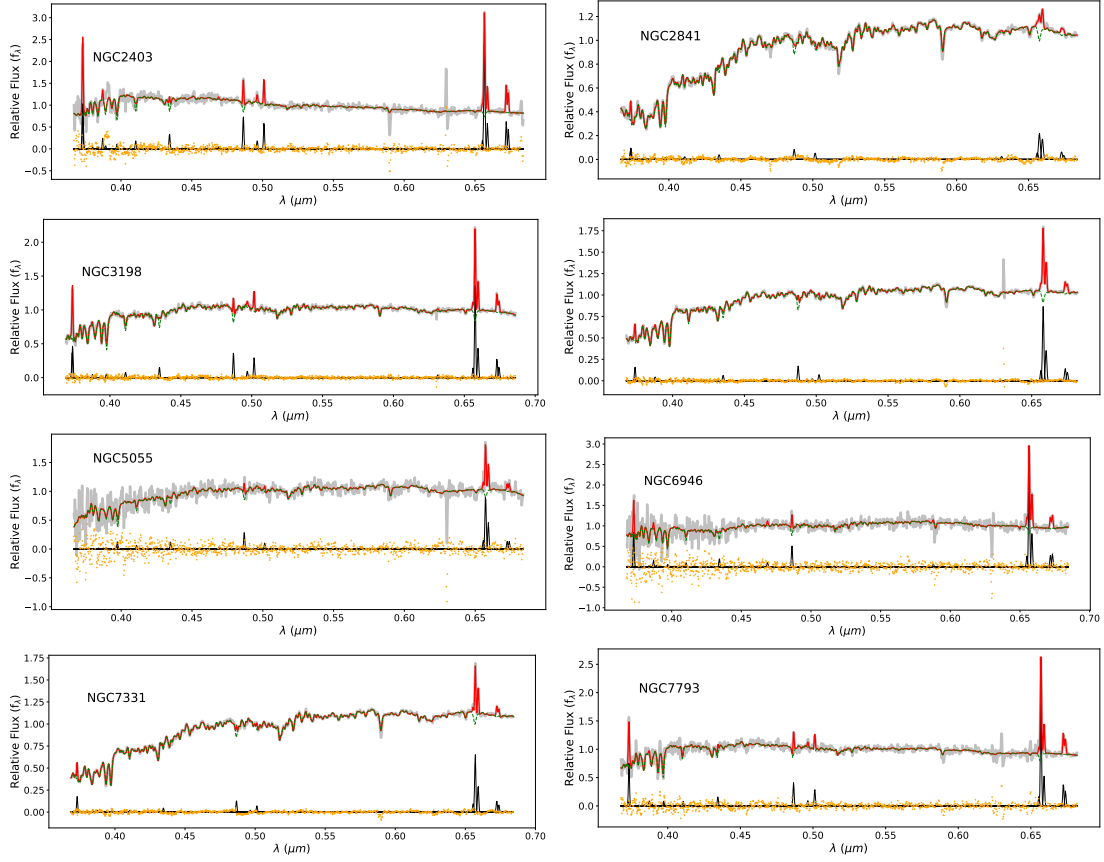


FIGURE 3.20 – Spectra-only fits of the selected galaxies. Same as Fig. 3.9. Each galaxies are labeled in the panels.

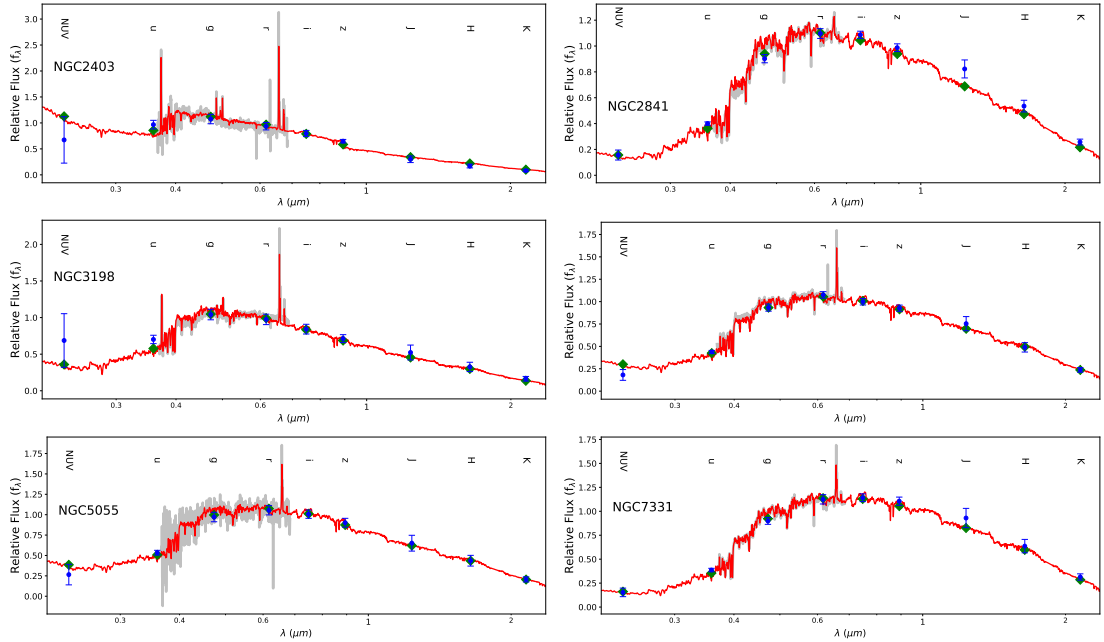


FIGURE 3.21 – Spectra and photometry fits of the selected galaxies. Same as Figure 3.10. Each galaxies are labeled in the panels.

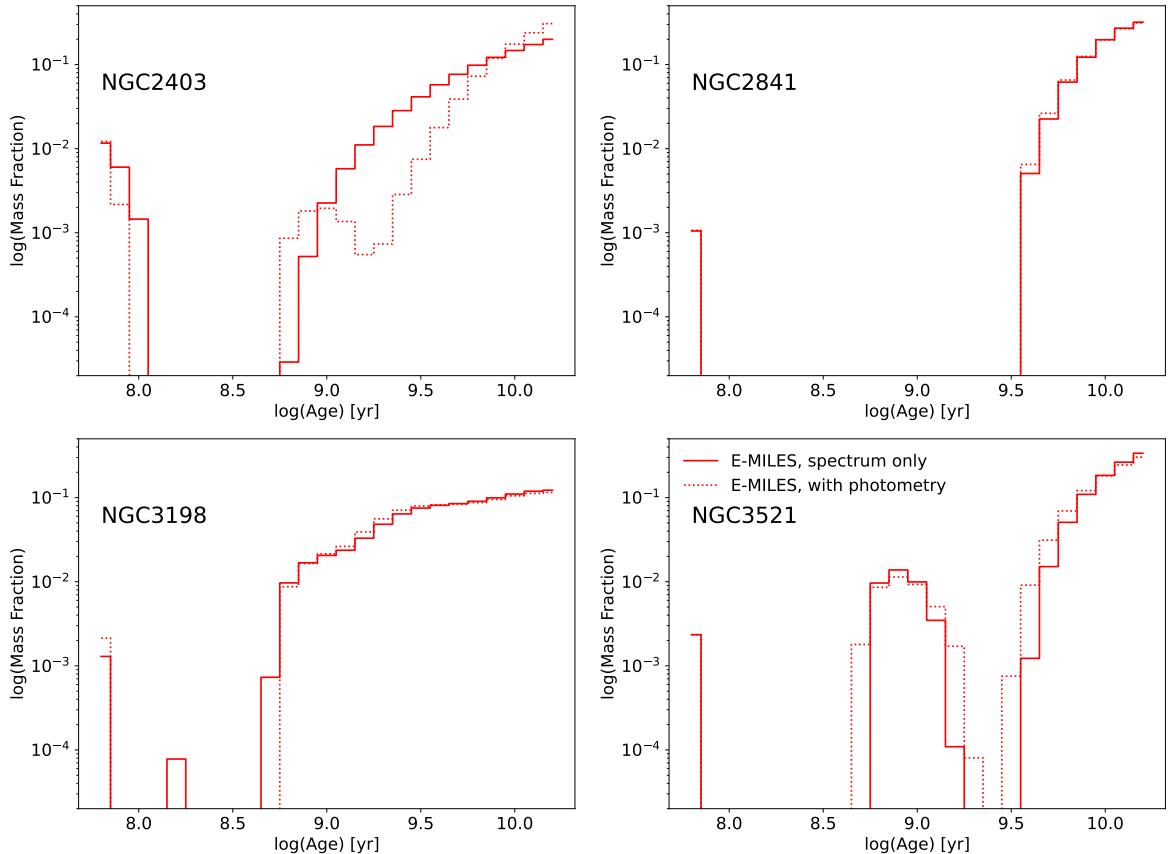


FIGURE 3.22 – The age distribution of the stellar population of the selected galaxies. Only use the E-MILES SPS model to fit the spectra and photometry. Each galaxies are labeled in the panels.

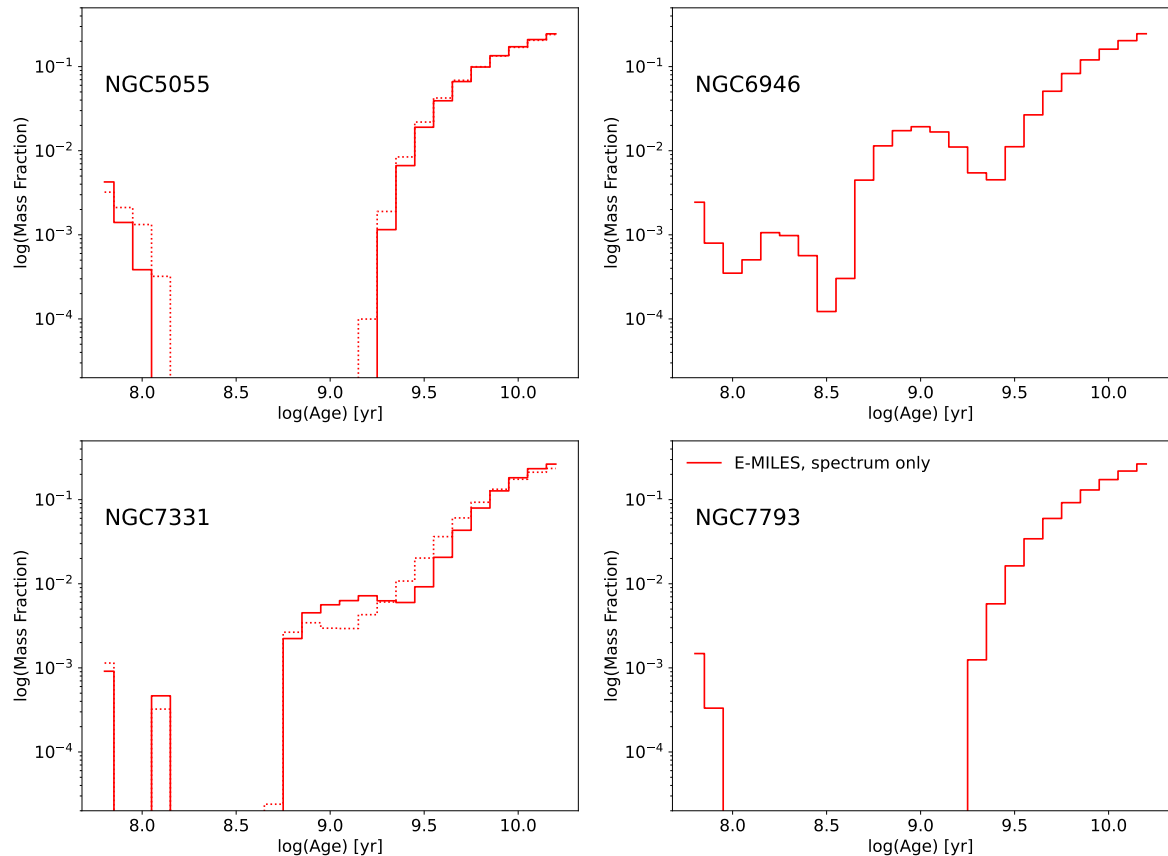


FIGURE 3.23 – The age distribution of the stellar population of the selected galaxies. Same as Figure 3.22. Each galaxies are labeled in the panels.

Chapitre 4

The Milky Way dwarf galaxies

Contents

1	Introduction	106
1.1	Historical perspective	106
1.2	Observations	107
1.3	Ram-pressure and tidal shock scenario	110
1.4	MW mass estimator	114
2	Comparison to cosmological simulations	116
2.1	Simulation samples	117
2.2	Methodology	119
2.3	Results	126
2.4	Discussion	128
3	Fornax	134
3.1	Data	134
3.2	Models and Results	137
3.3	Discussion	140
4	Conclusion	145

1 Introduction

The most widely accepted cosmological model, the Λ Cold Dark Matter (Λ CDM) paradigm, posits that structure formation in the universe proceeds bottom-up. According to this model, smaller galaxies form first and are the fundamental building blocks for larger ones. Massive galaxies subsequently emerge hierarchically through mergers or the accretion of these smaller systems (Chapter 1, Section 3.3). As predicted, the overwhelming majority of galaxies in the universe are dwarf galaxies. Therefore, studying dwarf galaxies is essential for understanding the formation and evolution of massive galaxies, including the Milky Way (MW).

Dwarf galaxies in the MW are particularly valuable for near-field cosmology due to their proximity, which allows for precise estimations of their intrinsic properties through large-scale surveys. These galaxies are generally considered to be dark matter (DM) dominated, with mass-to-light ratios (M/L) as high as $\sim 10^3$ under the assumption of self-equilibrium (Section 1.2.2). Over the past few decades, significant research has been conducted on their structure and kinematics (Mateo, 1998; Tolstoy et al., 2009; Walker et al., 2009b; Wolf et al., 2010; Battaglia et al., 2013; Muñoz et al., 2018; Simon, 2019), alongside comparisons with cosmological simulations (Moreno et al., 2022; Santistevan et al., 2023; Grand et al., 2024). The Gaia astrometric mission has further revolutionized the field, enabling multiple studies (Fritz et al., 2018; McConnachie & Venn, 2020; Li et al., 2021a; Battaglia et al., 2022) to derive six-dimensional phase-space information from a large number of stars.

By studying the orbital energy and infall times of dwarf galaxies, Hammer et al. (2023, 2024) have demonstrated that most dwarf galaxies are relatively recent arrivals in the MW halo. Their gas-rich progenitors likely lost the gas component through ram-pressure stripping and MW tidal shocks (Hammer et al., 2018b, 2019) during their recent accretion into the Galactic halo, which has contributed to the observed excess in velocity dispersion. This mechanism provides new insights into the nature of dwarf galaxies, the accretion history of the MW, and the broader context of galaxy evolution.

1.1 Historical perspective

Dwarf spheroidals (dSphs) are a class of dwarf galaxies characterized by absolute visual magnitudes ranging from -7.7 (Simon, 2019) to -18 (McConnachie, 2012), and central surface brightness values of $\nu_{\text{o},V} \sim 22 - 27$ mag, arcsec $^{-2}$. Dwarf galaxies with fainter absolute magnitudes are classified as ultra-faint dwarfs (UFDs, Simon, 2019). The Large and Small Magellanic Clouds (LMC/SMC), which are visible to the naked eye, are usually classified as dwarf irregular galaxies (dIrrs). The first dSphs, Sculptor, and following Fornax, were discovered by Shapley in 1938 using photographic plates (Shapley, 1938b,a). Subsequent discoveries of similar systems such as Leo I, Leo II, Draco, Ursa Minor, and Carina were identified by Harrington & Wilson (1950), Wilson (1955), and Cannon et al. (1977), also using photographic plates. The discovery of Sextans by the Automated Photographic Measuring (APM) facility at the University of Cambridge completed the census of the eight *classical* MW dSphs (Irwin et al., 1990).

In the new century, the discovery of dwarf galaxies has accelerated significantly, thanks to

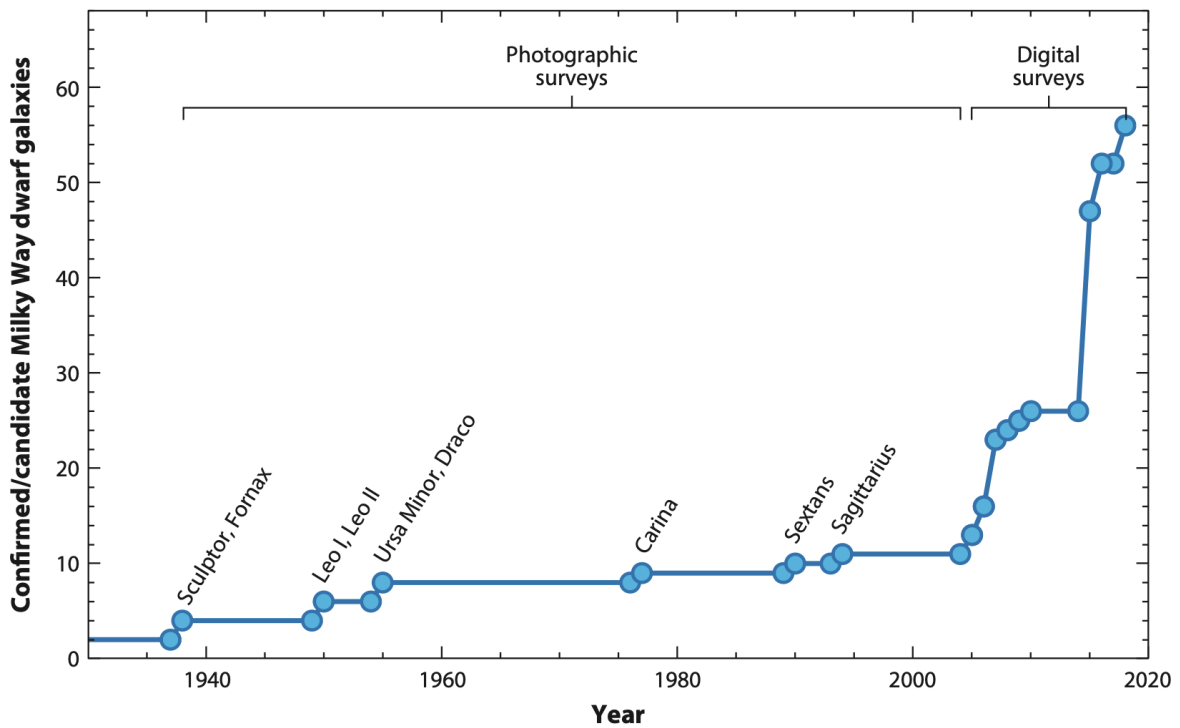


FIGURE 4.1 – Census of Milky Way dwarf galaxies as a function of time until 2019. This figure is adapted from Simon (2019).

large-scale surveys like the Sloan Digital Sky Survey (SDSS; 2005–2010), the Dark Energy Survey (DES), and the *Gaia* mission. Numerous studies have contributed to these discoveries (with a review provided by Simon, 2019). To date, approximately 60 dwarf galaxies have been identified (Figure 4.1).

A particularly notable discovery in the field came from spectroscopy rather than imaging. Ibata et al. (1994) identified the Sagittarius (Sgr) dwarf galaxy as an excess of stars with a narrow velocity distribution distinct from that of the MW bulge members during a stellar kinematic survey of the bulge. Subsequent observations revealed that the tidal tails of Sgr wrap extensively around the entire sky (Mateo et al., 1996; Ibata et al., 1997; Majewski et al., 2003; Belokurov et al., 2006b). Due to its tidal disruption, Sgr is often not considered a simple equilibrium system and is therefore excluded from some studies of dSph (e.g., Walker, 2013).

1.2 Observations

1.2.1 Surface brightness

The surface brightness profile of dSphs can be derived from stellar number counts. However, different studies often report varying results due to differences in photometric depth, completeness, spatial coverage, and the regions available for accurately determining the foreground stellar density. Much of the literature focuses on fitting different density profiles and searching for evidence of tidal stripping by the Milky Way in the outer regions of these galaxies.

Empirical King models (King, 1962) generally provide a better fit to the surface stellar number count profiles of Milky Way dSphs compared to simple exponential profiles (Irwin & Hatzidimitriou, 1995). Among the eight classical dSphs, only Leo II has not exhibited a “break” in its surface density profile. However, King models often fail to accurately represent the outer regions of these galaxies, typically underestimating the observed stellar densities (e.g., Irwin & Hatzidimitriou, 1995; Martínez-Delgado et al., 2001; Wilkinson et al., 2004; Coleman et al., 2005; Battaglia et al., 2006, 2008b). In some cases, a Sersic profile (Sersic, 1968), which declines more steeply than an exponential, or a Plummer profile (Plummer, 1911), can provide a better fit (e.g., Odenkirchen et al., 2001; Battaglia et al., 2006, 2008b; Yang et al., 2022).

This discrepancy is interesting because the excess stellar component in the outer regions could suggest the presence of a massive DM halo. Under this assumption, the stars in dSphs are embedded in extended, massive DM halos and therefore affected by the MW tidal effects (Section 1.2.2), or absence of DM halo, which suggests the ram-pressure and tidal shock scenario (Section 1.3).

1.2.2 Kinematics

Accurately measuring proper motions for individual stars in dwarf galaxies is extremely challenging, given their typical heliocentric distances ranging from 75 to 250 kpc. As a result, early studies of the internal kinematics of dwarf galaxies relied primarily on their line-of-sight velocity distributions (LOSVD).

The first measurement of LOSVD for a dwarf galaxy was made for the Draco dSph, with a value of 6.5 km s^{-1} based on observations of just three carbon stars (Aaronson, 1983). This hinted that the mass-to-light ratio (M/L) of Draco was several orders of magnitude higher than expected based on stellar mass alone, assuming the system was in equilibrium. Subsequent studies, incorporating larger samples that included red giant stars, confirmed this result (e.g., Armandroff & Da Costa, 1986; Aaronson & Olszewski, 1987; Hargreaves et al., 1994a,b).

Mateo et al. (1991) measured the kinematics of approximately 30 stars in the Fornax dSph, revealing that the flatness of the LOSVD profile suggested the presence of an extended DM halo. Subsequent large spectroscopic surveys (e.g., Queloz et al., 1995; Mateo et al., 1998; Tolstoy et al., 2004; Muñoz et al., 2006; Helmi et al., 2006; Battaglia et al., 2008a; Walker et al., 2009a) have greatly expanded the number of observed dwarfs, providing an extensive dataset to study their internal properties and better understand their DM content and kinematic behavior.

Significant efforts have been made in data analysis to derive reliable velocity dispersion (VD) profiles, accounting for factors such as measurement errors (e.g., Koposov et al., 2011), the impact of binary stars (Minniti et al., 2010; McConnachie & Côté, 2010; Martinez et al., 2011), and foreground star contamination (Martin et al., 2007; Siegel et al., 2008; Battaglia et al., 2008b; Willman et al., 2011). Figure 4.2 presents VD profiles for eight classical Milky Way dSphs, showing that the VDs in the luminous regions of these dSphs remain approximately constant. However, mass distributions derived from King models based on standard M/L ratios fail to reproduce the large VDs observed at large radii.

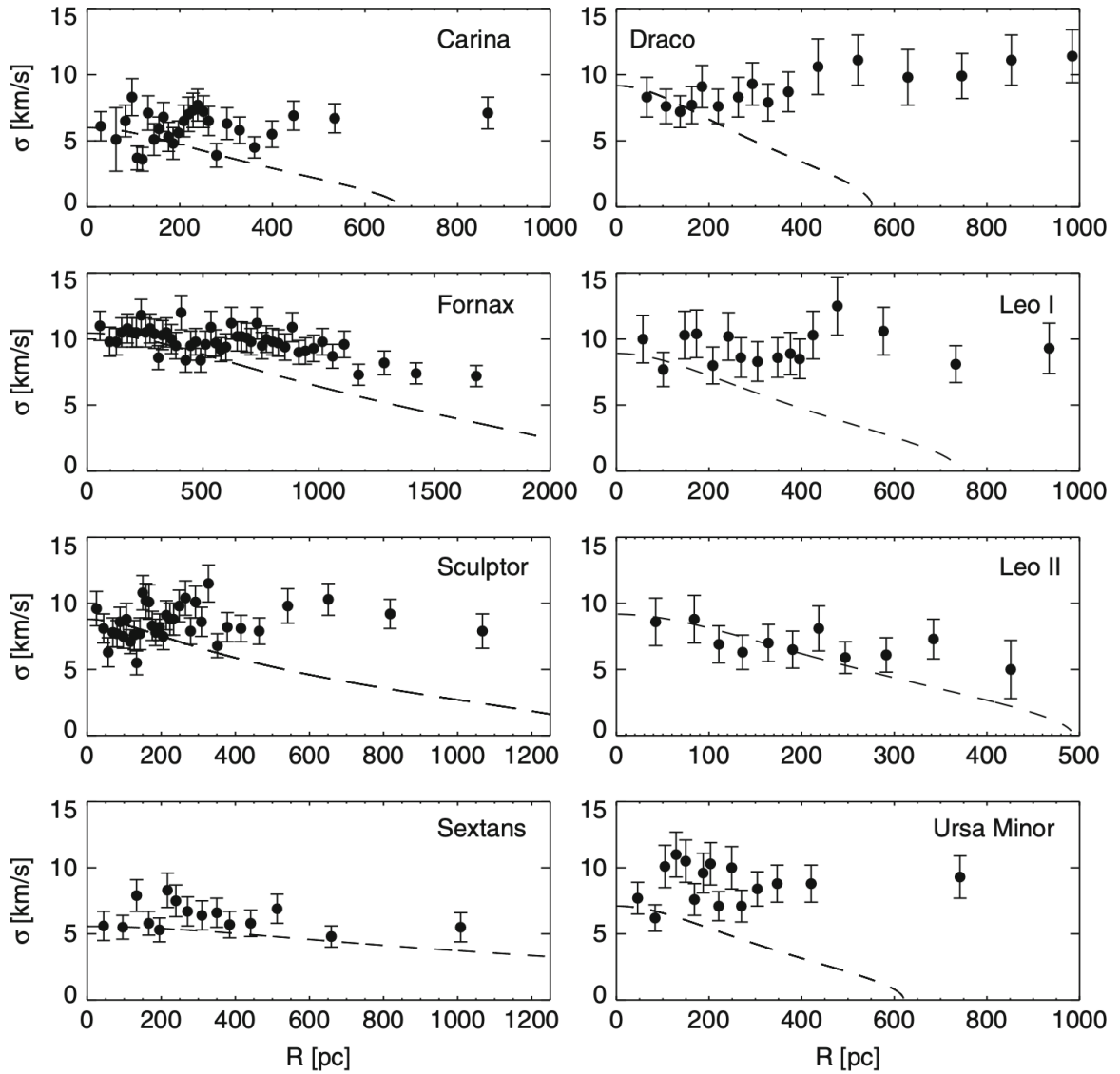


FIGURE 4.2 – Velocity dispersion profiles observed for 8 classical dSphs. Dash lines are King models based on M_\odot/L_\odot normalized to reproduce the observed central velocity dispersions. This figure is adapted from Walker (2013).

To use dynamical modeling to explain the flat behavior of VD in dSphs, it is crucial to determine whether these systems are in equilibrium. Most dSphs do not exhibit clear signs of tidal disturbance from the MW, such as tidal tails or isophote twists. Early studies suggested that most dSphs are gas-poor and predominantly composed of old stars. To explain their extended star formation histories (SFHs) and broad metallicity distributions (e.g., Tolstoy et al., 2004; Battaglia et al., 2006, 2011; Koch et al., 2006; Starkenburg et al., 2010), many studies have assumed that dSphs have been long-lived satellites of the MW for up to \sim 8–10 Gyr.

Under the assumption that these systems are long-lived satellites and in self-equilibrium, both theoretical models and simulations suggest that MW tides could create *breaks* in the density profiles of dSphs (e.g., Read et al., 2006; Muñoz et al., 2008; Peñarrubia et al., 2008; Klimentowski et al., 2009; Kazantzidis et al., 2011). However, these tidal forces alone cannot account for the high central VD values observed in these galaxies (e.g., Oh et al., 1995; Piatek & Pryor, 1995). To explain the large VD, dSphs must be dominated by DM. In this scenario, MW tides primarily affect the outskirts of classical dSphs, while stars in their cores are shielded by DM halos, allowing them to remain in approximate dynamical equilibrium (e.g., Muñoz et al., 2008; Battaglia et al., 2013; Walker, 2013; Simon, 2019).

Based on this assumption and the virial theorem, various dynamical analyses have been applied to constrain the DM density distribution in dSphs within the framework of Newtonian gravity. These methods include the use of analytic distribution functions (e.g., Wilkinson et al., 2002; Amorisco & Evans, 2011; Strigari et al., 2017), Schwarzschild orbit superposition techniques (e.g., Jardel et al., 2013; Breddels & Helmi, 2013; Hagen et al., 2019), and Jeans equations (e.g., Evans et al., 2009; Walker et al., 2009b; Walker, 2013; Wolf et al., 2010). Figure 4.3 presents the M/L ratio for classical dSphs and UFDs, showing that the dynamical M/L ratio increases monotonically as luminosity decreases, ranging from $M_{\text{dyn}}/L \sim 10$ for dSphs to $\sim 10^3$ for the faintest systems.

Although the virial mass of dwarf galaxies is poorly constrained due to the lack of tracers at large radii and uncertainties associated with extrapolating from tidal effects (Errani et al., 2015), there is consensus that a substantial amount of DM is required (Battaglia et al., 2013). Therefore, dwarf galaxies are considered prime candidates for the detection of DM particle annihilation signals (Walker, 2013; Strigari et al., 2018).

1.3 Ram-pressure and tidal shock scenario

Recent studies are challenging the assumption that dSphs are long-lived MW satellites. Using deep wide-field photometry and color-magnitude diagram (CMD) analysis, de Boer et al. (2013) reconstructed the star formation history (SFH) of Fornax, revealing a stellar population approximately 100 Myr old with near-solar metallicity. Similarly, Weisz et al. (2014a), using CMDs from *Hubble Space Telescope* (HST) imaging, obtained precise SFHs, showing that galaxies such as Carina, Fornax, Leo I, Ursa Minor, and Leo II sustained star formation until as recently as 1–2 Gyr ago. These findings suggest that gas played a significant role in the late-stage dynamical evolution of dSphs, as gas is the primary fuel for star formation, highlighting the importance of

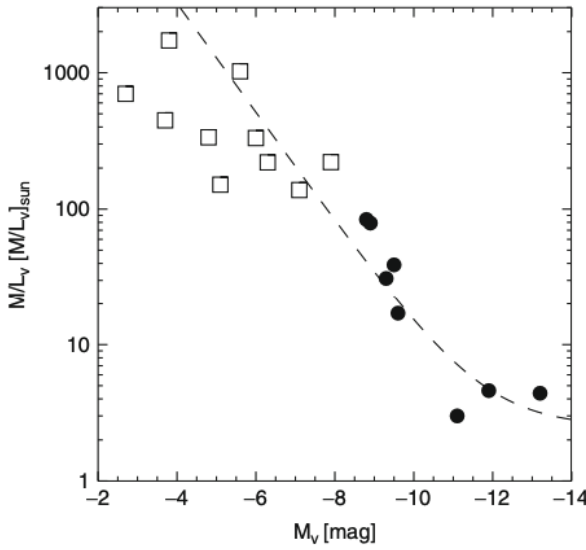


FIGURE 4.3 – Dynamical M/L ratio derived from mass-follows-light models as a function of luminosity. Data for the classical dSphs (filled circles) are from the review of Mateo (1998). Data for the UFDs (open squares) are from Simon & Geha (2007) and Martin et al. (2007). The dotted line corresponds to $M/L = 2.5 + 10^7 / (L/L_\odot)$. This figure is adapted from Walker (2013).

gas dynamics in shaping the recent history of these systems.

Most dwarf galaxies are observed near their pericenter, which is inconsistent with the distribution expected for long-lived satellites, as Kepler’s laws suggest they should predominantly be found near their apocenter. As shown in Figure 4.4. The orbital phase probability is defined by (Hammer et al., 2020):

$$P = \frac{t_{\text{peri}}}{t_{\text{peri}} - \min(t_{\text{apo}}, 300 \text{ kpc})}. \quad (4.1)$$

where t_{peri} is the orbital time for reaching or leaving the pericenter, and $\min(t_{\text{apo}}, 300 \text{ kpc})$ is the time taken from the pericenter to min(apocenter, 300 kpc). Therefore, Figure 4.4 presents the cumulative probability of having an excess of dwarf galaxy locations near the pericenter, assuming different MW mass models. Hammer et al. (2018b, 2019) identified a significant anti-correlation between the internal acceleration (measured as $\sigma_{\text{l.o.s}}^2 / r_{\text{half}}$) of dSphs and their Galactocentric distance. In the DM scenario, where DM dominates the internal dynamics, such a relationship with Galactocentric distance would not be expected. However, this anti-correlation aligns with predictions from models where dSphs are undergoing tidal shocks from the MW, consistent with the impulse approximation for high-velocity encounters (Binney & Tremaine, 2008).

This suggests that the progenitors of dSphs were initially gas-rich dwarf galaxies that entered the MW halo within the last few billion years. As they approached the MW, they lost their gas due to ram-pressure stripping caused by the MW hot halo gas. The subsequent loss of a significant portion of their gravitational potential caused the stellar populations to expand spherically. Additionally, some of the residual stellar body experiences energy exchange through tidal shocks from the MW. This process could explain the high VDs observed in dSphs without

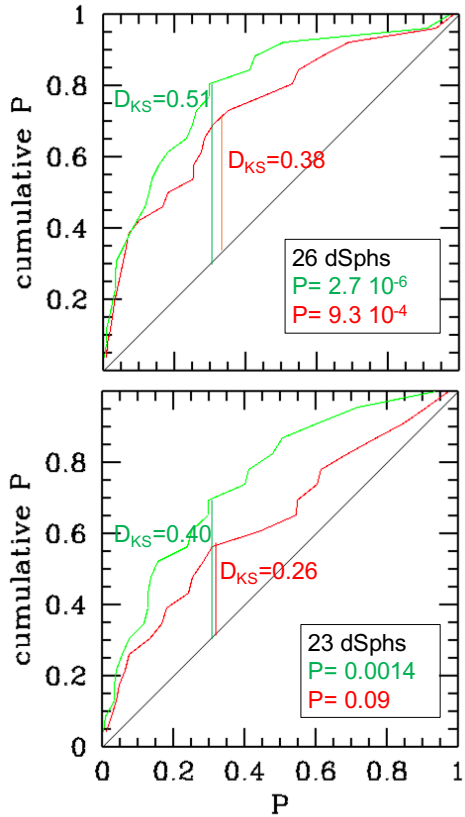


FIGURE 4.4 – Cumulative distribution of time to reach the pericenter divided by the time taken from pericenter to $\min(\text{apocenter}, 300 \text{ kpc})$. The black solid line shows the null hypothesis, i.e., dwarf galaxies have locations randomly distributed from pericenter to $\min(\text{apocenter}, 300 \text{ kpc})$. Green and red lines represent the NFW model fitted by Eilers et al. (2019, $M_{\text{tot}} = 8.1 \times 10^{11} M_{\odot}$), and the most massive Einasto profile able to fit the MW RC from Jiao et al. (2021, $M_{\text{tot}} = 15 \times 10^{11} M_{\odot}$), respectively. D_{max} values and associated probabilities of the Kolmogorov-Smirnov tests are given in the Figures, top and bottom panels representing the 90.5 (dubbed as small volume) and the 181 kpc (dubbed as large volume) distance slices of Drlica-Wagner et al. (2020), respectively. This figure is adapted from Li et al. (2021a).

requiring the presence of a DM-dominated halo.

For this scenario to be viable, the MW halo must be filled with diffuse, ionized gas at temperatures of several million Kelvin, commonly referred to as the Circumgalactic Medium (CGM, Tumlinson et al., 2017). Direct evidence for the CGM includes the detection of diffuse gas surrounding the MW (Anderson & Bregman, 2010; Miller & Bregman, 2013), while indirect evidence comes from the differing distributions of dSphs and dwarf irregular galaxies inside and beyond 300 kpc (Grcevich & Putman, 2009). A clear example of this process is seen in the Magellanic Stream, where ram pressure tails trailing behind the Magellanic Clouds have been observed (Mathewson et al., 1974; Nidever et al., 2010) and successfully modeled by the *ram-pressure and collision*¹ scenario (Hammer et al., 2015; Wang et al., 2019a). It is plausible that similarly strong ram pressure forces could strip gas from other infalling dwarf galaxies in the

1. A recent collision between Large Magellanic Cloud and Small Magellanic Cloud

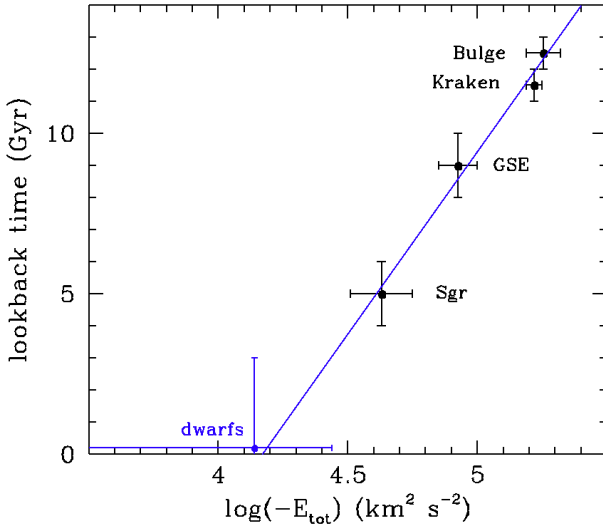


FIGURE 4.5 – Lookback time of stellar system entry in the Milky Way halo as a function of current binding energy for different families of globular clusters, and for the 25 dwarf galaxies that do not belong to the low energetic Sgr system (excluding then Sgr, Segue II, Tucana III, and Willman I) or to the high energetic LMC system (Carina II, Carina III, Horologium I, Hydrus I, Phoenix II, and Reticulum II). The *blue line* is a quick linear fit. A naïve interpretation is that dwarf satellites with $\log(-E_{\text{tot}}/\text{[km}^2 \text{ s}^{-2}\text{]}) < 4.17$ are on their initial approach, a value very close to the logarithm of the average energy (4.14) of 25 dwarfs, whose scatter provides an upper limit of $-E_{\text{tot}} = 4.34$. The latter combined with the linear fit suggests a lookback time of halo entry smaller than 3 Gyr. This figure is adapted from Hammer et al. (2023).

MW halo.

Hammer et al. (2023) explored the relationship between the half-light radius and orbital parameters (such as pericenter and total energy) of GCs and dwarf galaxies. Their study suggests that tidal forces from the MW could account for the observed correlation between the half-light radius and total energy. Using a MW mass model from Eilers et al. (2019), with a total mass of $8.3 \times 10^{11} M_\odot$, Hammer et al. (2023) identified a strong linear correlation between the look-back infall time and the logarithm of the binding energy for the MW, as illustrated in Figure 4.5. This analysis included GCs associated with the bulge, Kraken, Gaia-Sausage-Enceladus (GSE), and Sgr infalls, using estimates from Malhan et al. (2022) and Kruijssen et al. (2020). According to these studies, the respective events are estimated to have occurred approximately 12.5 ± 0.5 , 11.5 ± 0.5 , 9 ± 1 , and 5 ± 1 Gyr ago.

Cosmological simulations have also recovered a tight linear correlation between the look-back infall time and the logarithm of the binding energy, showing more than 1 dex evolution with a scatter of only 0.13 dex (Rocha et al., 2012). MW dwarf galaxies have much smaller binding energies significantly lower than those of the GSE GCs—by a factor of six on average—implying that they were accreted during a later epoch, rather than around 9 Gyr ago. In a follow-up study, Hammer et al. (2024) confirmed that ram-pressure stripping and Galactic tidal shocks significantly contribute to the large values of LOSVD in the dwarfs.

This mechanism has been previously explored through numerical simulations by Mayer et al. (2006) and Yang et al. (2014). Mayer et al. (2006) used hydrodynamical simulations to show that

the combined effects of ram-pressure stripping and tidal forces are more effective at removing gas from dwarf galaxies than either process acting alone. Similarly, Yang et al. (2014) demonstrated that low-mass tidal dwarf galaxies are particularly vulnerable to interactions with the MW disk and the halo hot gas. These interactions progressively drive the stellar populations of these dwarfs out of equilibrium, leading to significant expansion and the formation of low-surface-brightness features, while also mimicking high dynamical mass-to-light (M/L) ratios. The simulations also predict anisotropic VDs, with larger values along the line of sight (aligned roughly with the Galactocentric direction) and smaller values perpendicular to the orbital motion of dwarfs (Hammer et al., 2018b).

In more recent work, Wang et al. (2024) used hydrodynamical simulations to reproduce the structural properties of three dwarf galaxies—Sculptor, Antlia II, and Crater II—by assuming that their progenitors were gas-rich, rotation-supported dwarfs in their first infall (less than 3 Gyr ago). These simulations predict that a small fraction of young stars could still be present in both the cores and outskirts of these dwarfs. Yang et al. (2022) studied Fornax and found an extended stellar halo around it. In an upcoming study, Yang et al. (2024, accepted) analyzed data from *Gaia* DR3 and discovered that almost all dSphs contain young stellar populations, supporting the predictions of the ram-pressure stripping scenario.

1.4 MW mass estimator

Dwarf galaxies have long been used to constrain the mass of the MW. Before the *Gaia* mission, proper motion (PM) measurements were available for only a few of these galaxies, and most were assumed to be long-lived satellites in dynamic equilibrium with the MW potential. By making assumptions about velocity isotropy or anisotropy, the MW's mass profile, and the spatial distribution of dwarfs, researchers could estimate the enclosed mass using just the line-of-sight velocity and the Jeans equation. Watkins et al. (2010) applied a power-law mass estimator and derived a mass within 300 kpc of $M(< 300\text{kpc}) = (0.9 \pm 0.3) \times 10^{12}, M_{\odot}$ under the assumption of isotropy. When considering velocity anisotropy, they reported a broader range of $(0.7 - 3.4) \times 10^{12}, M_{\odot}$.

One peculiar case is Leo I, which has a large Galactocentric distance and high velocity ($d_{\text{GC}} = 257.9_{-14.6}^{+17.0}$ kpc and $v_{3\text{D}} = 190.2_{-11.9}^{+15.9}$ km s $^{-1}$, Li et al., 2021a). In their analysis, Leo I alone contributed approximately 27% of the total influence on the MW mass estimate compared to other satellites. Boylan-Kolchin et al. (2013) showed that assuming Leo I is a bound satellite results in an overestimation of the MW's mass by about 30%.

With the advent of *Gaia* DR2 PM data, Fritz et al. (2018) robustly identified member stars of 39 MW dwarf galaxies and provided average PMs for these systems. By considering constraints such as maintaining reasonable orbital apocenter distributions and ensuring a plausible fraction of bound satellites, they argued that a more massive MW, with a mass of $1.6 \times 10^{12} M_{\odot}$, is more likely than a lighter MW of $0.8 \times 10^{12} M_{\odot}$. Fritz et al. (2020) expanded on this work, applying the mass estimator from Watkins et al. (2010) to 45 satellites using *Gaia* PMs. Accounting for systematic uncertainties, especially those related to the Large Magellanic Cloud (LMC) and its

satellites, they estimated the MW enclosed mass to be $5.8^{+1.5} - 1.4 \times 10^{11} M_{\odot}$ within 64 kpc and $14.3^{+3.5} - 3.2 \times 10^{11} M_{\odot}$ within 273 kpc.

Given that the assumption of virial equilibrium may be questionable for the satellite population, some studies have shifted to estimating the MW mass by comparing the distribution of satellites with cosmological simulations. These simulations are considered to provide more reliable dynamical models for dwarf galaxies within the framework of hierarchical structure formation. The phase-space distribution functions (DFs) offer a complete description of the dynamical structure of a system. By expressing these DFs in terms of classical integrals of motion or actions, one can use them to fit the observed positions and velocities of tracer objects, such as dwarf satellites, and thereby constrain the MW gravitational potential. This method leverages the full phase-space information, including both spatial and velocity data, to obtain a more accurate estimate of the MW mass.

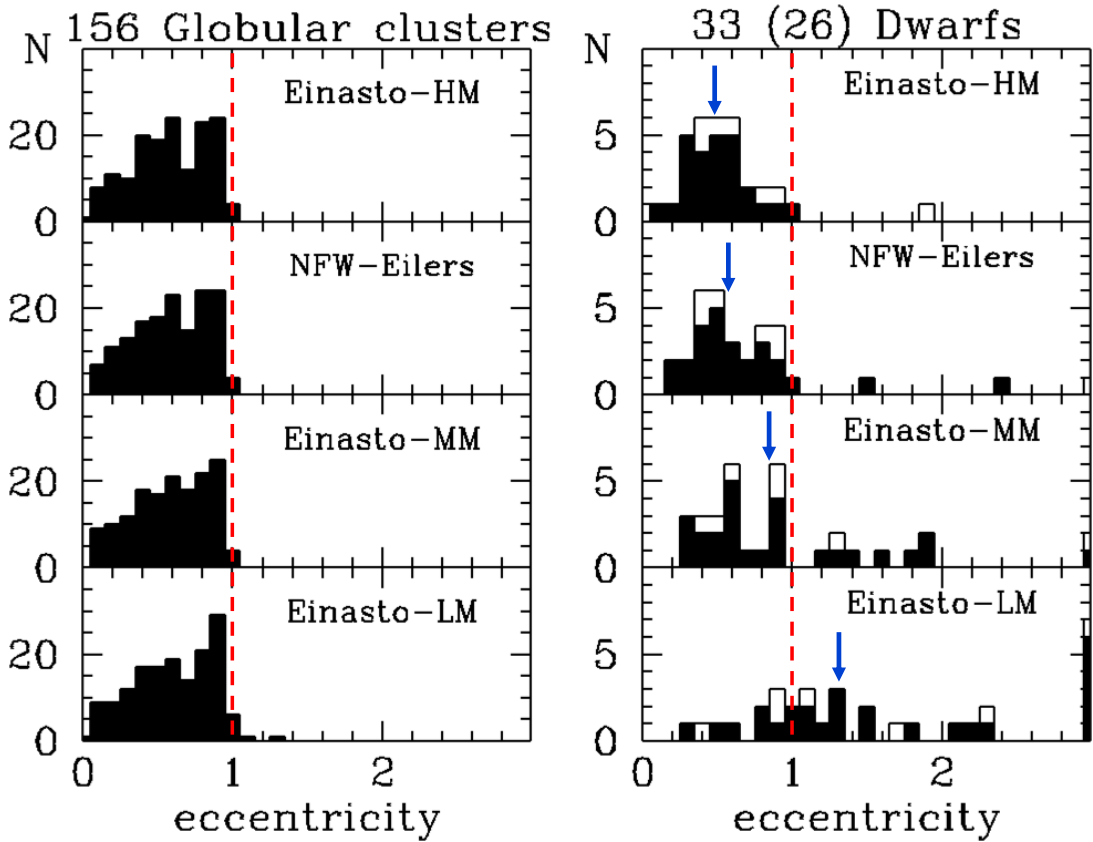


FIGURE 4.6 – Histograms of the eccentricity distribution of GCs (*left*) and dwarf galaxies (*right*) for four MW mass models (decreasing total mass from top to bottom) that are consistent with the MW rotation curve (Jiao et al., 2021). *Open* and *filled histograms* represent all the 33 dwarfs, and a subsample of 26 of them having their internal velocity dispersion measured. The *blue arrows* in the right panels indicate the median eccentricities of 0.478, 0.581, 0.829, and 1.301 from the top to the bottom. The *vertical red-dashed line* delimits $\text{ecc}=1$.

Little & Tremaine (1987) applied a statistical analysis based on the Bayesian theorem, fitting the DF to the observed positions and velocities of 8 dwarf galaxies (including the LMC and SMC) and 7 GCs, estimating the MW median mass to be $2.4 \times 10^{11} M_{\odot}$ at a radius of 107 kpc and

providing an upper limit of $5.2 \times 10^{11} M_{\odot}$ at the 95% confidence level. Since then, this DF method has been widely adopted to estimate the MW mass, not only using tracers like dwarf galaxies and GCs but also incorporating stars and stellar streams (e.g., Kochanek, 1996; Sakamoto et al., 2003; Deason et al., 2012; Binney & Wong, 2017; Li et al., 2020; Vasiliev et al., 2021; Wang et al., 2022a; Koposov et al., 2023; Ibata et al., 2024).

Studies focusing on dwarf galaxies have confirmed that excluding certain peculiar dwarfs, such as Leo I, from the sample can significantly lower the estimated MW mass. For instance, using both GCs and the MW RC from *Gaia* DR2, Wang et al. (2022a) found that excluding Crater and Pyxis, which have large orbital energies, reduced their MW mass estimate from $5.73^{+0.76} - 0.58 \times 10^{11} M_{\odot}$ to $5.36^{+0.81} - 0.68 \times 10^{11} M_{\odot}$, assuming an Einasto profile. Similarly, Hammer et al. (2024) demonstrated that including GCs does not significantly impact MW mass estimates. As illustrated in Figure 4.6, the eccentricities of GCs remain below 1 for a wide MW mass range of $2.8 - 15 \times 10^{11} M_{\odot}$. However, a lower MW mass results in a greater number of dwarfs having eccentricities greater than 1, suggesting that these dwarfs may not be gravitationally bound to the MW.

2 Comparison to cosmological simulations

In the hierarchical galaxy formation scenario, structures grow from the inside out (Chapter 1, Section 3.3). As a result, recently accreted satellites tend to have lower binding energies compared to those captured earlier by the host galaxy. Since the host galaxy's mass increases over time, the satellites accreted earlier are naturally more gravitationally bound (Rocha et al., 2012; Boylan-Kolchin et al., 2013). In addition, early-arriving satellites experience more orbital interactions and encounters, which lead to the gradual loss of their orbital energies (Hammer et al., 2023, 2024). Cosmological simulations reveal a strong linear correlation between the look-back infall time and the logarithm of binding energy (Rocha et al., 2012). This relationship is consistent with the slope derived from the MW accretion history (Hammer et al., 2023), suggesting that most MW dwarf galaxies have infall look-back times of less than 3 Gyr.

Dwarf galaxies have long been regarded as ideal tracers for measuring the MW's mass at large radii. However, recent studies have demonstrated that MW mass estimates can be significantly impacted by the inclusion of peculiar dwarfs, as previously discussed (Chapter 4, Section 1.4). Comparing the observed relationship between infall lookback time and binding energy with cosmological simulations provides a more reliable approach to mass estimation because, in principle, this method does not depend on the assumption of dynamical equilibrium. A more massive galaxy has a deeper gravitational potential well, allowing it to capture satellites with lower binding energies (e.g., Leo I).

This is particularly relevant given that MW mass estimates derived from RCs using *Gaia* data are substantially lower than other estimates (Chapter 2). Our goal is to estimate the MW mass by comparing the infall lookback time and binding energy of MW satellites with predictions from cosmological simulations. In principle, simulations that accurately reproduce the infall lookback times and binding energies of key structures such as the bulge, GSE, and Sgr GCs should yield

reliable estimates of the MW mass.

This research has been submitted to *Astronomy & Astrophysics* as a letter (First author: François Hammer) and is currently under review. My contribution involved deriving the data from cosmological simulations. The following sections present the simulations used, the data extraction process, and the comparisons made to the observed properties of the MW. Section 2.1 provides a brief overview of the cosmological simulations used in this study. Section 2.2 details the method for deriving data from these simulations. Section 2.3 presents the comparisons between the observed MW properties and the selected cosmological simulations. Finally, Section 2.4 discusses the relevance of cosmological simulations for reproducing MW properties.

2.1 Simulation samples

Rocha et al. (2012) used the Via Lactea II (VL2) simulation for their analysis of satellite orbits and infall times (Diemand et al., 2007; Kuhlen et al., 2010). The VL2 simulation is a high-resolution Λ CDM cosmological simulation that focuses on a DM halo of approximately the same size as the one that hosts the MW, with a maximum circular velocity $V_{\max} = 201 \text{ km s}^{-1}$ at $z=0$. The cosmology assumed in this simulation is taken from the flat-universe six-parameter analysis of the *Wilkinson Microwave Anisotropy Probe* (WMAP) 3-year data set (Spergel et al., 2007): $\Omega_m = 0.238$, $\Omega_\Lambda = 0.762$, $h = 0.73$, $n_s = 0.951$, $\sigma_8 = 0.74$. The resolution of VL2 is high enough, with particle masses of $4.1 \times 10^3 M_\odot$ each, to resolve thousands of subhaloes bound to the main host. Rocha et al. (2012) have selected a sample of ~ 2000 bound subhaloes with maximum circular velocities $V_{\max} > 5 \text{ km s}^{-1}$ at $z=0$ and studied their dynamics. In this study, we directly use this subhalo sample.

We also use the cosmological zoom-in baryonic simulations of MW-mass galaxies in both isolated and LG-like environments from the Feedback In Realistic Environments (FIRE) project² (Hopkins et al., 2018). FIRE simulations using the hydrodynamic plus N -body code GIZMO (Hopkins, 2015), with the mesh-free finite-mass (MFM) hydrodynamics method (Hopkins, 2015), and the FIRE-2 physics model that includes several radiative heating and cooling processes such as Compton scattering, Bremsstrahlung emission, photoionization and recombination, photoelectric, metal-line, molecular, fine-structure, dust-collisional, and cosmic-ray heating across temperatures $10-10^{10} \text{ K}$ (Hopkins et al., 2018). The FIRE-2 physics model also includes the spatially uniform and redshift-dependent cosmic ultraviolet (UV) background from Faucher-Giguère et al. (2009), for which H I reionization occurs at $z_{\text{reion}} \approx 10$. Stars form in gas that is self-gravitating, Jeans unstable, molecular (following Krumholz & Gnedin, 2011), and dense ($n_H > 1000 \text{ cm}^{-3}$), and represent single stellar populations, assuming a Kroupa (2001) initial mass function. Stars then evolve along stellar population models from STARBURST99 v7.0 (Leitherer et al., 1999), inheriting masses and elemental abundances from their progenitor gas cells. FIRE-2 simulations include stellar feedback processes like core-collapse and white-dwarf (Type Ia) supernovae, stellar winds, and radiation pressure.

We selected seven m12* simulations from FIRE-2 DR (Wetzel et al., 2023) with mass range

2. See the FIRE project website: <http://fire.northwestern.edu>

$1 - 2 \times 10^{12} M_{\odot}$ (except m12z), which is slightly larger than most mass estimates. Considering they provide the mass of M_{200m} at the radius ($\sim 300 - 400$ kpc) within which the mean density is 200 times the matter density of the universe, these masses are reasonable. We did not select MW+M31 pairs to prevent potential interactions between these two massive galaxies. Table 4.1 lists the properties of selected halos at $z=0$ and associated simulation details. We use python packages GIZMOANALYSIS (Wetzel & Garrison-Kimmel, 2020a) and HALOANALYSIS (Wetzel & Garrison-Kimmel, 2020b) to derive the quantities we need.

 TABLE 4.1 – Selected 7 simulations at $z=0$ from FIRE-2 cosmological simulations.

Name	M_{200m} M_{\odot}	R_{200m} kpc	$M_{\text{star},90}$ M_{\odot}	m_{baryon} M_{\odot}	m_{dm} M_{\odot}	$\epsilon_{\text{gas,min}}$ pc	ϵ_{star} pc	ϵ_{dm} pc	N_{dm}	cosmology	reference
m12z	9.25×10^{11}	307	2.0×10^{10}	4200	21,000	0.4	3.2	33	1.27×10^8	Z	G19
m12w	1.08×10^{12}	319	5.7×10^{10}	7100	39,000	1.0	4.0	40	7.33×10^7	P	S20
m12i	1.18×10^{12}	336	6.3×10^{10}	7100	35,000	1.0	4.0	40	7.05×10^7	A	W16
m12c	1.35×10^{12}	351	5.8×10^{10}	7100	35,000	1.0	4.0	40	1.51×10^8	A	G19
m12b	1.43×10^{12}	358	8.5×10^{10}	7100	35,000	1.0	4.0	40	7.45×10^7	A	G19
m12m	1.58×10^{12}	371	1.1×10^{11}	7100	35,000	1.0	4.0	40	1.41×10^8	A	H18
m12f	1.71×10^{12}	380	7.9×10^{10}	7100	35,000	1.0	4.0	40	9.62×10^7	A	G17

Name: this generally indicates the (log) halo mass, to order of magnitude. M_{200m} and R_{200m} : total mass and spherical radius within which the mean density is 200 times the matter density of the universe. $M_{\text{star},90}$: stellar mass within a spherical radius that encloses 90% of the stellar mass within 20 kpc. m_{baryon} and m_{dm} : initial masses of baryonic (gas or star) and dark-matter particles; gas cells can be up to 3 times more massive than this, because they gain mass from stellar ejecta/winds; for star particles this represents the typical mass at formation, but because of stellar mass loss, the typical star particle is $\approx 30\%$ smaller than this. $\epsilon_{\text{gas,min}}$: minimum adaptive force softening (Plummer equivalent) for gas cells (equals the hydrodynamic smoothing kernel). ϵ_{star} and ϵ_{dm} : force softening (Plummer equivalent) for star and dark-matter particles. N_{dm} : number of high-resolution dark-matter particles in the zoom-in region; the total number of particles (including gas and stars) is approximately twice this. Cosmology: cosmological parameters used in the simulation, as follows: A ('AGORA': $\Omega_m = 0.272, \Omega_{\Lambda} = 0.728, \Omega_b = 0.0455, h = 0.702, \sigma_8 = 0.807, n_s = 0.961$); P ('Planck': $\Omega_m = 0.31, \Omega_{\Lambda} = 0.69, \Omega_b = 0.048, h = 0.68, \sigma_8 = 0.82, n_s = 0.97$); N ($\Omega_m = 0.266, \Omega_{\Lambda} = 0.734, \Omega_b = 0.044, h = 0.71, \sigma_8 = 0.801, n_s = 0.963$); E ($\Omega_m = 0.266, \Omega_{\Lambda} = 0.734, \Omega_b = 0.0449, h = 0.71, \sigma_8 = 0.801, n_s = 0.963$). Z ($\Omega_m = 0.2821, \Omega_{\Lambda} = 0.7179, \Omega_b = 0.0461, h = 0.697, \sigma_8 = 0.817, n_s = 0.9646$); Reference: Wetzel et al. 2016 (W16); Garrison-Kimmel et al. 2017 (G17); Hopkins et al. 2018 (H18); Garrison-Kimmel et al. 2019a (G19); Samuel et al. 2020 (S20).

Auriga is a suite of gravo-magnetohydrodynamic cosmological zoom-in simulations run with the moving-mesh code AREPO. All simulations follow the evolution of gas, dark matter, stars, and black holes according to a comprehensive galaxy formation model from a starting redshift of 127 down to the present day. We selected 6 MW-size halos and 9 low-mass MW halos with resolution “level 3” and “level 4”, respectively. Table 4.2 lists some details of selected halos. More details about simulations, including initial conditions, numerical methods, and physical models are presented in Grand et al. (2024).

TABLE 4.2 – Selected 15 simulations at $z=0$ from Auriga cosmological simulations.

Name	M_{200c} $10^{10} M_\odot$	R_{200c} kpc	M_{star} $10^{10} M_\odot$	m_{baryon} M_\odot	m_{DM} M_\odot	ϵ_{comov} cpc	$\epsilon_{\text{phys}}(z < 1)$ pc
Level 4 resolution							
L1	51.230	168.673	2.099	5×10^4	4×10^5	750	375
L2	84.380	199.194	2.704	5×10^4	4×10^5	750	375
L3	97.621	209.118	4.979	5×10^4	4×10^5	750	375
L5	67.605	185.005	3.026	5×10^4	4×10^5	750	375
L6	72.729	189.571	3.885	5×10^4	4×10^5	750	375
L7	67.286	184.717	3.287	5×10^4	4×10^5	750	375
L8	84.468	199.266	5.287	5×10^4	4×10^5	750	375
L9	53.354	170.974	2.905	5×10^4	4×10^5	750	375
L10	71.805	188.755	4.006	5×10^4	4×10^5	750	375
Level 3 resolution							
6	101.480	211.834	6.395	6×10^3	5×10^4	375	178
16	150.430	241.530	9.098	6×10^3	5×10^4	375	178
21	141.548	236.688	8.800	6×10^3	5×10^4	375	178
23	150.374	241.501	8.996	6×10^3	5×10^4	375	178
24	146.791	239.568	8.698	6×10^3	5×10^4	375	178
27	169.632	251.400	9.876	6×10^3	5×10^4	375	178

Name: ‘L’ means low-mass MW halos. M_{200c} and R_{200c} : total mass and spherical radius at where the mean density is 200 times the critical density of the universe. M_{star} : stellar mass within R_{200c} . m_{DM} : the dark matter particle mass. M_{baryon} the baryonic particle/cell mass. ϵ_{comov} : the comoving softening length in unit of cpc. $\epsilon_{\text{phys}}(z < 1)$: the maximum physical softening length. The adopted cosmological parameters are $\Omega_m = 0.307$, $\Omega_b = 0.048$, $\Omega_\Lambda = 0.693$, $\sigma_8 = 0.8288$, and a Hubble constant of $H_0 = 100 h \text{ km s}^{-1} \text{ Mpc}^{-1}$, where $h = 0.6777$, taken from Planck Collaboration et al. (2014).

2.2 Methodology

Our goal was to account for isolated simulated galaxies as well as to account for the simulations with the highest resolution as well as considering the largest possible range for the simulated halo masses. FIRE simulations provided infall look-back times for identified sub-halos related to the main halo (Wetzel et al., 2023), while Auriga did not release this quantity. To derive the infall look-back time of sub-halo in Auriga simulations, we have generated the whole orbital history of sub-halos and compared their orbits to the evolution of R_{200} . Rocha et al. (2012) used the virial radius R_{200m} for estimating the infall times as well as probably done by FIRE, while AURIGA provides the virial radius R_{200c} at which the mean density is 200 times the critical density. For consistency reasons, we have calculated the virial radius R_{200m} of 15 MW-like simulations from AURIGA at $z = 0$ (the last snapshot) with $\Omega_m = 0.30966$ (Planck

Collaboration et al., 2020) and $\rho_{\text{crit}} = 1.34 \times 10^{-7} M_{\odot} \text{ pc}^{-3}$ (Hinshaw et al., 2013). We perform a linear fit on these radii and then roughly convert *all* R_{200c} values of *all* simulations at *each* redshift to R_{200m} using this linear relation as presented in Figure 4.7. Finally, we assume the infall epoch to be that of the last entry of the sub-halo within R_{200m} as shown in the top panel of Figure 4.8.

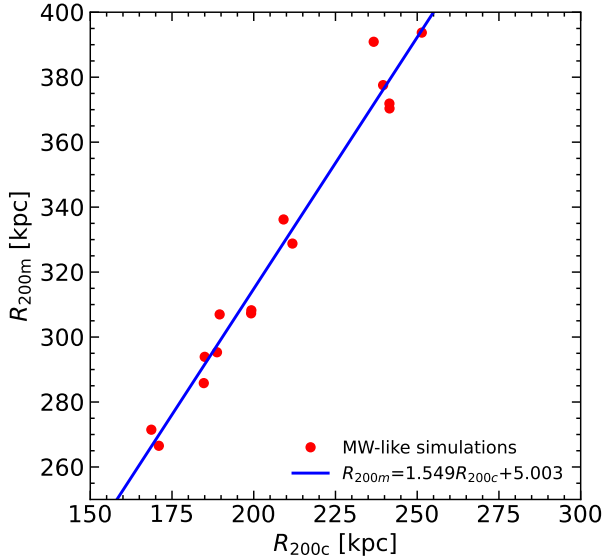


FIGURE 4.7 – Linear relation of R_{200m} and R_{200c} for different MW-like galaxies realized from Auriga simulations.

During this exercise, we realized that some sub-halos were lacking information about their orbital positions (e.g. bottom panel in Figure 4.8), which renders unreliable the infall time estimate. Going one step further, we found this to occur essentially for high-resolution (resolution 3, $5 \times 10^4 M_{\odot}$ per DM particle) simulated sub-halos with less than 100 particles. Therefore, we have adopted a secure mass limit for sub-halos to be $10^7 \times M_{\odot}$, a value we have also adopted for FIRE simulated sub-halos ($3.5 \times 10^4 M_{\odot}$ per DM particle). We have also used the same mass limit for low-resolution (resolution 4, $4 \times 10^5 M_{\odot}$ per DM particle) low-mass, AURIGA sub-halos because otherwise, their numbers become too small to allow an efficient fit of the MW accretion history relation. It means that the latter relation is less precise for low-mass AURIGA halos L1 to L10.

In Figure 4.9, we present the relationship between total velocity and infall look-back time for sub-halos in the m12c and m12z simulations from FIRE2, as well as level 3, halo 6 and 27 from Auriga. Notably, the distribution of derived infall look-back times for sub-halos in the Auriga simulations shows significant differences when compared to those in FIRE, despite comparing different simulations. In the figure, we only include sub-halos with masses greater than $10^7 M_{\odot}$.

First, in the FIRE simulations, there are almost no recently accreted sub-halos; most have infall times greater than ~ 3 Gyr. In contrast, the Auriga simulations show that most sub-halos appear to have been accreted more recently (within the past 4 Gyr). Secondly, sub-halos close to the center in the Auriga simulations tend to either be recently accreted (around 2 Gyr)

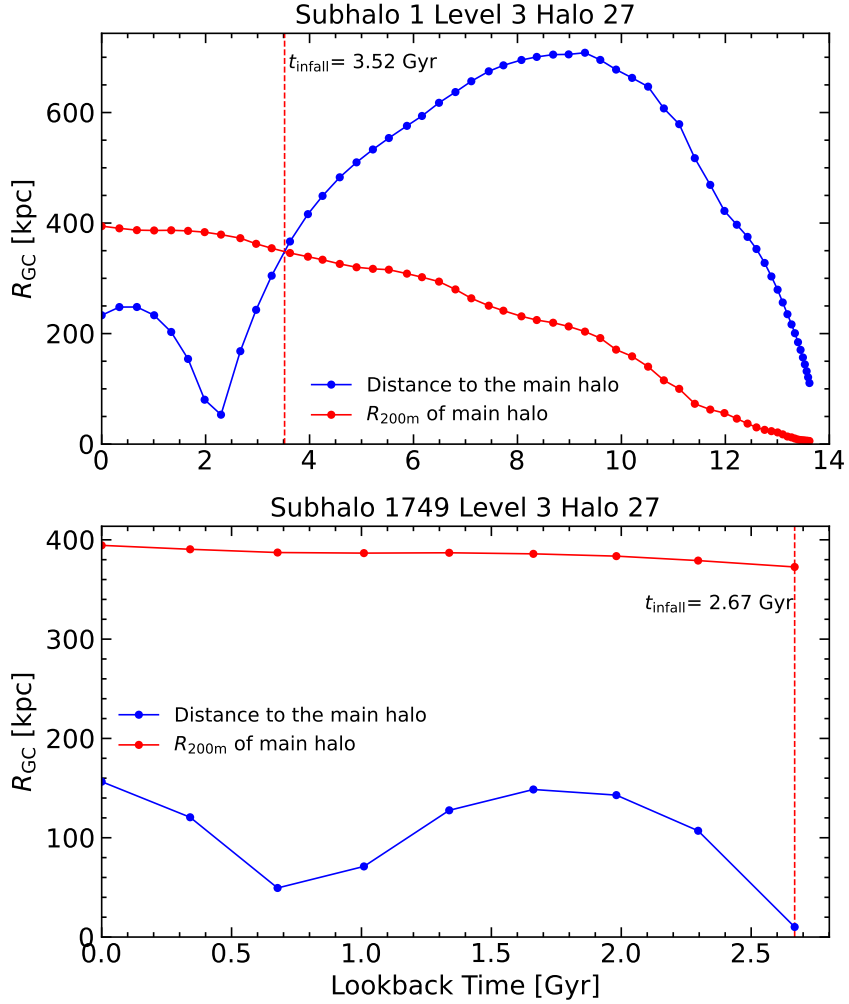


FIGURE 4.8 – Example of calculation of infall time for Auriga simulations. Blue points and dash lines indicate the distance of Subhalo 1 (top panel) and 1749 (bottom) from Auriga MW-like Level 3 resolution Halo 27 to the main host galaxy center. Red points and dash lines indicate the virial radius R_{200m} of the main host galaxy at different epochs using the linear relation in Figure 4.7. Some Auriga simulations have been considered to be representative of the infall of GSE or of the LMC, which is indicated in the bottom panel of the corresponding simulations.

or belong to very old components (infall times greater than 7 Gyr). In the FIRE simulations, however, the sub-halos are more evenly distributed over a broader infall time range of 4-13 Gyr. These discrepancies may be caused by the methods used to derive infall times or the different dynamical evolution processes applied in the two sets of simulations.

To derive the gravitational potential of sub-halos, we employed different methods. Santistevan et al. (2023) used GALPY to fit the enclosed mass profiles of host galaxies in the FIRE simulations by modeling the galaxies as a combination of disk and halo components. For the DM halo, they used the spherically symmetric `TwoPowerSphericalPotential`, while for the inner and outer disks, they applied the axisymmetric `DoubleExponentialDiscPotential`. Specifically, they modeled the disk as the sum of two double exponential disks: one representing the inner disk or bulge, and the other for the outer disk, with a density profile given by:

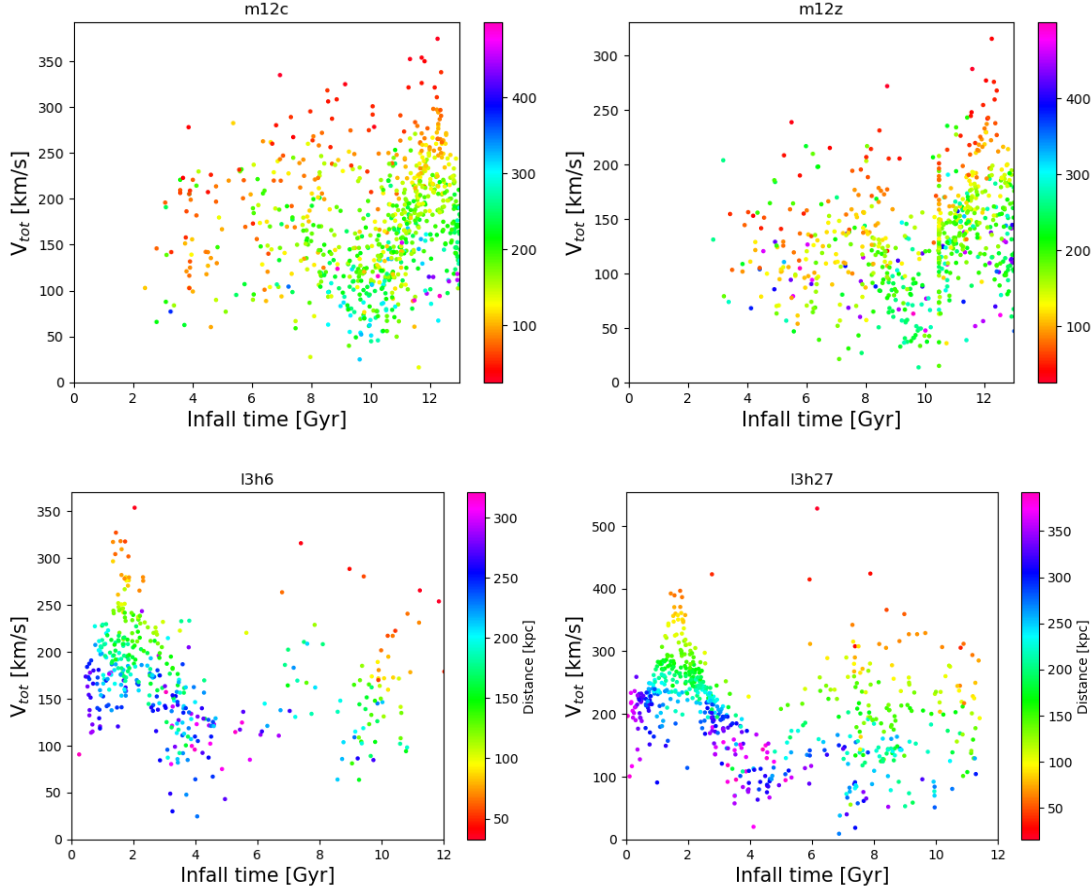


FIGURE 4.9 – Examples of the relation between total velocity and infall look-back time for m12c and m12z from FIRE2 and level 3, halo 6 and 27 from Auriga. Colorbars present the distances of subhalos to the host galaxy centers. We only present subhalos with a total mass larger than $10^7 M_\odot$.

$$\rho(R, Z) = A_{\text{disc}}^{\text{inner}} e^{-R/R_{\text{disc}}^{\text{inner}} - |Z|/h_z} + A_{\text{disc}}^{\text{outer}} e^{-R/R_{\text{disc}}^{\text{outer}} - |Z|/h_z} \quad (4.2)$$

where $A_{\text{disc}}^{\text{inner}}$ and $A_{\text{disc}}^{\text{outer}}$ are amplitudes of mass density (M_\odot / kpc^3), $R_{\text{disc}}^{\text{inner}}$ and $R_{\text{disc}}^{\text{outer}}$ are disc scale radii, and h_z is the disc scale height. The halo components are modeled by the generalized form of the spherical NFW profile:

$$\rho(r) = \frac{A_{\text{halo}}}{4\pi a_{\text{halo}}^3} \frac{1}{(r/a_{\text{halo}})^\alpha (1+r/a_{\text{halo}})^{\beta-\alpha}} \quad (4.3)$$

where A_{halo} is the amplitude, a_{halo} is the scale radius, and α and β are the slopes of the inner and outer density profile. Table 4.3 lists the fit parameters. With these parameters, we could calculate each sub-halo's potential at a given radius.

TABLE 4.3 – Best-fit parameters to mass profile for FIRE2 simulation

Name	A_{halo} $10^{11} M_{\odot}$	a_{halo} kpc	α	β	$A_{\text{disc}}^{\text{inner}}$ $10^9 M_{\odot} \text{kpc}^{-3}$	$R_{\text{disc}}^{\text{inner}}$ kpc	$A_{\text{disc}}^{\text{outer}}$ $10^8 M_{\odot} \text{kpc}^{-3}$	$R_{\text{disc}}^{\text{outer}}$ kpc	h_z kpc
m12m	3.78	17.32	1.57	2.78	6.47	0.79	7.98	4.41	0.64
m12b	3.84	16.89	1.48	2.82	18.0	0.65	6.08	4.24	0.51
m12f	3.65	14.77	1.45	2.74	8.39	0.84	2.11	7.40	0.54
m12i	5.70	32.15	1.58	2.99	9.10	0.78	3.87	4.56	0.55
m12c	7.93	24.37	0.90	3.05	7.05	0.71	6.41	3.65	0.57
m12w	2.99	22.87	1.61	2.73	5.53	0.68	11.7	2.19	0.67
m12z	3.22	33.96	1.58	2.69	0.59	0.40	1.73	2.94	1.54

Best-fit parameters to the double-exponential disc profile (Eq. (4.2)) and the generalized NFW profile for the halo (Eq. (4.3)). Columns: Name of host; halo amplitude, A_{halo} ; halo scale radius, a_{halo} ; halo inner slope, α ; halo outer slope, β ; disc inner amplitude, $A_{\text{disc}}^{\text{inner}}$; disc inner scale length, R_{inner} ; disc outer amplitude, $A_{\text{disc}}^{\text{outer}}$; disc outer scale length, R_{outer} ; disc scale height, h_z .

For the Auriga simulations, Grand et al. (2024) provides the gravitational potential of DM and baryonic particles. We derive the potential for each DM particle, as shown in Figure 4.10. The red and blue lines represent the median and mean potential values for DM particles within each 0.1-kpc-wide bin. At large radii, the potential values can be affected by massive sub-halos. Therefore, we use the maximal value in each bin instead of the median or mean, which should not introduce significant bias.

It is important to note that the potential values directly from the simulation snapshot output are relatively meaningless in periodic cosmological boxes—they can be positive or negative depending on whether particles are located in under-dense or over-dense regions of the Universe. The critical parameter for gravitational calculations in cosmological simulations is the acceleration, or the gradient of the potential, that particles experience.

Since Rocha et al. (2012) assumed a potential that rises to zero at a distance of 1 Mpc, we have scaled all of the halo potentials in our analysis to similarly reach zero at a radius of 1 Mpc, ensuring consistency in our comparison.

The top left panel of Figure 4.11 compares the binding energy of sub-halos from the Rocha et al. (2012) simulations (black dots) with that of GCs associated with the bulge, GSE, and Sgr (red dots). The Rocha et al. (2012) model is with a large total mass³ ($M_{200c} = 1.4 \times 10^{12} M_{\odot}$). However, this prediction faces two major issues:

- The simulated subhalos exhibit binding energies that are two to three times smaller than those of the Sgr and GSE GCs. Reconciling this discrepancy would require unrealistically large look-back times for these MW substructures.

3. In this Section, R_{200c} is the virial radius for which the enclosed mass, dubbed as M_{200c} , corresponds to an over-density of 200 times the critical density. M_{200c} value has been converted from the Rocha et al. (2012) $M_{200m} = 1.9 \times 10^{12} M_{\odot}$, which corresponds to an over-density of 200 times the mass density.

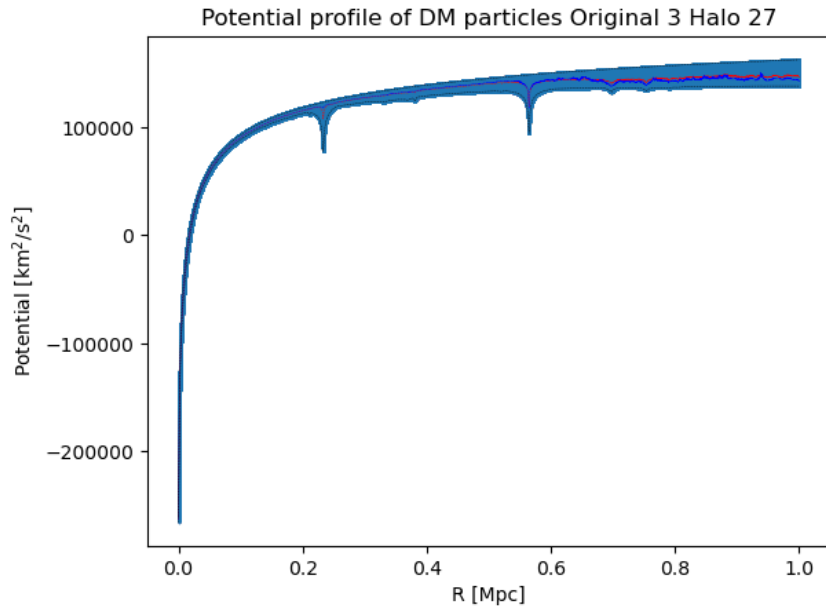


FIGURE 4.10 – Potential of DM particles for Auriga level 3 halo 27. Red and blue solid lines correspond to the median and mean value in each 0.1-kpc width bin.

- The DM halo in the Rocha et al. (2012) model is too massive to be consistent with the MW RC.

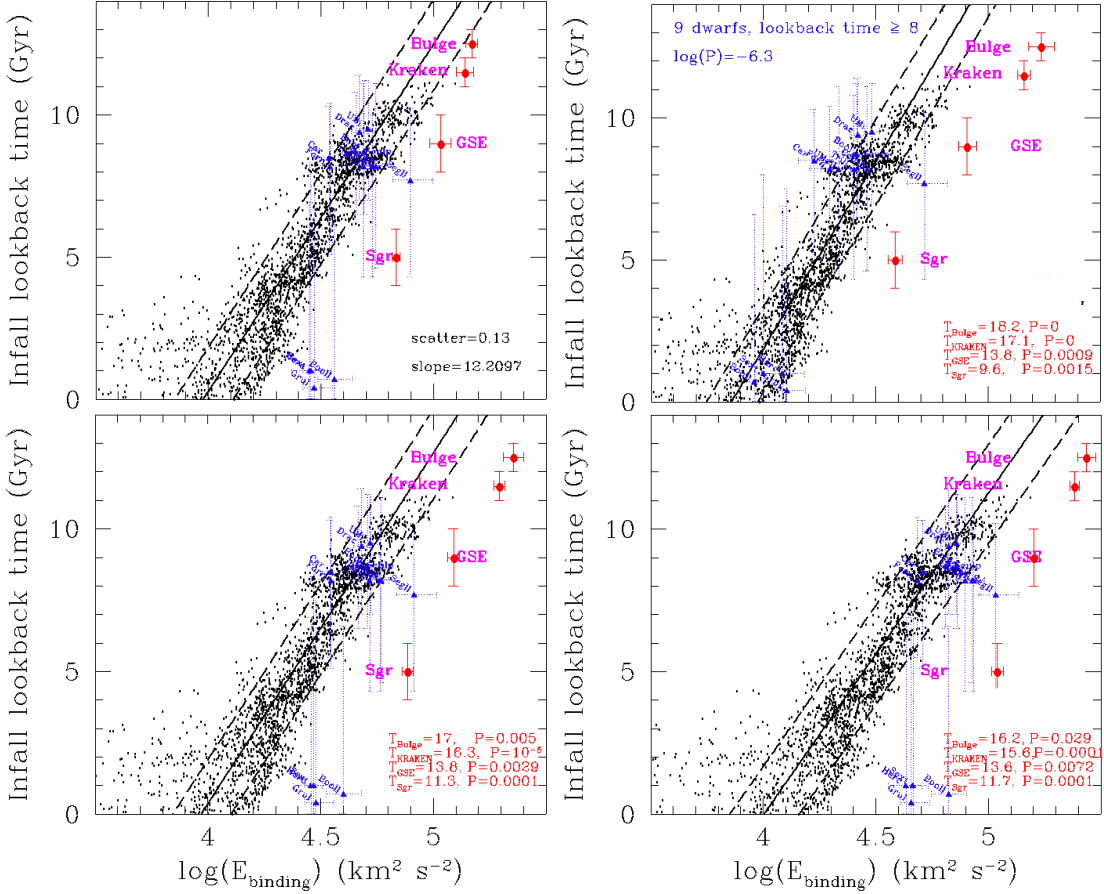


FIGURE 4.11 – Relation between infall look-back time and the logarithm of the binding energy. for which black dots represent subhalos associated to the Rocha et al. (2012) simulation, the solid line representing the best fit, and the dashed lines its one σ scatter. Red dots and error bars show the average locations of globular clusters associated with bulge, Kraken, GSE, and Sgr events, respectively. Binding energies of dwarf galaxies (blue triangles) and of GCs associated to MW events (red dots with corresponding labels in magenta color) are calculated using the observed kinetic energy together with the potential of the main halo. The blue triangles indicate the location of dwarf galaxies having a very good accuracy (<0.1 dex) in binding energy, and for which we have adopted the predicted dwarf infall time of Barmentloo & Cautun (2023). **Top left panel:** Rocha et al. (2012) simulated sub-halos (black dots) showing a scatter of 0.13 dex in $\log(E_{\text{binding}})$ and a slope of $12.2 \text{ Gyr km}^{-2} \text{ s}^2$. **Bottom left panel:** Same as the top left panel but for which we have added a baryonic mass ($6.2 \times 10^{10} M_{\odot}$) after a slight re-scaling of the dark matter halo mass from $1.4 \times 10^{12} M_{\odot}$ to $1.34 \times 10^{12} M_{\odot}$. In the bottom right of this panel, the numbers indicate the predicted time for GCs associated to bulge, GSE, and Sgr when they are inserted into the corresponding halo potential, as well as the probability they can lie in the distribution of sub-halos. **Top right panel:** Same as bottom left panel, but for different mass re-scalings. Here we have scaled down the Rocha et al. (2012) main halo mass to $7.4 \times 10^{11} M_{\odot}$. **Bottom right panel:** Same as top right panel but scaled up the main halo mass to $19.4 \times 10^{11} M_{\odot}$.

We have also considered the model by Rocha et al. (2012) with varying total mass. Using a re-scaling method, the binding energies and infall times of subhalos in the Rocha et al. (2012) simulations can be adjusted for halos with similar concentrations but different masses. The binding energy at the virial radius, R_{200} , follows $E_{\text{binding}}(R_{200}) \propto V_{200}^2$, where $V_{200}^2 = G, M_{200}/R_{200}$ represents the square of the circular velocity at the virial radius. Since the mean density within the virial radius is constant across halos at any epoch, we have $R_{200} \propto M_{200}^{1/3}$, and $V_{200} \propto M_{200}^{1/3}$.

Thus, $E_{\text{binding}}(R_{200}) \propto M_{200}^{2/3}$.

As halo concentration varies only weakly with mass ($c \propto M^{-0.1}$, Navarro et al. 1997), reducing the halo mass by a factor $\mu = 1.9$ results in only a 6% increase in concentration. Therefore, to first order, mass re-scaling is self-similar and should not affect the orbital parameters of satellites when considered in virial units. Consequently, reducing the halo mass by a factor μ causes the binding energies to scale by $\mu^{-2/3}$. However, the circular orbital times of dwarf galaxies at the MW virial radius, $t_{\text{orb,circ}} \propto R_{200}/V_{200}$, remain independent of μ . As a result, orbital times for general orbits within the MW halo are unaffected by μ , as are the infall and look-back times corresponding to a given fraction of the current virial radius.

In summary, re-scaling the MW virial mass by a factor μ shifts the location of the infall look-back time vs. binding energy of dSphs by a linear factor of $(2/3)\log(\mu)$ along the logarithmic energy axis, without affecting the infall lookback time. This maintains the slope of the correlation.

However, adding the same baryonic component (disk and bulge) as in Jiao et al. (2023) and Ou et al. (2024) to the Rocha et al. (2012) simulations, combined with a slight reduction of the DM halo mass from $1.4 \times 10^{12} M_\odot$ to $1.34 \times 10^{12} M_\odot$, does not reproduce the positions of the bulge, Kraken, GSE, and Sgr systems in the bottom-left panel of Figure 4.11. This is because adding a concentrated mass component increases the binding energy, worsening the offset.

Using the re-scaled DM halo, we further tested adjustments to the Rocha et al. (2012) main halo mass, as shown in the top-right and bottom-right panels of Figure 4.11. While keeping the kinetic energies of the bulge, Kraken, GSE, and Sgr GCs consistent with bulk LOS velocities and *Gaia* proper motions, we adopted the re-scaled potential of the simulation for the potential energy terms. Any re-scaling of the simulation shifts the positions of these four systems (red points) in the same direction as the subhalos (black points), though by a smaller amount.

2.3 Results

Most MW-like galaxies simulated by the FIRE project fail to reproduce the observed slope of the MW RC at large radii (see Figures 4.12 and 4.13) due to their large halo radii (R_{200c} ranging from 168 to 251 kpc), indicating significant mass beyond ~ 20 kpc. Additionally, these simulations do not match the slope of the relation between infall epoch and binding energy, with slopes ranging from 27 to 37 Gyr km^{-2}s^2 , which are two to three times steeper than the observed value of 12.2 Gyr km^{-2}s^2 . This prompted us to investigate MW-mass galaxies in the Auriga simulations, particularly on the “low-MW mass” subsample.

For example, the RCs of Auriga ‘low MW mass’ halo 3 and 8 are consistent with observed values between 15 and 20 kpc (see Figure 4.14). However, their RCs remain too flat and fail to reproduce the observed MW RC. Even in cases where the RC velocities are underestimated (as seen in halos 1 and 9), the simulations suggest a need for a more concentrated DM halo to address the discrepancy. A more significant problem is that most of the MW-like galaxies in the Auriga simulations show very steep slopes in the relation between infall epoch and binding energy, predicting binding energies that are approximately 0.4 to 0.8 dex smaller at the formation

epochs of the bulge, GSE, and Sgr.

FIRE m12c (Garrison-Kimmel et al., 2019b) is found to be the best simulation to reproduce both the MW RC and its accretion history (Figure 4.12). With a total mass of $M_{200} = 9.12 \times 10^{11}$, M_\odot —about 10% larger than the models used by Eilers et al. (2019) or Bovy (2015)—the m12c halo shares many similarities with these models. The top panel of Figure 4.12 shows that this model reproduces the *Gaia* DR3 MW RC fairly well, with an associated χ^2 probability of $P = 0.33$.

Additionally, the predicted slope of the relation between infall epoch and binding energy in the m12c simulation (31 Gyr km^{-2}s^2) is more than double the observed value for the MW. When taking both the MW RC and its accretion history into account, the m12c halo can be excluded with a probability of $P = 2 \times 10^{-4}$. While still problematic, this result is significantly better than that of any other simulated halo tested. It is also worth noting that the FIRE halos m12b and m12m could be re-scaled in terms of total mass to reproduce the relation with similar accuracy to m12c. However, these halos would still exhibit slopes in this relation that are too steep, failing to fully align with MW observations.

The blue triangles in Figure 4.11 show the binding energies of 14 dSphs, which were calculated using the accretion history relation. Barmentloo & Cautun (2023) analyzed 1 628 simulated MW-like halos from the *EAGLE* simulation suite (Grand et al., 2017), with total masses ranging from 0.5 to 2×10^{12} , M_\odot . We adopted their predicted infall lookback times for 14 dwarf spheroidal galaxies (dSphs), including Carina, Draco, Fornax, Sculptor, Sextans, and Ursa Minor, as well as Bootes I and II, Coma Berenices, Grus I, Hercules, Segue II, Triangulum II, and Ursa Major II.

Figure 4.11 supports the prediction by Rocha et al. (2012) that most dSphs have infall lookback times within the range of 8 to 9 Gyr. However, this requires a high MW mass, similar to estimates derived from assuming dwarf orbits are in equilibrium with the MW potential (e.g., $M_{200c} = 1.3 \times 10^{12}$, M_\odot ; Li et al. 2017). However, reproducing the MW accretion history relation requires a lower mass, such as that seen in the FIRE m12c simulation. The bottom panel of Figure 4.12 shows that, if most dwarfs had infall lookback times between 5 and 9 Gyr, this would result in extremely low probabilities for matching the MW accretion history (as seen in the top-left corner of the figure). In contrast, lookback times below 3 Gyr are far more likely for most dwarfs, except for Segue II.

In summary, when a cosmologically simulated halo successfully fits the MW relation between binding energy and infall time, it implies very low probabilities for most dwarfs to have entered the MW halo around the same epoch as the GSE event. The infall times predicted by Barmentloo & Cautun (2023) come with large uncertainties and are impacted by the inclusion of many halos that do not fit the MW’s accretion history or RC, as well as by the use of several additional parameters that are insensitive to infall time.

2.4 Discussion

The correlation between the infall epoch and binding energy is robust enough to be indicative of the MW accretion history. However, Pagnini et al. (2023) have raised concerns about the reliability of linking GCs to past merger events in the MW (Kruijssen et al., 2019, 2020; Malhan et al., 2022). Their simulations, which modeled mergers between galaxies with their own GC systems, demonstrated that GCs progressively lose energy after being stripped during a 1:10 minor merger event, making it challenging to accurately date these mergers based on GCs. Nevertheless, it is widely accepted that most GCs formed during periods of intense star formation, approximately 12 to 9 billion years ago (Haywood et al., 2016), a period that coincides with significant mergers such as Kraken and GSE (De Lucia et al., 2024; Valenzuela et al., 2024). The 1:10 mass ratio used by Pagnini et al. (2023) may not be representative of these larger events, and Naidu et al. (2021) have suggested that mass ratios between 1:2 and 1:4 are more typical for spiral galaxies like the MW (Chapter 1, Section 3.3). Therefore, only a relatively small fraction of MW GCs may have been accreted through the mechanism proposed by Pagnini et al. (2023).

D’Souza & Bell (2022) suggested that the relationship between infall epoch and binding energy could become highly uncertain for halos with active merger histories. However, the MW is known to have a relatively calm merger history compared to other spiral galaxies of similar mass (Hammer et al., 2007). For instance, more than half of spiral galaxies experienced its last major merger around 6 Gyr ago, the MW most recent major merger, GSE, occurred approximately 8–10 Gyr ago (Haywood et al., 2018; Helmi et al., 2018). This suggests that the MW is unlikely to be among the few galaxies with the most complex merger histories, which aligns with the well-established linear relation (Hammer et al., 2023). Therefore, the relation between the infall epoch and binding energy in the MW should be relatively tight and robust.

The MW mass can be constrained by comparing its accretion history to that of cosmological simulations. However, this constraint mainly pertains to the most distant GCs, i.e., those associated with the Sgr, which have an average distance of approximately 21 kpc. Within this radius, we estimate a mass of $2.05 \times 10^{11} M_{\odot}$ for the m12c simulated halo (Figure 4.12). This estimate aligns well with GC-based mass estimates from Watkins et al. (2019, $2.05 \times 10^{11} M_{\odot}$), as well as with RC-based estimates of $2 - 2.5 \times 10^{11} M_{\odot}$.

Cosmological simulations that can reproduce the binding energy of GSE GCs (Figures 4.12 and 4.13) suggest that dwarf galaxies were not bound to the MW between 8 and 10 billion years ago, supporting the ram-pressure scenario from Hammer et al. (2023) that these galaxies are newcomers, with an infall lookback time of less than 3 billion years. This indicates that these systems are likely out of equilibrium (Wang et al., 2024). As a consequence, determining the MW total mass based on the orbits of dwarf galaxies, under the assumption that they have been long-term satellites, may lead to systematic overestimation of the MW mass. This conclusion is further supported by the fact that an MW mass exceeding $10^{12}, M_{\odot}$ cannot reproduce the binding energies of the bulge, GSE, and Sgr GCs (Figures 4.11 and 4.13), as well as the MW RC.

By comparing the MW data with cosmological hydrodynamical simulations from both the

FIRE and Auriga projects, we identified discrepancies in the MW RC and its accretion history. Additionally, Rocha et al. (2012) and the Auriga simulations reveal sub-halo systems that are dynamically hot, likely due to the numerous minor mergers these systems experienced. This results in binding energies 3 to 9 times smaller than those of the Sgr, GSE, and bulge GCs. To improve our understanding of spiral galaxy formation and evolution, it would be valuable to focus on simulations that have undergone major mergers, either in the distant past similar to the MW, or more recently, such as in the case of M31. Studying these scenarios would provide better insights into the dynamics of galaxies with more significant merger histories.

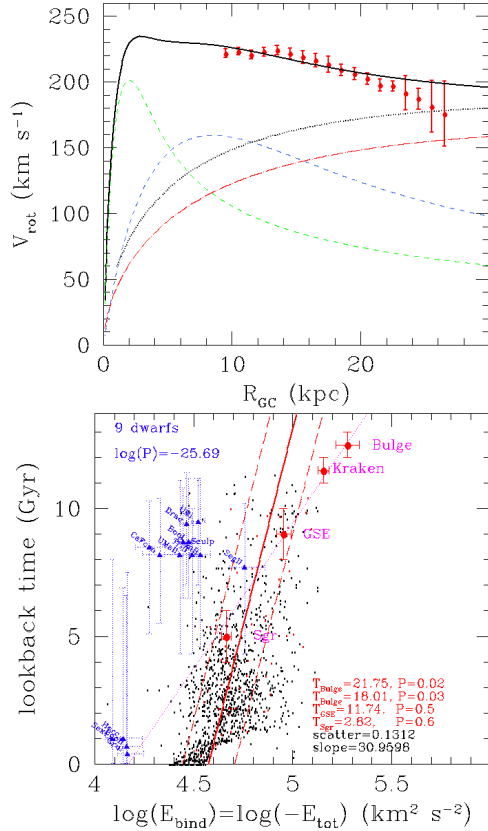


FIGURE 4.12 – Top panel: Rotation curve from an isolated MW-like galaxy from FIRE (halo m12c) compared to Gaia DR3 data (red points from Jiao et al. (2023) that includes measurements from Wang et al. 2023 to which very large systematic errors have been added). Contribution from the DM halo, bulge, and disk is given by red long-dashed, green short-dashed, and blue short-dashed lines, respectively. To illustrate the impact of the very massive halo from Rocha et al. (2012), we have also added its contribution (black dotted line) which is far larger than the FIRE m12c DM halo. **Bottom panel:** Same as the bottom panel of Figure 4.11 but for FIRE halo m12c. The binding energy of dwarf galaxies and of GCs associated with MW events are calculated using the observed kinetic energy together with the potential of each main halo. On the top-left of the panel is indicated the combined probability that the 9 dwarfs have infall lookback times larger than 8 Gyr as predicted by Barmentloo & Cautun (2023). In the bottom right of the panel, the numbers indicate the predicted time for GCs associated with the bulge, GSE, and Sgr when they are inserted into the m12c halo potential, as well as the probability they can lie in the distribution of sub-halos.

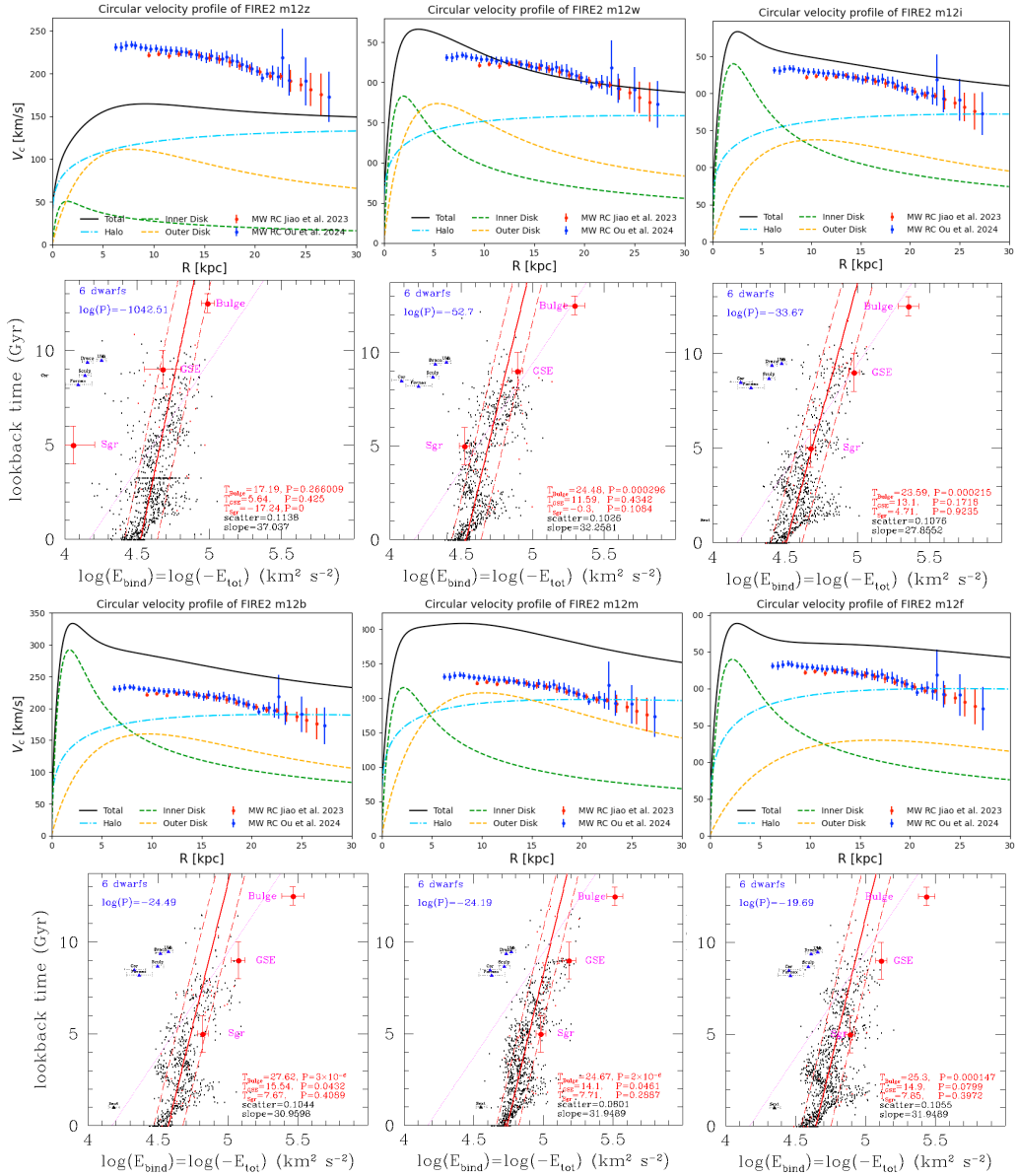


FIGURE 4.13 – Rotation curves (top panels) and accretion history (bottom panels) from isolated MW-mass galaxies from FIRE. The same symbols for points and lines than in Figure 4.12. For simplicity, here we have only shown the six classical dwarfs (blue triangles) and buge, GSE, and Sgr GCs (red crosses).

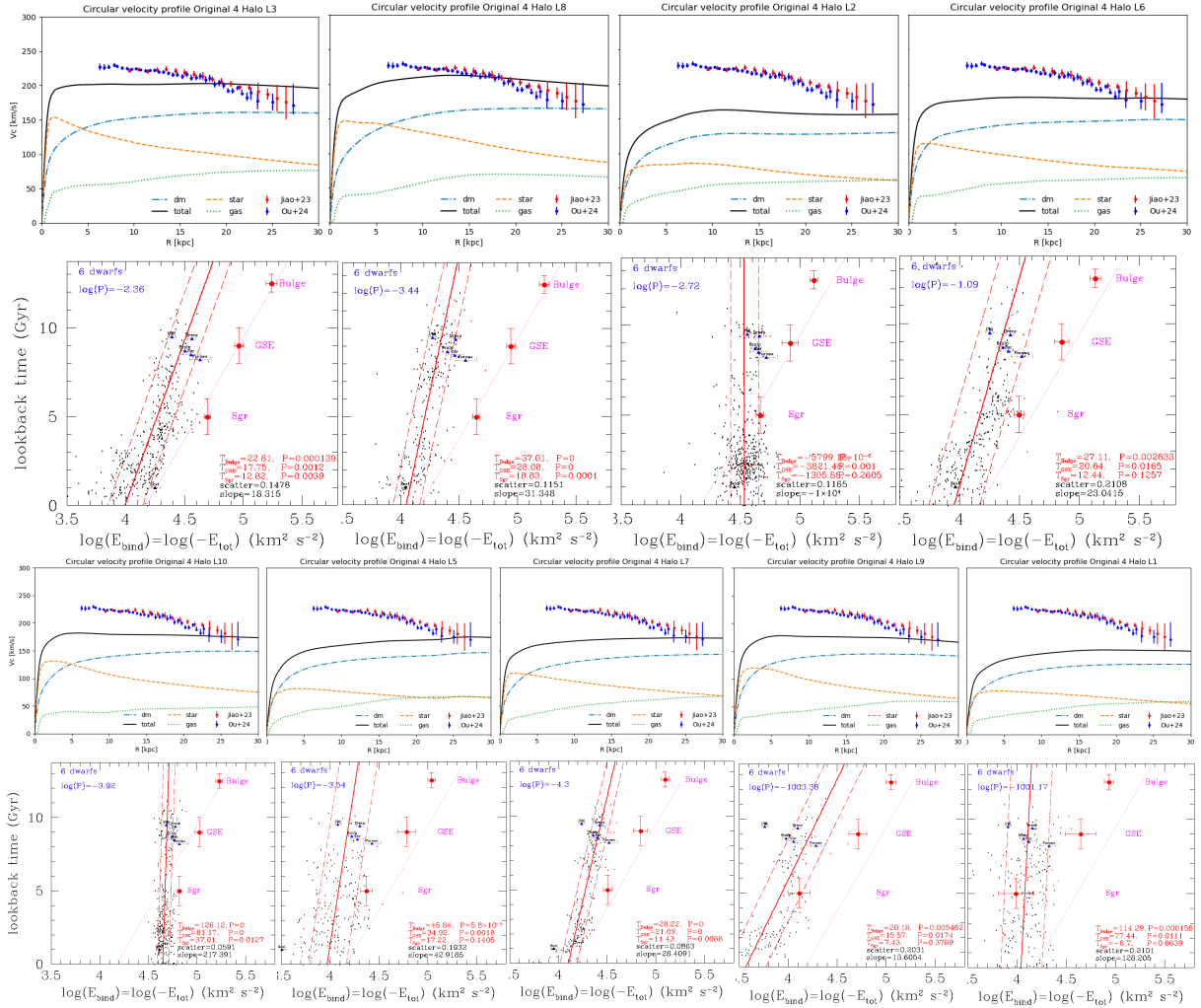


FIGURE 4.14 – Rotation curves (top) and accretion history (bottom) from low MW-mass galaxies from Auriga. The same symbols for points and lines as in Figure 4.13.

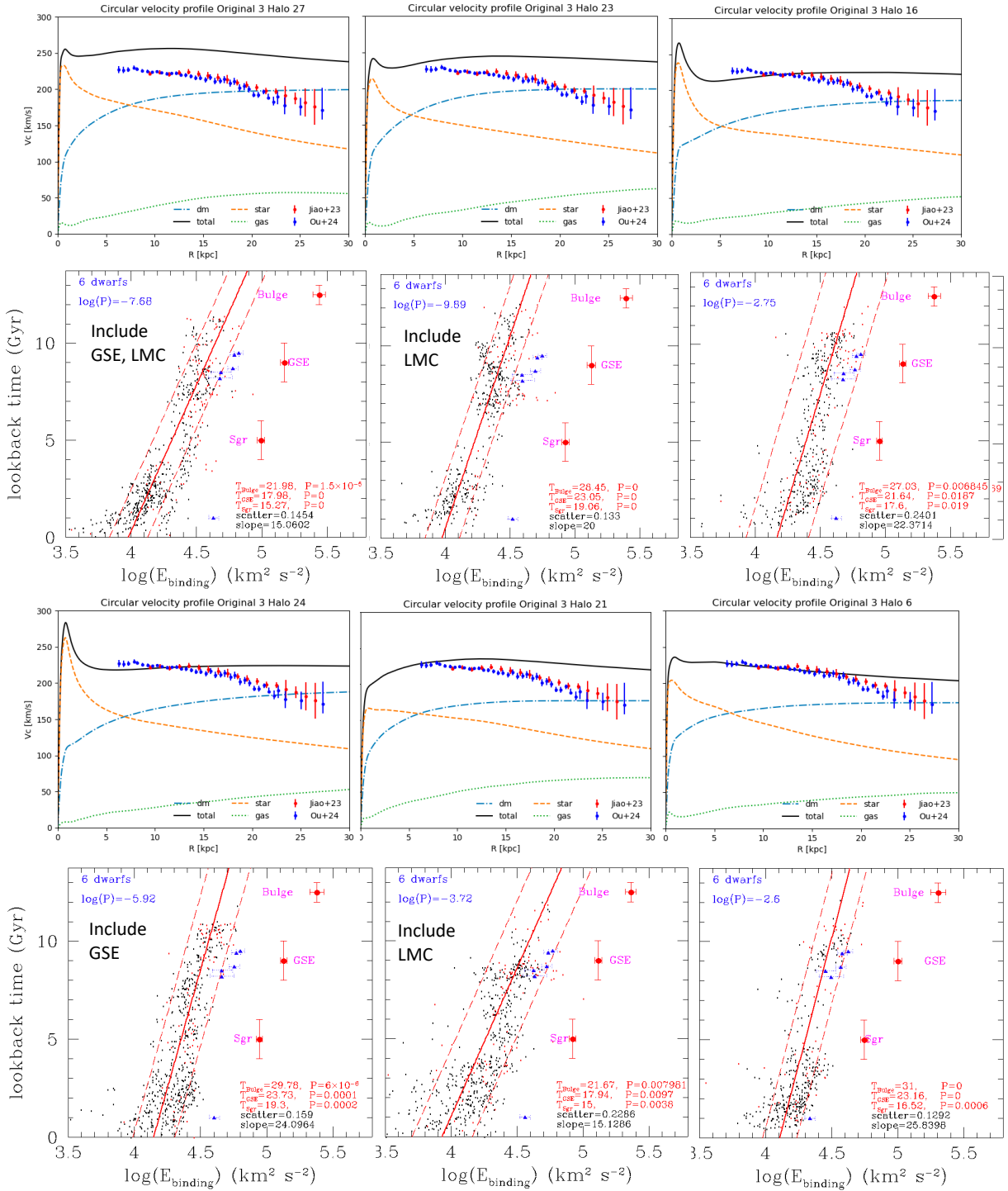


FIGURE 4.15 – Rotation curves (top) and accretion history (bottom) from high MW-mass galaxies from Auriga. The same symbols for points and lines as in Figure 4.13.

3 Fornax

Fornax was first discovered by Shapley (1938a) while studying photographic plates of the constellation with the same name. Fornax has been shown to host young and intermediate-age stellar populations (Buonanno et al., 1999; del Pino et al., 2013; Weisz et al., 2014b), along with a predominantly older component, as expected (Battaglia et al., 2006; Hendricks et al., 2014). One peculiar finding about Fornax is that it contains six GCs (Baade & Hubble, 1939; Shapley, 1939; Hodge, 1961; Wang et al., 2019b). Similar to other dSphs, Fornax is thought to have a DM-dominated halo (Battaglia et al., 2006; Walker & Peñarrubia, 2011; Amorisco et al., 2013). However, based on the ram-pressure stripping scenario (Chapter 4, Sec. 1.3), if Fornax was originally a gas-rich galaxy and is currently undergoing its first infall into the MW halo, it could lose its gas due to ram pressure from the MW halo gas. This loss of gas would result in the spherical expansion of its stars, as a significant portion of its gravitational potential would be lost. To test this hypothesis and assess how MW tidal forces influence the expanded stellar population, it is necessary to observe the true edges of Fornax, minimizing contamination from non-member stars.

This paper is published on *Monthly Notices of the Royal Astronomical Society* and is available at <https://doi.org/10.1093/mnras/stac644>. My contribution is to fit different profiles to the observational data. In Section 3.1, I will briefly present how Yang et al. (2022) selected stars belonging to Fornax. In Section 3.2, I will present the models used to fit the density profile of Fornax and the resulting findings. In Section 3.3, we will discuss the origin of the extended stellar halo.

3.1 Data

Yang et al. (2022) used the data from *Gaia* EDR3 covering a 20 by 20-degree field centered on Fornax. For the Galactic extinction, Yang et al. (2022) adopted a value of $E(B - V) = 0.04$. To effectively identify member stars and minimize contamination, Yang et al. (2022) employed three selection criteria: (i) proper motion (PM), (ii) color-magnitude diagrams (CMDs), and (iii) parallax.

CMDs are commonly used to identify candidate members of various stellar populations. Although the *Gaia* data provides shallower photometry and less precise color measurements compared to ground-based observations, the RGB of Fornax can still be easily recognized. Yang et al. (2022) selected only RGB candidates to analyze its morphology and possible stellar debris, with the assumption that the RGB could represent the overall stellar population of Fornax.

The *Gaia* mission also provides PM measurements for all sources, which serve as an independent method for star selection beyond CMD analysis. Therefore firstly, Yang et al. (2022) defined a core sample within an elliptical region of 1-degree radius, based on Fornax's morphological parameters. Using this core sample, Yang et al. (2022) calculated the error-weighted average PM, along with the axis ratio and orientation of the ellipse describing the PM distribution. Stars were then selected based on their consistency within three times the PM uncertainty and the correlation between the two PM components.

The distance to Fornax from the Sun is estimated to be 147 ± 4 kpc (de Boer & Fraser, 2016), corresponding to a parallax of 0.00680 mas, which is significantly smaller than the typical error for individual sources in *Gaia*. Therefore, Yang et al. (2022) selected stars with $|\text{parallax_over_error}| \leq 3.5$ to compile the third sample.

The three final samples of Fornax member candidates" S_0 , S_1 , and S_2 , as shown in Figure 4.16, are briefly summarized based on the following criteria from Yang et al. (2022):

- 1 S_0 : Included the largest number of member candidates possible, with additional constraints $G < 20.8$ and $\text{BP-RP} > 0.8$.
- 2 S_1 : Limited the color to be redder ($\text{BP-RP} > 1.1$) to better remove QSOs and MW stars that overlap in color with Fornax RGB.

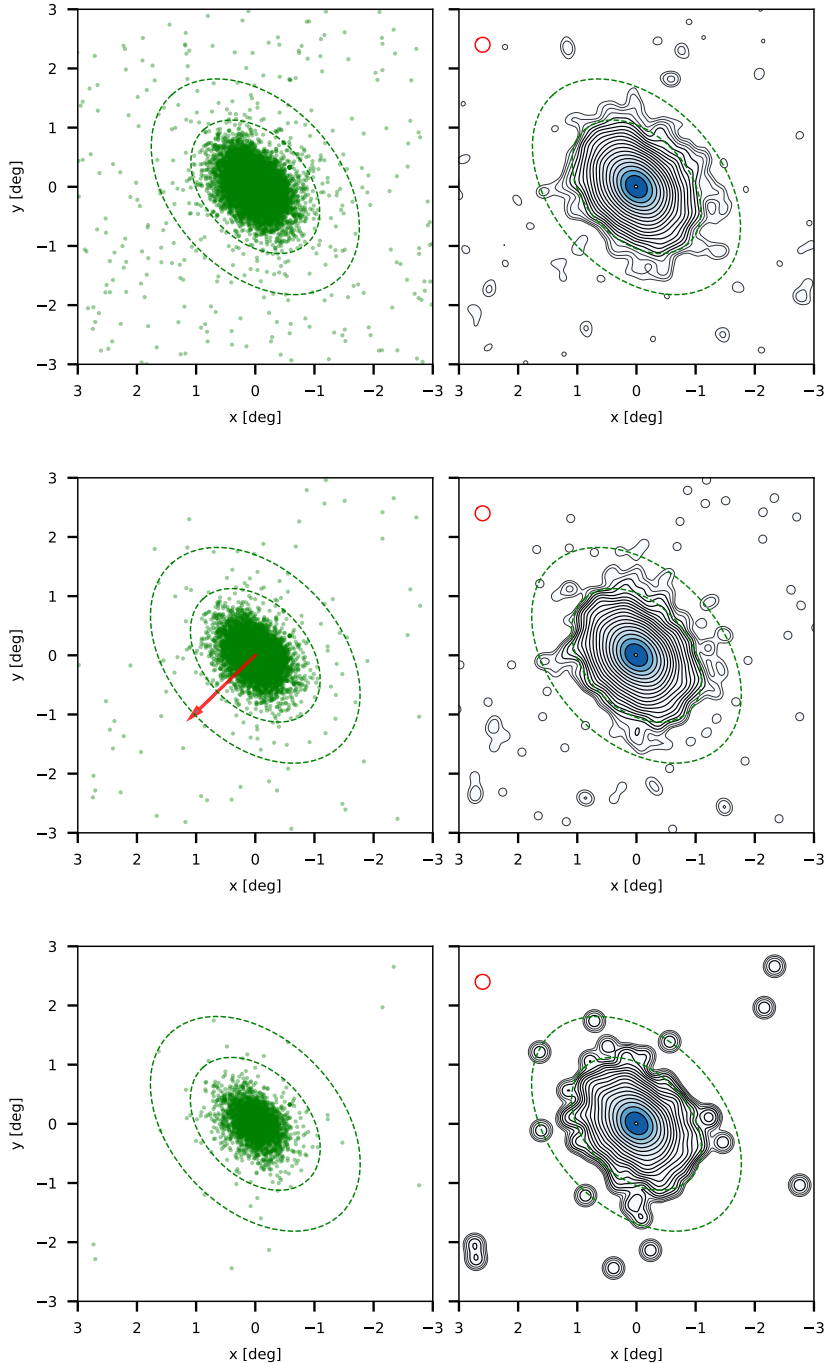


FIGURE 4.16 – Morphology of Fornax by S_0 , S_1 and S_2 , from top to bottom, respectively. Direct dot plots are shown in the left panels, and the smoothed contour maps are shown on the right. In all panels, two ellipses (gray dashed lines) of 1.3 and 2.1 degrees in radius, describing the morphological shape, are superposed. The red arrow in the left-middle panel indicates the mean PM of Fornax. For S_0 , contour levels range from 5.30×10^{-3} to 14.1 counts/arcmin 2 with logarithmic interval factor 1.483. For S_1 , 2.75×10^{-3} to 9.87 counts/arcmin 2 , the interval factor 1.490. For S_2 , 0.740×10^{-3} to 3.10 counts/arcmin 2 , the interval factor 1.510. Note that the peak density is lower than that of 1D density profile, because the contours have been smoothed by a constant Gaussian kernel of 0.25 degree, indicated by a red circle at the top-left corner. In all contour maps, thin and dark-gray contours are between 3 to 10 sigma significance above the 2D background fluctuations. This figure is adapted from Yang et al. (2022).

S_2 : A very strict sample of bright stars with the best PM and parallax measurements ($G < 19.2$).

Using the method described by Irwin & Hatzidimitriou (1995) and Battaglia et al. (2006), the radial profile was constructed directly from the candidate catalog by calculating the mean stellar density within each elliptical annulus, indexed by the semi-major axis. Figures 4.17 to 4.19 present the radial surface-density profiles for S_0 , S_1 , and S_2 , respectively. The error bars are estimated based on Poisson noise derived from the star counts in each annulus. Additionally, Yang et al. (2022) required a minimum of nine stars per radial bin (leading to a statistical error of up to 33 percent); if this threshold was not met, the bin was combined with its neighboring annulus.

3.2 Models and Results

Following Battaglia et al. (2006), we fitted various theoretical density profiles to the data, including an empirical King profile (King, 1962), an exponential profile, a Sersic profile (Sersic, 1968), and a Plummer model (Plummer, 1911).

The King model has been extensively used to describe the surface density profile of dSphs:

$$I_K(R) = I_{0,K} \left(\frac{1}{\sqrt{1 + \left(\frac{R}{r_c}\right)^2}} - \frac{1}{\sqrt{1 + \left(\frac{r_t}{r_c}\right)^2}} \right)^2 \quad (4.4)$$

with 3 parameters: a characteristic surface density, $I_{0,K}$, core radius, r_c and tidal radius, r_t . This radius is set by the tidal field of the host galaxy. In this study, we let this parameter vary to get the best fitting.

The Sersic profile is known to provide a good empirical formula to fit the projected light distribution of elliptical galaxies and the bulges of spiral galaxies:

$$I_S(R) = I_{0,S} \exp \left[- \left(\frac{R}{R_S} \right)^{1/m} \right] \quad (4.5)$$

where $I_{0,S}$ is the central surface density, R_S is a scale radius and m is the surface density profile shape parameter. The de Vaucouleurs law and exponential are recovered with $m = 4$ and $m = 1$, respectively; for $m < 1$ the profile is steeper than an exponential; $m = 1/2$ gives a Gaussian.

We used the minimum chi-square (χ^2) method to estimate the parameters, with the results summarized in Table 4.4. The Plummer profile consistently resulted in very high reduced- χ^2 values, leading us to reject this model. While the exponential profile provided slightly better fits, it exhibited systematic deviations at different radii. For instance, in the middle panel of Figure 4.18, the best-fit exponential profile noticeably diverges from the data points.

The Sersic profile provided a significantly better fit to the data out to a radius of 1 degree, particularly when compared to the King profile, which failed to account for the excess of stars in the outer regions. The observed deviation, or “break,” beyond this radius suggests the presence of an additional component in Fornax. To further characterize this component, we employed a

double-Sersic model to decompose the density profile. This model led to a marked improvement in the fit, as evidenced by the considerable reduction in the mean χ^2 , as shown in the last columns of [Table 4.4](#), confirming the necessity of this additional component.

The second Sersic component, labeled “c.2” in [Figure 4.17](#), begins to dominate the density profile at 1 degree, where both components converge to the same density. This second component contributes 10%, 9%, and 12.4% of the total stellar counts for S_1 , S_0 , and S_2 , respectively, based on the integration of the theoretical profiles. Given the nearly symmetric 2D morphology, this second component likely represents a surrounding halo, although projection effects may also be influencing this result.

TABLE 4.4 – Best-fitting parameters of different theoretical density profiles

Model	Sample	parameters			χ^2/ν	$\overline{\chi_*^2}$
King		$I_{0,K}$	$r_c [']$	$r_t [']$		
	S_0	33.9 ± 3.6	15.3 ± 1.7	76.0 ± 5.2	1.16	-
	S_1	24.4 ± 2.8	15.4 ± 1.9	71.6 ± 5.2	1.28	-
	S_2	7.5 ± 1.3	14.7 ± 2.5	76.3 ± 8.7	0.88	-
Sersic		$I_{0,S}$	$R_S [']$	m		
	S_0	25.4 ± 2.7	14.5 ± 0.6	0.83 ± 0.04	1.41	5.15
	S_1	17.4 ± 2.0	14.7 ± 0.7	0.80 ± 0.04	1.26	4.64
	S_2	5.8 ± 1.0	14.1 ± 1.0	0.84 ± 0.07	0.92	3.83
double-Sersic						
c.1	S_0	22.3 ± 2.6	15.8 ± 0.8	0.74 ± 0.05	1.07	0.94
		1.0 ± 0.8	$18.7^{+3.3}_{-6.5}$	$1.00^{+0.12}_{-0.29}$		
c.1	S_1	15.0 ± 1.9	15.9 ± 0.9	0.71 ± 0.05	0.97	0.60
		0.83 ± 0.65	$19.7^{+3.3}_{-6.6}$	$0.91^{+0.11}_{-0.29}$		
c.1	S_2	4.8 ± 0.9	15.5 ± 1.2	0.73 ± 0.08	0.78	0.37
		0.33 ± 0.3	$19.6^{+4.0}_{-12.}$	$0.92^{+0.14}_{-0.90}$		
Exponential						
		$I_{0,E}$	$r_e [']$			
	S_0	34.5 ± 3.6	10.7 ± 0.4		2.48	-
	S_1	24.6 ± 2.8	10.3 ± 0.5		2.47	-
	S_2	7.65 ± 1.3	10.6 ± 0.7		1.25	-
Plummer						
		$I_{0,P}$	$b [']$			
	S_0	27.0 ± 2.8	16.4 ± 0.7		10.85	-
	S_1	19.6 ± 2.2	15.4 ± 0.7		12.01	-
	S_2	6.1 ± 1.1	16.0 ± 1.1		4.56	-

King model (core radius, r_c , tidal radius, r_t), Sersic model (Sersic radius, R_S , shape index, m), exponential model (scale radius, r_s) and Plummer model (scale radius, b). The peak density of each profile I_0 are all in unit stars/arcmin 2 . The last columns give the reduced and the mean χ^2 , respectively. The latter is evaluated for the points between 1.3 to 2.1 degrees. The goal is to compare between Sersic and double-Sersic model.

We find that within 1 degree, the density profiles derived for Fornax in this study are in agreement with previous results. As shown in Figures 4.17 to 4.19, we compared with the estimates from Battaglia et al. (2006, squares) and Coleman et al. (2005, triangles).

By correcting for crowding effects near the core of Fornax, Bate et al. (2015) derived a

similar characteristic radius using a single Sersic profile, which aligns with our analysis and is smaller than the estimate from Battaglia et al. (2006). These comparisons suggest that the relatively shallower photometric data from *Gaia*, combined with its high image quality, allows for measurements that are less affected by crowding in Fornax’s central regions.

3.3 Discussion

In this study, we have examined the stellar structure of the Fornax dSph over a large area, 400 sq degrees, and reached extreme photometric depth, reaching 12 magnitudes fainter than Fornax’s central density. Our fittings revealed the presence of a significant secondary component in the Fornax dSph, which resembles a stellar halo due to its nearly symmetric morphology. This component comprises approximately 10% of Fornax total mass and extends out to 2.1 degrees (equivalent to 5.4 kpc, or nearly seven times the half-light radius). This outer component is well modeled by a Sersic profile with an index of $0.92^{+0.11}_{-0.29}$, which is consistent with an exponential profile, suggesting that Fornax may extend even farther than previously thought.

Battaglia et al. (2015) conducted a series of simulations to model Fornax as a DM-dominated, long-lived satellite of the MW. Their models, with the exception of one that has less mass, could successfully reproduce both the radial VD profile and the observed morphology out to 1.3 degrees (Battaglia et al., 2006). However, these models cannot predict the secondary component we have identified using *Gaia* data because the stellar component of Fornax are protected by the DM halo and remain highly stable against tidal stripping.

Genina et al. (2020) proposed that the Fornax dSph could exhibit tidal tails, which is only 6 magnitudes fainter than the central density by analyzing analogs of Fornax from cosmological simulations. In contrast, our analysis of Fornax density profile, using *Gaia* data across a much broader 12-magnitude range, revealed no indications of such tidal tails in the surrounding region.

Contrary to the hypothesis of tidal stripping in Fornax, we observed that the outer regions of the galaxy, i.e., $r_{\text{ell}} > 1.3$ degrees, exhibit a halo-like structure due to their relatively symmetric morphology. This implies that mechanisms other than tidal stripping may be shaping Fornax’s structure.

Therefore, We propose that Fornax may have evolved from a gas-rich dwarf galaxy progenitor and experienced tidal shocks from the MW (Section 1.3). When Fornax entered the MW halo approximately 2 Gyr ago, a significant portion of the cold gas within the galaxy would have been removed by the ram-pressure from the hot gas in the MW halo. This pressure would have compressed the gas, igniting some star formation, and eventually led to the gas being fully stripped away in the recent few hundred million years.

This process could explain the multiple epochs of star formation observed in the last 1-2 Gyr (Weisz et al., 2014a; Rusakov et al., 2021). The second stellar component revealed by this study may be due to the recent expansion of stars in Fornax. Yang et al. (2014) have tested this scenario using numerical simulations. Detailed numerical simulations for Fornax will be required to accurately model the properties under the ram-pressure scenario. Such modeling could provide crucial insights into Fornax complex dynamical state and the significant second

component observed in its stellar halo.

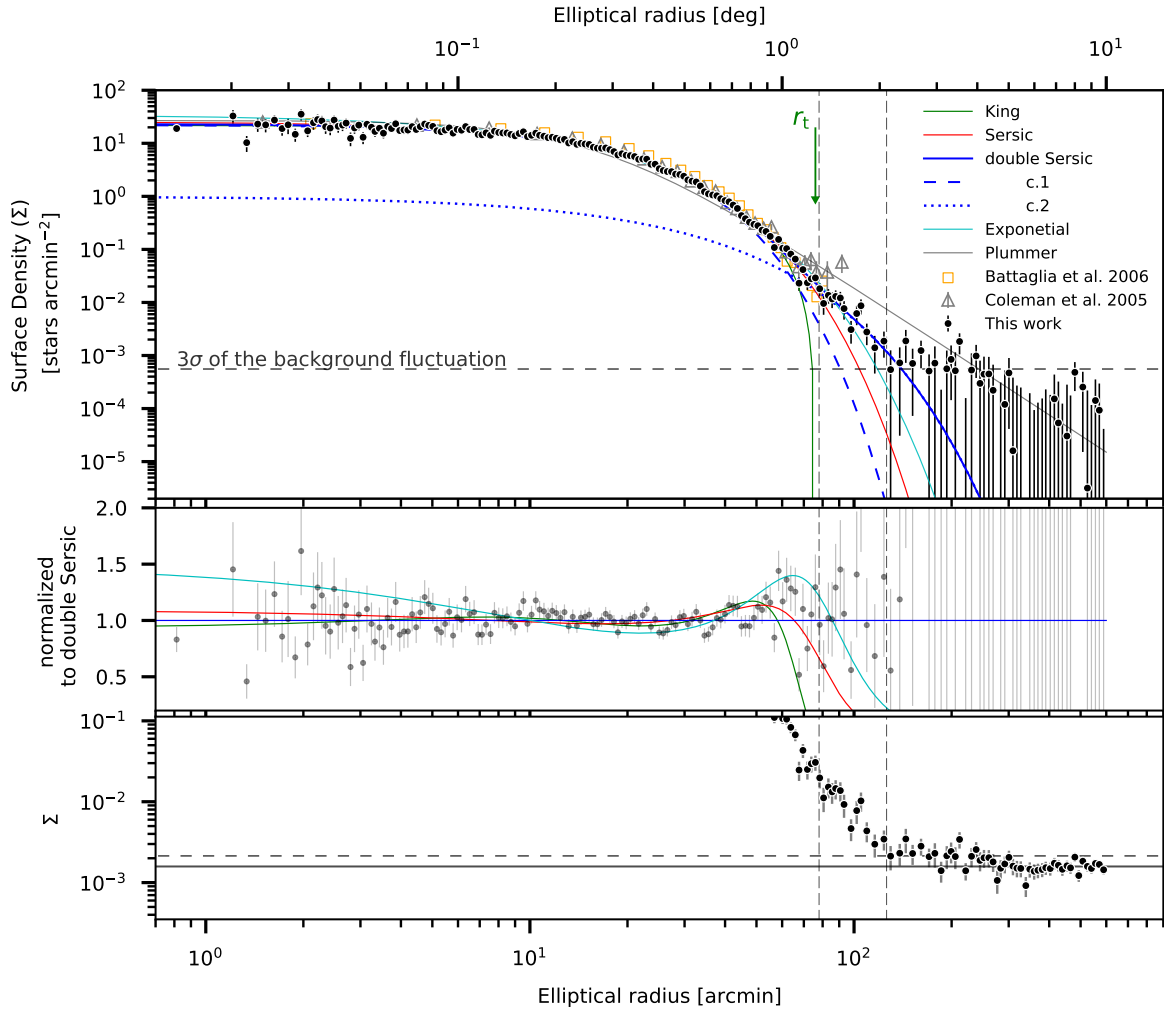


FIGURE 4.17 – Surface density profile indexed by elliptical radius for S_0 . In the main panel (top), the corresponding background densities have been subtracted. The horizontal dashed lines indicate the detection limits. Different best-fitting theoretical density profiles and observed profiles are shown (see the legend). The two components of the double-Sersic profile are denoted by "c.1" and "c.2". The vertical dashed lines indicate 1.3 and 2.1 degrees, respectively. The green arrow indicates the location of the best-fitting King tidal radius r_t . Two diagnostic panels are shown below: 1) Normalised data (dimmed into gray) and different models concerning the double-Sersic model; 2) the density profile zoomed to the background level (gray solid and dashed lines for the mean and 3-sigma uncertainty, respectively), for inspecting how density profiles vary at large radii before subtracting the mean background. This figure is adapted from Yang et al. (2022).

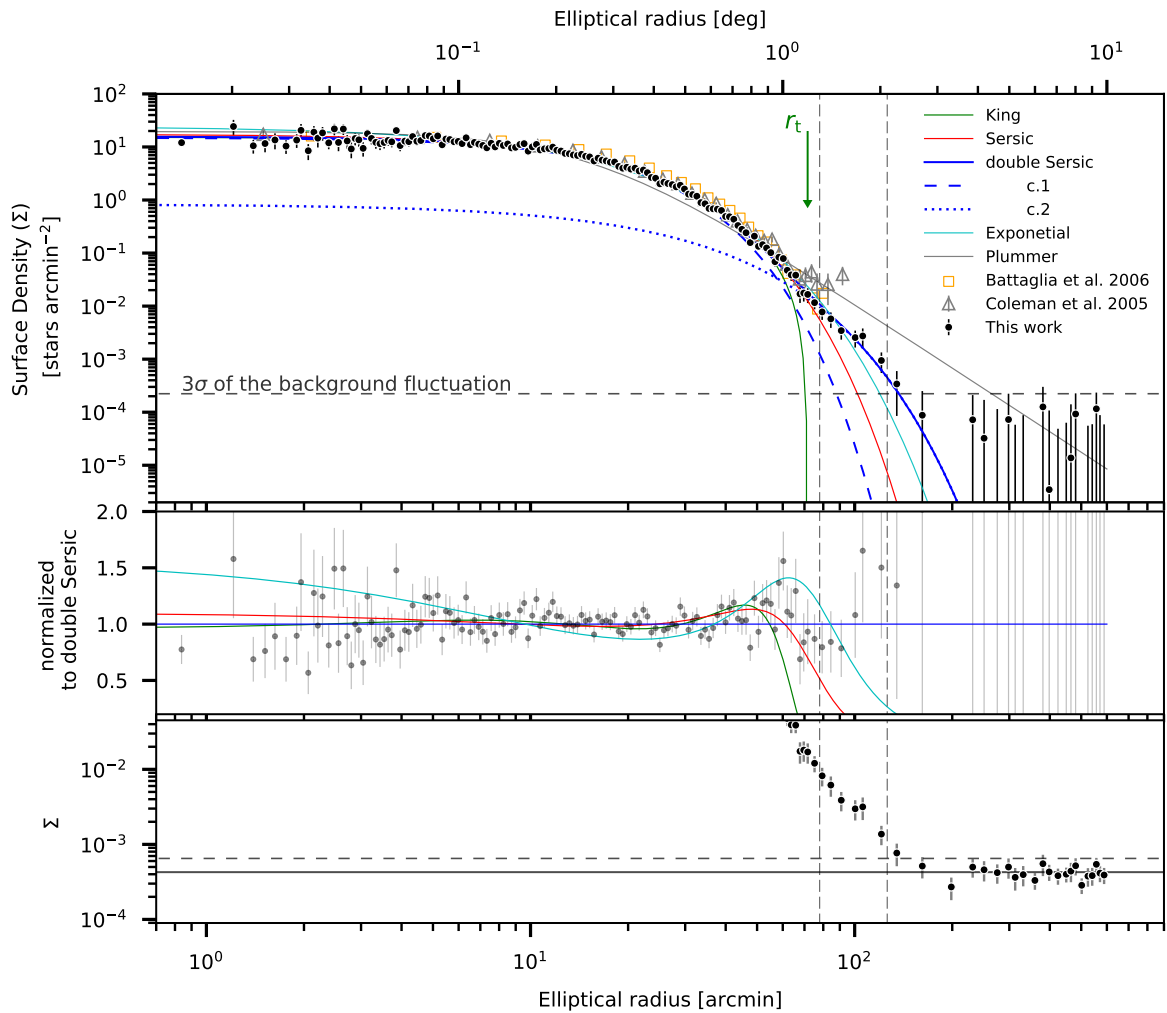


FIGURE 4.18 – Same as Figure 4.17 but for star sample S_1 . This figure is adapted from Yang et al. (2022).

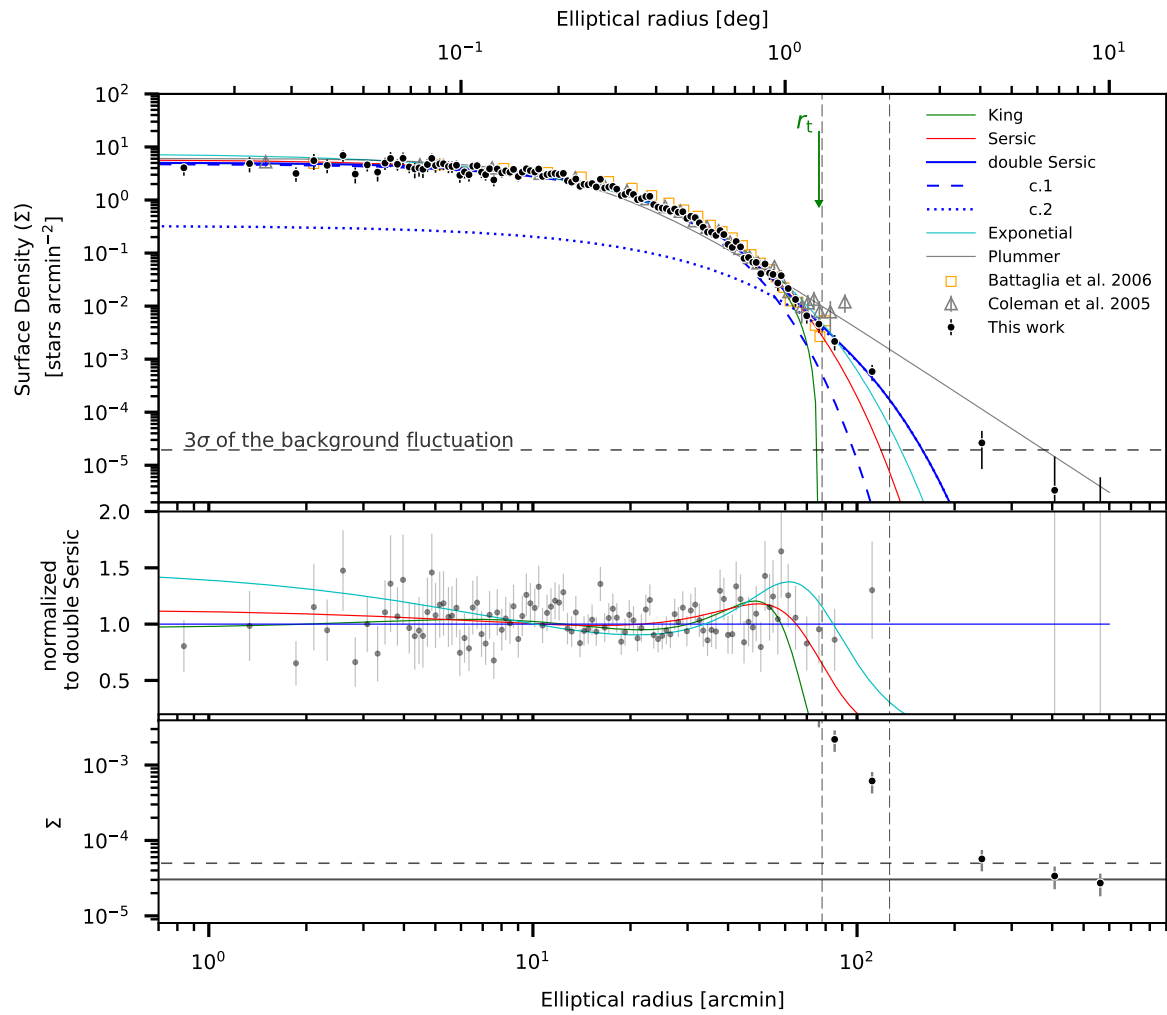


FIGURE 4.19 – Same as Figure 4.17 but for star sample S_2 . This figure is adapted from Yang et al. (2022).

4 Conclusion

We used *Gaia* data to investigate the extended stellar halo of the Fornax dSph, revealing a secondary stellar component that extends up to 2.1 degrees (Section 3). The presence of this secondary component aligns with the predictions of the ram-pressure stripping scenario, which proposes that Fornax lost a significant portion of its gas due to ram pressure from the MW halo gas. This gas loss would have caused the stars in Fornax to expand spherically, leading to the formation of the extended stellar halo observed today. Our findings provide new insights into the formation and evolution of the Fornax dSph, underscoring the importance of hydrodynamical simulations in understanding the complex dynamical processes shaping dwarf galaxies within the MW halo.

The ram-pressure stripping and tidal shock scenario has been proposed to explain the large VDs observed in dwarf galaxies without a DM-dominated halo, challenging the assumption that most dwarfs are long-term satellites of the MW. This scenario posits that many dwarfs are newcomers in the MW halo and have lost their gas due to ram pressure from the MW halo gas. As the gas, which accounts for much of the gravitational potential, is stripped away, the stars expand spherically, which explains the observed high VD in these systems. These processes have been extensively simulated by Wang et al. (2024), who predict that stars in the outskirts of dwarfs should exhibit spherical expansion and be detectable. Observations of extended stellar halos in Fornax (Yang et al., 2022) and the detection of young stellar populations in the outskirts of dSphs (Yang et al. 2024, accepted) support the ram-pressure stripping and tidal shock scenario.

Under this scenario, dSphs cannot reliably be used to estimate the MW mass if the assumption of equilibrium is required. However, by considering the simple idea that early-arriving objects have higher binding energies while newcomers possess lower binding energies, which is confirmed by cosmological simulations, we can use binding energy comparisons between observations and simulations to constrain the MW mass (Section 2). Using simulations from the FIRE project, the Auriga project, and Rocha et al. (2012), we found that a massive MW, with a mass of approximately $10^{12} M_{\odot}$, is inconsistent with the binding energies of the bulge, GSE, and Sgr GCs, as well as with the MW RC. This suggests that the MW mass may be lower than previous estimates.

Discussion

Measuring the mass of galaxies is of critical importance in astronomy. Based on the Λ Cold Dark Matter (Λ CDM) scenario, galaxies primarily form through hierarchical mergers, where small systems merge into larger ones. The mass of a galaxy plays a key role in shaping both its structure and kinematics. Understanding how matter is distributed within a galaxy provides insights into the behavior of its stars, gas, dust, and other components. By comparing a galaxy's total mass to its visible mass, astronomers can infer the presence of "missing" mass, typically attributed to the dark matter (DM) or possibly indicative of alternative gravitational interactions, such as Modified Newtonian Dynamics (MOND).

Moreover, determining the mass of galaxies is fundamental to the study of galaxy formation and evolution. By comparing the mass of galaxies at different stages in the universe's history, one can infer how galaxies grow and transform over time. This knowledge could help researchers in constructing models of cosmic evolution and in understanding the large-scale structure of the universe.

Given the critical role that galaxy masses play in understanding galaxy formation and evolution, the fraction of different components within galaxies has been extensively studied. In the early universe, dark matter and baryonic matter were uniformly and homogeneously distributed, with a baryon fraction of $f_b = 0.1574 \pm 0.0014$ (Planck Collaboration et al., 2020)⁴. If this primordial mix remains intact as gravitationally bound structures form over the course of cosmic evolution, the baryonic mass of a given object would be expected to follow a relatively tight relation: $M_b = f_b M_{\text{tot}}$. Since gravity is the primary driver of galaxy evolution, and dark matter interacts with baryonic matter exclusively through gravitational interaction.

McGaugh et al. (2010) explored the relation between baryonic mass and total mass of cosmic structures using pressure-supported systems such as galaxy clusters (blue squares, Giordini et al., 2009), rotation-supported galaxies (round symbols, McGaugh, 2005; Stark et al., 2009; Trachternach et al., 2009), and Local Group dwarf satellites (red squares, Walker et al., 2009b). The results are shown in Figure 5.1. The dashed line represents the Baryonic Tully–Fisher relation fitted by disk galaxies. The dashed line represents the Baryonic Tully–Fisher relation (BTFR) fitted for disk galaxies, which extends over five orders of magnitude in mass and holds tightly for disk galaxies. However, both the galaxy clusters (blue squares) and Local Group dwarf satellites (red squares) show systematic deviations from this relation, suggesting that the formation and

4. Calculated from $\Omega_b h^2$ and $\Omega_m h^2$ based on *Planck* TT, TE, EE+lowE+lensing data, with 1σ uncertainties.

evolution processes for dwarf galaxies, disk galaxies, and galaxy clusters may differ significantly.

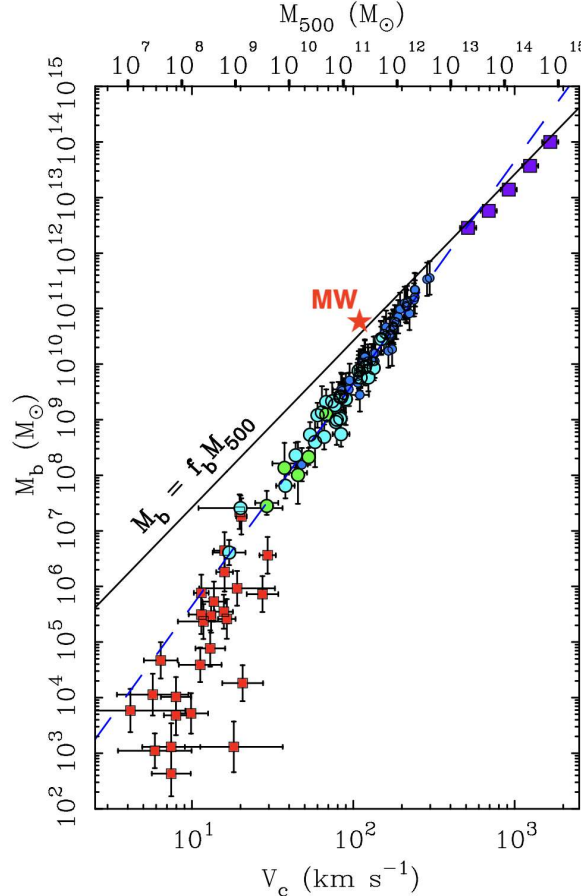


FIGURE 5.1 – Relation between baryonic mass and rotation velocity adapted from McGaugh et al. (2010). The y -axis presents the detected baryonic mass. The upper x -axis represents the mass enclosed by an over-density of 500 times the critical density while the lower x -axis represents the circular velocity estimated by McGaugh et al. (2010). Round symbols represent rotationally supported disk galaxies, and square symbols represent pressure-supported systems. Larger symbols correspond to systems whose baryonic mass is dominated by gas and smaller symbols those dominated by stars. Dark blue circles are for star-dominated spirals (McGaugh, 2005). Light blue (Stark et al., 2009) and green (Trachternach et al., 2009) circles represent recent work on gas-dominated disks. Red squares represent Local Group dwarf satellites (Walker et al., 2009b). Purple squares represent the mean of many galaxy clusters (Giordini et al., 2009). The solid line represents the relation of baryon fraction $f_b = 0.17$ (Komatsu et al., 2009). The dashed line represents the Baryonic Tully–Fisher relation for rotating disks. The red pentagram represents the Milky Way using the mass estimation from Jiao et al. (2023).

The solid line in Figure 5.1 represents the universal baryon fraction, $f_b = 0.17$ (Komatsu et al., 2009). All cosmic structures, except for the MW as estimated by Jiao et al. (2023), fall below this line, indicating that the fraction of detected baryons is consistently lower than the cosmic fraction across all scales. Concerns may arise regarding the accuracy of baryonic mass estimates. Gas mass is generally measured with higher accuracy, as the emission mechanisms are well understood. McGaugh et al. (2010) argued that the uncertainty in the stellar mass-to-light

(M/L) ratio is only about a factor of ~ 2 , which is insufficient to explain the large discrepancy between the observed baryon fraction and the universal cosmic fraction.

One possible explanation is that not all baryons have had enough time to cool into the observed cold gas and stellar components in galaxies, meaning a significant fraction of baryons may still be mixed with the DM halo. Hot gas has been detected in galaxy clusters, where it constitutes a significant fraction of the baryons, resulting in a relatively small deviation from the universal baryon fraction (< 0.1 dex). However, early direct searches for hot halo gas in individual galaxies have led to inconclusive results (Bregman, 2007; Anderson et al., 2009), and the fraction of missing baryons remains significantly large at the scale of individual galaxies and dwarf galaxies. Assuming that the baryonic mass estimates are relatively accurate, the missing mass must consist largely of DM. This leads to the conclusion that DM is the dominant mass component in all cosmic structures, with a DM-to-baryon ratio ranging from a factor of ~ 10 in galaxy clusters to over 10^3 in dwarf galaxies.

However, one should also be cautious about the total mass estimation. In principle, dynamical tracers such as rotation curves and velocity dispersion are expected to reliably trace the total mass, because both baryons and dark matter interact gravitationally. However, the application of these tracers requires a well-defined range where they are valid. For example, Gnedin & Ostriker (1999) suggested that an object must have completed at least 3-5 orbits after a perturbation to reach dynamical equilibrium. In the case of a galaxy surrounding a galaxy cluster at a radius of 1 Mpc, if one assumes a rotational velocity of 1000 km s^{-1} (as shown in [Figure 5.1](#)), the time required to complete 3 orbits would be approximately 18.43 Gyr, which is longer than the age of the universe. Therefore, the outer regions of galaxy clusters might not be in equilibrium, resulting in potentially unreliable mass estimates based on velocity dispersion.

Accurately estimating the mass of galaxies is therefore essential for understanding their formation and evolution, particularly because the fraction of missing mass is larger in galaxies than in clusters. More precise mass estimates will deepen our understanding of dark matter and guide direct detection experiments. For example, the dark matter fraction in dwarf galaxies is expected to exceed 10^3 . If dwarf galaxies are indeed the most dark matter-dominated systems, they would represent ideal targets for direct detection experiments.

Significant theoretical and observational progress has been made recently. Simulations show that gas-rich mergers are highly efficient at reforming disks in merger remnants (Hopkins et al., 2010; Sauvaget et al., 2018), supporting the rebuilding disk scenario, where disk galaxies form through gas-rich major mergers. Observational data also indicate that approximately 50% of spiral galaxy progenitors were in a merger phase around 6 Gyr ago (Hammer et al., 2009; Delgado-Serrano et al., 2010). Hammer et al. (2018a) used a gas-rich major merger with a mass ratio of 4:1, which occurred 2-3 Gyr ago, to explain almost all exceptional features of M31. As large-scale observations with high resolution and accuracy become increasingly available, it will enable more precise studies of galaxy dynamics. This is also the main focus of my PhD study, particularly on the Milky Way, Local Group dwarfs, and nearby spiral galaxies.

1 Is the Milky Way an exceptional galaxy?

The most striking aspect of Figure 5.1 is the position of the MW. The MW is located above the universal baryon fraction line and exceeds all other disk galaxies, suggesting it has a higher baryon fraction than expected. This result is based on the mass estimation from Jiao et al. (2023), who derived the RC from *Gaia* DR3. Similar results were also reported by Ou et al. (2024), who estimated that the MW DM mass to be $1.82^{+0.06}_{-0.05} \times 10^{11} M_{\odot}$, with a baryon fraction of ~ 0.25 , using a different sample of stars based on *Gaia*. This leads to tension between the MW and other galaxies, shifting the missing baryon problem into an excess baryon problem.

The main reason for the low MW DM mass estimation is the Keplerian decline detected by Jiao et al. (2023) in the RC beyond ~ 19 kpc, which may indicate a cut-off in the mass distribution. Noordermeer et al. (2007, see also Zobnina & Zasov 2020) specifically studied spirals with declining RCs and found none that have a fully Keplerian decline in their outer regions. In the THINGS project, de Blok et al. (2008) demonstrated that higher-resolution observations did not confirm the previously reported RC decline of NGC 3521 by Casertano & van Gorkom (1991). Another example of a declining RC in M81 is likely caused by galaxy interactions. Upon reviewing disk galaxies, van der Kruit & Freeman (2011) noted that no spiral galaxies show a genuine decline in their RCs.

Stacy McGaugh (private communication) suggested that *Gaia* is optimized for observing nearby stars within a few kpc, but its reliability may decrease beyond 20 kpc. *Gaia* provides parallax measurements with 10% accuracy at a distance of 10 kpc from the Sun and 20% accuracy out to 20 kpc. Proper motions have similar precision, with transverse velocities measured to better than 1 km/s out to 20 kpc for typical Sun-like stars (Gaia Collaboration et al., 2023). Gaia Collaboration et al. (2021a) used *Gaia* EDR3 to study the structure and properties of the Magellanic Clouds at distances of approximately 50 kpc, suggesting it is reasonable to trust *Gaia* data at 20 kpc.

The scale length of the exponential disk used in deriving the RC by the Jeans equation has also been questioned. In particular, Koop et al. (2024) argued that the MW might have a truncated disk. Modeling a truncated disk with an exponential density profile could indeed lead to an underestimation of the rotational velocity in the outer regions. Additionally, Gary Mamon (private communication) also found that some MW-like galaxy simulations from TNG50 have larger scale lengths in their inner regions. In response, we tested various scale lengths using the same data and found that reducing the scale length by a factor of 2-3 did not significantly affect the RC. To maintain a flat RC in the outer regions, the scale length would need to approach nearly *zero* (Chapter 2, Section 3.2.2). However, most spiral galaxies are observed to have larger scale lengths in their outskirts. The MW itself has been measured to have a thin disk with a scale length of 2.6 kpc and an extended thick disk with a scale length of 3.6 kpc (Jurić et al., 2008). Therefore, it is unreasonable to assume that the MW has a truncated disk.

We also selected a smaller but more complete sample of stars to study the scale length of the MW, which we found to be smaller—ranging from the 2.5 kpc used in Jiao et al. (2023) to 1.65 kpc (Chapter 2, Section 4.2). Despite this, the RC remains in decline and still produces low

mass estimates (Chapter 2, Section 4.3).

The Jeans equation we used to derive the RC is valid for axisymmetric systems. Therefore, there might be concerns that the Galactic disk is not in dynamical equilibrium, potentially leading to asymmetries. However, the MW is a relatively isolated system, with its last major merger, Gaia-Sausage-Enceladus, occurring approximately 8-10 Gyr ago (Belokurov et al., 2018; Haywood et al., 2018; Helmi et al., 2018). Since then, the MW disk is likely to have not experienced large-scale perturbations. Assuming a star rotating at 170 km s^{-1} at a radius of 30 kpc, it would have completed around 4.5 orbits since the GSE, which could be considered sufficient to assume the system has reached dynamical equilibrium (Gnedin & Ostriker, 1999).

Minor mergers are expected to impact the outer regions of the disk. The Large Magellanic Cloud (LMC), which is currently undergoing its first passage, may have affected the position of the MW disk relative to its halo—a phenomenon referred to as the ‘sloshing’ of the Galactic disk (Conroy et al., 2021; Erkal et al., 2021). However, this is unlikely to have significantly influenced the internal dynamics or morphology of the disk itself (Laporte et al., 2018). The infall of Sagittarius dwarf galaxy (Sgr) 4-6 Gyr ago, might have perturbed the MW outer disc, possibly explaining the Galactic disk warp (Bailin, 2003) and the observed vertical oscillations (Laporte et al., 2018). Koop et al. (2024) used a numerical simulation of Sgr from (Laporte et al., 2018) to study the impact of Sgr on the MW disk and concluded that it could lead to an underestimation of rotational velocity up to 15% at large radii.

However, Laporte et al. (2018) used a much more massive model of Sagittarius (Sgr), approximately 16 times larger than that employed by Vasiliev et al. (2021), which more accurately reproduces the Sgr stream. Regarding the impact of Sgr on the MW RC, it can be argued that reducing the perturbing mass by a factor of ~ 16 would decrease the predicted changes in rotational velocity by a factor of ~ 4 , assuming linear perturbations. This would lower the 15% uncertainty suggested by Koop et al. (2024) to align with the systematic uncertainties of around 4%, as discussed in Chapter 2, Section 4.2. Additionally, Wang et al. (2022b) studied the infall of Sgr and successfully reproduced its core morphology, kinematics, and streams. This research could be valuable in future studies to better estimate the impact of Sgr on the MW disk.

Compared with other spiral galaxies, the *Gaia* mission provides six-dimensional phase space information of stars in the MW, which allows us to derive the orbits of stars and study the dynamics of the MW disk with unprecedented precision. In Ou et al. (2024) data sample, 244 stars were used in the outer region ($R > 20 \text{ kpc}$), with only 3 stars having highly eccentric orbits (Chapter 2, Section 4.1). Therefore, the data sample we used is relatively axisymmetric and suitable for use in the Jeans equation.

There may also be concerns about the representativeness of the sample for the entire Galactic disk. On one hand, we have estimated the asymmetry drift (AD) using the Jeans equation and by splitting the data sample, resulting in two systematic uncertainty estimates, which are consistent with each other ($\sim 2\%$ at $R < 20 \text{ kpc}$ and $\sim 5\%$ at $R > 20 \text{ kpc}$, Chapter 2, Section 4.2). On the other hand, the AD correction is indeed imperfect because the observations are limited to the stars on the same side of the Sun. Additionally, the data used for the outskirts are confined to the anticenter direction, which is not fully representative of the entire disk. Due to dust extinction

and distance, it is currently impossible to measure the parallaxes and proper motions of stars on the opposite side of the MW disk. With the accumulation of more infrared survey data over time, it may become feasible to better measure stars on the far side and study the kinematics of the entire disk.

The choice of dark matter (DM) profile can significantly affect mass estimates. Both the low DM mass estimates and high baryon fractions reported by Jiao et al. (2023) and Ou et al. (2024) were derived using the Einasto profile. In contrast, the gNFW profile used by Ou et al. (2024) estimates a virial DM mass of $M_{200} = 6.94^{+0.12}_{-0.11} \times 10^{11} M_\odot$, corresponding to a baryon fraction of approximately 0.08. This would place the MW in closer alignment with other disk galaxies in Figure 5.1. However, the gNFW profile *cannot* reproduce the Keplerian decline observed in the outer regions of the MW's RC, as shown in Figure 5.2.

Given the rapid decline in the circular velocity, particularly the Keplerian decline beyond $R > 19\text{kpc}$, the exponential decrease in the Einasto profile allows for a much steeper fall-off in density at larger radii compared to the gNFW profile, which has a power-law slope of $3-\beta$ (with a maximum slope of 3). As a result, while the gNFW profile from Ou et al. (2024) fits the inner regions well ($R < 17$ kpc), it fails to fit the Keplerian decline in the outer regions.

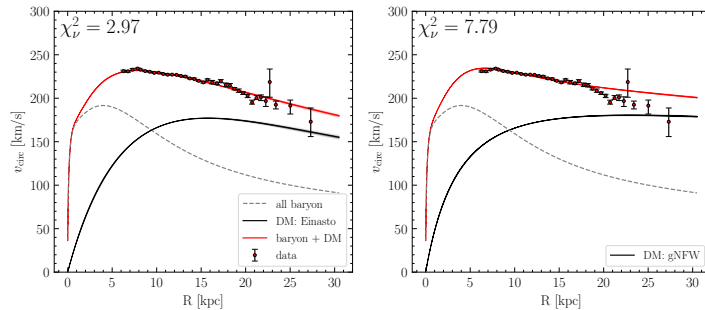


FIGURE 5.2 – Comparison between Einasto (left) and gNFW (right) profile fit to the MW RC from Ou et al. (2024, Figure 8).

Another issue with the gNFW profile is that it is extrapolated out to a radius of 186.81 kpc, which extends far beyond the range of the observed data. In contrast, the extrapolation of the Einasto profile is constrained by the Keplerian decline in the rotation curve, as discussed in the previous paragraph. For the Einasto profile, the mass increase beyond the observed data is negligible, whereas for the gNFW profile, it accounts for a significant portion of the total mass.

It is important to note that the extrapolation is based on the assumption that the chosen density profile is representative of the true DM distribution, though our understanding of the nature of DM remains limited. Any extrapolation has to be model-dependent. Therefore, mass extrapolation introduces significant uncertainties in the overall mass estimation. Future studies should emphasize mass estimates enclosed within specific radii that are constrained by observed data and explore more flexible functional forms for density profiles.

A potential issue lies in the fitting method. The mass estimates by Ou et al. (2024) and Jiao et al. (2023) were obtained using the MCMC (Markov Chain Monte Carlo) method. However,

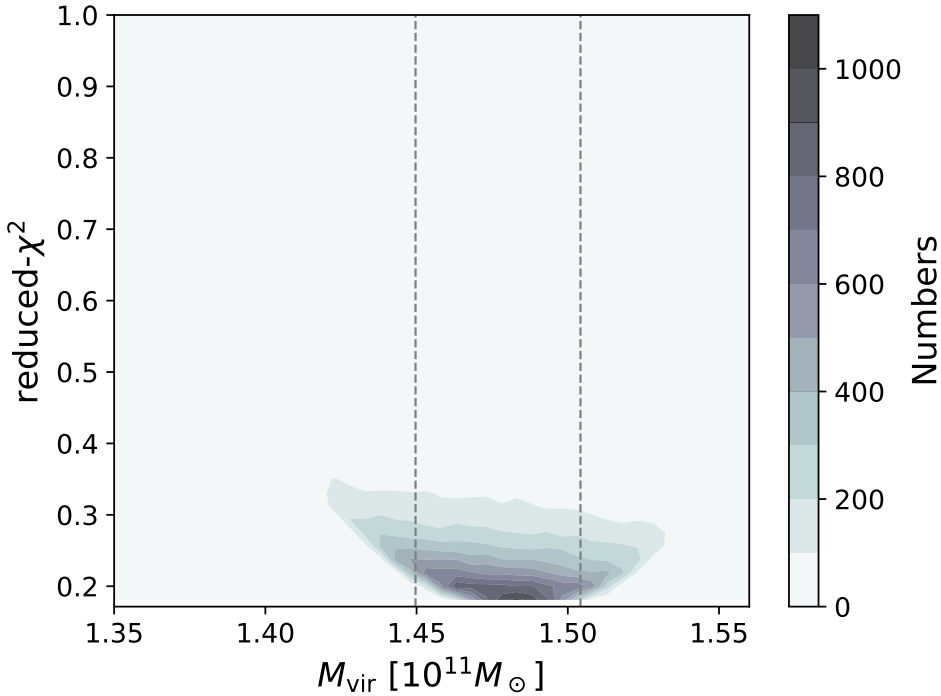


FIGURE 5.3 – Reduced χ^2 distribution of the virial mass from the parameter space of the Einasto profile fit to the MW RC from Ou et al. (2024) using the MCMC method. The red dashed line represents the 1σ confidence level.

this approach might overly constrain the parameter space around the best-fit values, possibly underestimating the associated uncertainties. For instance, in Figure 5.3, we illustrate the reduced χ^2 distribution for the virial mass obtained from the Einasto profile fit to the MW RC, as conducted by Ou et al. (2024) using the MCMC method. The reduced χ^2 values are generally below 0.4. This can be attributed to two factors: on the one hand, systematic uncertainties may have been overestimated (Chapter 2, Section 4.2); on the other hand, the MCMC method assumes that each data point is independent, which may not be the case for the MW RC due to the measurement uncertainties.

Due to these limitations, Jiao et al. (2023) further derived a maximal mass by replacing each data with its 1σ upper limits. In Chapter 2, Section 4, we employed a traditional χ^2 fitting method. This approach yielded larger uncertainties compared to the MCMC method, resulting in a broader mass estimate for $M_{200} = 4.1 - 5.6 \times 10^{11} M_{\odot}$ at the 1σ confidence level (Chapter 2, Section 4.3). Under this scenario, the baryon fraction of the MW would fall between approximately 0.09 and 0.14, positioning the MW more consistently with other disk galaxies, as shown in Figure 5.1.

2 Could we consider all spiral galaxies at equilibrium?

The *Gaia* mission provides six-dimensional measurements of stars in the MW, enabling the derivation of the most accurate RC among all spiral galaxies, as discussed earlier. The main

advantage is that these measurements allow us to verify whether stellar orbits are circular or not, making the MW RC particularly robust and reliable. Unfortunately, this level of precision is not feasible for other galaxies, highlighting the need to reconsider the methodologies used for deriving RCs in external spiral galaxies.

To obtain the most extended RCs for spiral galaxies and detect the flat behavior indicative of DM, HI observations are commonly used, as gas disks typically extend farther than stellar disks. However, for external spiral galaxies, it is impossible to measure both the three-dimensional velocities and positions of the gas. As a result, the standard method is to assume that the gas disk is in equilibrium and that gas follows circular orbits. The rotational velocities are then derived from the line-of-sight velocity (V_{LOS}), corrected for the inclination angle of the disk.

The rebuilding disk scenario proposed by Hammer et al. (2005, 2009) suggests that the formation of spiral galaxies results from gas-rich major mergers. In this framework, the bulge and thick disk are formed from pre-existing stars in the progenitor galaxies, while the thin disk is built from gas that accretes onto the galaxy from the merger remnant, with the thin disk forming from the inside out. If the gas fraction is sufficiently high (around 50%), this scenario predicts that the reformed disk can become the dominant component of the reshaped galaxy. Simulations have demonstrated that the disk rebuilding scenario can reproduce several observed properties of spiral galaxies, such as the radial age and metallicity gradients of disk stars, as well as the size-mass relation.

According to the disk rebuilding scenario, gas disks settle from the inside out, making it critical to consider the equilibrium state of the gas disk. If the gas has not yet reached equilibrium, its kinetic energy—particularly for gas recently accreted from tidal tails or other merger remnants—may be dominated by its potential energy at apocenter (the infall velocity). This could lead to an overestimation of the rotational velocity, as the gas may still be in the process of settling into circular orbits within the disk, rather than already moving in equilibrium.

Hammer et al. (2009) and Delgado-Serrano et al. (2010) have shown that, on average, more than half of spiral galaxies were in a merger phase around 6 Gyr ago. Assuming a rotational velocity of 200 km s^{-1} , gas particles could have completed three orbits out to a radius of 65 kpc during this time. However, this is based on overall statistical studies, and estimating the timing of recent major mergers requires specific measurements for individual galaxies.

For example, M31, located 760 kpc away from the MW, has been found to have undergone significant star formation 2-4 Gyr ago through deep surveys (Bernard et al., 2015; Williams et al., 2015). M31 also features a 10-kpc star formation ring (Barmby et al., 2006; Gordon et al., 2006) and various streams in its halo (Ibata et al., 2014), including the Giant Stream (Ibata et al., 2001). All these exceptional features of M31 have been reproduced in hydrodynamical simulations of a gas-rich, mass ratio 4:1 major merger that occurred 2 to 3 Gyr ago (Hammer et al., 2018a).

Assuming M31 experienced a major merger 2.5 Gyr ago, the gas particles that have experienced 5 orbits, which we could consider that they are fully in equilibrium, could only reach a radius of 20 kpc based on the RC from Chemin et al. (2009). In contrast, according to the MW RC, stars at a radius of 20 kpc would have completed at least 14 orbits, suggesting they are likely

in equilibrium. This is under the assumption that the last major merger, the Gaia-Enceladus-Sausage (GSE) event, occurred around 8-10 Gyr ago (Belokurov et al., 2018; Haywood et al., 2018; Helmi et al., 2018). A detailed study on the impact of recent mergers on the RC of M31, using numerical simulations, is currently in preparation (Hammer et al. 2024, in preparation). Preliminary results indicate that the observed rise in the RC of M31 beyond $R > 130$ arcmin, as shown in Figure 5.4, is due to non-equilibrium gas particles in the disk.

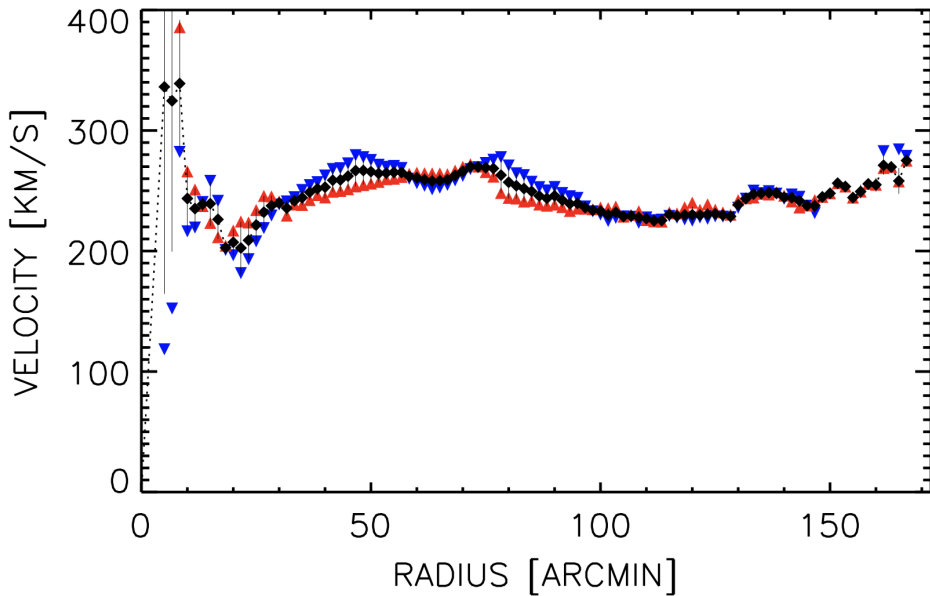


FIGURE 5.4 – HI rotation curve of Messier 31. The filled diamonds are for both halves of the disk fitted simultaneously while blue downward/red upward triangles are for the approaching/receding sides fitted separately. This figure is adapted from Chemin et al. (2009).

Martínez-Delgado et al. (2010) used small ($D = 0.1 - 0.5$ m) robotic telescopes with exquisite surface brightness sensitivity ($\mu_{\text{lim}} \sim 28.5 \text{mag arcsec}^{-2}$) to obtain ultra-deep, wide-field imaging of 8 isolated spiral galaxies in the Local Volume. Among these, NGC 3521 and NGC 5055 are part of our nearby galaxy sample (Chapter 3). All these galaxies are found to contain significant numbers of gigantic stellar structures. Martínez-Delgado et al. (2010) suggested that these structures are the remnants of ancient, fully disrupted satellites from minor mergers, or recent infall of small dwarf galaxies, similar to the Sgr in the MW. They mentioned that major mergers would completely destroy the pre-existing disk, while minor mergers would only perturb it. However, they did not account for the gas component, which can be accreted from the remnants of gas-rich major mergers and contribute to rebuilding a new stellar thin disk. The M31 major merger model by Hammer et al. (2018a) suggests that these features could be better explained by the gas-rich major merger scenario.

A detailed comparison of the morphologies of NGC 3521 in different bands, including the optical image from Martínez-Delgado et al. 2010, is presented in Chapter 3, Section 3.1. We also compared these observations with gas-rich major merger simulations and found that the stellar structures, as well as the asymmetric gas disk, could be reproduced by these simulations (Chapter 3, Section 4.1). Additionally, we studied the stellar populations of NGC 3521 and

derived its star formation history, which suggests that a recent major merger occurred about 1-3 Gyr ago (Chapter 3, Section 3.4). This leads us to consider that the large discrepancy in the rotation curve (RC) starting at \sim 17 kpc between the approaching and receding sides of NGC 3521 (Chapter 3, Section 3.2) is likely caused by non-equilibrium conditions in the outskirts, which is due to a recent major merger. Assuming at least three orbits, it would take approximately 1.5 Gyr for the gas to settle and reach equilibrium at 17 kpc, which is consistent with the timing of the recent major merger as estimated from the SFH.

However, this estimation might not be entirely accurate. For example, Williams et al. (2015) used deep surveys to resolve individual stars in M31 inner disk and identified a major global enhancement in star formation 2-4 Gyr ago. In contrast, for our target galaxies, we do not have the same resolution to study individual stars. As a result, we may need to rely on M31 simulations to link recent major mergers with other observable features, such as large stellar structures, gas disk asymmetries, and velocity differences between the approaching and receding sides of the galaxy.

We applied the same analysis to other spiral galaxies in our sample and found that NGC 2841, NGC 3198, NGC 5055, NGC 6946, and NGC 7331 may have also experienced recent major mergers (Chapter 3, Section 5.2). This highlights the importance of considering how the non-equilibrium state of the gas disk can affect both the RC and mass estimation of spiral galaxies. Consequently, we suggest that for methods based on a limited volume, such as the H I RC, substructures surrounding the disk, or escape velocity, the calculated DM mass should be confined to a relatively limited volume. This approach aligns with the concept of what constitutes the missing mass in galaxies.

3 Are dwarf galaxies around the Milky Way dark matter dominated?

Most dwarf galaxies do not exhibit clear signs of tidal disturbance. Early studies suggested that most dwarf galaxies lack gas and are predominantly composed of old stars (e.g., Tolstoy et al., 2004; Battaglia et al., 2006). As a result, many studies assumed that dwarf galaxies have been long-lived satellites of the MW for up to \sim 8-10 Gyr and are in a state of self-equilibrium. Based on the LOS velocity measurements, the dwarfs were found to have large velocity dispersions with a flat profile (Chapter 4, Section 1.2.2). This led to the conclusion that dwarf galaxies are DM-dominated systems. As shown in Figure 5.1, the dwarf galaxies are located in the lower-left corner of the plot. Comparing their total mass to their baryonic mass, one can infer that the ratio of DM to baryonic matter exceeds 10^3 , which has prompted many researchers to consider dwarf galaxies as ideal targets for studying the nature of DM and for direct DM detection experiments.

However, recent studies are challenging the assumption that most dwarfs are long-lived MW satellites. Deep wide-field photometric analyses have revealed that Fornax, Carina, Leo I, Ursa Minor, and Leo II experienced recent star formation events around \sim 1-2 Gyr ago (de Boer et al.,

2013; Weisz et al., 2014a). This suggests that gas may play a significant role in the late-stage evolution of dwarf galaxy dynamics. Additionally, most dwarf galaxies are observed near their pericenter, which is unexpected for long-lived satellites. Hammer et al. (2018b, 2019) identified a strong anti-correlation between the internal acceleration ($\sigma_{\text{I.o.s}}^2/r_{\text{half}}$) of dwarf spheroidal galaxies (dSphs) and their Galactocentric distance. Such an anti-correlation should not exist in dark matter-dominated systems, suggesting instead that these dwarf galaxies are experiencing tidal shocks from the MW (Binney & Tremaine, 2008).

Based on these recent observations, we propose that the dwarf galaxies are not long-lived satellites, but rather newcomers of gas-rich dwarf galaxies that have only recently approached the MW (Yang et al., 2014; Hammer et al., 2018b, 2019, 2023, 2024). These gas-rich dwarf galaxies approached the MW within the past few billion years and subsequently lost their gas due to the ram-pressure stripping, induced by the MW's circumgalactic medium (CGM) (Anderson & Bregman, 2010; Miller & Bregman, 2013; Tumlinson et al., 2017). The loss of gas, which constituted a significant portion of their gravitational potential, caused the remaining stars to expand spherically, leading to the observed high velocity dispersions. In this scenario, dwarf galaxies cannot have massive DM halos, as a large DM halo would prevent the expansion of their stellar components after the loss of significant gas.

Wang et al. (2024) used hydrodynamical simulations to study the infall of gas-rich dwarfs into the MW halo and predict that a small fraction of young stars could be present in both the cores and outskirts of these dwarfs. Yang et al. (2022) studied Fornax and found an extended stellar halo around it. Yang et al. (2024, accepted) used data from *Gaia* DR3 and further found that almost all dSphs have young stellar populations, which is consistent with the prediction of the ram-pressure stripping scenario.

This ram-pressure and tidal shock scenario also provides a good explanation for the relationship between the lookback time of the stellar system entry of the MW halo and its binding energy. Using the orbital parameters of the dwarfs from Li et al. (2021a) based on *Gaia* EDR3, Hammer et al. (2023) found that MW dwarf galaxies have much smaller binding energies compared to those of GSE GCs, with a difference by a factor of 6 on average. Stellar systems that entered the MW halo earlier are expected to have smaller binding energies because, first, the MW has grown in mass over time, and second, early-arriving systems have experienced multiple orbits, giving them more opportunities to interact with other systems and lose energy. Therefore, the low binding energy of the dwarfs suggests that most of them are recent newcomers to the MW halo.

This relation was also confirmed by Rocha et al. (2012) using DM-only cosmological simulations, which revealed a tight linear correlation between the lookback infall time and the logarithm of the binding energy. Their simulations showed more than 1 dex of evolution with a scatter of only 0.13 dex (Chapter 4, Figure 4.11). Hammer et al. (2023) identified the same tight linear correlation between the lookback infall time and the logarithm of the binding energy for MW dwarf galaxies, as well as globular clusters associated with the bulge, Kraken, GSE, and the Sagittarius (Sgr) infall [Figure 4.5](#).

Dwarf galaxies have long been considered ideal targets for measuring the mass of the MW

at large radii under the assumption that they are long-lived satellites. However, recent studies suggest that these dwarfs are newcomers and may not be in equilibrium. During their first infall into the MW, their kinematics are still dominated by the initial infall velocity, which could lead to a significant overestimation of the MW mass. As Hammer et al. (2024) show, the smaller the MW mass model used, the more dwarfs are found to have eccentricities larger than 1, indicating that they may not be bound to the MW (Chapter 4, Section 1.4). Consequently, these dwarfs cannot be reliably used to estimate the MW mass.

However, using the relationship between infall lookback time and binding energy offers a more reliable approach to mass estimation because this relation does not depend on the assumption of equilibrium. This approach is presented in Chapter 4, Section 2. By selecting 22 MW-like galaxies from cosmological simulations in the FIRE-2 and Auriga projects, we found that simulations capable of reproducing the binding energy of GSE GCs confirm that the dwarfs with larger binding energies are indeed recent newcomers to the MW halo, as predicted by Hammer et al. (2023). Additionally, these comparisons show that MW mass estimates exceeding $10^{12} M_{\odot}$ cannot reproduce the binding energies of the bulge, GSE, and Sgr GCs. This suggests that mass estimations of the MW based on the long-lived satellite assumption for dwarfs will systematically overestimate the true MW mass.

In addition, Rocha et al. (2012) and the Auriga simulations show that sub-halo systems are dynamically hot, which may be because these simulations underwent numerous minor mergers, resulting in binding energies that are 3 to 9 times smaller than those of the Sgr, GSE, and bulge GCs. Therefore, it would be valuable to focus on simulations that have experienced old major mergers, similar to the Milky Way, or recent major mergers, to better study the formation and evolution of spiral galaxies like M31.

4 Gas component should be considered more carefully

Within the hierarchical galaxy formation framework (e.g., White & Frenk 1991), major mergers were long believed to lead to the destruction of any pre-existing stellar disks (Toth & Ostriker, 1992). As a result, disk galaxies were assumed to maintain stable rotation since very early epochs. However, this hypothesis encountered the problem of insufficient angular momentum to support the formation of disk galaxies (Navarro & Steinmetz, 2000), where galactic disks formed from cosmological fluctuations were too small.

The main problem was that the gas component was often neglected or not modeled in early simulations. Gas is more challenging to simulate than stars, which are typically modeled as collisionless particles treated as point masses in simulations. Even simulating the stellar component is complex, as it requires accounting for processes like feedback. Early efforts primarily focused on dark matter-only simulations. However, the gas component is far more intricate, as it is influenced by hydrodynamic forces, capable of cooling, heating, and condensing into stars. Gas is not only the main fuel for star formation but also plays a critical role in the formation and evolution of galaxies.

Significant progress has been made in both observations and simulations. Hammer et al.

(2009) and Delgado-Serrano et al. (2010) accurately compared distant and nearby galaxies, showing that more than half of spiral galaxies were in a merger phase approximately 6 Gyr ago. On the simulation side, gas components have been successfully modeled in recent cosmological simulations using smoothed particle hydrodynamics (SPH) techniques, based on derivatives of the GASOLINE (Wadsley et al., 2004) or GADGET (Springel, 2005) codes. In particular, the GIZMO implementation, built on the GADGET framework, has shown great promise in modeling the gas component with higher accuracy. As simulation software continues to improve, gas components can now be modeled more reliably.

Hammer et al. (2018a) used GIZMO to simulate a gas-rich, mass ratio 4:1 major merger that occurred 2 to 3 Gyr ago, successfully explaining all of the exceptional features of M31. This result strongly supports the disk rebuilding scenario, in which gas-rich major mergers play a central role in the formation of spiral galaxies (see the discussion above, as well as Chapter 1, Section 3.3).

The gas component is also crucial for understanding the evolution of dwarf galaxies. Based on the ram-pressure stripping and tidal shock scenario (see above discussion, as well as in Chapter 4, Section 1.3), we suggest that the dwarfs are descendants of gas-rich dwarf galaxies that have recently lost their gas due to the ram-pressure from the MW halo gas.

Hot gas is also considered a key component in addressing the missing baryon problem. It has been detected in galaxy clusters and constitutes a significant fraction of the baryon, leading to only a small deviation of galaxy clusters from the universal baryon fraction (smaller than 0.1 dex as shown in Figure 5.1). However, it remains unclear how much hot gas is present in the MW halo. This hot gas is expected to reside in the circumgalactic medium (CGM), which is difficult to detect. Recent space missions, such as eROSITA, are expected to provide more information about the hot gas in the MW halo and in the halos of other galaxies.

In summary, the gas component must be carefully considered in the study of galaxy formation and evolution. Gas plays a crucial role in the formation and evolution of structures on different scales, and its dynamics can significantly influence stellar kinematics and mass estimation for galaxies. Future studies should focus on improving gas modeling in simulations and incorporating gas dynamics into the analysis of observational data.

Conclusion et perspectives

1 Conclusions (English version)

In this thesis, I present my studies on galaxy dynamics, focusing on the mass estimates from the Milky Way (MW) to nearby spiral galaxies.

My research on the MW has greatly benefited from the *Gaia* mission. Using the RC from *Gaia* DR2, I tested various dark matter profiles and estimated the mass of the MW. The analysis demonstrated that the Einasto profile provided a better fit, whereas the NFW and generalized NFW profiles were too shallow to accurately fit the declining RC. This result emphasizes the suitability of the Einasto profile for modeling RCs and estimating the total mass of galaxies. Using *Gaia* DR3, I derived an updated MW RC and conducted a detailed analysis of systematic uncertainties. For the first time, we detected a Keplerian decline in the MW RC beyond 19 kpc, revealing a significant deviation from the commonly recognized flat RC in most spiral galaxies.

Additionally, we are currently examining the systematic uncertainties in the RC based on *Gaia* DR3 data, with the goal of establishing a robust upper limit on the MW mass. The MW mass is estimated to be $2.5 \times 10^{11} M_{\odot}$, with an upper limit of $5.6 \times 10^{11} M_{\odot}$ at the 1σ level. This implies a baryonic mass fraction of 0.25 for the MW, which is higher than the universal estimate of 0.17 from the Λ CDM model, suggesting that the MW may not face the missing baryon problem.

I extended my research to nearby galaxies, which are selected from the SPARC and THINGS databases. In this work, I analyzed the morphological features of nine nearby galaxies, conducted spectral and photometric fitting, reconstructed their star formation histories, and explored their dynamical structures as revealed by HI observations. From this analysis, we inferred the epochs of recent major mergers and found that six of the galaxies likely experienced a recent major merger. We are currently investigating the impact of these mergers on their dynamical structures, particularly their RCs, by comparing the observational data with hydrodynamical simulations.

I was also involved in projects that study dwarf galaxies surrounding the MW. I provided mass models of the MW, which were used in the dynamical modeling of dwarf galaxies. I contributed to research that explores the relationship between dwarf galaxy infall times and binding energy using cosmological simulations. I derived the relevant data from the cosmological simulations. By comparing the predicted relationships from different simulations with observations, and assuming the MW potential, we concluded that most dwarf galaxies are likely to have been

recently accreted.

In addition, I also contributed to a study on the Fornax dwarf spheroidal galaxy, where my main work is to fit observed stellar profiles, highlighting the significance of an extended stellar halo around Fornax. All of these studies are in agreement with the ram-pressure stripping theory for dwarf galaxies, suggesting that most dwarf galaxies are newcomers in the MW halo, having lost their gas recently, which has led to the spherical expansion of their stellar components. This stands in contrast to the view that dwarf galaxies are long-lived MW satellites with dark matter-dominated halos.

2 Conclusions (French version)

Dans cette thèse, je présente mes études sur la dynamique des galaxies, en mettant l'accent sur les estimations de masse de la Voie Lactée et des galaxies spirales voisines.

Mes recherches sur la Voie Lactée ont grandement bénéficié de la mission *Gaia*. En utilisant la courbe de rotation de la Voie Lactée basée sur *Gaia* DR2, j'ai testé divers profils de matière sombre et estimé la masse de la Voie Lactée. L'analyse a montré que le profil Einasto fournissait un meilleur ajustement, tandis que les profils NFW et NFW généralisé étaient trop peu profonds pour ajuster précisément la courbe de rotation décroissante. Ce résultat souligne la pertinence du profil Einasto pour modéliser les courbes de rotation et estimer la masse totale des galaxies. En utilisant *Gaia* DR3, j'ai dérivé une courbe de rotation de la Voie Lactée et mené une analyse détaillée des incertitudes systématiques. Pour la première fois, nous avons détecté un déclin képlérien dans la courbe de rotation de la Voie Lactée au-delà de 19 kpc, révélant un écart significatif par rapport à la courbe de rotation plate communément reconnue dans la plupart des galaxies spirales.

De plus, nous examinons actuellement les incertitudes systématiques dans la courbe de rotation basée sur les données de *Gaia* DR3, dans le but d'établir une limite supérieure robuste sur la masse de la Galaxie. La masse totale est estimée à $2,5 \times 10^{11} M_{\odot}$, avec une limite supérieure de $5,6 \times 10^{11} M_{\odot}$ au niveau 1σ . Cela implique une fraction de masse baryonique de 0,25 pour la Voie Lactée, qui est plus élevée que l'estimation universelle de 0,17 du modèle Λ CDM, suggérant que la Voie Lactée ne serait pas confrontée au problème des baryons manquants.

J'ai étendu mes recherches aux galaxies voisines, sélectionnées dans les bases de données SPARC et THINGS. Dans ce travail, j'ai analysé les caractéristiques morphologiques de neuf galaxies voisines, réalisé des ajustements spectraux et photométriques, reconstruit leurs histoires de formation stellaire et exploré leurs structures dynamiques révélées par les observations de hydrogène neutre. De cette analyse, nous avons déduit les époques des récentes fusions majeures et constaté que six des galaxies ont probablement connu une récente fusion majeure. Nous étudions actuellement l'impact de ces fusions sur leurs structures dynamiques, en particulier leurs courbes de rotation, en comparant les données observationnelles avec des simulations hydrodynamiques.

J'ai également participé à des projets qui étudient les galaxies naines entourant la Voie Lactée. J'ai fourni des modèles de masse de la Voie Lactée, qui ont été utilisés dans la modélisation dynamique des galaxies naines. J'ai contribué à une recherche qui explore la relation entre le

temps de chute des satellites dans le halo de la Galaxie et l'énergie de liaison en utilisant des simulations cosmologiques. J'ai dérivé les données des simulations cosmologiques. En comparant les relations prédictives par différentes simulations avec les observations, et en supposant le potentiel de la Voie Lactée, nous avons conclu que la plupart des galaxies naines sont susceptibles d'avoir été récemment accrétées.

De plus, j'ai également contribué à une étude sur la galaxie naine sphéroïdale de Fornax, où mon travail principal consiste à ajuster les profils stellaires observés, mettant en évidence l'importance d'un halo stellaire étendu autour de Fornax. Toutes ces études sont en accord avec la théorie de *ram-pressure* pour les galaxies naines, suggérant que la plupart des galaxies naines sont arrivées bien plus récemment dans le halo de la Galaxie, ayant perdu leur gaz, ce qui a conduit à l'expansion sphérique de leurs composants stellaires. Cela s'oppose à l'idée que les galaxies naines sont des satellites de longue date de la Galaxie avec des halos dominés par la matière sombre.

3 Perspectives

The globally decreasing Milky Way rotation curve (RC) derived by Jiao et al. (2023), which exhibits a Keplerian decline at large radii, stands in contrast to the flat RCs observed in most spiral galaxies. Our study used six-dimensional data of stars from Gaia, which provides the most precise astrometric measurements. Given that the Milky Way last major merger occurred approximately 9-10 Gyr ago, its disk is currently in equilibrium out to 27 kpc, which is about 10 times the scale length of the Milky Way disk (~ 2.6 kpc). These ensure the robustness of the Milky Way mass measurements.

However, the dynamical equilibrium of disks, particularly beyond which radius, has not been extensively studied in other spiral galaxies. For example, the RC of Andromeda Galaxy (M31) was measured up to 40 kpc (Chemin et al., 2009), while Hammer et al. (2024, in preparation) found that the gas disk of M31 is in equilibrium only up to 25 kpc, only about 3 times its disk scale length (~ 6 kpc). Therefore, investigating the dynamical equilibrium in spiral galaxies is crucial for understanding the discrepancy between the Milky Way and other spiral galaxies.

Mergers leave behind numerous remnants in the galactic halo, such as tidal tails and stellar rings, which require deep observations to detect. Recent deep surveys have already accumulated a lot of observations of spiral galaxies. Major mergers have been proven to result in the formation of spiral galaxies. Sauvaget et al. (2018) has already prepared a library of generic gas-rich hydrodynamical major merger simulations. By comparing observed structures with these simulations at specific epochs, future works will identify the best models to replicate the formation histories of the selected galaxies and quantitatively estimate the impact of recent major mergers on their RCs and mass estimates.

Liste des publications

Articles à comité de lecture

Yongjun Jiao, François Hammer, Jianling Wang, Yanbin Yang. "*Which Milky Way masses are consistent with the slightly declining 5-25 kpc rotation curve?*". *Astronomy & Astrophysics*. DOI: [10.1051/0004-6361/202141058](https://doi.org/10.1051/0004-6361/202141058)

Yongjun Jiao, François Hammer, Haifeng Wang, Jianling Wang, Amram Philippe, Chemin Laurent, Yanbin Yang. "*Detection of the Keplerian decline in the Milky Way rotation curve*". *Astronomy & Astrophysics*. DOI: [10.1051/0004-6361/202347513](https://doi.org/10.1051/0004-6361/202347513)

Conférences internationales (premier auteur)

Yongjun Jiao, François Hammer, Haifeng Wang, Jianling Wang, Yanbin Yang. "*Revisiting mass estimates of the Milky Way*". IAU Symposium 379: Dynamical Masses of Local Group Galaxies, Potsdam, March 20-24, 2023.

Yongjun Jiao, François Hammer, Haifeng Wang, Jianling Wang, Amram Philippe, Chemin Laurent, Yanbin Yang. "*Detection of the Keplerian decline in the Milky Way rotation curve*". Rencontres de Moriond, Electroweak Interactions & Unified Theories, La Thuile, March 24-31, 2024.

Bibliographie

- Aaronson M., 1983, *ApJ*, 266, L11
- Aaronson M., Olszewski E. W., 1987, *AJ*, 94, 657
- Agertz O., Kravtsov A. V., 2015, *ApJ*, 804, 18
- Agertz O., Teyssier R., Moore B., 2011, *MNRAS*, 410, 1391
- Agertz O., Kravtsov A. V., Leitner S. N., Gnedin N. Y., 2013, *ApJ*, 770, 25
- Alberts S., et al., 2011, *ApJ*, 731, 28
- Alpher R. A., Bethe H., Gamow G., 1948, *Physical Review*, 73, 803
- Amorisco N. C., Evans N. W., 2011, *MNRAS*, 411, 2118
- Amorisco N. C., Agnello A., Evans N. W., 2013, *MNRAS*, 429, L89
- Anderson M. E., Bregman J. N., 2010, *ApJ*, 714, 320
- Anderson M. E., Bregman J. N., Butler S. C., Mullis C. R., 2009, *ApJ*, 698, 317
- Aniyan S., Ponomareva A. A., Freeman K. C., Arnaboldi M., Gerhard O. E., Coccato L., Kuijken K., Merrifield M., 2021, *MNRAS*, 500, 3579
- Armandroff T. E., Da Costa G. S., 1986, *AJ*, 92, 777
- Ashman K. M., 1992, *PASP*, 104, 1109
- Athanassoula E., Rodionov S. A., Peschken N., Lambert J. C., 2016, *ApJ*, 821, 90
- Aumer M., White S. D. M., Naab T., 2014, *MNRAS*, 441, 3679
- Baade W., Hubble E., 1939, *PASP*, 51, 40
- Babcock H. W., 1939, *Lick Observatory Bulletin*, 498, 41
- Bailin J., 2003, *ApJ*, 583, L79
- Baldwin J. A., Phillips M. M., Terlevich R., 1981, *PASP*, 93, 5
- Balick B., Brown R. L., 1974, *ApJ*, 194, 265
- Balogh M. L., Pearce F. R., Bower R. G., Kay S. T., 2001, *MNRAS*, 326, 1228
- Barmby P., et al., 2006, *ApJ*, 650, L45

Bibliographie

- Barmentloo S., Cautun M., 2023, *MNRAS*, 520, 1704
- Barnes J. E., 1988, *ApJ*, 331, 699
- Barnes J., Efstathiou G., 1987, *ApJ*, 319, 575
- Bate N. F., McMonigal B., Lewis G. F., Irwin M. J., Gonzalez-Solares E., Shanks T., Metcalfe N., 2015, *MNRAS*, 453, 690
- Battaglia G., et al., 2006, *A&A*, 459, 423
- Battaglia G., Irwin M., Tolstoy E., Hill V., Helmi A., Letarte B., Jablonka P., 2008a, *MNRAS*, 383, 183
- Battaglia G., Helmi A., Tolstoy E., Irwin M., Hill V., Jablonka P., 2008b, *ApJ*, 681, L13
- Battaglia G., Tolstoy E., Helmi A., Irwin M., Parisi P., Hill V., Jablonka P., 2011, *MNRAS*, 411, 1013
- Battaglia G., Helmi A., Breddels M., 2013, *New A Rev.*, 57, 52
- Battaglia G., Sollima A., Nipoti C., 2015, *MNRAS*, 454, 2401
- Battaglia G., Taibi S., Thomas G. F., Fritz T. K., 2022, *A&A*, 657, A54
- Begeman K. G., Broeils A. H., Sanders R. H., 1991, *MNRAS*, 249, 523
- Bekenstein J. D., 2004, *Phys. Rev. D*, 70, 083509
- Bekenstein J., Milgrom M., 1984, *ApJ*, 286, 7
- Belokurov V., 2013, *New A Rev.*, 57, 100
- Belokurov V., et al., 2006a, *ApJ*, 642, L137
- Belokurov V., et al., 2006b, *ApJ*, 642, L137
- Belokurov V., Erkal D., Evans N. W., Koposov S. E., Deason A. J., 2018, *MNRAS*, 478, 611
- Bensby T., Feltzing S., Oey M. S., 2014, *A&A*, 562, A71
- Bernard E. J., Ferguson A. M. N., Chapman S. C., Ibata R. A., Irwin M. J., Lewis G. F., McConnachie A. W., 2015, *MNRAS*, 453, L113
- Bertola F., Capaccioli M., 1975, *ApJ*, 200, 439
- Bertone S., Conselice C. J., 2009, *MNRAS*, 396, 2345
- Bertone G., Hooper D., 2018, *Reviews of Modern Physics*, 90, 045002
- Binney J., Piffl T., 2015, *MNRAS*, 454, 3653
- Binney J., Tremaine S., 2008, *Galactic Dynamics*: Second Edition. Princeton University Press
- Binney J., Wong L. K., 2017, *MNRAS*, 467, 2446
- Binney J., Gerhard O., Spergel D., 1997, *MNRAS*, 288, 365
- Bissantz N., Gerhard O., 2002, *MNRAS*, 330, 591

- Bissantz N., Englmaier P., Gerhard O., 2003, *MNRAS*, 340, 949
- Bland-Hawthorn J., Gerhard O., 2016, *ARA&A*, 54, 529
- Blitz L., 1979, *ApJ*, 231, L115
- Bond J. R., Cole S., Efstathiou G., Kaiser N., 1991, *ApJ*, 379, 440
- Boomsma R., 2007, PhD thesis, University of Groningen, Kapteyn Astronomical Institute
- Bosma A., 1978, PhD thesis, University of Groningen, Netherlands
- Bosma A., 1981, *AJ*, 86, 1825
- Bournaud F., Jog C. J., Combes F., 2007, *A&A*, 476, 1179
- Bovy J., 2015, *ApJS*, 216, 29
- Bovy J., Rix H.-W., 2013, *ApJ*, 779, 115
- Bovy J., Rix H.-W., Liu C., Hogg D. W., Beers T. C., Lee Y. S., 2012a, *ApJ*, 753, 148
- Bovy J., et al., 2012b, *ApJ*, 759, 131
- Boylan-Kolchin M., Bullock J. S., Sohn S. T., Besla G., van der Marel R. P., 2013, *ApJ*, 768, 140
- Breddels M. A., Helmi A., 2013, *A&A*, 558, A35
- Bregman J. N., 2007, *ARA&A*, 45, 221
- Brook C. B., Kawata D., Gibson B. K., Freeman K. C., 2004, *ApJ*, 612, 894
- Brook C. B., Stinson G., Gibson B. K., Roškar R., Wadsley J., Quinn T., 2012, *MNRAS*, 419, 771
- Bruzual G., Charlot S., 2003, *MNRAS*, 344, 1000
- Bullock J. S., Dekel A., Kolatt T. S., Kravtsov A. V., Klypin A. A., Porciani C., Primack J. R., 2001, *ApJ*, 555, 240
- Buonanno R., Corsi C. E., Castellani M., Marconi G., Fusi Pecci F., Zinn R., 1999, *AJ*, 118, 1671
- Burbidge E. M., Burbidge G. R., Prendergast K. H., 1959, *ApJ*, 130, 26
- Burton W. B., Gordon M. A., 1978, *A&A*, 63, 7
- Cannon R. D., Hawarden T. G., Tritton S. B., 1977, *MNRAS*, 180, 81P
- Cappellari M., 2017, *MNRAS*, 466, 798
- Cappellari M., 2023, *MNRAS*, 526, 3273
- Cappellari M., Emsellem E., 2004, *PASP*, 116, 138
- Casertano S., van Gorkom J. H., 1991, *AJ*, 101, 1231
- Cautun M., et al., 2020, *MNRAS*, 494, 4291

- Chabrier G., 2003, *PASP*, 115, 763
- Chan M. H., 2024, *ApJ*, 969, 151
- Chemin L., Carignan C., Foster T., 2009, *ApJ*, 705, 1395
- Chemin L., de Blok W. J. G., Mamon G. A., 2011, *AJ*, 142, 109
- Chonis T. S., Martínez-Delgado D., Gabany R. J., Majewski S. R., Hill G. J., Gralak R., Trujillo I., 2011, *AJ*, 142, 166
- Christensen C. R., Davé R., Governato F., Pontzen A., Brooks A., Munshi F., Quinn T., Wadsley J., 2016, *ApJ*, 824, 57
- Chrobáková Ž., López-Corredoira M., Sylos Labini F., Wang H. F., Nagy R., 2020, *A&A*, 642, A95
- Churchwell E., et al., 2009, *PASP*, 121, 213
- Clarkson W., et al., 2008, *ApJ*, 684, 1110
- Clemens D. P., 1985, *ApJ*, 295, 422
- Clowe D., Bradač M., Gonzalez A. H., Markevitch M., Randall S. W., Jones C., Zaritsky D., 2006, *ApJ*, 648, L109
- Coleman M. G., Da Costa G. S., Bland-Hawthorn J., 2005, *AJ*, 130, 1065
- Conroy C., Gunn J. E., 2010, *ApJ*, 712, 833
- Conroy C., Gunn J. E., White M., 2009, *ApJ*, 699, 486
- Conroy C., Naidu R. P., Garavito-Camargo N., Besla G., Zaritsky D., Bonaca A., Johnson B. D., 2021, *Nature*, 592, 534
- Coquery E., Blanchard A., 2024, arXiv e-prints, p. arXiv:2407.18846
- Corbelli E., Lorenzoni S., Walterbos R., Braun R., Thilker D., 2010, *A&A*, 511, A89
- Courteau S., et al., 2014, *Reviews of Modern Physics*, 86, 47
- Cox T. J., Loeb A., 2008, *MNRAS*, 386, 461
- Cox T. J., Jonsson P., Primack J. R., Somerville R. S., 2006, *MNRAS*, 373, 1013
- D’Souza R., Bell E. F., 2022, *MNRAS*, 512, 739
- Dalcanton J. J., et al., 2012, *ApJS*, 200, 18
- Dale D. A., et al., 2017, *ApJ*, 837, 90
- De Lucia G., 2012, *Astronomische Nachrichten*, 333, 460
- De Lucia G., Kruijssen J. M. D., Trujillo-Gomez S., Hirschmann M., Xie L., 2024, *MNRAS*, 530, 2760
- Deason A. J., Belokurov V., Evans N. W., An J., 2012, *MNRAS*, 424, L44

- Delgado-Serrano R., Hammer F., Yang Y. B., Puech M., Flores H., Rodrigues M., 2010, [A&A](#), **509**, A78
- Demers S., Battinelli P., 2007, [A&A](#), **473**, 143
- Deng M., Du C., Yang Y., Liao J., Ye D., 2024, arXiv e-prints, p. arXiv:2409.03264
- Diemand J., Kuhlen M., Madau P., 2007, [ApJ](#), **667**, 859
- Dreyer J. L. E., 1888, [MmRAS](#), **49**, 1
- Drimmel R., Spergel D. N., 2001, [ApJ](#), **556**, 181
- Drlica-Wagner A., et al., 2020, [ApJ](#), **893**, 47
- Dutton A. A., Macciò A. V., 2014, [MNRAS](#), **441**, 3359
- Dwek E., et al., 1995, [ApJ](#), **445**, 716
- Efstathiou G., Jones B. J. T., 1979, [MNRAS](#), **186**, 133
- Efstathiou G., Silk J., 1983, [Fund. Cosmic Phys.](#), **9**, 1
- Eggen O. J., Lynden-Bell D., Sandage A. R., 1962, [ApJ](#), **136**, 748
- Eilers A.-C., Hogg D. W., Rix H.-W., Ness M. K., 2019, [ApJ](#), **871**, 120
- Einasto J., Saar E., Kaasik A., Chernin A. D., 1974, [Nature](#), **252**, 111
- Eisenstein D. J., et al., 2005, [ApJ](#), **633**, 560
- Eliche-Moral M. C., Rodríguez-Pérez C., Borlaff A., Querejeta M., Tapia T., 2018, [A&A](#), **617**, A113
- Erkal D., et al., 2021, [MNRAS](#), **506**, 2677
- Errani R., Penarrubia J., Tormen G., 2015, [MNRAS](#), **449**, L46
- Evans N. W., An J., Walker M. G., 2009, [MNRAS](#), **393**, L50
- Ewen H. I., Purcell E. M., 1951, [Nature](#), **168**, 356
- Faber S. M., Gallagher J. S., 1979, [ARA&A](#), **17**, 135
- Falcón-Barroso J., Sánchez-Blázquez P., Vazdekis A., Ricciardelli E., Cardiel N., Cenarro A. J., Gorgas J., Peletier R. F., 2011, [A&A](#), **532**, A95
- Fall S. M., Efstathiou G., 1980, [MNRAS](#), **193**, 189
- Famaey B., McGaugh S. S., 2012, [Living Reviews in Relativity](#), **15**, 10
- Farouki R. T., Shapiro S. L., 1982, [ApJ](#), **259**, 103
- Faucher-Giguère C.-A., Lidz A., Zaldarriaga M., Hernquist L., 2009, [ApJ](#), **703**, 1416
- Fich M., Blitz L., Stark A. A., 1989, [ApJ](#), **342**, 272
- Friedmann A., 1922, [Zeitschrift fur Physik](#), **10**, 377

Bibliographie

- Fritz T. K., Battaglia G., Pawlowski M. S., Kallivayalil N., van der Marel R., Sohn S. T., Brook C., Besla G., 2018, [A&A](#), **619**, A103
- Fritz T. K., Di Cintio A., Battaglia G., Brook C., Taibi S., 2020, [MNRAS](#), **494**, 5178
- Fukugita M., Hogan C. J., Peebles P. J. E., 1998, [ApJ](#), **503**, 518
- GRAVITY Collaboration et al., 2019, [A&A](#), **625**, L10
- Gaia Collaboration et al., 2021a, [A&A](#), **649**, A7
- Gaia Collaboration et al., 2021b, [A&A](#), **649**, A8
- Gaia Collaboration et al., 2023, [A&A](#), **674**, A1
- Gamow G., 1946, [Physical Review](#), **70**, 572
- Gamow G., 1948, [Physical Review](#), **74**, 505
- Gamow G., Teller E., 1939, [Nature](#), **143**, 116
- Garrison-Kimmel S., et al., 2017, [MNRAS](#), **471**, 1709
- Garrison-Kimmel S., et al., 2019a, [MNRAS](#), **487**, 1380
- Garrison-Kimmel S., et al., 2019b, [MNRAS](#), **487**, 1380
- Genina A., et al., 2020, [MNRAS](#), **498**, 144
- Gerhard O. E., 1981, [MNRAS](#), **197**, 179
- Gilbert K. M., et al., 2009, [ApJ](#), **705**, 1275
- Gingold R. A., Monaghan J. J., 1977, [MNRAS](#), **181**, 375
- Giodini S., et al., 2009, [ApJ](#), **703**, 982
- Gnedin O. Y., Ostriker J. P., 1999, [ApJ](#), **513**, 626
- Gordon K. D., et al., 2006, [ApJ](#), **638**, L87
- Governato F., et al., 2010, [Nature](#), **463**, 203
- Grand R. J. J., et al., 2017, [MNRAS](#), **467**, 179
- Grand R. J. J., Fragkoudi F., Gómez F. A., Jenkins A., Marinacci F., Pakmor R., Springel V., 2024, [MNRAS](#), **532**, 1814
- Gravity Collaboration et al., 2023, [A&A](#), **677**, L10
- Grcevich J., Putman M. E., 2009, [ApJ](#), **696**, 385
- Grillmair C. J., 2006, [ApJ](#), **645**, L37
- Hagen J. H. J., Helmi A., Breddels M. A., 2019, [A&A](#), **632**, A99
- Hammer F., Flores H., Elbaz D., Zheng X. Z., Liang Y. C., Cesarsky C., 2005, [A&A](#), **430**, 115
- Hammer F., Puech M., Chemin L., Flores H., Lehnert M. D., 2007, [ApJ](#), **662**, 322

- Hammer F., Flores H., Puech M., Yang Y. B., Athanassoula E., Rodrigues M., Delgado R., 2009, *A&A*, **507**, 1313
- Hammer F., Yang Y. B., Wang J. L., Puech M., Flores H., Fouquet S., 2010, *ApJ*, **725**, 542
- Hammer F., Yang Y. B., Flores H., Puech M., Fouquet S., 2015, *ApJ*, **813**, 110
- Hammer F., Yang Y. B., Wang J. L., Ibata R., Flores H., Puech M., 2018a, *MNRAS*, **475**, 2754
- Hammer F., Yang Y., Arenou F., Babusiaux C., Wang J., Puech M., Flores H., 2018b, *ApJ*, **860**, 76
- Hammer F., Yang Y., Wang J., Arenou F., Puech M., Flores H., Babusiaux C., 2019, *ApJ*, **883**, 171
- Hammer F., Yang Y., Arenou F., Wang J., Li H., Bonifacio P., Babusiaux C., 2020, *ApJ*, **892**, 3
- Hammer F., et al., 2023, *MNRAS*, **519**, 5059
- Hammer F., et al., 2024, *MNRAS*, **527**, 2718
- Hargreaves J. C., Gilmore G., Irwin M. J., Carter D., 1994a, *MNRAS*, **269**, 957
- Hargreaves J. C., Gilmore G., Irwin M. J., Carter D., 1994b, *MNRAS*, **271**, 693
- Harrington R. G., Wilson A. G., 1950, *PASP*, **62**, 118
- Hawkins K., Jofré P., Masseron T., Gilmore G., 2015, *MNRAS*, **453**, 758
- Haywood M., Lehnert M. D., Di Matteo P., Snaith O., Schultheis M., Katz D., Gómez A., 2016, *A&A*, **589**, A66
- Haywood M., Di Matteo P., Lehnert M. D., Snaith O., Khoperskov S., Gómez A., 2018, *ApJ*, **863**, 113
- Helmi A., 2008, *A&A Rev.*, **15**, 145
- Helmi A., et al., 2006, *ApJ*, **651**, L121
- Helmi A., Babusiaux C., Koppelman H. H., Massari D., Veljanoski J., Brown A. G. A., 2018, *Nature*, **563**, 85
- Hendricks B., Koch A., Lanfranchi G. A., Boeche C., Walker M., Johnson C. I., Peñarrubia J., Gilmore G., 2014, *ApJ*, **785**, 102
- Hinshaw G., et al., 2013, *ApJS*, **208**, 19
- Hodge P. W., 1961, *AJ*, **66**, 83
- Hogg D. W., Eilers A.-C., Rix H.-W., 2019, *AJ*, **158**, 147
- Honma M., Sofue Y., 1997, *PASJ*, **49**, 453
- Honma M., et al., 2012, *PASJ*, **64**, 136
- Hopkins P. F., 2015, *MNRAS*, **450**, 53
- Hopkins P. F., et al., 2010, *ApJ*, **715**, 202

- Hopkins P. F., Quataert E., Murray N., 2011, [MNRAS](#), **417**, 950
- Hopkins P. F., Kereš D., Oñorbe J., Faucher-Giguère C.-A., Quataert E., Murray N., Bullock J. S., 2014, [MNRAS](#), **445**, 581
- Hopkins P. F., et al., 2018, [MNRAS](#), **480**, 800
- Huang Y., et al., 2016, [MNRAS](#), **463**, 2623
- Hubble E. P., 1917, PhD thesis, University of Chicago
- Hubble E. P., 1925, [The Observatory](#), **48**, 139
- Hubble E. P., 1926, [ApJ](#), **64**, 321
- Hubble E., 1929, [Proceedings of the National Academy of Science](#), **15**, 168
- Hubble E. P., 1936, [Realm of the Nebulae](#). Yale University Press
- Hui X., Ford H. C., Freeman K. C., Dopita M. A., 1995, [ApJ](#), **449**, 592
- Ibata R. A., Gilmore G., Irwin M. J., 1994, [Nature](#), **370**, 194
- Ibata R. A., Wyse R. F. G., Gilmore G., Irwin M. J., Suntzeff N. B., 1997, [AJ](#), **113**, 634
- Ibata R., Irwin M., Lewis G., Ferguson A. M. N., Tanvir N., 2001, [Nature](#), **412**, 49
- Ibata R. A., et al., 2013, [Nature](#), **493**, 62
- Ibata R. A., et al., 2014, [ApJ](#), **780**, 128
- Ibata R., et al., 2021, [ApJ](#), **914**, 123
- Ibata R., et al., 2024, [ApJ](#), **967**, 89
- Illingworth G., 1977, [ApJ](#), **218**, L43
- Irwin M., Hatzidimitriou D., 1995, [MNRAS](#), **277**, 1354
- Irwin M. J., Davies J. I., Disney M. J., Phillipps S., 1990, [MNRAS](#), **245**, 289
- Izumiura H., Deguchi S., Hashimoto O., Nakada Y., Onaka T., Ono T., Ukita N., Yamamura I., 1995, [ApJ](#), **453**, 837
- Izumiura H., Deguchi S., Fujii T., Kameya O., Matsumoto S., Nakada Y., Ootsubo T., Ukita N., 1999, [ApJS](#), **125**, 257
- Jacoby G. H., Ciardullo R., Ford H. C., 1990, [ApJ](#), **356**, 332
- Jardel J. R., Gebhardt K., Fabricius M. H., Drory N., Williams M. J., 2013, [ApJ](#), **763**, 91
- Jeans J. H., 1902, [Philosophical Transactions of the Royal Society of London Series A](#), **199**, 1
- Jeans J. H., 1929, [Astronomy and cosmogony](#). Cambridge University Press
- Jiao Y., Hammer F., Wang J. L., Yang Y. B., 2021, [A&A](#), **654**, A25
- Jiao Y., Hammer F., Wang H., Wang J., Amram P., Chemin L., Yang Y., 2023, [A&A](#), **678**, A208

- Jing Y. P., Suto Y., 2002, [ApJ](#), 574, 538
- Jogee S., et al., 2008, in Funes J. G., Corsini E. M., eds, Astronomical Society of the Pacific Conference Series Vol. 396, Formation and Evolution of Galaxy Disks. p. 337 ([arXiv:0802.3901](#)), doi:10.48550/arXiv.0802.3901
- Jurić M., et al., 2008, [ApJ](#), 673, 864
- Kahn F. D., Woltjer L., 1959, [ApJ](#), 130, 705
- Kallivayalil N., van der Marel R. P., Alcock C., 2006, [ApJ](#), 652, 1213
- Kamphuis J., Sancisi R., 1993, [A&A](#), 273, L31
- Kant I., 1755, Allgemeine Naturgeschichte und Theorie des Himmels. Fischer
- Karukes E. V., Benito M., Iocco F., Trotta R., Geringer-Sameth A., 2020, [J. Cosmology Astropart. Phys.](#), 2020, 033
- Katz N., 1992, [ApJ](#), 391, 502
- Katz N., Gunn J. E., 1991, [ApJ](#), 377, 365
- Katz N., Weinberg D. H., Hernquist L., 1996, [ApJS](#), 105, 19
- Kauffmann G., et al., 2003, [MNRAS](#), 346, 1055
- Kazantzidis S., Łokas E. L., Callegari S., Mayer L., Moustakas L. A., 2011, [ApJ](#), 726, 98
- Kennicutt Robert C. J., 1992, [ApJS](#), 79, 255
- Kennicutt R. C., Evans N. J., 2012, [ARA&A](#), 50, 531
- Kennicutt R. C., et al., 2011, [PASP](#), 123, 1347
- Kereš D., Katz N., Weinberg D. H., Davé R., 2005, [MNRAS](#), 363, 2
- Kerr F. J., 1957, [AJ](#), 62, 93
- Kewley L. J., Dopita M. A., Sutherland R. S., Heisler C. A., Trevena J., 2001, [ApJ](#), 556, 121
- Khoperskov S. A., Bertin G., 2015, [Journal of Plasma Physics](#), 81, 495810607
- King I., 1962, [AJ](#), 67, 471
- Klimentowski J., Łokas E. L., Kazantzidis S., Mayer L., Mamon G. A., 2009, [MNRAS](#), 397, 2015
- Klypin A., Kravtsov A. V., Valenzuela O., Prada F., 1999, [ApJ](#), 522, 82
- Koch A., Grebel E. K., Wyse R. F. G., Kleyna J. T., Wilkinson M. I., Harbeck D. R., Gilmore G. F., Evans N. W., 2006, [AJ](#), 131, 895
- Kochanek C. S., 1996, [ApJ](#), 457, 228
- Komatsu E., et al., 2009, [ApJS](#), 180, 330
- Koop O., Antoja T., Helmi A., Callingham T. M., Laporte C. F. P., 2024, [arXiv e-prints](#), p. [arXiv:2405.19028](#)

- Koposov S. E., et al., 2011, *ApJ*, 736, 146
- Koposov S. E., et al., 2023, *MNRAS*, 521, 4936
- Kroupa P., 2001, *MNRAS*, 322, 231
- Kroupa P., Theis C., Boily C. M., 2005, *A&A*, 431, 517
- Kroupa P., Pflamm-Altenburg J., Mazurenko S., Wu W., Thies I., Jadhav V., Jerabkova T., 2024, *ApJ*, 970, 94
- Kruijssen J. M. D., Pfeffer J. L., Reina-Campos M., Crain R. A., Bastian N., 2019, *MNRAS*, 486, 3180
- Kruijssen J. M. D., et al., 2020, *MNRAS*, 498, 2472
- Krumholz M. R., Gnedin N. Y., 2011, *ApJ*, 729, 36
- Kuhlen M., Weiner N., Diemand J., Madau P., Moore B., Potter D., Stadel J., Zemp M., 2010, *J. Cosmology Astropart. Phys.*, 2010, 030
- Lacey C., Cole S., 1993, *MNRAS*, 262, 627
- Lackner C. N., Cen R., Ostriker J. P., Joung M. R., 2012, *MNRAS*, 425, 641
- Laporte C. F. P., Johnston K. V., Gómez F. A., Garavito-Camargo N., Besla G., 2018, *MNRAS*, 481, 286
- Larson R. B., 1974, *MNRAS*, 166, 585
- Larson R. B., 1975, *MNRAS*, 173, 671
- Larson R. B., 1976, *MNRAS*, 176, 31
- Le Fèvre O., et al., 2000, *MNRAS*, 311, 565
- Leitherer C., et al., 1999, *The Astrophysical Journal Supplement Series*, 123, 3
- Lelli F., McGaugh S. S., Schombert J. M., 2016, *AJ*, 152, 157
- Lemaître G., 1927, *Annales de la Société Scientifique de Bruxelles*, 47, 49
- Lemaître G., 1931, *Nature*, 127, 706
- Li Z.-Z., Jing Y. P., Qian Y.-Z., Yuan Z., Zhao D.-H., 2017, *ApJ*, 850, 116
- Li Z.-Z., Qian Y.-Z., Han J., Li T. S., Wang W., Jing Y. P., 2020, *ApJ*, 894, 10
- Li H., Hammer F., Babusiaux C., Pawlowski M. S., Yang Y., Arenou F., Du C., Wang J., 2021a, *ApJ*, 916, 8
- Li S., Riess A. G., Busch M. P., Casertano S., Macri L. M., Yuan W., 2021b, *ApJ*, 920, 84
- Lian J., Zasowski G., Chen B., Imig J., Wang T., Boardman N., Liu X., 2024, *Nature Astronomy*,
- Licquia T. C., Newman J. A., 2015, *ApJ*, 806, 96
- Lifshitz E. M., 1946, *Zhurnal Eksperimentalnoi i Teoreticheskoi Fiziki*, 16, 587

- Lindqvist M., Winnberg A., Habing H. J., Matthews H. E., 1992, *A&AS*, **92**, 43
- Little B., Tremaine S., 1987, *ApJ*, **320**, 493
- Liu X.-L., Zhu M., Xu J.-L., Jiang P., Zhang C.-P., Yu N.-P., Wang J.-J., Yang Y.-B., 2024, *Research in Astronomy and Astrophysics*, **24**, 075020
- López-Corredoira M., Betancort-Rijo J., Beckman J. E., 2002a, *A&A*, **386**, 169
- López-Corredoira M., Cabrera-Lavers A., Garzón F., Hammersley P. L., 2002b, *A&A*, **394**, 883
- López-Sanjuan C., Balcells M., Pérez-González P. G., Barro G., García-Dabó C. E., Gallego J., Zamorano J., 2009, *A&A*, **501**, 505
- Lotz J. M., Jonsson P., Cox T. J., Croton D., Primack J. R., Somerville R. S., Stewart K., 2011, *ApJ*, **742**, 103
- Lucy L. B., 1974, *AJ*, **79**, 745
- Lucy L. B., 1977, *AJ*, **82**, 1013
- Lundmark K., 1925, *MNRAS*, **85**, 865
- Lundmark K., 1927, *Meddelanden fran Astronomiska Observatorium Uppsala*, **22**, 1
- Machalski J., Kozieł-Wierzbowska D., Jamrozy M., Saikia D. J., 2008, *ApJ*, **679**, 149
- Majewski S. R., Skrutskie M. F., Weinberg M. D., Ostheimer J. C., 2003, *ApJ*, **599**, 1082
- Majewski S. R., et al., 2004, *AJ*, **128**, 245
- Malhan K., et al., 2022, *ApJ*, **926**, 107
- Marinacci F., Pakmor R., Springel V., 2014, *MNRAS*, **437**, 1750
- Martin N. F., Ibata R. A., Chapman S. C., Irwin M., Lewis G. F., 2007, *MNRAS*, **380**, 281
- Martínez-Delgado D., Alonso-García J., Aparicio A., Gómez-Flechoso M. A., 2001, *ApJ*, **549**, L63
- Martínez-Delgado D., et al., 2010, *AJ*, **140**, 962
- Martinez G. D., Minor Q. E., Bullock J., Kaplinghat M., Simon J. D., Geha M., 2011, *ApJ*, **738**, 55
- Masseron T., Gilmore G., 2015, *MNRAS*, **453**, 1855
- Mateo M. L., 1998, *ARA&A*, **36**, 435
- Mateo M., Olszewski E., Welch D. L., Fischer P., Kunkel W., 1991, *AJ*, **102**, 914
- Mateo M., Mirabal N., Udalski A., Szymanski M., Kaluzny J., Kubik M., Krzeminski W., Stanek K. Z., 1996, *ApJ*, **458**, L13
- Mateo M., Olszewski E. W., Morrison H. L., 1998, *ApJ*, **508**, L55
- Mathewson D. S., Cleary M. N., Murray J. D., 1974, *ApJ*, **190**, 291
- Mayall N. U., 1951, *Publications of Michigan Observatory*, **10**, 19

Bibliographie

- Mayer L., Mastropietro C., Wadsley J., Stadel J., Moore B., 2006, MNRAS, 369, 1021
- McConnachie A. W., 2012, AJ, 144, 4
- McConnachie A. W., Côté P., 2010, ApJ, 722, L209
- McConnachie A. W., Venn K. A., 2020, AJ, 160, 124
- McGaugh S. S., 2005, ApJ, 632, 859
- McGaugh S. S., 2016, ApJ, 816, 42
- McGaugh S. S., Schombert J. M., 2014, AJ, 148, 77
- McGaugh S. S., Schombert J. M., Bothun G. D., de Blok W. J. G., 2000, ApJ, 533, L99
- McGaugh S. S., Schombert J. M., de Blok W. J. G., Zagursky M. J., 2010, ApJ, 708, L14
- McWilliam A., Zoccali M., 2010, ApJ, 724, 1491
- Meekins J. F., Fritz G., Chubb T. A., Friedman H., 1971, Nature, 231, 107
- Meidt S. E., et al., 2014, ApJ, 788, 144
- Merrifield M. R., 1992, AJ, 103, 1552
- Messier C., 1781, Catalogue des Nébuleuses et des Amas d'Étoiles (Catalog of Nebulae and Star Clusters), Connoissance des Temps ou des Mouvements Célestes, for 1784, p. 227-267
- Milgrom M., 1983a, ApJ, 270, 365
- Milgrom M., 1983b, ApJ, 270, 371
- Milgrom M., 1983c, ApJ, 270, 384
- Miller M. J., Bregman J. N., 2013, ApJ, 770, 118
- Minniti D., et al., 2010, New A, 15, 433
- Mo H. J., White S. D. M., 1996, MNRAS, 282, 347
- Momany Y., Zaggia S., Gilmore G., Piotto G., Carraro G., Bedin L. R., de Angeli F., 2006, A&A, 451, 515
- Moore B., Governato F., Quinn T., Stadel J., Lake G., 1998, ApJ, 499, L5
- Moreno E., Fernández-Trincado J. G., Pérez-Villegas A., Chaves-Velasquez L., Schuster W. J., 2022, MNRAS, 510, 5945
- Moustakas J., Kennicutt Robert C. J., 2006, ApJS, 164, 81
- Moustakas J., Kennicutt Robert C. J., Tremonti C. A., Dale D. A., Smith J.-D. T., Calzetti D., 2010, ApJS, 190, 233
- Mróz P., et al., 2019, ApJ, 870, L10
- Muñoz R. R., et al., 2006, ApJ, 649, 201
- Muñoz R. R., Majewski S. R., Johnston K. V., 2008, ApJ, 679, 346

- Muñoz R. R., Côté P., Santana F. A., Geha M., Simon J. D., Oyarzún G. A., Stetson P. B., Djorgovski S. G., 2018, [ApJ](#), **860**, 65
- Müller O., Pawłowski M. S., Jerjen H., Lelli F., 2018, [Science](#), **359**, 534
- Naidu R. P., et al., 2021, [ApJ](#), **923**, 92
- Nataf D. M., Udalski A., Gould A., Fouqué P., Stanek K. Z., 2010, [ApJ](#), **721**, L28
- Navarro J. F., Benz W., 1991, [ApJ](#), **380**, 320
- Navarro J. F., Steinmetz M., 1997, [ApJ](#), **478**, 13
- Navarro J. F., Steinmetz M., 2000, [ApJ](#), **538**, 477
- Navarro J. F., White S. D. M., 1993, [MNRAS](#), **265**, 271
- Navarro J. F., White S. D. M., 1994, [MNRAS](#), **267**, 401
- Navarro J. F., Frenk C. S., White S. D. M., 1995, [MNRAS](#), **275**, 56
- Navarro J. F., Frenk C. S., White S. D. M., 1997, [ApJ](#), **490**, 493
- Negroponte J., White S. D. M., 1983, [MNRAS](#), **205**, 1009
- Neichel B., et al., 2008, [A&A](#), **484**, 159
- Nelson D., et al., 2015, [Astronomy and Computing](#), **13**, 12
- Nelson D., et al., 2019, [MNRAS](#), **490**, 3234
- Neyman J., Page T., Scott E., 1961, [AJ](#), **66**, 633
- Nicastro F., Senatore F., Krongold Y., Mathur S., Elvis M., 2016, [ApJ](#), **828**, L12
- Nidever D. L., Majewski S. R., Butler Burton W., Nigra L., 2010, [ApJ](#), **723**, 1618
- Nishiyama K., Nakai N., 1998, in Sofue Y., ed., IAU Symposium Vol. 184, The Central Regions of the Galaxy and Galaxies. p. 245
- Noordermeer E., van der Hulst J. M., Sancisi R., Swaters R. S., van Albada T. S., 2007, [MNRAS](#), **376**, 1513
- O'Donnell J. E., 1994, [ApJ](#), **422**, 158
- Odenkirchen M., et al., 2001, [AJ](#), **122**, 2538
- Oei M. S. S. L., et al., 2024, [Nature](#), **633**, 537
- Oh K. S., Lin D. N. C., Aarseth S. J., 1995, [ApJ](#), **442**, 142
- Oh S.-H., et al., 2015, [AJ](#), **149**, 180
- Okamoto T., Eke V. R., Frenk C. S., Jenkins A., 2005, [MNRAS](#), **363**, 1299
- Oman K. A., Riley A. H., 2024, [MNRAS](#), **532**, L48
- Oort J. H., Rougoor G. W., 1960, [MNRAS](#), **121**, 171

- Ortolani S., Renzini A., Gilmozzi R., Marconi G., Barbuy B., Bica E., Rich R. M., 1995, *Nature*, **377**, 701
- Ostriker J. P., Peebles P. J. E., Yahil A., 1974, *ApJ*, **193**, L1
- Ou X., Eilers A.-C., Necib L., Frebel A., 2024, *MNRAS*, **528**, 693
- Pagnini G., Di Matteo P., Khoperskov S., Mastrobuono-Battisti A., Haywood M., Renaud F., Combes F., 2023, *A&A*, **673**, A86
- Pawlowski M. S., Pflamm-Altenburg J., Kroupa P., 2012, *MNRAS*, **423**, 1109
- Peñarrubia J., McConnachie A. W., Navarro J. F., 2008, *ApJ*, **672**, 904
- Peebles P. J. E., 1965, *ApJ*, **142**, 1317
- Peebles P. J., 1966, *Phys. Rev. Lett.*, **16**, 410
- Peebles P. J. E., 1971, *A&A*, **11**, 377
- Penzias A. A., 1961, *AJ*, **66**, 293
- Penzias A. A., Wilson R. W., 1965, *ApJ*, **142**, 1149
- Persic M., Salucci P., eds, 1997, Dark and Visible Matter in Galaxies Astronomical Society of the Pacific Conference Series Vol. 117
- Peschken N., Łokas E. L., Athanassoula E., 2020, *MNRAS*, **493**, 1375
- Piatek S., Pryor C., 1995, *AJ*, **109**, 1071
- Piatek S., Pryor C., Olszewski E. W., 2008, *AJ*, **135**, 1024
- Piatti A. E., Webb J. J., Carlberg R. G., 2019, *MNRAS*, **489**, 4367
- Piddington J. H., Minnett H. C., 1951, *Australian Journal of Scientific Research A Physical Sciences*, **4**, 459
- Piffl T., et al., 2014, *MNRAS*, **445**, 3133
- Pillepich A., et al., 2018, *MNRAS*, **473**, 4077
- Pilyugin L. S., Tautvaišienė G., Lara-López M. A., 2023, *A&A*, **676**, A57
- Planck Collaboration et al., 2014, *A&A*, **571**, A16
- Planck Collaboration et al., 2020, *A&A*, **641**, A6
- Plummer H. C., 1911, *MNRAS*, **71**, 460
- Poggio E., et al., 2018, *MNRAS*, **481**, L21
- Portail M., Wegg C., Gerhard O., Martinez-Valpuesta I., 2015, *MNRAS*, **448**, 713
- Posti L., 2022, *Research Notes of the American Astronomical Society*, **6**, 233
- Queloz D., Dubath P., Pasquini L., 1995, *A&A*, **300**, 31
- Read J. I., Wilkinson M. I., Evans N. W., Gilmore G., Kleyna J. T., 2006, *MNRAS*, **366**, 429

- Reid M. J., 2008, in Jin W. J., Platais I., Perryman M. A. C., eds, IAU Symposium Vol. 248, A Giant Step: from Milli- to Micro-arcsecond Astrometry. pp 141–147, doi:10.1017/S1743921308018929
- Reid M. J., Brunthaler A., 2004, *ApJ*, 616, 872
- Reid M. J., et al., 2014, *ApJ*, 783, 130
- Reid M. J., et al., 2019, *ApJ*, 885, 131
- Reinmuth K., 1926, Veroeffentlichungen der Badischen Landes-Sternwarte zu Heidelberg, 9, 1
- Reshetnikov V., Combes F., 1998, *A&A*, 337, 9
- Revaz Y., Pfenniger D., 2004, *A&A*, 425, 67
- Reynolds J. H., 1920, *MNRAS*, 80, 746
- Roberts M. S., 1966, *ApJ*, 144, 639
- Roberts M. S., 1975, in Hayli A., ed., IAU Symposium Vol. 69, Dynamics of the Solar Systems. p. 331
- Roberts M. S., Rots A. H., 1973, *A&A*, 26, 483
- Robertson B., Yoshida N., Springel V., Hernquist L., 2004, *ApJ*, 606, 32
- Robertson B., Bullock J. S., Cox T. J., Di Matteo T., Hernquist L., Springel V., Yoshida N., 2006, *ApJ*, 645, 986
- Rocha M., Peter A. H. G., Bullock J., 2012, *MNRAS*, 425, 231
- Rogstad D. H., Shostak G. S., 1972, *ApJ*, 176, 315
- Rubin V. C., Ford W. Kent J., 1970, *ApJ*, 159, 379
- Rubin V. C., Ford W. K. J., Thonnard N., 1978, *ApJ*, 225, L107
- Rusakov V., Monelli M., Gallart C., Fritz T. K., Ruiz-Lara T., Bernard E. J., Cassisi S., 2021, *MNRAS*, 502, 642
- Sakamoto K., Okumura S. K., Ishizuki S., Scoville N. Z., 1999, *ApJS*, 124, 403
- Sakamoto T., Chiba M., Beers T. C., 2003, *A&A*, 397, 899
- Samuel J., et al., 2020, *MNRAS*, 491, 1471
- Sánchez-Blázquez P., et al., 2006, *MNRAS*, 371, 703
- Sánchez-Saavedra M. L., Battaner E., Guijarro A., López-Corredoira M., Castro-Rodríguez N., 2003, *A&A*, 399, 457
- Sancisi R., 2004, in Ryder S., Pisano D., Walker M., Freeman K., eds, IAU Symposium Vol. 220, Dark Matter in Galaxies. p. 233 ([arXiv:astro-ph/0311348](https://arxiv.org/abs/astro-ph/0311348)), doi:10.48550/arXiv.astro-ph/0311348
- Sandage A., 1961, The Hubble Atlas of Galaxies. Carnegie Institution of Washington

- Sandage A., 2005, *ARA&A*, **43**, 581
- Santistevan I. B., Wetzel A., Tollerud E., Sanderson R. E., Samuel J., 2023, *MNRAS*, **518**, 1427
- Sauvaget T., Hammer F., Puech M., Yang Y. B., Flores H., Rodrigues M., 2018, *MNRAS*, **473**, 2521
- Schaye J., et al., 2015, *MNRAS*, **446**, 521
- Schlafly K. C., et al., 2009, *ApJ*, **703**, 2177
- Schlegel D. J., Finkbeiner D. P., Davis M., 1998, *ApJ*, **500**, 525
- Schmidt M., 1963, *ApJ*, **137**, 758
- Schönrich R., Binney J., Dehnen W., 2010, *MNRAS*, **403**, 1829
- Schwarzschild M., 1954, *AJ*, **59**, 273
- Sellwood J. A., Debattista V. P., 2022, *MNRAS*, **510**, 1375
- Sersic J. L., 1968, Atlas de Galaxias Australes. Observatorio Astronomico, Cordoba, Argentina
- Shapley H., 1918, *PASP*, **30**, 42
- Shapley H., 1927, Harvard College Observatory Bulletin, **849**, 1
- Shapley H., 1938a, *Nature*, **142**, 715
- Shapley H., 1938b, Harvard College Observatory Bulletin, **908**, 1
- Shapley H., 1939, *Proceedings of the National Academy of Science*, **25**, 565
- Shen J., Sellwood J. A., 2006, *MNRAS*, **370**, 2
- Siegel M. H., Majewski S. R., Reid I. N., Thompson I. B., 2002, *ApJ*, **578**, 151
- Siegel M. H., Shetrone M. D., Irwin M., 2008, *AJ*, **135**, 2084
- Silk J., 1968, *ApJ*, **151**, 459
- Simon J. D., 2019, *ARA&A*, **57**, 375
- Simon J. D., Geha M., 2007, *ApJ*, **670**, 313
- Skowron D. M., et al., 2019, *Science*, **365**, 478
- Skrutskie M. F., et al., 2006, *AJ*, **131**, 1163
- Slipher V. M., 1914, Lowell Observatory Bulletin, **2**, 66
- Smith J. D. T., et al., 2007, *ApJ*, **656**, 770
- Sofue Y., 1996, *ApJ*, **458**, 120
- Sofue Y., 2013, *PASJ*, **65**, 118
- Sofue Y., 2015, *PASJ*, **67**, 75
- Sofue Y., Rubin V., 2001, *ARA&A*, **39**, 137

- Sohn S. T., Anderson J., van der Marel R. P., 2012, *ApJ*, 753, 7
- Sommer-Larsen J., Gelato S., Vedel H., 1999, *ApJ*, 519, 501
- Spergel D. N., et al., 2007, *ApJS*, 170, 377
- Springel V., 2005, *MNRAS*, 364, 1105
- Springel V., Hernquist L., 2005, *ApJ*, 622, L9
- Stark D. V., McGaugh S. S., Swaters R. A., 2009, *AJ*, 138, 392
- Starkenburg E., et al., 2010, *A&A*, 513, A34
- Staudaher S. M., Dale D. A., van Zee L., Barnes K. L., Cook D. O., 2015, *MNRAS*, 454, 3613
- Stewart K. R., Bullock J. S., Wechsler R. H., Maller A. H., 2009, *ApJ*, 702, 307
- Stinson G. S., Bailin J., Couchman H., Wadsley J., Shen S., Nickerson S., Brook C., Quinn T., 2010, *MNRAS*, 408, 812
- Strigari L. E., Frenk C. S., White S. D. M., 2017, *ApJ*, 838, 123
- Strigari L. E., Frenk C. S., White S. D. M., 2018, *ApJ*, 860, 56
- Sutter J., Fadda D., 2022, *ApJ*, 926, 82
- Tapia T., Eliche-Moral M. C., Aceves H., Rodríguez-Pérez C., Borlaff A., Querejeta M., 2017, *A&A*, 604, A105
- Tarter J., Silk J., 1974, *QJRAS*, 15, 122
- Thacker R. J., Couchman H. M. P., 2000, *ApJ*, 545, 728
- Tolstoy E., et al., 2004, *ApJ*, 617, L119
- Tolstoy E., Hill V., Tosi M., 2009, *ARA&A*, 47, 371
- Toomre A., 1977, in Tinsley B. M., Larson Richard B. Gehret D. C., eds, Evolution of Galaxies and Stellar Populations. p. 401
- Toomre A., Toomre J., 1972, *ApJ*, 178, 623
- Toth G., Ostriker J. P., 1992, *ApJ*, 389, 5
- Trachternach C., de Blok W. J. G., McGaugh S. S., van der Hulst J. M., Dettmar R. J., 2009, *A&A*, 505, 577
- Trimble V., 1987, *ARA&A*, 25, 425
- Tully R. B., et al., 2023, *ApJ*, 944, 94
- Tumlinson J., Peebles M. S., Werk J. K., 2017, *ARA&A*, 55, 389
- Turnrose B. E., Rood H. J., 1970, *ApJ*, 159, 773
- Valenzuela L. M., Remus R.-S., McKenzie M., Forbes D. A., 2024, *A&A*, 687, A104
- Van den Bergh S., 1969, *Nature*, 224, 891

- Vasiliev E., Belokurov V., Erkal D., 2021, [MNRAS](#), **501**, 2279
- Vazdekis A., Koleva M., Ricciardelli E., Röck B., Falcón-Barroso J., 2016, [MNRAS](#), **463**, 3409
- Vorontsov-Vel'Yaminov B. A., Arkhipova V. P., 1962, Morphological catalogue of galaxies, [C01](#), **0**
- Wadsley J. W., Stadel J., Quinn T., 2004, [New A](#), **9**, 137
- Wagoner R. V., Fowler W. A., Hoyle F., 1967, [ApJ](#), **148**, 3
- Walker M., 2013, in Oswalt T. D., Gilmore G., eds, , Vol. 5, Planets, Stars and Stellar Systems. Volume 5: Galactic Structure and Stellar Populations. Springer, p. 1039, doi:[10.1007/978-94-007-5612-0_20](https://doi.org/10.1007/978-94-007-5612-0_20)
- Walker M. G., Peñarrubia J., 2011, [ApJ](#), **742**, 20
- Walker M. G., Mateo M., Olszewski E. W., 2009a, [AJ](#), **137**, 3100
- Walker M. G., Mateo M., Olszewski E. W., Peñarrubia J., Evans N. W., Gilmore G., 2009b, [ApJ](#), **704**, 1274
- Walter F., Brinks E., de Blok W. J. G., Bigiel F., Kennicutt Robert C. J., Thornley M. D., Leroy A., 2008, [AJ](#), **136**, 2563
- Wang J., Hammer F., Athanassoula E., Puech M., Yang Y., Flores H., 2012, [A&A](#), **538**, A121
- Wang J., Hammer F., Puech M., Yang Y., Flores H., 2015, [MNRAS](#), **452**, 3551
- Wang H.-F., Liu C., Xu Y., Wan J.-C., Deng L., 2018, [MNRAS](#), **478**, 3367
- Wang J., Hammer F., Yang Y., Ripepi V., Cioni M.-R. L., Puech M., Flores H., 2019a, [MNRAS](#), **486**, 5907
- Wang M. Y., et al., 2019b, [ApJ](#), **875**, L13
- Wang W., Han J., Cautun M., Li Z., Ishigaki M. N., 2020a, [Science China Physics, Mechanics, and Astronomy](#), **63**, 109801
- Wang H. F., et al., 2020b, [ApJ](#), **897**, 119
- Wang J., Hammer F., Yang Y., 2022a, [MNRAS](#), **510**, 2242
- Wang H.-F., Hammer F., Yang Y.-B., Wang J.-L., 2022b, [ApJ](#), **940**, L3
- Wang H.-F., Chrobáková Ž., López-Corredoira M., Sylos Labini F., 2023, [ApJ](#), **942**, 12
- Wang J., Hammer F., Yang Y., Pawłowski M. S., Mamon G. A., Wang H., 2024, [MNRAS](#), **527**, 7144
- Warren M. S., Quinn P. J., Salmon J. K., Zurek W. H., 1992, [ApJ](#), **399**, 405
- Watkins L. L., Evans N. W., An J. H., 2010, [MNRAS](#), **406**, 264
- Watkins L. L., van der Marel R. P., Sohn S. T., Evans N. W., 2019, [ApJ](#), **873**, 118
- Wegg C., Gerhard O., 2013, [MNRAS](#), **435**, 1874

- Wegg C., Gerhard O., Portail M., 2015, [MNRAS](#), **450**, 4050
- Weiland J. L., et al., 1994, [ApJ](#), **425**, L81
- Weinberg M. D., Blitz L., 2006, [ApJ](#), **641**, L33
- Weisz D. R., et al., 2014a, [ApJ](#), **789**, 24
- Weisz D. R., Dolphin A. E., Skillman E. D., Holtzman J., Gilbert K. M., Dalcanton J. J., Williams B. F., 2014b, [ApJ](#), **789**, 147
- Wetzel A., Garrison-Kimmel S., 2020a, GizmoAnalysis: Read and analyze Gizmo simulations, Astrophysics Source Code Library, record ascl:2002.015
- Wetzel A., Garrison-Kimmel S., 2020b, HaloAnalysis: Read and analyze halo catalogs and merger trees, Astrophysics Source Code Library, record ascl:2002.014
- Wetzel A. R., Hopkins P. F., Kim J.-h., Faucher-Giguère C.-A., Kereš D., Quataert E., 2016, [ApJ](#), **827**, L23
- Wetzel A., et al., 2023, [ApJS](#), **265**, 44
- White S. D. M., Frenk C. S., 1991, [ApJ](#), **379**, 52
- White S. D. M., Rees M. J., 1978, [MNRAS](#), **183**, 341
- Wilkinson M. I., Kleyna J., Evans N. W., Gilmore G., 2002, [MNRAS](#), **330**, 778
- Wilkinson M. I., Kleyna J. T., Evans N. W., Gilmore G. F., Irwin M. J., Grebel E. K., 2004, [ApJ](#), **611**, L21
- Williams B. F., et al., 2015, [ApJ](#), **806**, 48
- Willis A. G., Strom R. G., Wilson A. S., 1974, [Nature](#), **250**, 625
- Willman B., Geha M., Strader J., Strigari L. E., Simon J. D., Kirby E., Ho N., Warres A., 2011, [AJ](#), **142**, 128
- Wilson A. G., 1955, [PASP](#), **67**, 27
- Wolf M., 1908, [MNRAS](#), **69**, 117
- Wolf M., 1914, [Ges](#), **49**, 162
- Wolf J., Martinez G. D., Bullock J. S., Kaplinghat M., Geha M., Muñoz R. R., Simon J. D., Avedo F. F., 2010, [MNRAS](#), **406**, 1220
- Wright T., 1750, An original theory or new hypothesis of the universe : founded upon general phaenomena of the visible creation; and particularly the Via the laws of nature, and solving by mathematical principles : the Lactea ...compris'd in nine familiar letters from the author to his friendand : illustrated with upward of thirty graven and mezzotinto plates Chapelle, doi:10.3931/e-rara-28672
- Yang Y., Hammer F., Fouquet S., Flores H., Puech M., Pawlowski M. S., Kroupa P., 2014, [MNRAS](#), **442**, 2419
- Yang Y., Hammer F., Jiao Y., Pawlowski M. S., 2022, [MNRAS](#), **512**, 4171

Bibliographie

- Young J. S., et al., 1995, [ApJS](#), **98**, 219
- Zhang J., Abraham R., van Dokkum P., Merritt A., Janssens S., 2018, [ApJ](#), **855**, 78
- Zhou Y., Li X., Huang Y., Zhang H., 2023, [ApJ](#), **946**, 73
- Zobnina D. I., Zasov A. V., 2020, [Astronomy Reports](#), **64**, 295
- Zwicky F., 1933, [Helvetica Physica Acta](#), **6**, 110
- de Blok W. J. G., Walter F., Brinks E., Trachternach C., Oh S. H., Kennicutt R. C. J., 2008, [AJ](#), **136**, 2648
- de Boer T. J. L., Fraser M., 2016, [A&A](#), **590**, A35
- de Boer T. J. L., Tolstoy E., Saha A., Olszewski E. W., 2013, [A&A](#), **551**, A103
- de Vaucouleurs G., 1948, [Annales d'Astrophysique](#), **11**, 247
- de Vaucouleurs G., 1959, [Handbuch der Physik](#), **53**, 311
- del Pino A., Hidalgo S. L., Aparicio A., Gallart C., Carrera R., Monelli M., Buonanno R., Marconi G., 2013, [MNRAS](#), **433**, 1505
- van de Hulst H. C., 1945, [Nederlandsch Tijdschrift voor Natuurkunde](#), **11**, 210
- van de Hulst H. C., Raimond E., van Woerden H., 1957, [Bull. Astron. Inst. Netherlands](#), **14**, 1
- van der Kruit P. C., Bosma A., 1978, [A&AS](#), **34**, 259
- van der Kruit P. C., Freeman K. C., 2011, [ARA&A](#), **49**, 301
- van der Marel R. P., Fardal M., Besla G., Beaton R. L., Sohn S. T., Anderson J., Brown T., Guhathakurta P., 2012, [ApJ](#), **753**, 8

RÉSUMÉ

La masse est une quantité physique fondamentale dans l'étude des galaxies, influençant notre compréhension de la formation et de l'évolution des galaxies. Dans cette thèse, j'étudie les méthodes d'estimation de la masse des galaxies, en me concentrant sur la Voie Lactée et les galaxies spirales voisines.

La mission *Gaia* fournit des données en six dimensions sur les étoiles, permettant de dériver la courbe de rotation de la Voie Lactée la plus précise. En utilisant la courbe de rotation basée sur *Gaia* DR2, j'ai comparé divers profils de matière sombre et j'ai constaté que le profil Einasto fournit une meilleure estimation de la masse par rapport aux profils NFW et gNFW, qui sont trop peu profonds pour ajuster la courbe de rotation décroissante. Avec *Gaia* DR3, j'ai dérivé une nouvelle courbe de rotation de la Voie Lactée, menant une analyse complète des incertitudes systématiques. Pour la première fois, nous avons détecté un déclin Képlérien dans la courbe de rotation, commençant au bord du disque (19 kpc). Nos estimations actuelles placent la masse de la Galaxie à environ $2,5 \times 10^{11} M_{\odot}$ dans 25 kpc, avec une limite supérieure de $5,6 \times 10^{11} M_{\odot}$. En conséquence, la fraction de masse baryonique semble plus grande que l'estimation universelle du modèle Λ CDM, suggérant que la Voie Lactée ne fait pas face au problème des baryons manquants, mais plutôt à un excès de baryons. Cette découverte remet en question notre compréhension de la distribution de masse entre la matière sombre et les baryons pour notre Galaxie.

Le déclin Képlérien observé dans la courbe de rotation de la Voie Lactée contraste avec les courbes de rotation plates trouvées dans la plupart des galaxies spirales. Cependant, les observations suggèrent que la plupart des galaxies spirales ont subi une grande fusion en moyenne il y a environ 6 Gyr. Cela m'a amené à étendre mes recherches aux galaxies voisines, évaluant la fiabilité de leurs courbes de rotation à grands rayons pour déterminer si ces courbes de rotation suivent la distribution de masse après des fusions récentes. J'ai sélectionné neuf galaxies des bases de données SPARC et THINGS et, en examinant leurs caractéristiques morphologiques, leurs structures cinématiques et leurs histoires de formation stellaire, j'ai conclu que certaines d'entre elles ont probablement connu une grande fusion récente. En comparant ces observations avec des simulations hydrodynamiques, j'ai évalué l'impact de ces fusions sur les courbes de rotation et les estimations de masse. Cette étude suggère que l'utilisation des courbes de rotation pour estimer la distribution de masse des galaxies spirales à grands rayons doit être abordée avec prudence, en particulier l'état d'équilibre des galaxies.

Le scénario de formation hiérarchique prédit une corrélation entre le temps de chute des satellites dans le halo de la Galaxie et leur énergie de liaison, une relation soutenue par des simulations cosmologiques avec une faible dispersion. Nous avons dérivé cette relation pour diverses simulations cosmologiques. En comparant ces relations avec les mesures de *Gaia* des amas globulaires et des galaxies naines autour de la Voie Lactée avec une hypothèse de potentiel de la Voie Lactée, nous avons constaté que cette relation suggère que la plupart des galaxies naines sont arrivées bien plus récemment dans le halo de la Galaxie et qu'une masse de la Galaxie de $2 \times 10^{11} M_{\odot}$ dans les 21 kpc s'aligne bien avec la relation prédictive entre le temps de chute et l'énergie de liaison.

MOTS CLÉS

Galaxies: cinématique et dynamique, Galaxies: contenu stellaire, Galaxies: structure, Galaxies: paramètres fondamentaux

ABSTRACT

The mass is a fundamental physical quantity in galaxy studies, influencing our understanding of galaxy formation and evolution. In this thesis, I investigate mass estimation methods for galaxies, focusing on the Milky Way (MW) and nearby spiral galaxies.

The *Gaia* mission provides six-dimensional data of stars, enabling the derivation of the most accurate MW rotation curve (RC). Using the RC based on *Gaia* DR2, I compared various dark matter (DM) profiles and found that the Einasto profile provides a better mass estimate compared to the NFW and gNFW profiles, which are too shallow to fit the declining RC. With *Gaia* DR3, I derived a new MW RC, conducting a comprehensive analysis of systematic uncertainties. For the first time, we detected a Keplerian decline in the RC, starting at the edge of the disk (19 kpc). Our current estimates place the MW mass within 25 kpc at approximately $2.5 \times 10^{11} M_{\odot}$, with an upper limit of $5.6 \times 10^{11} M_{\odot}$. Consequently, the baryonic mass fraction appears larger than the universal estimate from the Λ CDM model, suggesting that the MW may not face the missing baryon problem, but rather an excess baryon problem. This finding challenges our current understanding of the mass distribution between DM and baryons for our Galaxy.

The observed Keplerian decline in the MW RC contrasts with the flat RCs found in most spiral galaxies. However, observations suggest that most spiral galaxies underwent a major merger on average approximately 6 Gyr ago. This led me to extend my research to nearby galaxies, assessing the reliability of their RCs at large radii to determine whether these RCs follow the mass distribution after recent major mergers. I selected nine galaxies from the SPARC and THINGS databases and, by examining their morphological features, kinematical structures, and star formation histories, concluded that some of them likely experienced a recent major merger. By comparing these observations with hydrodynamical simulations, I assessed the impact of these mergers on the RCs and mass estimations. This study suggests that using RCs to estimate the mass distribution of spiral galaxies at large radii should be approached with caution, particularly regarding the equilibrium state of galaxies.

The hierarchical formation scenario predicts a correlation between the infall lookback time of satellites and their binding energy, a relationship supported by cosmological simulations with a small scatter. We derived this relation for various cosmological simulations and compared it with *Gaia* measurements of globular clusters and dwarf galaxies around the MW, assuming an MW potential. Our results suggest that most dwarf galaxies are newcomers in the MW halo, and that the MW mass of $2 \times 10^{11} M_{\odot}$ within 21 kpc aligns well with the predicted relationship between infall lookback time and binding energy.

KEYWORDS

Galaxies: kinematics and dynamics, Galaxies: stellar content, Galaxies: structure, Galaxies: fundamental parameters